DISSERTATION

PRECIPITATING CONVECTIVE CLOUD DOWNDRAFT STRUCTURE: A SYNTHESIS OF OBSERVATIONS AND MODELING

Submitted by

Kevin Robert Knupp

Department of Atmospheric Science

In partial fulfillment of the requirements

for the Degree of Doctor of Philosophy

Colorado State University

Fort Collins, Colorado

Spring, 1985

COLORADO STATE UNIVERSITY

February 27, 1985

WE HEREBY RECOMMEND THAT THE THESIS PREPARED UNDER OUR SUPERVISION BY KEVIN R. KNUPP ENTITLED PRECIPITATING CONVECTIVE CLOUD DOWNDRAFT STRUCTURE: A SYNTHESIS OF OBSERVATIONS AND MODELING BE ACCEPTED AS FULFILLING IN PART REQUIREMENTS FOR THE DEGREE OF DOCTOR OF PHILOSOPHY.

COMMITTEE ON GRADUATE WORK

John Thomas Bunn

Duane E. Stevens

Peter C. Sinclair

Bogan Bernhardt

William R. Cotton

Adviser

Department Head

ABSTRACT OF DISSERTATION

PRECIPITATING CONVECTION CLOUD DOWNDRAFT STRUCTURE:
A SYNTHESIS OF OBSERVATIONS AND MODELING

This study represents a comprehensive investigation in which observations are integrated with three-dimensional cloud model results to examine the kinematic, dynamic and thermodynamic structure of downdrafts associated with precipitating convection. One particular downdraft type, the low-level precipitation-associated downdraft, is investigated in considerable detail. It is shown that this downdraft exhibits significant structural, dynamic and thermodynamic properties which differ appreciably from other independent downdrafts within precipitating convective clouds.

General airflow and trajectory patterns within low-level downdrafts are typically convergent from ~ 0.8 km upwards to downdraft top, typically less than 5 km AGL. Observed mass flux profiles often increase rapidly with decreasing height as a result of strong buoyancy forcing below the melting level. Such patterns indicate that strong cooling by melting and evaporation within statically unstable low levels generates low perturbation pressure by virtue of buoyantly-induced pressure perturbations. Cloud model results verify this process and indicate that pressure perturbations are strongest during downdraft developing stages. Maximum modeled pressure reductions up to 2 mb are located within downdrafts and precipitation about 0.6 km below the 273 K level approximately 10 min after heavy precipitation ($\gtrsim$ 2 g kg^{-1}) enters

low levels. The magnitude of this buoyantly-produced pressure reduction is influenced by temperature, static stability, relative humidity and precipitation characteristics.

Model results and related calculations indicate that cooling provides the impetus for downdraft formation. Melting, in particular is generally found to make significant contribution to total cooling in cases having relatively shallow (< 2 km) PBL. Cooling by evaporation becomes increasingly important as PBL depth increases.

Inflow to the low-level downdraft, although vertically continuous, can be separated into two branches. The up-down branch originating within the PBL initially rises up to 4 km and then descends within the main precipitation downdraft. The midlevel branch, most pronounced during early downdraft stages, originates from above the PBL and transports low-valued θ_e to low levels. Pressure forces important along both branches act to lift stable air along the up-down branch, and provide downward forcing of positively-buoyant air in the upper regions of both branches.

Two primary conclusions are drawn from the results of this study: (1) Downdrafts are driven at low levels within regions of strong static instability by strong cooling provided by melting and evaporation. Cloud level entrainment effects make secondary contributions. (2) Precipitation size and phase (e.g. melting) are probably the most important controlling parameters for downdraft strength.

Kevin Robert Knupp
Dept. of Atmospheric Science
Colorado State University
Fort Collins, Colorado 80523
Spring 1985

ACKNOWLEDGEMENTS

The unfailing support and ecnouragement from my thesis advisor, William R. Cotton, during this research program is greatly appreciated. He and other committee members, Drs. John M. Brown, Duane Stevens, Peter Sinclair, and Bogusz Bienkiewicz made valuable comments which have helped shape the final version of this manuscript.

Brenda Thompson and Nancy Duprey are recognized for efficient and expert manuscript preparation, and Lucy McCall helped in drafting many of the figures appearing in this report. Thanks are given to both who willingly put in many tedious hours. Appreciation is also extended to Jeanne Knupp who assisted in manuscript preparation and supported the author during the prolonged and final stages of this work.

Significant indirect contributions from a number of individuals helped make a comprehensive study such as this possible. Greg Tripoli is gratefully acknowledged for assististance with and discussions concerning cloud model and related analysis program software. He is recognized for writing, managing and maintaining much of the cloud model code and analysis programs. Other individuals from NCAR also deserve recongnition. Carl Mohr and Joanne Parish provided assistence with implementation of Doppler analysis and related software used in the radar analyses appearing in this report. These individuals along with L.J. Miller wrote and documented an excellent Doppler radar analysis software package. A surface objective analysis package was written and documented by Robin Vaughan and Carl Mohr, and an aircraft analysis

package was put together by James Fankhauser, Robin Vaughan and Carl Mohr. Discussions with Dr. Charles Knight on the 12 June CCOPE case, and with Jerome Schmidt on the 2 August CCOPE case were highly beneficial.

Most of the data used and analyzed in this report was provided by outside agencies. The Field Observing Facility of the National Center for Atmospheric Research (NCAR) furnished Doppler radar, aircraft, rawinsonde and surface mesonet data. Additional Doppler data were procured from the Wave Propagation Laboratory of the National Oceanic and Atmospheric Administration, and surface mesonet data and additional sounding information were afforded by the Bureau of Reclamation.

All computations were done on the NCAR Cray-1A computers. This research was sponsored by the National Science Foundation under Grants ATM-7908297, ATM-8113082 and ATM-8312077, by the National Aeronautics and Space Administration under Grant NSG-5341, and by the Air Force Geophysics Laboratory under Grant F19628-84-C-0005.

TABLE OF CONTENTS

LIST OF TABLES

LIST OF FIGURES

1. INTRODUCTION

Downdrafts associated with thunderstorms have long been recognized but are not fully understood. Early descriptions of thunderstorm phenomena by McFarland (1901), Humphries (1914) and others identified the presence of cold low-level outflow which originated from precipitating thunderstorm regions. These investigators correctly hypothesized that such flow was associated with downdrafts driven by precipitation evaporation and loading. Subsequent observational investigations since the 1940's have provided measurements of in-cloud downdraft properties and of downdraft outflow thermodynamics. More recently, multiple Doppler radar data and three-dimensional cloud modeling studies have further uncovered general convective storm properties, including downdraft characteristics. However, mechanisms which govern downdraft structure and dynamics remain rather nebulous.

Downdrafts are important in several respects. First, they accomplish significant vertical transport of static energy, mass and momentum within and near precipitating convective clouds, particularly at low levels. Such transports can significantly alter boundary layer thermodynamics over land masses and especially over oceans where fluxes of temperature and moisture from the surface can be significantly increased. Downdraft transports of mass and momentum additionally produce the low-level gust front which influences individual convective cloud propagation. Such transports also provide a means of low-level interaction among convective clouds comprising larger-scale convective

systems. Finally, downdraft mass and momentum transports occasionally produce damaging low-level winds and wind shears hazardous to aviation. Understanding of general downdraft processes therefore could potentially improve: (i) forecasting and nowcasting of severe downdraft outflows, (ii) understanding of convective storm dynamics, and (iii) current downdraft parameterizations in existing mesoscale numerical models.

This study represents a comprehensive observational and cloud modeling investigation on precipitating convective cloud downdraft structure and dynamics. Observational platforms include multiple Doppler radar, surface mesonet, aircraft and rawinsondes. Analysis of several data sets encompassing a variety of environmental conditions over the High Plains has been conducted from a case study approach. These observations are integrated with three-dimensional cloud model numerical experiments to examine the kinematic, dynamic and thermodynamic structure of downdrafts associated with precipitating convection.

At the onset of this investigation it was hypothesized that midlevel entrainment, or mixing between cloud and environment occurring as a result of midlevel environmental air entering cloud and precipitation regions, exerts an important influence on initiation and maintenance of downdrafts which produce cold surface outflow. Results quickly indicated that precipitation effects (evaporation, melting and loading) at low levels may dominate downdraft structure at low levels and above. Although important, cloud-level entrainment effects were found to make more secondary contributions.

Findings in this investigation were obtained from several sources. First, previous observational and modeling work on convective clouds was

examined closely and interpreted to provide a general (but limited) description of convective cloud downdraft structure. Compilation of many studies indicates that several types of independent downdrafts may exist simultaneously within precipitating convective clouds. These are: small-scale penetrative downdrafts, upper level downdrafts produced by updraft equilibrium overshoot, midlevel cloud-edge downdrafts, and low-level precipitation-associated downdrafts. Cloud-edge and precipitation-associated downdrafts represent the primary focus of this study.

Analyses of observations and related cloud model simulations described in Sections 4 and 5 further elucidate many aspects of middle to low-level downdraft structure. These analyses indicate that the precipitation-associated downdraft is strongest and most widespread at low levels near and below cloud base. Low-level downdraft structure exhibits a continuum of horizontal inflows from below cloud base up to middle levels in some cases. Two nebulous flow branches feeding the downdraft are defined according to level of origin: (i) a midlevel branch originating from the upwind direction (relative to the moving cloud) anywhere in the layer from cloud base to several kilometers above; and (ii) a low-level branch which starts within the PBL, rises up to 4 km and then descends within the primary downdraft. Low-level downdrafts may be located within the upshear or downshear cloud flank, dependent on wind shear magnitude and perhaps PBL convergence zones. Downshear downdrafts occur more typically under high shear conditions because precipitation responsible for downdraft maintenance is more effectively transported to the downshear flank.

Cooling within the low-level downdraft is accomplished primarily below the melting level by melting and evaporation of precipitation. Cooling by melting is variable along downdraft trajectories and may contribute to over 50% of total cooling in certain cases. Melting effects appear to be particularly important during developing downdraft stages when low pressure perturbations are generated by rapid increases in parcel buoyancy with decreasing height.

Factors which influence downdraft intensity are discussed in Section 6. Here, two basic downdraft intensity controls are discussed: precipitation influences and environmental influences. Thermodynamic processes which govern downdraft cooling rates and associated downflow magnitude are shown to be highly sensitive to precipitation phase, precipitation size, PBL depth and dryness of the environment at midlevels.

Section 7 presents a generalized downdraft conceptual model synthesized from results presented in Sections 4, 5 and 6. This model illustrates two basic processes: (i) the dependence of downdraft structure (location, depth and vertical variation) on environmental parameters, and (ii) dynamical and thermodynamic processes acting along given downdraft trajectories.

2. SUMMARIZATION AND INTERPRETATION OF PREVIOUS WORK

The literature contains numerous sources dealing with different aspects of convective clouds. In this section a large number of convective cloud observations (from various sources) and results of cloud model studies are assembled to present details on cloud-scale downdraft structure within convective clouds ranging from small nonprecipitating convective clouds to large precipitating convective clouds. First, general features of convective cloud structure, of which downdrafts form a part, are presented to provide a suitable background for those unfamiliar with convective cloud structure. Other background material including definitions of convective cloud flows and external mechanisms which govern precipitating convective cloud structure are also highlighted. The following subsections outline observational and cloud modeling studies of downdraft structure, dynamics and thermodynamics. These sections present details on four general types of downdrafts that can be identified: penetrative downdrafts, cloud-edge downdrafts, downdrafts resulting from updraft equilibrium overshoot, and precipitation-associated downdrafts. Characteristics of entrainment flows which comprise a fundamental component of downdraft circulations are also given. It is shown that downdrafts in precipitating clouds are fundamentally different from those in non-precipitating clouds. These differences, which include stronger, larger and more persistent downdrafts, are associated with large-scale cooling effects from precipitation.

2.1 General Features of Convective Clouds and Their Downdrafts

Downdrafts comprise one of the three elemental flows (the other two being updrafts and entrainment) in all types of convective clouds. Fig. 2.1 (Gamache and Houze, 1982) illustrates cloud features, general flow patterns, and relative downdraft locations in a fully-developed convective system, a tropical squall line in this case. Squall lines and other meso-β scale* convective systems (e.g., Maddox, 1980) are comprised of individual convective clouds (cumuli and cumulonimbi) and

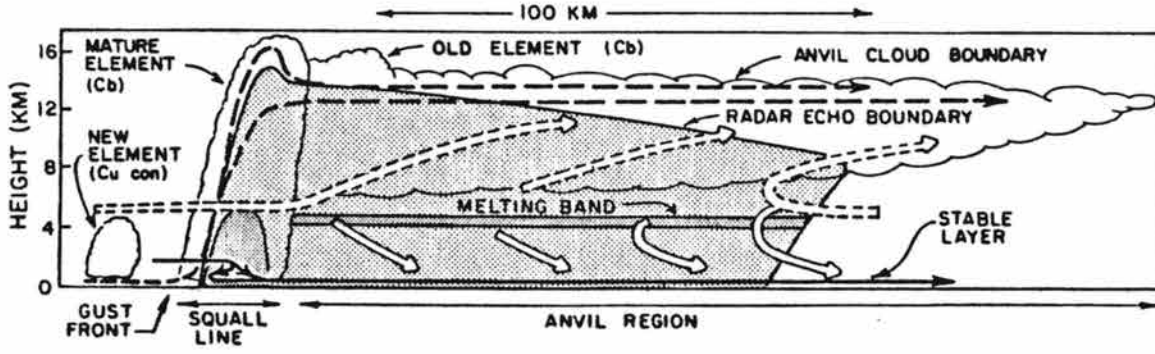

Fig. 2.1. Schematic cross section through a tropical squall system. Associated with the mature squall-line elements or convective cells (Cb), dashed streamlines show convective-scale updraft, solid streamlines show downdraft circulation. Associated with the trailing anvil, wide solid arrows show mesoscale downdraft circulation, wide dashed arrows show mesoscale updraft circulation. Dark shading shows strong radar echo in the melting band and in the heavy precipitation zone of the mature squall-line element. Light shading shows weaker radar echoes. Scalloped line indicates visible cloud boundary. Abbreviations are defined as follows: Cb-cumulonimbus, Cu con-cumulus congestus. Adapted from Gamache and Houze (1982).

extensive anvil clouds either trailing squall line convection (Zipser, 1969; 1977; Betts et al., 1976; Houze, 1977), or connecting individual cumulonimbi within more circular convective systems (Leary and Houze,

---

* We define meso-β scale, following Orlanski (1975), as those physical scale lengths within the interval 25-250 km.

1979a). Individual convective clouds exhibit typical updraft speeds and horizontal dimensions of 5-35 m s^{-1} and 1-15 km, the smaller range of values being more typical for non-precipitating midlatitude cumuli and tropical cumulonimbi. Convective cloud downdrafts exhibit similar horizontal dimensions, but smaller typical speeds in the range 1-15 m s^{-1}. Modeled and observationally-diagnosed mesoscale updrafts and downdrafts occupying the anvil region (Fig. 1) possess magnitudes in the range of 0.1 to 1.0 m s^{-1} and horizontal dimensions of 10 to 100 km (Brown, 1979; Gamache and Houze, 1982). Additional features on the structure of mesoscale updrafts and downdrafts are presented in the reviews of Houze and Betts (1981) and of Houze and Hobbs (1982).

More specific details on convective cloud downdrafts are presented in Fig. 2.2 and Table 2.1. Four types of downdrafts located within or

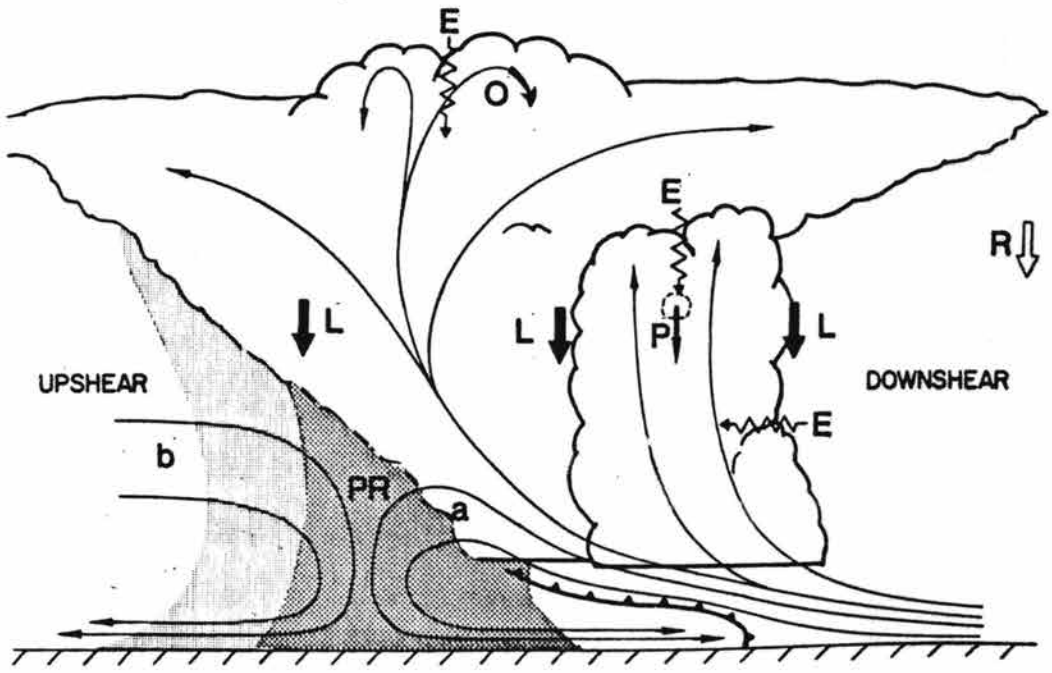

Fig. 2.2. Schematic of updraft, downdraft and entrainment flows within a typical Cb, based on a composite of observational studies and numerical model studies. All flows are storm relative. E denotes entrainment. Other symbols label downdraft circulations which are defined in Table 2.1.

TABLE 2.1. Features of Convective Cloud Downdraft Types

Downdraft type	Typical values speed ($m\ s^{-1}$)	width (km)	depth (km)	level*
precipitation (PR)	1-15	1-10	1-5	l,m
penetrative (P)	1-15	<1.0	1/2 to 5	m,u
regional compensating (R)	<1	5-25	1-5	m,u
cloud/updraft edge (L)	<1-5	<1-5	1-5	m,u
overshooting (O)	1-40	1/2 - 5	1-3	u

*relative cloud level: l - low, m - middle, u - upper

very near cloud edges, as portrayed in Fig. 2.2, were composited from a number of observations and numerical cloud model results summarized in the following sub-sections. Only the precipitation-associated downdraft (PR) systematically reaches the surface. The others appear to remain above cloud base and hence are termed "elevated" downdrafts throughout this paper. A fifth larger-scale downdraft region (R), usually far removed from the cloud, is included here for completeness because it is induced by cloud-scale circulations (see Fritsch, 1975).

For the purposes of this report, weak, moderate and strong updrafts are defined as having respective peak magnitudes $< 10\ m\ s^{-1}$, $10\text{-}25\ m\ s^{-1}$ and $> 25\ m\ s^{-1}$. Weak, moderate and strong downdrafts are similarly defined by the respective limits $< 5\ m\ s^{-1}$, $5\text{-}10\ m\ s^{-1}$ and $> 10\ m\ s^{-1}$. These values were subjectively and somewhat arbitrarily determined by examining a large number of aircraft measurements and cloud model results (see Tables 2.2 and 2.3 elsewhere in this section). Strong downdrafts have been termed "downbursts" by Fujita and Byers (1977).

The three basic convective cloud flows - updrafts, downdrafts and entrainment - are interrelated as indicated in Fig. 2.2. Entrainment is defined here as any flow which incorporates environmental air into the convective cloud system, either through cloud boundaries or into precipitating regions. Consequences of entrainment include cooling by evaporation of cloud and precipitation, and infusion of environmental momentum into the cloud. Entrainment flows may be turbulent in character as indicated by the jagged lines in Fig. 2.2, or entrainment may proceed more systematically on spatial scales typical of updraft and downdraft horizontal dimensions, as we shall see in Section 2.2.2. Although entrainment is usually detrimental to updrafts because buoyancy is decreased, some downdraft types such as penetrative downdrafts may be initiated by entrainment of subsaturated air (Squires, 1958), and perhaps even maintained by entrainment of cloudy air into a subsaturated penetrative downdraft blob or plume descending within the cloud interior (Emanual, 1981; Haman and Niewiadomski, 1980).

Updrafts and downdrafts differ in several other respects. Updrafts within clouds usually remain at or just above saturation (Paluch and Knight, 1984), in contrast to downdrafts which are usually appreciably subsaturated (Kamburova and Ludlam, 1966; Das and Subba Rao, 1972). Such subsaturation comes about in two different ways. First, cooling rates by precipitation evaporation and melting usually are lower in magnitude than adiabatic warming rates within descending air parcels (Das and Subba Rao, 1972). Second, penetrative downdrafts descending within cloud but outside of precipitation require transport (via entrainment) of cloud water from surrounding cloudy regions into the downdraft plume or blob. Because entrainment and associated transports

are probably slow and inversely proportional to downdraft horizontal dimensions (Emanual, 1981), subsaturated conditions may be expected within such downdrafts, particularly larger ones $\gtrsim$ 500 m in horizontal dimension. Other updraft-downdraft contrasts include differences in maximum speeds exhibited by each: updrafts may approach or exceed 50 m s^{-1} (Weisman et al., 1983), but downdrafts appear to be limited to ~ 20 m s^{-1} maximum speeds.

The vertical equation of motion further illustrates forcing of vertical cloud motions and will be referenced frequently in the following sections. If we average across a draft width, we can write (Cotton and Anthes, 1985):

$$\underset{(a)}{\frac{\partial \overline{w}}{\partial t}} = \underset{(b)}{-\frac{1}{\rho_o}\frac{\partial \overline{p'}}{\partial z}} + \underset{(c)}{g\left[\frac{\overline{\theta_v'}}{\theta_{vo}} - \frac{c_v}{c_p}\frac{\overline{p'}}{p_o}\right]} \underset{(d)}{- (r_c + r_r + r_i)]}$$

$$\underset{(e)}{+ \text{ viscous terms and eddy stress terms,}} \qquad (2.1)$$

where single-primed quantities denote departures from a basic state (subscript zero) which varies only in height. In Eq. (2.1), p is pressure, θ_v virtual potential temperature, r_c, r_r and r_i mixing ratios of cloud water, rain water and ice water. Ignoring frictional effects [term (e)], vertical accelerations are produced by perturbation pressure buoyancy and its vertical gradients [terms (c) and (a)], thermal buoyancy [term (b)] and condensate loading [term (d)]. Although not done here, the pressure term (a) can be subdivided into buoyant and

dynamic components (see e.g, Rotunno and Klemp, 1982; Klemp and Rotunno, 1983; Schlesinger, 1984a).

In reference to term (d) of Eq. (2.1), we note another updraft-downdraft difference: the condensate loading is beneficial to downdrafts but detrimental to updrafts. Moreover, it turns out that for scales $\gtrsim$ 1 km, updrafts exhibit significantly more positive buoyancy than downdrafts generate negative buoyancy above the subcloud layer. This is a facet that has been observed primarily from cloud model results (eg., Klemp and Wilhelmson, 1978a; Schlesinger, 1980). Because of this, individual parcel vertical excursions tend to be $\lesssim$ 4 km in downdrafts, and often $>$ 10 km (or the entire tropospheric depth) in updraft.

Individual convective cloud structure is controlled by a number of environmental and cloud physical factors which act to modulate individual acceleration components comprising Eq. (2.1). Some of these factors include: i) atmospheric static stability (i.e., temperature and moisture vertical profiles); ii) vertical shear of the horizontal wind (hereafter called vertical shear for brevity); iii) kinematic properties of horizontal airflow, such as convergence zones, and thermodynamical properties within the atmospheric boundary layer; iv) interactions with other convective clouds nearby; and v) internal cloud microphysical processes and structure.

Effects of wind shear on precipitating convective cloud structure have, in particular, received much attention in recent years. Observational studies (e.g. Marwitz, 1972a,b,c; Chisholm and Renick, 1972) indicate that convective storm structure can be categorized according to environmental wind shear magnitude. In very weak shear

conditions isolated single-cell* or short-lived multicell storms (e.g., Byers and Braham, 1949) appear to predominate. In their three-stage life-cycle model, Byers and Braham visualized three stages of thunderstorm cell development: cumulus, mature and dissipating. Following the updraft-dominated cumulus stage, the mature stage was marked by precipitation-associated downdrafts, adjacent to the updraft, beginning at the 6-8 km level. The final dissipating stage consisted of weak downdraft throughout the lower portion of the precipitating thunderstorm regions.

As environmental wind shear increases to moderate levels, multicell storms of the type described by Newton and Fankhauser (1975) and by Chalon et al. (1976) are typically found. Multicell storms are comprised of a number of cells in different stages of development. New cells often develop sequentially along preferred storm flanks. Finally, in strong shear conditions supercell storms begin to appear. Supercells are unique in that their composition is dominated by a large, long-lived and rotating updraft which propagates continuously, usually to the right of mean cloud level environmental flow. Characteristic features of supercell storms are summarized in Lemon and Doswell (1979).

Recent results from numerical cloud modeling (Weisman and Klemp, 1982; Rotunno and Klemp, 1982) have elucidated some of the physics associated with environmental wind shear controls on precipitating convection. Weisman and Klemp (1982) combined the environmental parameters wind shear and parcel buoyancy to define a non-dimensional

---

* The usual definition of cell as a region of updraft and associated reflectivity pattern is adopted here. Typical cell dimensions are of order several kilometers.

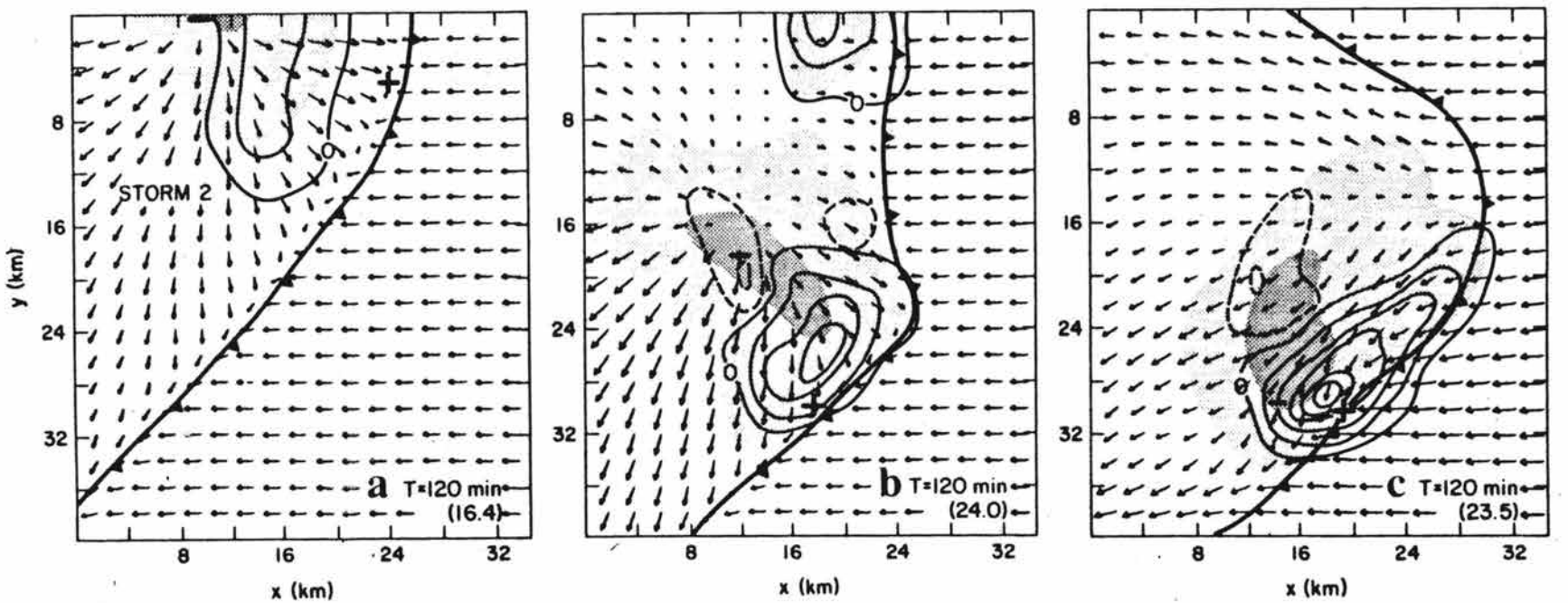

Fig. 2.3. Horizontal cross sections of simulated patterns of precipitating convection at low and middle levels after 120 min of numerical integration. Vectors represent storm-relative flow at 178 m, obtained by subtracting storm motion along the x-axis [12 m s-1, 19 m s-1 and 22.5 m s-1 for panels (a), (b) and (c), respectively] from horizontal flow fields. Maximum vector magnitudes (m/s) are shown in the lower right corner of each plot. The three panels represent increasing wind shear of the functional form u = us tanh (z/zs) for the values of zs = 3 km and (a) us = 15 m s-1, (b) us = 25 m s-1 and (c) us = 35 m s-1. The surface rain field is indicated by light stipling with rain areas >4 g kg-1 designated by dark stipling. The surface gust front is denoted by the solid barbed line and represents the -0.5°C temperature perturbation contour. The midlevel (4.6 km) vertical velocity field is contoured every 5 m s-1 for positive values and 2 m s-1 for negative values. The zero contours outside the main region of storm activity have been deleted. Plus and minus signs represent the location of the low-level (178 m) vertical velocity maximum and minimum, respectively. From Weisman and Klemp (1982).

bulk Richardson number (following Moncrieff and Green, 1972) as

$$R = \frac{B}{\frac{1}{2}\bar{u}^2} \quad , \tag{2.2}$$

where B is approximate parcel buoyancy (proportional to positive area on a thermodynamic diagram) and $\bar{u}$ is a measure of wind shear, defined as the vector magnitude difference between the pressure-weighted mean wind in the lowest 6 km and the mean wind in the lowest 500 m. The parameter R was used by Weisman and Klemp to illustrate how numerically-simulated convection in uniform environments becomes increasingly steady as R decreases (i.e., wind shear or $\bar{u}$ increases). Fig. 2.3 portrays composited mid- and low-level patterns after 120 min simulation from three cases in which wind shear of straight hodographs was varied in magnitude. For moderately low wind shear (Fig. 2.3a), a secondary storm which developed downshear (to the right) of the initial storm is located behind the gust front generated by precipitation-associated downdrafts. As shear is increased in Figs. 2.3b,c, storm splitting occurs and the right-moving storms exhibit increasingly stronger and more steady updrafts and downdrafts, typical of supercell storms. Left-moving storms generated by the splitting process (not shown) are essentially mirror images of the right-moving storms. Note that in higher shear simulations, the low-level gust front and midlevel updraft appear closely connected.

Subsequent model work by Rotunno and Klemp (1982), and Weisman and Klemp (1984) indicates that, in addition to buoyancy, updrafts are forced by upward-directed pressure gradients [term (a) of Eq. (2.1)], produced by interaction of updrafts with shear flow. Weisman and Klemp

(1984) indicate that such pressure forcing can match or exceed buoyancy forces in cases of high shear, a distinguishing feature which may dynamically separate supercell convection from single and multicell convection.

The three dimensional flow structure within a supercell storm presented in Fig. 2.4 portrays a highly three-dimensional circulation in which a primary downdraft branch originating from midlevels curls around the primary updraft tilting northward at low to midlevels. Such an

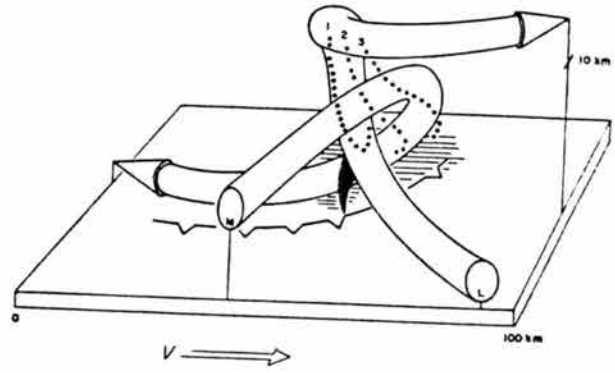

Fig. 2.4. Three-dimensional conceptual model of airflow within a severe right-moving storm. Updraft and downdraft branches are drawn relative to the moving storm. L (low) and M (middle) refer to the predominant levels of origin of the updraft and downdraft, respectively. Surface precipitation is denoted by hatching. Note the five-fold exaggeration of the vertical scale. From Browning (1964).

updraft tilt is thought to be mutually beneficial to the updraft and downdraft since precipitation falling from the updraft sustains the downdraft immediately below. For low shear situations, updrafts exhibit less tilt, become loaded with precipitation, weaken, and give way to downdrafts at low levels.

In this sub-section general aspects of convective cloud structure, factors which control this structure, and the general relationship between updrafts, downdrafts and entrainment have been summarized. The

following sub-sections present observed and modeled characteristics of downdraft kinematic structure, dynamics and thermodynamics.

2.2 Downdrafts in Non-Precipitating Convection

Aircraft observations have yielded abundant information on downdraft structure within non-precipitating cumuli (Cu). We begin this discussion by presenting observations which indicate that downdraft spatial scales are limited to < 1 km horizontal dimension, and that downdraft magnitudes fall in the range 1-10 m s^{-1}. Also included in the following subsections are observed and inferred characteristics of entrainment flows which appear to initiate downdrafts within non-precipitating cumuli. Because observed properties of downdrafts in nonprecipitating convection differ from those in precipitating convection where larger-scale drafts also exist (due to precipitation effects), observations of precipitating convective cloud downdrafts are included next in subsection 2.3.

2.2.1 Downdraft magnitudes and spatial scales

A number of aircraft penetrations into and beneath a variety of convective clouds, both precipitating and nonprecipitating, have been made during field programs beginning with the Thunderstorm Project in 1946-1947. Table 2.2 lists relevant penetration data from convective clouds of increasing intensity, beginning with nonprecipitating Cu (to which we draw attention to here) and ending with precipitating severe cumulonimbi (Cb). In some cases, maximum updraft/downdraft gusts are available, in other cases only means of median values are listed.

Some characteristics of non-precipitating cumulus clouds limited to less than one kilometer vertical extent have been described by Kitchen and Caughey (1981). Such cumuli, having extreme vertical motion

Table 2.2. Summary of draft magnitudes and widths as measured by penetrating aircraft.

Location	Reference	Penetration/ Clouds	Height of Penetration (km)MSL)	Updraft Speed (max/mean) (m/s)	Updraft Width (max/mean) (km)	Downdraft Speed (max/mean) (m/s)	Downdraft Width (max/mean) (km)	Cloud Type
England	Kitchen and Caughey (1981)		0.7-1.4 km	2+	~0.5/~0.1	2+	~0.5/~0.1	fair weather Cu hum 100-300 m deep
Carribbean	Malkus (1954, 1955)	6/2	0.7-1.7	6/-	0.6/-	6/-	0.5/-	Non precip. Cu con 2 km deep
Australian coastal area	Warner (1970)	68/21	0.2-2.4	13/5		9/3.5		Non precip. Cu con ~2 days
	Warner (1977)	28/9	0.9-2.4	8.5/4.5	1.3/0.7	7/3.8	0.8/0.3-0.4	
Canada	MacPherson and Isaac (1977)	33.16	1.5-5	11/-		7/-		Non precip. Cu con 1-4.5 km deep
Florida	Hallett et al. (1978)	12/6	5-6	30/12.6+	>3.5/1.7	8/4.8+	1.8/0.9	Precip. towering Cu near cloud top
Florida	Keller and Sax (1981)	7/1	~6	15.5/7.5+	3/2.5+	7/2.5+	4.8/2.1	Precip. towering Cu con to Cb, near cloud top
Florida	Willis et al. (1982)	4/1	6.1-6.7	13/8.8+	1.6/0.9+	6/4.1+	1.1/0.8	Precip. towering Cu con ~500 m below cloud top
Florida	Xu and Reinking (1982)	22/7	5.2-7.0	/4.8*		/2.0*		Precip. towering Cu
Florida	Wiggert et al. (1982)	35/15		31.5/16.8+		23.5/6.8+		Precip. towering Cu and Cb
Illinois	Wiggert et al. (1982)	16/16		20.5/7.2+		7.8/3.5+		Precip. towering Cu and Cb
Hurricanes	Jorgensen (1984)		0.5-6.1	average 6/1.5 median		average 5/1.5 median		4 hurricanes, inner core and outer bands
Tropical Atlantic	LeMone and Zipser (1980)		0.15-8.0	14/2.9[x]	7/~1.8[x]	7/~1.8[x]	7/~1[x]	Precip. and non-precip. Cu con to Cb

Table 2.2. Continued.

Colorado	Rodi et al. (1983)	3/1	2.7	6/3.6+	1.5/0.9+	15/11	8/4.5	3 km below base of Cu con w/light precip.
Florida, Ohio	Byers and Braham (1949)	1363/76	2-8	26/7	11.5/1.5	24/5	7/1.2	precip. Cb
N.E. Colorado	Musil et al. (1973)	2/1	-6	18/12+	6/3.7	10/-6+	4/2.5	precip. Cb
N.E. Colorado	Musil et al. (1976)	1/1	-7	18/-	10/-	7/-	4/-	precip. Cb
N.E. Colorado	Musil et al. (1977)	108/24	5-7	40/10-15+	10/2-3+	20/5-10	8/2.5	precip. Cb, some intense
N.E. Colorado	Sand (1976)	7/3	5-7	18/11+	9/3.4+	11/7+	3/1.8+	precip. Cb
Colorado & Oklahoma	Sinclair (1973)		9.2-9.8	26/	15/	10/	12/	precip. Cb
Oklahoma	Sinclair (1979)		4.5-6.0	20/		>20/		precip. Cb
N.E. Colorado	Heymsfield and Musil (1982)	3/1	7	26/17+	7.5/4.5+	14/12+	3.6/3.2	precip. Cb, hail
Oklahoma	Heymsfield and Hjelmfelt (1981)	1/1	6-7	40/26+	6.5/4+	-10-20/8.5+	-6/-2	squall line
E. Montana	Musil et al. (1982)	1/1	6-7	40/-	9.5/-	20/	9/-	Severe storm

*mean of mean + mean of max. gusts x median values

magnitudes within the interval $\pm$ 5 m/s, are usually considered to be an extension of the planetary boundary layer whose height is limited by a capping inversion. Some of the most descriptive measurements within clouds of this type are presented in the Kitchen and Caughey (1981) study, in which data from three levels of a tethered balloon system were analyzed to describe the flow, thermodynamic and microphysical structure of cumuli 100–300 m deep. In-cloud downdrafts having ~ 1 m s^{-1} magnitudes were typically located downshear of the primary cloud updraft. Kitchen and Caughey postulated that these downdrafts were part of a return flow from updrafts, perhaps reinforced by cooling from cloud top entrainment processes which are discussed below. Somewhat weaker downdrafts exhibiting more coherency in the vertical were often located along the upshear flank just outside the cloud boundary. Because these clouds are strongly influenced by boundary layer fluxes of heat and moisture from below and the capping inversion above, downdraft patterns indicated here may not be generally relevant to those of deeper Cu and Cb described below.

The updraft/downdraft structure within nonprecipitating cumulus congestus (Cu con) one to four kilometers deep has been examined by Malkus (1954, 1955), Warner (1970, 1977) and MacPherson and Isaac (1977). Maximum measured downdraft gust speeds range from 6 to 9 m s^{-1}, 50–100% of the magnitude of maximum updraft gusts. Downdraft widths are no larger than ~0.5 km in this data set. The available observations generally indicate that non-precipitating Cu con display updraft and downdraft maximum gusts which increase with height above cloud base (e.g., Fig. 3 in Warner, 1970).

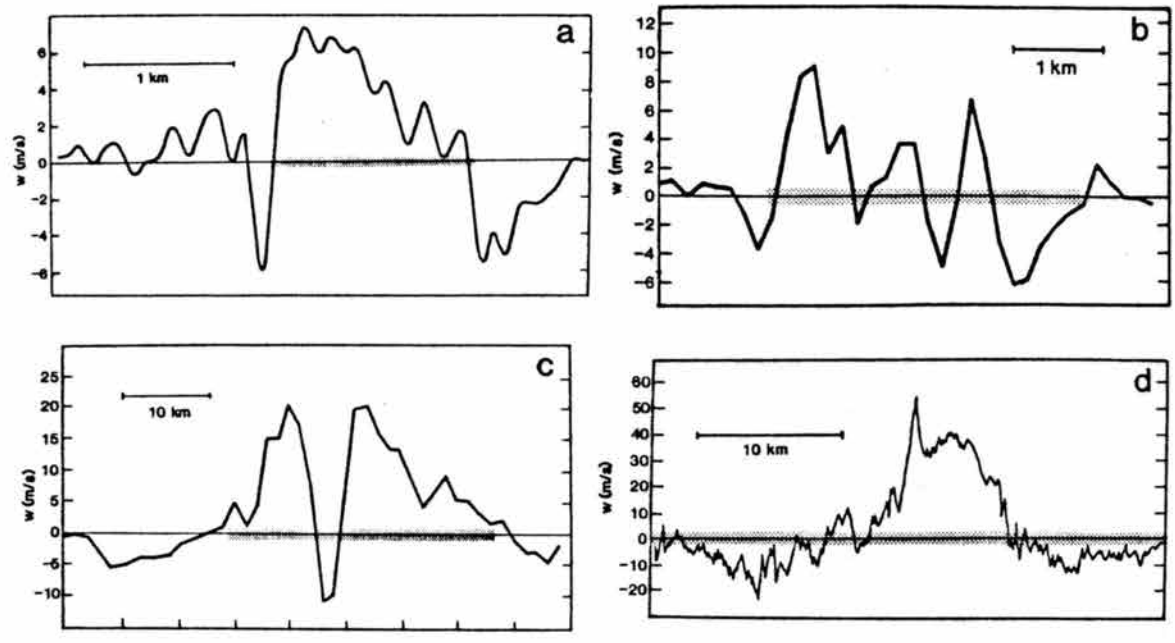

Fig. 2.5. Aircraft-measured vertical velocity time series through four different clouds. Cloudy regions are represented by stippling. (a) Midlevel penetration through a Cu con 1.7 km deep. Adapted from Warner (1970). (b) Penetration ~ 0.5 km below the top of a 6 km deep lightly precipitating towering Cu con over Florida. Adapted from Willis et al. (1982). (c) Pentration at the 9.8 km level of an intense convective storm over NE Colorado on 21 June 1972. Adapted from Sinclair (1973). (d) Penetration at the 6 km level of a severe, heavily precipitating Cb (tops to 16 km) over SE Montana. Adapted from Musil et al., 1982.

Air motions in non-precipitating cumulus clouds often exhibit a tendency to reside on distinct spatial scales. For example, Kitchen and Caughey (1981) found that kinetic energy of small cumulus clouds resided on two scales, one being the 500 m scale of updrafts and downdrafts and the other being a turbulent scale of ~ 10 m. Similar multiple spectral peaks at scales of ~ 1 km, ~ 0.5 km and ~ 0.1 km have been observed in larger cumulus clouds by MacPherson and Isaac (1977) and by Warner (1970).

Fig. 2.5a from Warner (1970) illustrates a typical w profile through a Cu con 1.7 km deep, showing 5 m s^{-1} downdrafts near and beyond the cloud edges. Both Malkus (1955) and MacPherson and Isaac (1977) presented similar patterns. They also found that downdrafts near cloud top on the downshear cloud edge were especially pronounced and comparable in magnitude to updrafts, consistent with the patterns analyzed by Kitchen and Caughey (1981.) Heymsfield et al. (1978) similarly observed that the downshear cloud sector of a NE Colorado Cu con was a region of pronounced mixing. Further details on this "downshear entrainment flow" appear in the following subsection on entrainment flows.

2.2.2 Relationships between downdrafts and entrainment

Observational and modeling studies described in the previous section indicated that inflow or entrainment of environmental air into convective clouds was a common feature. Aircraft measurements furthermore suggested that small-scale downdrafts typically of ~ 500 m lateral scale or smaller were associated with entrainment of dry environmental air into the cloud. Because cloud downdrafts are presumably closely associated with entrainment processes, particularly

in non-precipitating cumuli, a brief review of entrainment mechanisms and related observations is presented here.

Numerous in situ observations of cloud water have indicated that Cu clouds of all sizes are diluted to varying degrees by entrainment of subsaturated environmental air which decreases cloud buoyancy and liquid water content. If entrainment is appreciable, certain mixtures of environmental and cloudy updraft air may have virtual temperatures colder than the environmental virtual temperature and thus descend as negatively-buoyant downdrafts. For typical environmental conditions, simple calculations (e.g., Betts, 1982a) indicate that negatively buoyant parcels are produced from a mixture of cloud and environmental air containing something less than ~ 50% mass of cloud air. The coldest possible mixture if one that just evaporates all available cloud water [Betts (1982a), Paluch and Breed (1984)].

Figure 2.6, a presentation of results of some calculations given in Paluch and Breed (1984), illustrates maximum cooling and downdraft penetration depths for an environment supportive of Cu con and moderately intense precipitating Cb. Here, the solid line depicts the environmental virtual potential temperature profile, the dashed line represents the virtual potential temperature of cloud air ascending unmixed from cloud base, and the dot-dashed line gives the vertical profile of minimum virtual potential temperature produced by mixing of undiluted cloud air and environmental air at that level. In this case the coldest mixtures forming at dry midlvels (~ 8 km MSL) have a virtual temperature deficit (including cloud water) of about 2 K, which is typical of many environments. These cold parcels are then able to descend 1-2 km as downdrafts, whose paths are indicated by dots in Fig.

2.6, before losing negative buoyancy. Betts (1982a) has graphically illustrated these processes using thermodynamic diagrams, and presents several examples illustrating the thermodynamics of downdrafts and mixing processes.

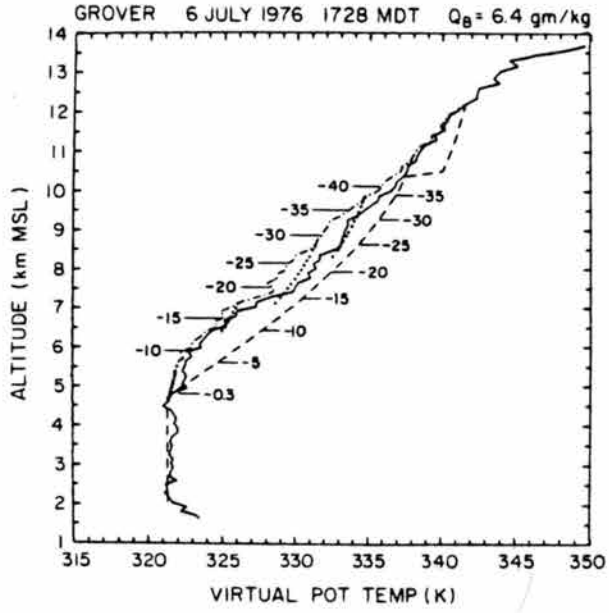

Fig. 2.6. Virtual potential temperature vertical profiles from the sounding of 6 July 1976 over northeastern Colorado. The solid line indicates the clear-air environmental sounding, the dashed line portrays unmixed air ascending from cloud base, the dot-dashed line shows the minimum virtual temperature resulting from lateral mixing, and the dotted line represents the minimum virtual potential temperature of descending mixed air parcels. From Paluch and Breed (1984).

In cases where downdrafts induced by mixing are able to entrain cloud water while descending <u>within</u> cloud, downdraft penetration depths may exceed several kilometers (Paluch, 1979; Emanuel, 1981). It is thought by Emanual (1981) and by Randall (1980) that such downdrafts would necessarily be of small scale ($\lesssim$ 0.5 km) so that entrainment of cloud water, which is inversely proportional to downdraft diameter in some entrainment models (see Emanuel, 1981), can supply sufficient cloud water to maintain negatively-buoyant downdrafts.

Models of entrainment which have been devised over the years can be classified into two general types: lateral entrainment and cloud top entrainment. The lateral entrainment process, first considered by Normand (1946) and Stommel (1947), and later applied to 1-D cloud models (see Simpson, 1971), incorporates environmental air horizontally into the cloud through its lateral boundaries. Such mixing has been envisioned to occur in two ways depending on whether the convection is steady (jet-like) or discrete (bubble-like). For the steady case, entrainment may occur along the boundaries of a vertically-continuous jet as a consequence of mass continuity due to vertical stretching. (Houghton and Cramer (1951) considered this to be a form of dynamic entrainment, different from asymmetrical entrainment flows associated with pressure perturbations. Further details of this entrainment process are given below.) Lateral entrainment may also occur within regions where fluid shear instabilities (e.g., Drazin and Howard, 1964) between cloud and environmental flows produce onset of turbulence.

A conceptual model of flow patterns associated with an asymmetric dynamic entrainment, or "wake entrainment," is portrayed in Fig. 2.7. This model, based on the observational studies of the previous section and on the numerical cloud model results of Cotton and Tripoli (1978) and Rotunno and Klemp (1982), illustrates that perturbations in relative flow occur near the cloud. Airflow is diverted by high perturbation pressure around the upshear edge, where an unmixed cloud regin may be located. Contrastingly, the downshear cloud sector, or wake, is dominated by cloud scale inflow, driven by low pressure perturbations. In their analysis and conceptual model, Heymsfield et al. (1978)

depicted this downshear inflow as one similar to the turbulent wake downstream of high Reynolds number flow around cylinders.

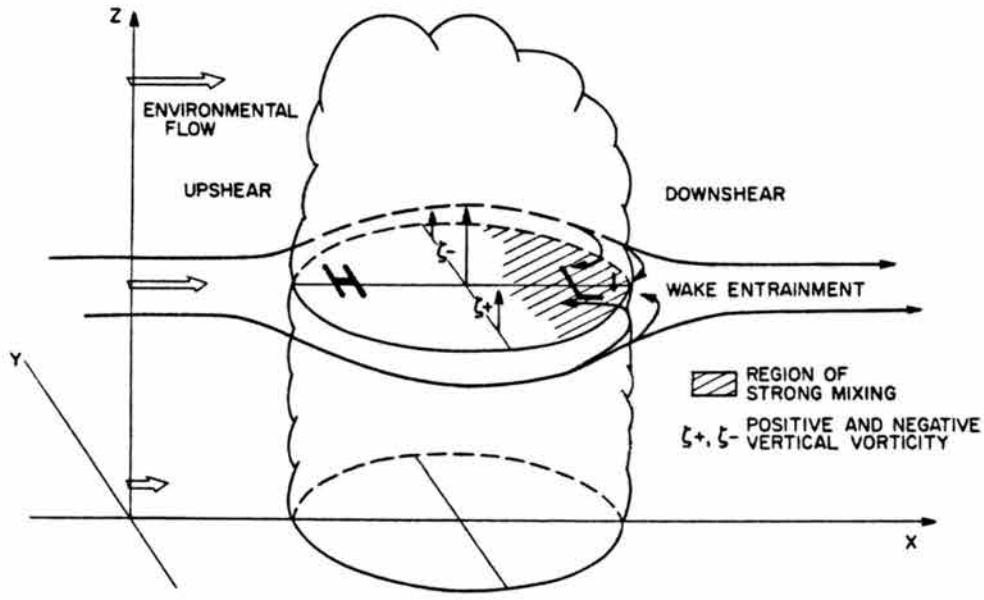

Fig. 2.7. Schematic diagram illustrating wake entrainment within the downshear flank of a convective cloud. The symbols H and L represent high and low pressure perturbations. These perturbations, along with the vertical vorticity patterns, are produced by cloud vertical motion interacting with environmental flow increasing in strength with height in this case.

Results of numerical cloud modeling studies (Cotton and Tripoli, 1978, Rotunno and Klemp, 1982) demonstrate that this downshear inflow is of cloud scale and organized, in contrast to turbulent entrainment flows. This inflow is forced by pressure perturbations produced by interaction of cloud updrafts with environmental flow exhibiting vertical shear. For the situation illustrated in Fig. 2.7, vortex line tilting along the north and south updraft fringes generates positive and negative vertical vorticity as indicated along the respective south and north flanks. This distribution of vorticity then induces inflow and

low pressure perturbations within the downshear flank. The magnitude of pressure perturbations induced by such interactions was considered by Rotunno and Klemp (1982) who derived the expression

$$p' \sim \frac{d\vec{V}}{dz} \cdot \nabla w \quad , \tag{2.3}$$

where $\vec{V}$ is the horizontal environmental wind vector and w is cloud vertical motion. The magnitude of p' is thus dependent on the magnitudes of wind shear and horizontal gradients in updraft speed.

For both bubble and jet-like convection, lateral entrainment rates have been parameterized in the form

$$E = \frac{1}{M}\frac{dM}{dz} = \frac{const}{R} \quad , \tag{2.4}$$

where E is the rate of entrainment, M the vertical mass flux and R cloud radius. The entrainment rate is inversely proportional to cloud radius in this model. In situ measurements only weakly uphold (2.4), as reported by McCarthy (1974) whose results have been questioned by Warner (1975). Many measurements fail to show a significant relationship between E and R (e.g., Sloss, 1967). However, it should be pointed out that accurate and representative measurements are difficult to obtain by aircraft because of the time required to make several penetrations of a given cloud.

The lateral entrainment model also fails to account for other small Cu cloud properties such as approximate top-hat horizontal profiles of cloud water commonly measured (e.g., Warner, 1955, 1969). Furthermore, significant horizontal fluctuations in cloud water and vertical motion are measured, in contrast to smoother Gaussian-like distributions

predicted by lateral entrainment. Squires (1958) attempted to alleviate these inconsistencies by introducing the cloud top entrainment concept, whereby environmental air is enveloped near cloud top, cools by evaporation and forms penetrative downdrafts which mix with the cloud interior below.

Paluch (1979) used two conserved thermodynamic tracers (total water consisting of cloud water and water vapor, and "wet" equivalent potential temperature) for nonprecipitating convection and aircraft data from nonprecipitating cumulus congestus clouds to substantiate Squires' cloud top mixing hypothesis. Data analyses indicated that the air sampled was a mixture of updraft air and environmental air entrained discretely at a higher level. Boatman and Auer (1983), who recently presented further evidence using comparable techniques in similar clouds, found that entrained air had descended ~ 100 mb to the observation level. Numerical experiments by Raymond (1981) with a two-scale 1-D cloud model having convective turbulence also emphasized the importance of cloud top mixing. Raymond concluded that evaporation at cloud top, while the rising cloud top penetrated midlevels, produced downdrafts and associated mixing. Other numerical experiments conducted by Emanuel (1981) indicate that quite vigorous small-scale downdrafts produced by entrainment of subsaturated air may descend appreciable distances within cloud provided that cloud water is continuously entrained into the descending blob or plume. Some results of his study are given in Section 2.4.2.

The mechanisms by which environmental air is entrained at cloud top still remain uncertain. Work by some investigators (Randall, 1980; Deardorff, 1980) on stratocumulus clouds, which are much less vigorous

than cumulus clouds, has shown that cloud top entrainment can form penetrative downdrafts which then descend and mix into the cloud region below. Formation of penetrative downdrafts proceeds upon passing the instability criterion,

$$\Delta\theta_e \leq (\Delta\theta_e)_{crit} \approx -1 \text{ to } -2 \text{ K} \quad ,$$

where $\Delta\theta_e$ is the jump in θ_e of environmental air above the cloud, to the θ_e of cloudy air below. Both Randall and Deardorff emphasize that onset of instability requires more than simply a cold mixture since virtual effects of cloud water (i.e., condensate loading) make the cloud environment more dense than clear air of the same temperature and water vapor content. Betts (1982a) has also considered this penetrative downdraft problem in stratocumulus from a more graphical viewpoint.

While this instability criterion is usually met in cumulus cloud environments (see Fig. 2.6) the physical processes by which envionmental air enters at cloud top remain uncertain. However, some insight into this problem has recently been provided by Klassen and Clark (1985), who presented some results of very high resolution two-dimensional simulations of shallow (< 1 km deep) cumuli. The simulations indicate that cloud top entrainment processes are apparently initiated by a fluid shear instability resulting from horizontal gradients in vertical motion along cloud edge. Once the point of instability is reached, nodes or proturbances build outwards from the cloud mass along the sides and top. Provided that the global cloud shape satisfies certain geometrical criteria, these nodes can build upwards at cloud top and engulf substantial environmental air. Subsequent cloud evaporation within the trapped blob was found to drive downdrafts of up to 3.5 m s^{-1}.

2.3 Downdrafts in Precipitating Convection

Downdraft observations in precipitating convection can be divided into the general categories of direct observations made by aircraft and by vertically-pointing Doppler radar, and indirect observations from which inferences on downdraft structure can be obtained. We begin by presenting direct observations which indicate that downdrafts assume spatial scales spanning a wider spectrum than seen in nonprecipitating cumuli. These are supplemented with additional data from indirect measurements (radar, surface mesonet, rawinsonde) which reveal some aspects of downdraft thermodynamics, relative location and origin.

2.3.1 Direct observations - downdraft magnitudes and spatial scales

Comparison of downdrafts measured within precipitating and non-precipitating convection (Table 2.2) indicates that downdrafts in the former exhibit larger downdraft spatial scales and greater magnitudes. Vertical velocity data tabulated from the Thunderstorm Project flights (Byers and Braham, 1949) reveal median downdraft speeds and widths of 5-6 m s^{-1} and 1.2 km, respectively. More recent data acquired from intense northeast Colorado Cb, as summarized by Musil et al. (1977), show a respective mean maximum downdraft speed and width of 8 m s^{-1} and 2.5 km. Maximum measured downdraft gusts and widths have exceeded 20 m s^{-1} and 7 km in several cases shown in Table 2.2, including the above two references. While these peak values are typically measured at and above middle levels, downdrafts of similar size and magnitude may also exist at low levels, since measurements within and near low-level precipitation cores have been avoided.

Fig. 2.5b from Willis et al. (1982) displays a penetration ~500 m below cloud top through a precipitating Florida Cu con ~6 km deep. Such

a turbulent structure near cloud top (which may be a manifestation of cloud top entrainment) is typical of the observations listed in Table 2.2, as is the preference for downdrafts near cloud edges. (A similar pattern was noted for nonprecipitating, shallower Cu con described above). Sinclair (1973, 1979) has also reported frequent occurrences of downdrafts at mid- to upper-levels in both clear and cloudy portions of intense Cb. Fig. 2.5c (Sinclair, 1973) gives an example of clear-air downdrafts with magnitudes of several meters per second and ~ 10 km widths bordering an active updraft. Temperatures within this clear-air downdraft were ~2 K warmer than adjacent environmental air, in contrast to relatively cold temperatures (-2 K) within the stronger cloud interior downdraft. Other indirect evidence supporting the presence of clear-air concentrated downdrafts or larger regions of weaker subsidence adjacent to precipitating convection is summarized in Fritsch (1975) and in Hoxit et al. (1976).

Fig. 2.5d adapted from Musil et al. (1982), illustrates an extreme case of an extensive and strong downdraft measured near the core of a large, severe storm in southeast Montana. In this case extensive downdrafts 5-10 km wide with 10-20 m s^{-1} amplitudes flanked an intense 40 m s^{-1} updraft at 6-7 km MSL. Somewhat smaller but intense downdrafts and updrafts were encountered on the upshear flank. Thus, we see that downdrafts within precipitating convective clouds assume a wide spectrum of magnitudes and sizes and are not limited to the 0.5 - 1.0 km scale as in the case of nonprecipitating Cu. Such a characteristic is believed to be related to wind shear, environmental stability and the intensity and extent of precipitation within and beneath the cloud.

Relative to midlatitude continental Cb, tropical maritime Cb contain much weaker updrafts and downdrafts. LeMone and Zipser (1980) summarized vertical motions measured within GATE convective clouds, and found maximum downdraft speeds of 10 m s^{-1} in rare instances, with a median value of 1.8 m s^{-1}. Jorgensen (1984) similarly composited draft profiles through hurricane convective bands and inner cores which appear similar to GATE profiles. His results, along with those of LeMone and Zipser (1980) show an increase with height in both updraft and downdraft magnitudes for GATE, Thunderstorm Project, and hurricane drafts, a characteristic similar to that measured in nonprecipitating Cu con. Both GATE and hurricane measured draft magnitudes were 1/3 to 1/2 the Thunderstorm Project draft magnitudes.

Some measurements within mid-latitude precipitating convection indicate that low-level downdrafts associated with precipitation may attain intense magnitudes. For example, 15 m s^{-1} peak downdrafts beneath cloud base have been recently measured within light precipitation beneath the bases of Cu con forming above deep dry mixed layers in Colorado (Rodi et al., 1983). Further evidence supporting the existence of strong low level downdrafts within continental Cb is provided by vertically-pointing Doppler (VPD) radar observations. Battan (1975, 1980) has presented the most comprehensive set (4 cases) of VPD observations. These are supplemented by additional VPD data contained in Battan and Theiss (1970), Strauch and Merrem (1976), Wilson and Fujita (1979), and Mueller and Hildebrand (1983). Fig. 2.8 is an example typical of those presented in Battan (1975, 1980). The VPD observations generally reveal vertically-continuous, large-scale downdrafts (6-12 m s^{-1} maximum) in the lowest 3-4 km. Pockets of

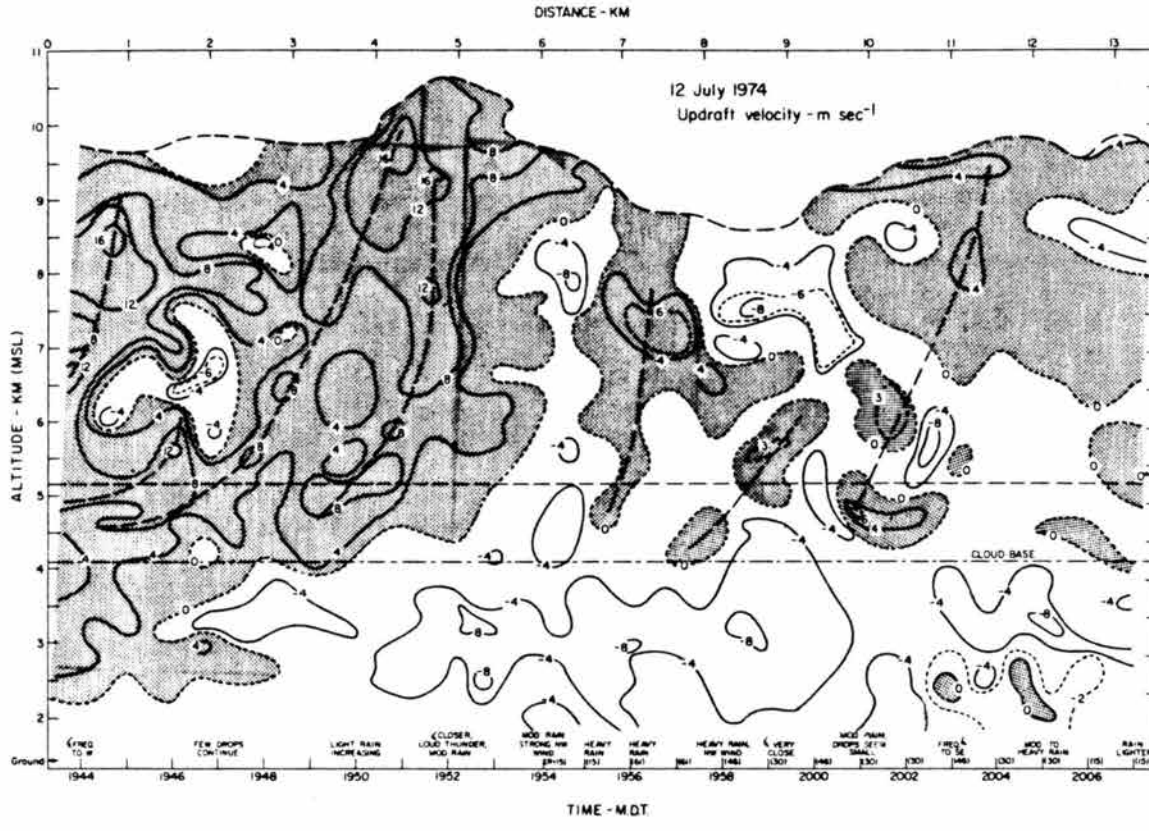

Fig. 2.8. Time-height section of estimated updraft velocity derived from a vertically-pointing Doppler radar. Heavy dashed lines indicate updraft cores. Contours are analyzed at 4 m s^{-1} intervals, updrafts are shaded. Vertical motion was estimated from $w = W - 3.8\ Z^{0.072}$ where Z is measured reflectivity factor and W is measured Doppler velocity. From Battan (1980).

downdraft which typify the mid- to upper-levels are representative of small scale drafts commonly measured by aircraft (e.g., Fig. 2.5b). The observations of Wilson and Fujita (1979) in particular show considerable variability in small-scale intense updrafts and downdrafts near echo top. The magnitude of such near cloud top (overshooting) downdrafts may approach 40 m s^{-1}, as Fujita (1974) has determined from airborne photogrammetric analyses of an intense Cb.

In summary, direct observations indicate that downdraft maximum speeds and horizontal dimensions range from a few meters per second and several hundred meters in nonprecipitating Cu con, to several km and 10-20 m/s in intense Cb. Downdraft structure tends toward uniformity and large scales within precipitation at low levels, but exhibits smaller scale and more inhomgeneity in nonprecipitating Cu con and in upper regions of precipitating Cu con and Cb. For isolated clouds consisting of one primary updraft, downdrafts are often located along cloud edges, with a preference for the downshear edge. The next section assembles a number of indirect observations to present a more detailed picture of downdraft characteristics.

2.3.2 Indirect observations - downdraft structure, origin and relationship to precipitation

Indirect observations on downdraft structure are derived from a number of sources: Doppler and non-Doppler radar, surface mesonet, radiosonde and photography. Such observations have provided valuable information on downdraft temporal and spatial scales, downdraft intensity variation, downdraft source levels and the relationship between downdrafts and precipitation.

Indirect observations also indicate that downdrafts assume a broad spectrum of intensities and sizes. In his analysis of tropical convective systems, Zipser (1969, 1977) distinguished 1-5 m/s downdrafts of scale ~1 km associated with active convective cloud cores from 0.1-0.5 m/s mesoscale downdrafts of scale 10-100 km associated with an extensive anvil cloud trailing the active convection. Other studies on both squall lines (Houze, 1977; Ogura and Liou, 1980) and Cb cloud clusters (Leary and Houze, 1979a) show similar scale separation between convective scale and mesoscale downdrafts (see Fig. 2.1).

Similar spatial scale variations greater than one order of magnitude appear in convective downdrafts. As discussed previously, direct aircraft observations revealed non-precipitating convective cloud downdrafts no greater than ~ 1 km in size, in contrast with ~ 10 km wide downdrafts occasionally measured within precipitating Cb. Indirect observations suggest a similar range of scales in intense downdrafts (downbursts). From their inspection of surface damage patterns and divergence inferred therefrom which exhibited scales from a few hundred meters to > 10 km, Fujita (1978), Fujita and Wakimoto (1981) and Forbes and Wakimoto (1983) inferred a wide spectrum of downburst sizes. Fujita (1981) also found short time scales (~5 min) of low level outflow wind associated with small downbursts.

A number of investigators have inferred downdraft source levels by analyzing thermodynamic tracers such as equivalent potential temperature (θ_e), wet bulb potential temperature (θ_w) or moist static energy ($h = c_pT + Lq + gz$) all of which are approximately conserved for dry and moist adiabatic processes assuming no mixing or ice phase change. Vertical profiles of θ_e in the environment of Cb typically show a

minimum near 500-600 mb. Desai and Mal (1938), Normand (1946) and Newton (1950) were among the first to apply this principle in inferring that cold downdraft air measured at the surface originated several kilometers above. Normand furthermore identified that cooling produced by evaporation of precipitation falling into low-valued θ_e air at middle levels may significantly augment thunderstorm kinetic energy production by conversion of potential energy.

Other investigators have subsequently indicated that low-valued midlevel θ_e air often reaches the surface within downdrafts. Using analysis of θ_e, Zipser (1969) inferred that midlevel air near the level of minimum θ_e descended ~500 mb to the surface behind a tropical squall line. Similar inferences concerning the origin of downdraft air are made using thermodynamic analysis in many other cases, for example, midlatitude convective storms [Foote and Fankhauser (1973), Fankhauser (1976), Lemon (1976), Barnes (1978a,b) and Ogura and Liou (1980)] and a strong GATE squall line (Johnson and Nichols, 1983). In cases of less intense thunderstorms, downdrafts apparently originate just above cloud base, significantly below the level of minimum θ_e. Betts (1976) estimated that downdraft air descended ~100 mb from just above the cloud base of Venezuelan storms. Barnes and Garstang (1982) inferred downdraft source levels near or below 750 mb for precipitating tropical convection of moderate intensity.

Many analyses indicate that low level downdrafts are closely associated with precipitation falling beneath cloud base from convective clouds of weak to severe intensity. Byers and Braham (1949) demonstrated a close association between downdrafts and surface rainfall. They inferred that downdrafts were initiated by precipitation

loading and maintained by evaporation of cloud and precipitation. Other striking examples showing this relationship can be seen in the surface mesonet analyses of Foote and Fankhauser (1973), Fankhauser (1976), Holle and Maier (1980), Fankhauser et al. (1982) and Wade and Foote (1982). Fujita (1981, Fig. 26) presents a photograph showing the co-location of an apparent downburst with a subcloud intense precipitation shaft. In other related observations Keller and Sax (1981) presented aircraft penetration data indicating a 5 km wide downdraft within precipitation at the 6.7 km MSL level in the optically clear wake of a rising cumulus tower. Although Keller and Sax say nothing on the origins of this downdraft, it may be inferred that evaporation of cloud water by vigorous lateral entrainment, as suggested by the clear conditions in the wake of the rising bubble, may have aided downdraft formation. Finally, Barnes and Garstang (1982) established a positive correlation between areal precipitation rate and downdraft transport of mass and low static energy (h) into the boundary layer. They determined that precipitation rates needed to exceed a threshold of ~2 mm/hr (averaged over a ~16 km^2 area) before low-valued h air was transported into the subcloud layer.

Fig. 2.9, derived from a detailed case study of a NE Colorado convective storm (Fankhauser, 1976, and Browning et al, 1976), shows the colocation of heavy precipitation, downdraft and low θ_e air. In other cases lowest θ_e air is located just upshear of the downdraft and precipitation core (e.g., Barnes, 1978a,b; Nelson, 1977; Lemon, 1976). The multiple Doppler radar presentations in Kropfli and Miller (1976), Ray et al. (1981), Foote and Frank (1983) and Wilson et al. (1984), among others, also illustrate that low level downdrafts are either

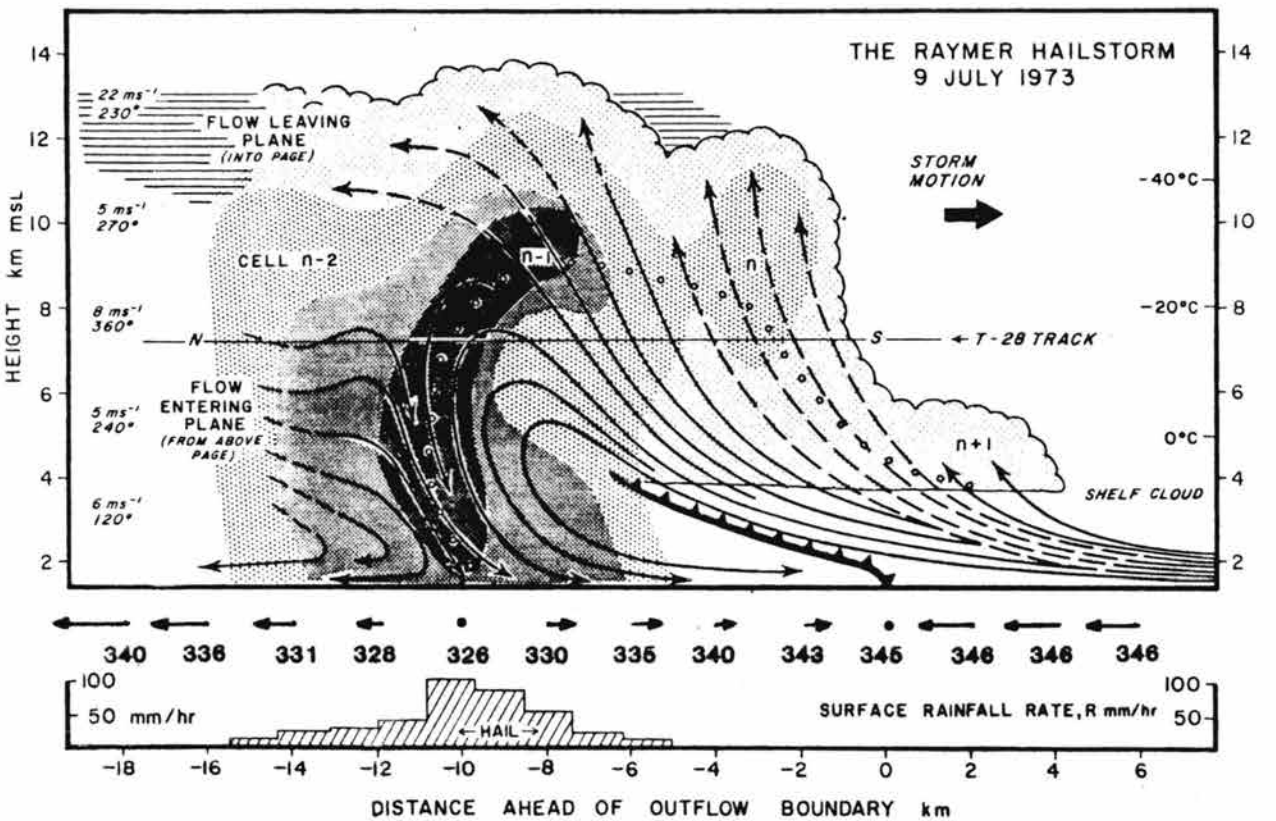

Fig. 2.9. Schematic model from a NE Colorado storm case study. Storm relative airflow is composited from aircraft, Doppler radar and surface mesonet measurements. Light stippling represents cloud; successively darker stippling denotes radar reflectivity of 35, 45 and 50 dBZ. Measurements of rain, Θe and wind (the component in the plane of the figure), from a surface station over which the storm passed, are shown in the lower portion. The maximum wind vector is 11 m s-1. Adapted from Browning et al. (1976) and Fankhauser (1976).

located within or along the upshear edge of greatest low level radar reflectivity. Another example shown in Fig. 2.10 (from Klemp et al., 1981) depicts flow patterns derived from a multiple Doppler radar analysis and a comparative three-dimensional cloud model simulation of a tornadic thunderstorm. In this case low-level downdrafts with magnitudes up to 10 m/s were located within and just upshear of the precipitation core [see also Ray et al. (1981) for additional details of this case]. Also note that downdraft regions located in the far eastern flank at midlevels (4 and 7 km) are significantly damped in the same relative locations at low levels. Downdraft air parcel trajectories analyzed from both observations and model results of this case indicated that little downdraft air ending at the surface originated above 3 km AGL.

The relationship between subcloud precipitation and downdrafts appears to be especially strong in cases where precipitating Cu con and Cb form above deep, dry boundary layers in the western U.S. Braham (1952) speculated that subcloud evaporation of a significant fraction of precipitation was of primary importance in dry regions. In his study on cold-air mesoscale outflows, Fujita (1959) indicated that the area integral of observed pressure excess beneath convective systems, which is related to total cooling from precipitation evaporation at low levels, was a function of the relative boundary layer dryness and total surface rainfall. Storm systems forming in relatively dry areas such as western Texas were observed to produce surface pressure rises essentially equal to those over southern and midwestern states where significantly more rain fell and where more moist and shallow boundary layers exist (Holzworth, 1964).

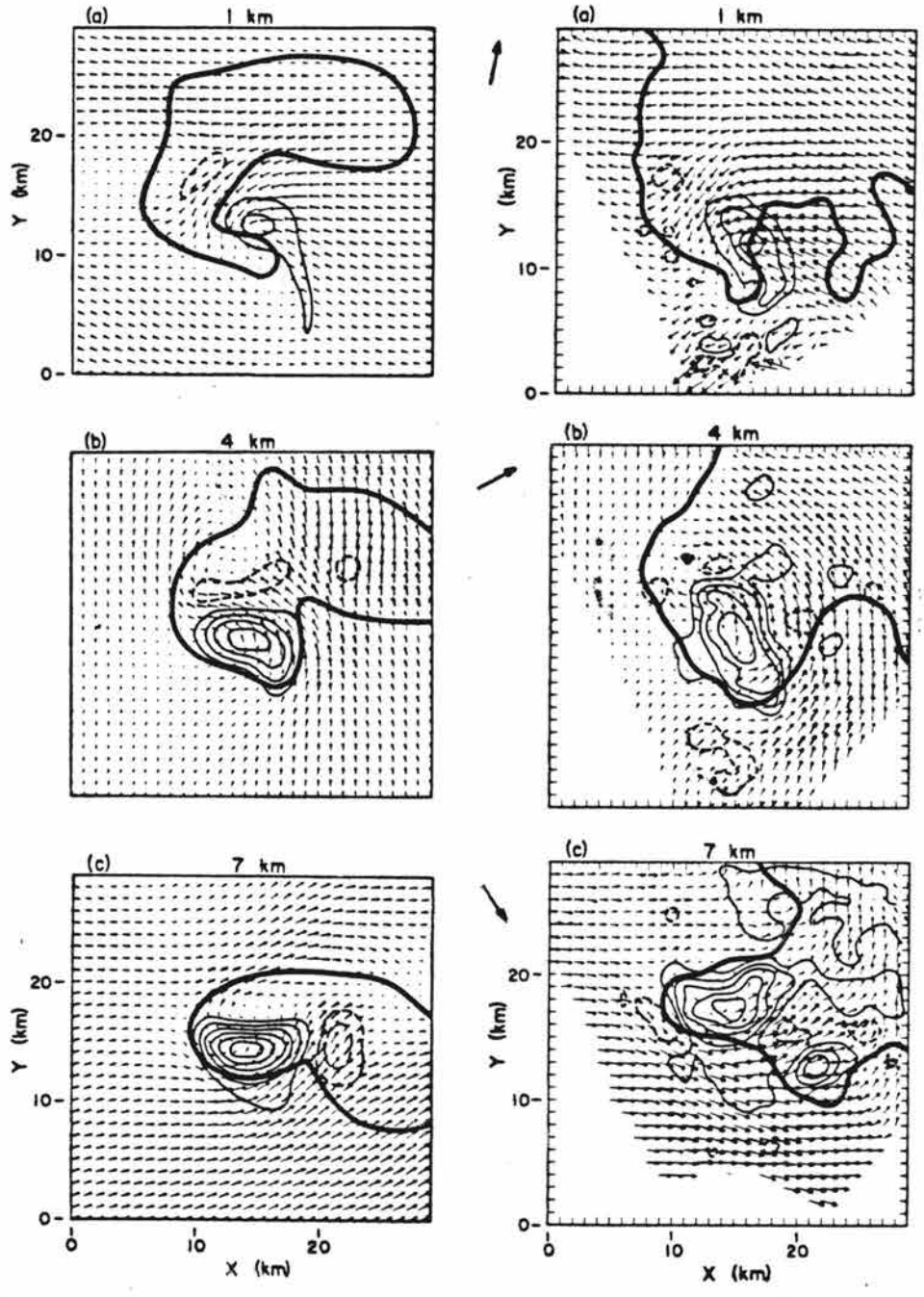

Fig. 2.10. Horizontal cross sections of flow patterns from a four Doppler radar analysis at 1833 CST (right column) and from a three-dimensional cloud model after 2 hr simulation (left column) initiated with a sounding considered representative of the observed storm's environment. Updrafts (solid lines) and downdrafts (dashed lines) are contoured at 5 m s^{-1} increments. Wind vectors are scaled such that one grid interval represents 20 m s^{-1}. The heavy solid line outlines the 0.5 g kg^{-1} rainwater contour for the model output (left) and the 30 dBZ radar reflectivity contour for the Doppler analysis (right). The local wind shear vector direction is indicated in the center. Taken from Klemp et al. (1981).

Krumm (1954) and MacDonald (1976) subsequently estimated that precipitation evaporation within a deep dry adiabatic layer alone could account for strong surface winds frequently experienced near high-based (3-4 km AGL) convective clouds. Brown et al. (1982) recently examined this problem further and found that even relatively shallow clouds producing virga and no lightning were capable of generating surface outflow winds in excess of 30 m/s. They constructed a composite sounding which depicts a dry adiabatic layer (3-4 g/kg mean mixing ratio) from the surface up to 500 mb. Brown et al. hypothesized that weak updrafts within such clouds produced small precipitation particles which melt and evaporate more readily than larger particles usually found in more intense Cb. Recently, in situ measurements beneath clouds of this type in Colorado (Rodi et al., 1983) have revealed a striking correlation between small-sized precipitation particles (most less than 1 mm diameter) and very strong downdrafts, or downbursts (up to 15 m/s), 3 km below the base of lightly-precipitating convection.

Although subcloud downdrafts within mixed boundary layers are often associated with precipitation, not all precipitation shafts generate strong downdrafts. A good example appears in Knight (1981) in which light precipitation from a rather long-lived Cb fell into a deep relatively dry mixed layer and failed to generate downdrafts and significant outflow. Limited precipitation observations indicated the presence of sparse, large particles which, due to their slow evaporation rates, may explain the lack of significant cooling and downdraft activity. Another closely-related example is seen in so-called "low-precipitation" storms recently documented by Bluestein and Parks (1983). Such rotating storms, which have a rather unique bell-shaped

appearance, lack extensive low-level precipitation and cold-air outflow, although large hail is frequently observed. Again, it may be argued that the apparent weakness of low-level downdrafts is explained by low rates of cooling by evaporation and melting of large-sized precipitation particles.

Occasionally low level downdrafts in severe storms appear to assume a two-celled pattern: one associated with heavy precipitation as described above and another located on the upshear flank within lighter precipitation. The schematic in Fig. 2.11 illustrates the relative locations of what Lemon and Doswell (1979) term a forward-flank downdraft (FFD) located within the precipitation core downshear, and a colder rear-flank downdraft (RFD) within lighter precipitation on the upshear storm flank. Lemon and Doswell speculate that the RFD is initially dynamically forced by perturbation pressure gradients [term

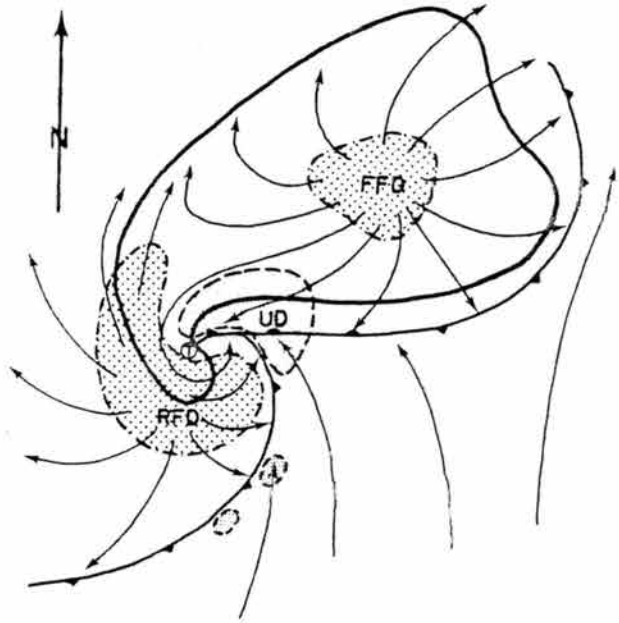

Fig. 2.11. Schematic plan view of surface features associated with a tornadic thunderstorm. Gust fronts are depicted by barbed frontal symbols. Low level positions of draft features are denoted by stippled areas, where UD is updraft, RFD rear flank downdraft, and FFD forward flank downdraft. Streamlines denote storm-relative flow. Taken from Lemon and Doswell (1979).

(a) of Eq. (2.1)] on the upshear flank at high levels (7-10 km), and then maintained by loading and evaporation of anvil precipitation at mid to lower levels. The pressure gradients were assumed to be generated by high pressure typically present within the upshear flank of updrafts (see Fig. 2.7) in which perturbation pressure increases with height up to midlevels [see Eq. (2.3)]. Qualitative aspects of such induced pressure pertubations given in Section 2.2 are more thoroughly discussed in Rotunno and Klemp (1982).

Although the existence of the RFD as distinct from the FFD is weakly supported by some surface mesonet analyses (Lemon, 1976; Barnes, 1978a,b) the RFD structure and dynamics are unclear. Many Doppler radar studies show horizontal continuity in downdrafts associated with precipitation and extending towards the upshear flank. Some investigations indicate that minimum θ_e air lies within downdraft cores (see Fig. 2.9) while in others the θ_e minimum lies on the upshear edge of the downdraft core. The example in Fig. 2.10 discussed above shows continuity of the low-level downdraft in both the Doppler and cloud model results. At 1 km both model and Doppler-derived wind fields indicate regions of weak downdraft which appear to be an extension of the stronger and more primary precipitation-associated downdraft located to the north and northeast. Air parcel trajectories constructed by Klemp *et al.* (1981) indicate that the low-valued θ_e downdraft outflow air residing along the upshear (rear) flank originated near the 4 km level and traveled around the eastern and northern sides of the primary updraft, rather than approaching directly from the upshear (southwest) flank.

Klemp and Rotunno (1983) examined characteristics of the rear-flank downdraft more closely by implementing an enhanced grid over the rotating portion of the storm simulated by Klemp et al. (1981). A summary of their results presented in Fig. 2.12 shows two downdraft regions, a large one associated with precipitation along the western or rear storm flank, and another small "occlusion" downdraft located within the strong storm-scale circulation (labeled T) at low levels. It was determined that this "occlusion" downdraft was forced by a downward directed pressure gradient, formed by a low level rotating wind field decreasing in magnitude with height.

The storm-scale rear flank downdraft (Fig. 2.12) may also be thermodynamically driven in special cases. A downdraft beneath the upshear precipitating anvil originating at midlevels is thermodynamically possible in cases of near dry-adiabatic environmental stratification. Harris (1977) presented calculations indicating that small quantities (~ 0.5 g kg^{-1}) of precipitation falling into a dry adiabatic layer may drive downdrafts up to 6 m s^{-1} within a 2 km distance by evaporation alone. Betts (1982a, 1984) has demonstrated that evaporation of only ~ 1 g kg^{-1} of precipitation can drive strong large-scale downdrafts in such cases. In particular, Betts (1984) inferred that small amounts of precipitation falling into a nearly dry adiabatic layer above cloud base can sufficiently cool that layer so that its virtual potential temperature matches that of the subcloud boundary layer. Subsequent precipitation evaporation and melting can then drive strong downdrafts over deep adiabatic layers in a manner similar to that discussed by Brown et al. (1982).

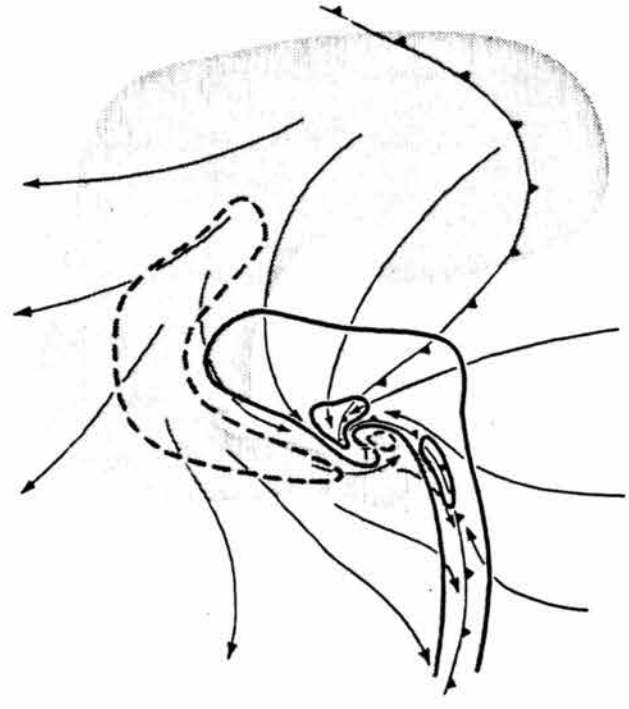

Fig. 2.12. Schematic low-level flow field from a composite of z = 250 m fields at 120 min in a storm-scale cloud model numerical simulation (one kilometer horizontal grid spacing), and at 6 min in a finer scale resolution numerical simulation. Vertical velocity is contoured approximately at 2 m s^{-1} intervals with the zero line omitted and the $-1^{\circ}C$ isotherm is denoted by the cold frontal boundary. Flow arrows represent storm relative surface streamlines and the region in which rainwater exceeds 0.5 g kg^{-1} is shaded. The location of maximum vertical vorticity is marked with a T. Note the storm-scale rear flank downdraft west of the updraft and the small-scale occlusion downdraft near the center of circulation. From Klemp and Rotunno (1983).

This section has further documented downdraft structure in terms of vertical extent, origin level, and association with precipitation. Thermodynamic analyses often indicate that origins of downdraft air reaching the surface lie between cloud base to several km above. Downdrafts and precipitation at low levels are closely associated, suggesting that precipitation effects provide primary forcing in low-level downdrafts.

The following section further illustrates some concepts described above and presents pictures of downdraft circulations derived from several detailed case studies.

2.3.3 Conceptual models of Cb downdraft circulations

Several conceptual models of Cb general circulation patterns have been constructed from analysis and synthesis of radar, mesonet and rawinsonde data. Two models mentioned previously are those of Byers and Braham (1949) and of Browning (1964), whose model is presented in Fig. 2.4. Another conceptual model devised by Browning and Ludlam (1962) was based on analysis of a severe hailstorm in England. This model portrays a downdraft circulation having relative inflow in the 6-8 km MSL (20,000-26,000 ft) interval, probably too high based on data presented previously. Such a flow configuration confined primarily to two dimensions may be most applicable to squall line thunderstorm systems.

A unique model proposed by Fujita and Byers (1977) suggests that strong downdrafts may originate near cloud top in association with overshooting updrafts. Although some observations indicate a relation between overshooting thunderstorm tops and subsequent low-level downburst activity, thermodynamic considerations suggest that overshooting updraft air would, upon sinking, regain sufficient positive

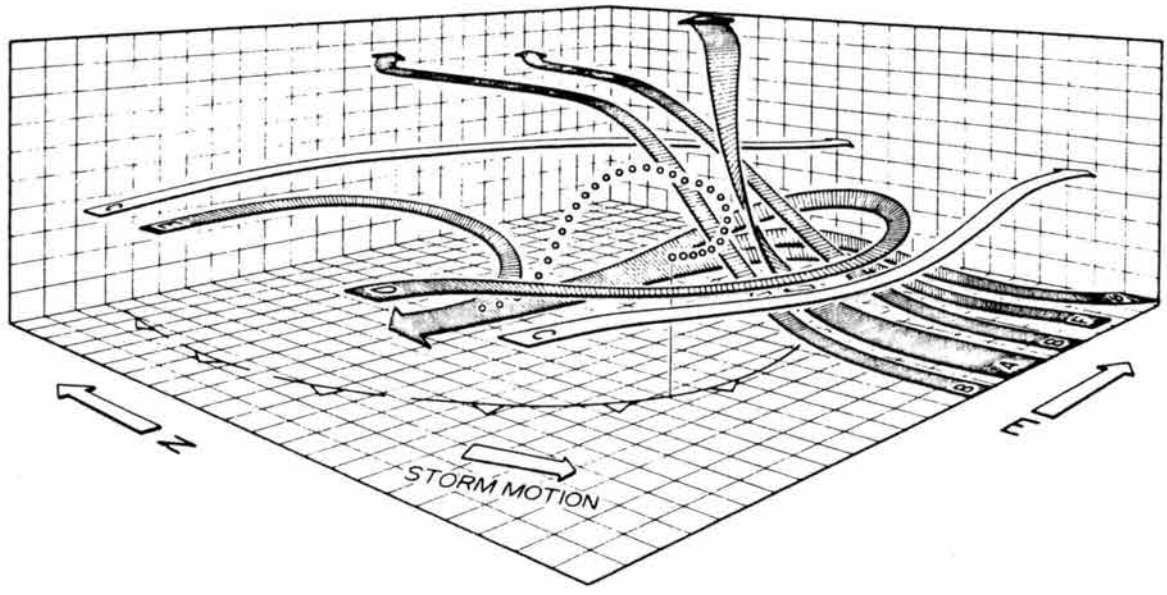

Fig. 2.13. Major components of airflow in a NE Colorado hailstorm. The strong updraft is depicted by the ribbon labeled A, which starts from low levels to the south-southeast of the storm, rises sharply in the storm interior, and leaves toward the northeast to form the anvil outflow. On the flanks of the strong updraft the air rises more slowly and penetrates farther to the rear of the storm before also turning to the northeast. In the middle levels there is a tendency for the westerly environmental flow to be diverted around the sides of the storm (streamlines labeled C) but some air also enters the storm (streamlines D and E) and contributes to the downdraft. A contribution to the downdraft flux is also made by air originally in the low levels to the southeast and east of the storm (streamlines F and G), which then rises several kilometers before turning downward in the vicinity of the echo core. The various streamlines are depicted relative to the storm, which is moving toward the south-southeast as shown. The small circles indicate the possible trajectory of a hailstone. From Foote and Frank (1983).

buoyancy to prevent it from descending more than a few kilometers below cloud top unless excessive precipitation loading and massive entrainment of dry midlevel environmental air occurred.

Another conceptual model constructed from a very comprehensive observational data set (Foote and Frank, 1983) is presented in Fig. 2.13. In this case several downdraft branches originating from mid to low levels converge near the precipitation core north of the updrafts. Midlevel branch D, similar to Browning's (1964) forward flank downdraft segment in Fig. 4, converges with another midlevel rear-flank branch (E) entering the northwest flank. Low-level branches F and G rise initially before entering the precipitation-filled downdrafts. Patterns similar to branches F and G also appear in the Doppler analyses of Knupp and Cotton (1982d).

In summary, all conceptual models depict organized midlevel flow of dry environmental air into a region within or near the precipitation core. Air within this flow may enter directly into the upshear flank or the downshear flank, or it may travel around the upshear flank of the updraft and intrude into the downshear flank. Preference of flow into the upshear or downshear flank probably depends on such factors as environmental shear, stability and moisture profiles, and the distribution of precipitation loading. The conceptual models further emphasize the close relationship between downdrafts and precipitation, a facet alluded to in the previous section. Other conceptual storm models (Knupp and Cotton, 1982a; Heymsfield, 1981; Kropfli and Miller, 1976; Browning et al., 1976 - see Fig. 2.9) indicate similar patterns.

From the foregoing, it appears that precipitating convection often exhibits systematic entrainment flows having large space and time scales

(1-10 km, 100-1000 s), in addition to the more turbulent entrainment and wake entrainment flows associated with nonprecipitating convection (see Section 4c). Large-scale organized lateral entrainment (or inflow) as depicted in Fig. 2.13 is believed to result from generation of storm-scale pressure perturbations produced by various mechanisms such as (i) pressure reductions induced by buoyantly-driven vertical accelerations, (ii) dynamic pressure changes produced by interaction of updrafts with shear flow [Eq. (2.3)], and (iii) pressure induced hydrostatically by warm and cold regions within and around clouds. Thus, detailed studies of pressure perturbations produced within convective clouds would greatly enhance understanding of entrainment.

Although observations have provided much information on variability in downdraft scales, intensity and structure, the dynamics of downdraft circulations remain speculative. Numerical model results summarized next shed additional light on downdraft dynamics and thermodynamics.

2.4 Modeling of Downdraft Dynamics and Thermodynamics

Observations of downdrafts outlined in the previous sections illustrated some aspects of downdraft structure and origin, but many details concerning downdraft dynamics and thermodynamics were not elucidated. This section contains results from an assortment of models ranging from one-dimensional (1-D) kinematic models which clarify downdraft microphysical-thermodynamical relationships, to fully elastic three dimensional (3-D) models that further depict downdraft structure.

Eq. (2.1) contains vertical forcing terms which have been mentioned only in passing to this point. Evaluation of each component of vertical force acting on parcels simultaneously within convective clouds has never been done with observed data, and accomplished to only a very

limited extent in 3-D cloud modeling work by Schlesinger (1980, 1984a,b), Rotunno and Klemp (1982) and Klemp and Rotunno (1983). Schlesinger found that both condensate loading (term (d)) and the perturbed vertical pressure gradient force (term (a)) were important and comparable to the thermal buoyancy (term (b)) in driving both updrafts and downdrafts. The pressure buoyancy force (term (c)) was of secondary importance. It seems probable that the relative importance of each term in (2.1) varies according to location in cloud and also depends on the environment, which ultimately controls storm (Cb) structure and intensity. Clearly, additional studies of a similar nature would greatly clarify draft dynamics.

2.4.1 Kinematic models

Before examining further details of the forcing terms in Eq. (2.1), some specifics on downdraft thermodynamics will be considered. Several steady state 1-D kinematic models have been used to examine the relationship between microphysical properties and thermodynamics in downdrafts. Hookings (1965) studied the steady properties of precipitation downdrafts by solving simplified (steady) equations for downdraft speed, thermodynamics and evaporation of drops of constant size. Assuming a vertical profile of temperature difference between downdraft and environmental air, Hookings (1965) determined that, with other factors remaining unchanged, more vigorous downdrafts occurred for (i) smaller drop sizes, (ii) greater liquid water content, and (iii) lower initial relative humidity at downdraft origin. Results from slightly different models in which downdraft speeds are specified (Kamburova and Ludlam, 1966; Das and Subba Rao; 1972) have illustrated that rates of evaporation and associated cooling are strongly dependent

on precipitation size and intensity. Fig. 2.14 displays temperature and mixing ratio profiles for several of the cases considered by Kamburova and Ludlam (1966). In their model various downdraft thermodynamic profiles were generated by varying the input parameters:

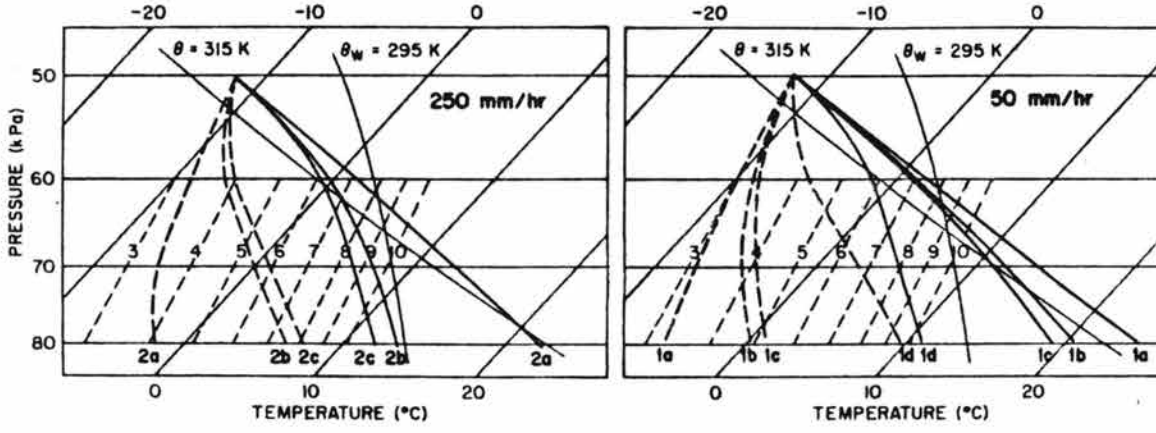

Fig. 2.14. Profiles of mixing ratio and temperature within strong ($w \simeq 20$ m s^{-1}) and weak ($w \simeq 2$ m s^{-1}) downdrafts beginning at 50 kPa. Each set of curves represents a given rainfall rate, raindrop dimeter and downdraft speed. Curves sublabeled with a,b and c,d have a constant raindrop size of 2.0 mm and 0.5 mm, respectively. Curves 1a, 2a, 1c, 2c represent strong downdrafts and curves 1b, 2b and 1d represent weak downdrafts. Adapted from Kamburova and Ludlam (1966).

uniform drop size (0.5 and 2.0 mm), rainfall rate (5, 50, 250 mm hr^{-1}), and mean downdraft speed (2, 10, 20 m s^{-1}) which obeyed ρw = const. Note that for strong downdrafts ($w \simeq 20$ m s^{-1}) temperature profiles closely follow dry adiabatic descent for a raindrop diameter of 2 mm. Moist adiabatic descent is approached only for very weak downdrafts within heavy precipitation consisting of small drops (curve 1d in Fig. 2.14). Curves 1b, 1c and 2b, 2c which probably bracket typical thunderstorm conditions indicate that downdraft air may commonly warm at rates halfway between moist and dry adiabatic, with ~ 2-4 g kg^{-1} rainwater evaporated in downdrafts descending from 500 mb to 800 mb.

One implication of these models is that downdraft intensity is not only a function of static stability, but also a function of the size distribution and concentration of raindrops. Strong downdrafts are easily produced by limited evaporation in nearly dry adiabatic atmospheres. However, for greater stability, greater evaporation rates may be needed to drive even relatively weak downdrafts and hence the precipitation microphysics becomes increasingly important. Only weak downdrafts would be expected within relatively deep layers having nearly moist adiabatic stratification (Fig. 2.5a), assuming that downdrafts are driven by negative buoyancy from evaporational cooling.

Betts and Silva Dias (1979) extended the kinematic models and derived expressions for potential temperature (θ) and mixing ratio (q) profiles within downdrafts. Assuming that θ_e is conserved in downdraft air, they obtained

$$\frac{dq}{dp} = \frac{\Delta q}{\pi_E} \quad ,$$

$$\frac{d\theta}{dp} = \frac{\Delta \theta}{\pi_E} \quad ,$$

where

$$\pi_E = \frac{\rho g w}{4\pi D F} \quad ,$$

$$\Delta q = q - q_w \quad ,$$

$$\Delta \theta = \theta - \theta_w \quad ,$$

$$F = \int n(r)\, r C_v(r)\, dr \quad ,$$

with the following definitions

w - downdraft speed

n - number of raindrops of size r

D - coefficient of diffusion of water vapor in air

C_v - ventilation coefficient for moving raindrops

ρ - air density

r - droplet radius

q_w - saturation mixing ratio at the wet bulb potential temperature

θ_w - wet bulb potential temperature.

Betts and Silva Dias call π_E a pressure scale for evaporation. Since π_E depends largely on downdraft speed (w), knowledge of w(p) allows determination of $\theta(p)$ and q(p) provided that F can be estimated and is constant.

The kinematic models have been applied in two cases (Ryan and Carstens, 1978; Leary, 1980) to infer thermodynamic profiles within mesoscale downdrafts. In the investigation by Leary (1980) realistic downdraft magnitudes in the range of those inferred from observations produced model profiles which show good agreement with Zipser's (1977) measurements within mesoscale downdrafts. These comparative studies suggest that mesoscale downdrafts can account for observed thermodynamic profiles beneath anvils of tropical squall lines and thus verify that such models can be used reliably for diagnostic purposes.

2.4.2 1-D and simplified 2-D time-dependent models

The relative importance of forcing terms in Eq. (2.1) can be evaluated by referring to simple 1-D and 2-D models. Ignoring evaporation, the relative importance of loading was examined by Clark and List (1971) in a 2-D incompressible model. A zone of hydrometeors (with a relatively large mixing ratio of 10 g kg^{-1}) 4 km wide and 2 km high was released at a height of 8 km through a neutral atmosphere at rest. After 750 s of simulation time, the resulting toroidal

circulations consisted of an 8 m/s downdraft located 3 km behind (above) the spreading particle zone which had fallen 5 km by this time. When stable stratification and evaporation thermodynamics were added by Girard and List (1975) this trailing downdraft was quickly transformed to an updraft as the air became positively buoyant from adiabatic warming. From the results of these experiments, one may infer that stronger downdrafts would result for small particles (with small terminal fall speeds) since particle residence time within a finite-sized parcel would be greater. Thus, accelerations would be produced over a larger time interval, leading to a stronger, more concentrated downdraft. However, increased evaporation and melting rates for small particles would probably dominate effects of increased particle residence times.

Several 1-D time dependent modeling studies (which ignore p') have examined effects of precipitation on downdraft formation. The models of Das (1964) and Srivastava (1967), both of which neglect entrainment effects (i.e., mixing of cloud and dry environmental air), develop downdrafts by precipitation loading near cloud base when rainwater produced higher in the cloud descends to lower levels. In both models downdrafts spread upward and downward from the genesis region below cloud base. Downdraft intensity is typically greatest in the adiabatic subcloud layer where both loading and precipitation evaporation operate. Das (1964) concluded that larger drops initiate downdrafts more quickly because of their ability to escape the updraft and fall to subcloud levels. (Recall that the kinematic model of Kamburova and Ludlam (1966) predicts that small drops, because of their greater evaporation rates, are more effective in driving downdrafts.)

Using a 1-D model including parameterized entrainment effects, Takeda (1966) noted that downdrafts were initiated by loading since the downdraft starting point occurred where the air was positively buoyant. Entrainment processes produced negligible effects even for small clouds which were subject to greater relative entrainment. (Such a finding may be related to the entrainment parameterization for this 1-D model). As a consequence larger simulated clouds produced more precipitation and hence stronger downdrafts.

In another 1-D time dependent model which included parameterized entrainment and hail microphysics, Wisner et al. (1972) noted that downdrafts of 8 m/s appeared only when hail formed within the simulated cloud and fell beneath the melting level into the subcloud layer where melting and evaporation occurred. When hail physics were deleted, downdrafts were absent because of the inability of raindrops to fall from the updraft into the subcloud layer and evaporate. Downdrafts were also absent in another experiment in which hail formation was allowed, but melting of hail deleted. However, when melting, but not evaporation was allowed, 4 m/s downdrafts developed, thus indicating the importance of cooling by melting. Multidimensional simulations and other diagnostic calculations examining effects of melting on downdraft dynamics are presented in following sections.

A more sophisticated 1-D model involving entrainment and updraft-downdraft interaction was initially described by Haman (1973) and later exercised by Haman and Niewiadomski (1980). Under the assumption that strong and steady downdrafts require a continuous supply of small droplets, a 1-D updraft/downdraft buoyancy model was used to test the hypothesis that entrainment and/or transport of water drops from the

updraft could maintain a downdraft capable of reaching the surface. Entrainment was parameterized between the updraft and environment, downdraft and environment, and updraft and downdraft. Results showed that downdrafts which entrain water from the updraft cannot descend to the surface because positive buoyancy and upward momentum are also entrained. Further experiments showed that sedimentation of small water droplets ($r \simeq 0.2$ mm) across a sloping updraft/downdraft interface produced stronger and deeper downdrafts. Other findings and conclusions from the experiments were:

i) Greater updraft entrainment of environmental air produces stronger downdrafts, as long as the updraft is not completely destroyed.

ii) Greater downdraft entrainment of environmental air leads to greater downdraft descent and strength provided that all water is not evaporated.

iii) Conditions for strong and penetrative downdrafts include low environmental stability, low humidity and entrainment of environmental air into both updraft and downdraft.

Another type of Lagrangian 1-D model based on similarity theory was used by Emanuel (1981) to study the theoretical behavior of small scale (~ 500 m) penetrative downdrafts. The validity of this model depends on several restrictive assumptions: i) that downdrafts assume a thermal- or plume-like behavior, ii) that downdraft characteristic profiles are similar across the downdraft width at all heights, iii) that entrainment velocities are proportional to a representative downdraft speed, and iv) that all water evaporates immediately (i.e., precipitation is absent). The similarity equations for thermal- or plume-like downdrafts include

conservation of momentum, mass, heat (buoyancy) and water. For cloud liquid water contents ranging from 1-3 g kg^{-1} and a cloud virtual temperature lapse rate of 8.4 K km^{-1} (a large value) model results produced downdraft speeds in the range 6-17 m s^{-1}, comparable to the observations in Table 2.1. Maximum penetration depths varied from 3 km to the entire cloud depth.* According to Emanuel, this simple theory explains observed phenomenon such as i) small-scale intense in-cloud downdrafts initiated by cloud-top entrainment instability, and ii) mamma formations beneath Cb anvils.

2.4.3 Fully prognostic 2-D and 3-D cloud models

The use of fully prognostic 2-D and 3-D cloud models for investigations of downdraft structure has been rather superficial to date. Most studies have focused on general cloud structure as determined by wind shear profiles. Nevertheless, examination of downdrafts produced by these models is worthwhile even though simulated downdraft structure may not be completely realistic due to (i) crude parameterization of turbulent mixing and microphysical processes and (ii) neglect of ice phase precipitation. (The critical dependence of downdraft structure on microphysics was demonstrated by kinematic model results described earlier).

In the following paragraphs recent modeling papers listed in Table 2.3 are summarized to illustrate: (i) the (close) relationship between precipitation and downdrafts; (ii) downdraft origin, intensity and location as a function of wind shear and static stability; and (iii) other characteristics relevant to downdraft dynamics. We emphasize that

---

* The values may be exaggerated due to the large assumed cloud lapse rate of 8.4 K km^{-1}.

Table 2.3. Draft statistics from cloud model simulations.

Author(s)	Abbreviation	Model Dimension	Wind Parcel Shear/Buoyancy*	Cloud type	W_{max}(m/s)	W_{min}(m/s)	Height of W_{min}(km)	T'_{min}
Takeda (1971)	T71	2D	0,1/1-2		8-16	-2 to -6	~2	
Hane (1973)	H73	2D	1-2.5/2	Squall line	25	-11	~3	-9
Orville and Kopp (1977)	OK77	2D	1-2/2.5	Cb	25-30	-10	~1	
Cotton and Tripoli (1978)	CT78	3D	0,1/1	Cu con	~10	--4		
Klemp and Wilhelmson (1978a)	KW78a	3D	0-2/2	Cb	21	-6^{ℓ}	~2	-5
Klemp and Wilhelmson (1978b)	KW78b	3D	2/2	Cb	15+	-5^{ℓ}		-4
Wilhelmson and Klemp (1978)	WK78	3D	2-3/2	Cb	20	-8		
Schlesinger (1978, 1980)	S78,S80	3D	2.5/2.5	Cb	37	-10^{u} -15^{ℓ}	4-6 1.5	-7
Miller (1978)	M78	3D	1.5/1.5	Cb	25	$--5^{\ell}$		-5
Thorpe and Miller (1978)	TM78	3D	1.5-2/1.5	Cb		$--5^{\ell}$		-5
Clark (1979)	C79	3D	2/2-2.5	Cb	35	-15^{u} -5^{ℓ}	7.0 1.5	-7
Tripoli and Cotton (1980)	TC80	3D	1.5/1	Cb	~15	$--5^{\ell}$		
Simpson and Van Helvoirt (1980)	SVH80	3D	1/1	Cb	7	-6	1.5	-5
Simpson et al. (1982)	SVHM82	3D	1/1	Cu con	7.5	-5	1.5	-4
Wilhelmson and Klemp (1981)	WK81	3D	2.5/2.5	Cb	40	-25^{u} -10^{ℓ}	~7 ~3	-8
Klemp et al. (1981)	KWR81	3D	2/2.5	Cb	35	-15^{u} -8^{ℓ}	~7 ~1.0	
Thorpe et al. (1982)	TMM82	2D		Squall line				
Wilhelmson and Chen (1982)	WC82	3D	1.5/2	Cb	~15	--5	~1	-10
Levy and Cotton (1984)	LC84	3D	1/1.5	Small Cb	30	-10	2-3	

* These are subjectively classified as weak (1), moderate (2), and strong (3). No shear is 0.

ℓ - lower downdraft ($z \leq 3$ km)

u - upper downdraft ($z > 4$ km)

each model will treat downdrafts differently because of varying treatments of microphysical and turbulent parameterization, other model physics and numerical procedures and resolution.

These cloud model studies cover a wide range of environmental and associated convective cloud types. Maximum modeled updraft speeds vary from < 10 m s^{-1} for weakly unstable, low shear tropical or subtropical atmospheres (CT78, SVH80, SVHM82), to > 30 m s^{-1} for midlatitude unstable atmospheres with high shear (S78, C78, KWR81, WK81). Maximum simulated downdrafts range from several to ~ 15 m s^{-1}.

In both 2-D and 3-D cloud simulations downdrafts are usually generated in two locations--an elevated downdraft located near the updraft edge at mid to upper levels, and a low level downdraft closely associated with precipitation. Fig. 2.15 illustrates downdrafts of each type from a 2-D simulation using the CSU cloud model as documented by Tripoli and Cotton (1982). (Also see Fig. 2.10.) The often transient upper level downdraft typically exhibits speeds of 5-15 m s^{-1} and may be the result of several mechanisms: localized mass compensation and associated perturbation pressure gradient forces (M78, S80), and evaporation near cloud edge (S80, TC80, C79). The low-level downdraft, having typical speeds of 5-10 m s^{-1}, is forced primarily by loading and evaporation of rain. When rain formation is inhibited the low level downdraft is either absent or strongly diminished as shown in KW78b, M78 and LC84. LC84 also noted that midlevel cloud downdrafts were increased by 50% when precipitation formation was inhibited, suggesting that additional cloud water acted to increase loading and evaporational cooling at higher levels.

In several of the model studies (SVH80, S78) downdraft maxima shift from upper to lower levels upon or shortly after precipitation arrival at low levels. Further downdraft/precipitation relationships are evident in the 2-D studies of T71, who noted that stronger downdrafts are correlated with stronger updrafts, the link being through heavier precipitation produced by stronger updrafts. Similar relationships are suggested in the 2-D model studies of H73, where downdraft maxima lagged updraft maxima by ~ 5 min, and in the 3-D modeling work of KW78a, where downdraft peaks followed updraft peaks by 12-15 min. In each case updrafts and downdrafts are coupled through precipitation produced within the updraft.

Of the 19 model simulations listed in Table 2.3, only one (CT78) simulates a non-precipitating cloud. In this case several meter per second downdrafts were generated beneath the cloud in association with evaporational cooling by dynamic entrainment, but these downdrafts did not reach the surface. Thus, although precipitation is not required for downdraft initiation, low level downdraft mass flux and intensity are apparently enhanced significantly when precipitation falls into the subcloud layer.

The model simulations also reveal a dependence of downdraft location, origin and intensity on wind shear and stability. Studies which have included shear and no shear comparisons show increased entrainment (CT78, SVHM82) and quicker downdraft development (S78, KW78a) with wind shear included. SVHM82 suggested that entrainment increases with wind shear, but their results do not suggest a similar relationship between shear and downdraft speed. Model simulations indicate that downdrafts form more quickly with shear. S78 noted that

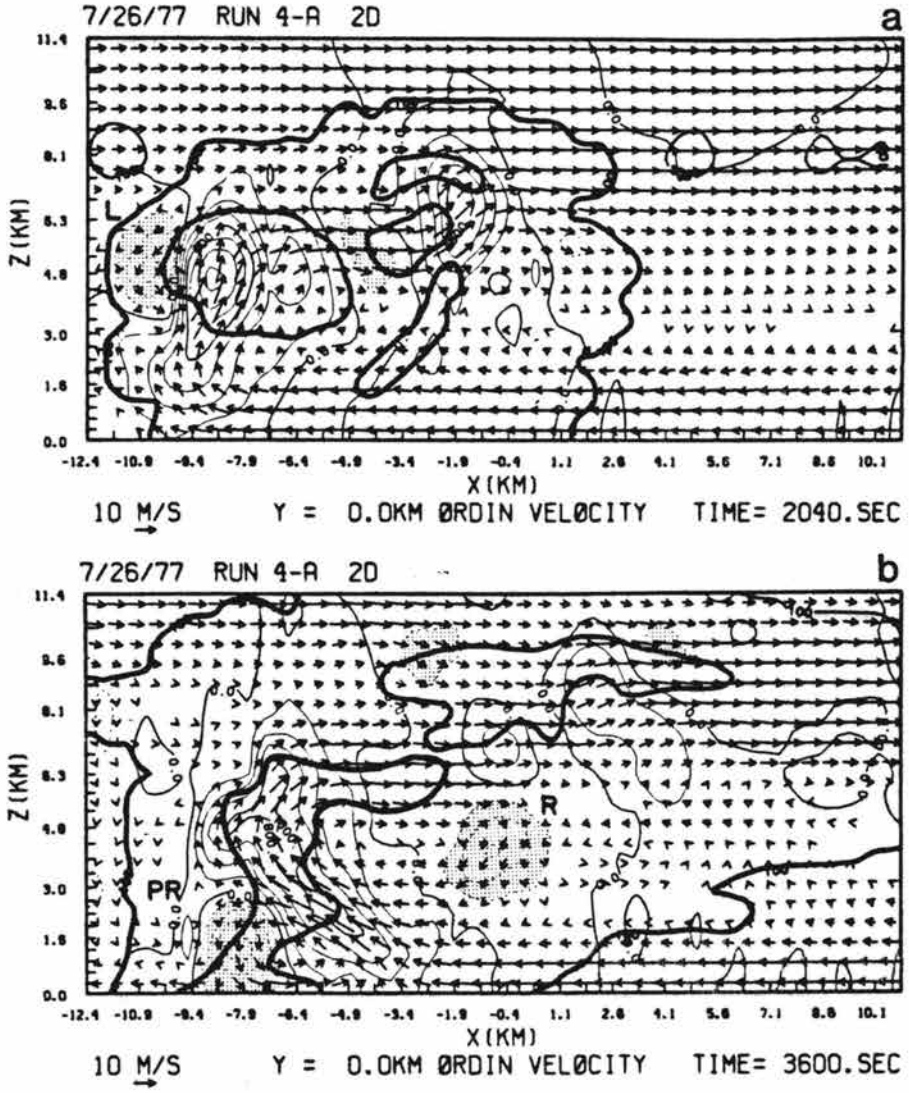

Fig. 2.15. Output at two different times from the CSU cloud model run in two dimensions. Vertical motion is contoured every 2 m s^{-1}, and heavy contours represent total condensate mixing ratios of ~ 0 and $\underline{2}_1$ g kg^{-1}. Downdrafts with magnitudes greater than 2 m s^{-1} are stippled.

downdrafts formed 12 min sooner for simulations with wind shear. Similar comparative studies by WK78 indicate slightly less time to downdraft maximum value when shear was doubled, but downdraft peaks were only 75% of those produced in the lower shear simulation. Such a behavior may be a consequence of two effects: (i) less precipitation being generated in simulations with shear due to increased entrainment; and (ii) decreased local precipitation intensity due to precipitation elements being distributed over a larger area.

In some cases increased midlevel entrainment may invigorate downdrafts over a limited height interval. In simulating glaciation from cloud seeding, LC84 found that increased buoyancy from latent heat released by water freezing induced an increased lateral entrainment of dry environmental air at and just below the seeding level. Evaporational cooling associated with this entrainment produced downdrafts of 1-2 m/s which penetrated only ~ 0.5 km below the level of entrainment.

Simulations having no wind shear produce downdrafts directly beneath updrafts either due to dynamic entrainment effects (CT78) or loading and evaporation of precipitation which falls from the updraft (S78, KW78a, SVHM82). Contrastingly, simulations in wind shear develop downdrafts with a preferred location upshear or downshear of updrafts. Two-dimensional simulations in environmental flow that increases monotonically with height typically produce upshear downdrafts as precipitation falls from upshear-tilted updrafts into lower midlevel subsaturated air (e.g., H73, OK77, TMM82). Fig. 2.15b illustrates such a configuration. Exceptions are seen in T71, in which downshear downdrafts seem to prevail for winds increasing with height. Upshear

downdrafts were produced only when wind decreased with height through a sufficiently deep layer (i.e., a low level jet existed).

Three-dimensional simulations also generate upshear or downshear downdrafts, but patterns are complicated and probably are dependent on details of the shear profile. Both downdraft types appear in S78, but the downshear downdraft seems to occur more commonly for a variety of shear conditions (e.g., M78, TM78, TC80, KWR81-see Fig. 22). TC80 suggest that downshear downdrafts form as a result of preferred entrainment into the downshear wake where pressure perturbations are low (Fig. 2.7). TM78 attributed downshear downdraft formation to the fact that downshear sloping updrafts dropped precipitation primarily on the downshear side suggesting both processes act concurrently to create and maintain a downshear downdraft. In a highly 3-D shear case KWR81 showed downdraft aligned downshear of the local shear vector at various levels as shown in Fig. 2.10.

Model simulations demonstrate that air which reaches the surface in low level downdrafts usually descends 2-5 km. Air within elevated downdrafts apparently does not reach the surface. Trajectory analyses done for several cases (M78, S80, KWR81) indicate that air enters the downdraft circulation primarily from the 1.5-4.0 km layer above the surface. These trajectories are highly three-dimensional, depicting airflow around the downshear (southeast) portion of the updraft which descends to the east and north in a manner similar to the Browning (1964) model in Fig. 2.4. Model simulations also indicate that upper portions of the low level precipitation-associated downdraft are warm (at 3-4 km), and the low portions cold, usually being more than 3 K cooler than ambient.

The influence of pressure perturbations (p') on downdraft initiation and maintenance has not been discussed in detail to this point. Rotunno and Klemp (1982) investigated pressure anomalies produced by the interaction of an updraft with shear flow using linear theory. They derived Eq. (2.3), which for normal wind shear (i.e., winds increasing with height as depicted in Fig. 2.7) would predict positive and negative p' on the respective upshear and downshear flanks of an updraft. This was used to qualitatively explain why convective storms tend to develop positive vorticity and rightward movement bias for wind shear profiles which often turn clockwise (i.e., local wind shear vectors which turn in a closkwise manner) with height. While opposite patterns would prevail for a downdraft, the applicability to downdraft circulations may not be as straightforward.

In another study alluded to in Section 2.3.2, Klemp and Rotunno (1983) simulated a downdraft within a mesocyclone in which the downdraft apparently was forced by a downward-directed $\frac{\partial p'}{\partial z}$ formed by a rotation decreasing in magnitude with height. This downdraft first formed at low levels and then spread upward as the flow adjusted to the induced pressure gradient. While this is obviously a special case, the importance of other mechanisms which force downdrafts by pressure perturbations needs to be evaluated further.

The 1-D kinematic model results discussed above suggested that downdraft intensity is a function of static stability. There is only one set of simulations in Table 2.3 in which static stability was varied. T71 ran a no-shear simulation with increased low level stability which produced weak updrafts, limited rain and very weak downdrafts. Close inspection of other model simulations and their

initial soundings suggests a possible relationship between stable layers and the lack of strong downdrafts within such layers. Although only limited conclusions can be drawn from examination of limited model output, additional sensitivity studies are needed to establish stability-downdraft relationships and effects of stable layers on downdraft circulations.

2.5 Summary

This section has described, using a number of different sources, many observed and modeled aspects of convective cloud downdrafts. These properties are listed below.

(a) Observed downdraft magnitudes within cumulus congestus (Cu con) and Cb clouds are typically 5-10 m s^{-1}. Maximum values appear to be limited to ~ 20 m s^{-1}.

(b) Direct measurements unveil a spectrum of cloud downdraft scales. Nonprecipitating clouds have downdraft scales with an upper limit of ~ 1 km. In contrast, precipitating clouds display downdraft scales over the range 100 m to 10 km. These convective scale downdrafts are distinct from mesoscale downdrafts which have representative magnitudes and spatial scales of ~ 10^{-1} m s^{-1} and ~ 100 km, respectively.

(c) Observations and cloud model results indicate that low level downdrafts are closely associated with precipitation. While precipitation loading and evaporation supply appreciable forcing, melting effects can also be significant and need further study.

(d) Cloud models typically produce two independent downdrafts. One is the precipitating downdraft described in (c). The other is often generated by numerical models and is sometimes observed at mid to upper

levels adjacent to the updraft (e.g., Fig. 2.15). Although at least partly driven by evaporation at cloud edge its structure and dynamics are unclear. Vertical transports associated with this downdraft need to be accounted for if an accurate downdraft parametric model is desired.

(e) Observational and modeling studies demonstrate that air within precipitating downdrafts descends to the surface from heights ranging from just above cloud base (1-2 km) up to heights ~5 km above ground level (AGL). Total vertical displacement of downdraft air is dependent on such factors as environmental stability and wind shear profiles, cloud vigor, precipitation intensity and particle-size spectrum, and the presence of melting precipitation, all of which may be interrelated.

(f) Observations indicate that downdrafts in both precipitating and nonprecipitating clouds are usually associated with entrainment. Systematic entrainment flows may resemble an organized inflow, on the order of the spatial scale of the updraft. Other turbulent-like entrainment mechanisms within nonprecipitating clouds and upper regions of precipitating clouds have not been well defined, but appear to be more random and less systematic in space and time. Another particular type of entrainment flow within precipitating and nonprecipitating convective clouds forming in a sheared environment is the wake entrainment occurring within the downshear portion of the updraft. The spatial scale of this systematic flow is also similar to the updraft scale.

(g) Results from simple 1-D kinematic-microphysical models demonstrate a strong dependence of downdraft strength on environmental stability and precipitation microphysics. Strong downdrafts are readily produced by only limited evaporation in dry adiabatic layers. For more

stable atmospheres, strong downdrafts require greater rates of evaporation and hence are favored by large concentrations of small precipitation particles.

Fig. 2.2, presented earlier, illustrates several of the observed and inferred downdraft features defined in Table 2.1: the precipitation downdraft and associated organized inflow (entrainment) and outflow, discrete entrainment at cloud sides and top with associated small-scale penetrative downdrafts, and elevated downdrafts adjacent to updrafts. The precipitating downdraft system, with its well organized inflow and outflow branches, is closely associated with the gust front which may maintain convective activity via low level convergence. Inflow into the top portion of this downdraft system implies low pressure there, but the mechanics of this process have yet to be elucidated. Less organized entrainment and penetrative downdrafts are inferred at cloud top and sides. These more discrete entrainment processes are also not fully understood, but the small-scale downdrafts may nonetheless attain significant speeds.

Many aspects of downdraft structure and dynamics depicted in Fig. 2.2 remain unclear. Some specific questions regarding these uncertainties are:

* What is the role of precipitation in determining downdraft structure? What, in particular, are the relative effects of precipitation loading, evaporation, and melting?
* What are the structural properties and dynamics of downdrafts which occur at mid to upper levels?
* What is the origin and significance of pressure forces associated with downdraft circulations?

* How does entrainment operate and what is the role of entrainment in initiating and sustaining downdrafts?
* How do environmental wind shear and stability profiles affect entrainment and downdraft structure. In particular, how are downdrafts influenced by stable layers which often exist?
* How do downdraft outflows affect storm structure, and how do downdraft transports influence larger scale processes?

The following sections address some of the questions listed above. Particular attention is paid to downdraft structure, both observed and modeled, and to the dynamics and thermodynamics of the low-level precipitation-associated downdraft.

3. RESOURCES

This study utilizes two primary sources of information, namely cloud model results and multiple Doppler radar data, to deduce the structure and dynamics of downdrafts. General aspects of the observational data and the CSU cloud model are given in the following subsections. Appendix A contains more detailed information on Doppler data reduction procedures and accuracy, and Appendix B provides information on data quality. Specific aspects of the CSU cloud model equations and other related items are presented in Appendix C.

3.1 Observational Data

The observational analyses presented in Section 4 include data from two field experiments, the South Park Area Cumulus Experiment (SPACE) conducted in central Colorado, and the Cooperative Convective Precipitation Experiment (CCOPE) conducted in SE Montana. Each program incorporated rawinsonde, surface mesonet and multiple Doppler radar observational platforms, the characteristics of which are described in Cotton et al. (1982) for SPACE and in Knight (1982) for CCOPE. Instrumentation locations for each experiment are portrayed in Figs. 3.1 and 3.2

Portable automated mesonet (PAM) surface stations available in both experiments measured temperature, humidity, pressure, wind and rainfall, with each parameter recorded at 1 minute intervals. The CCOPE program implemented additional PROBE (Portable Remote Observation of the Environment) stations which measured the same parameters but recorded

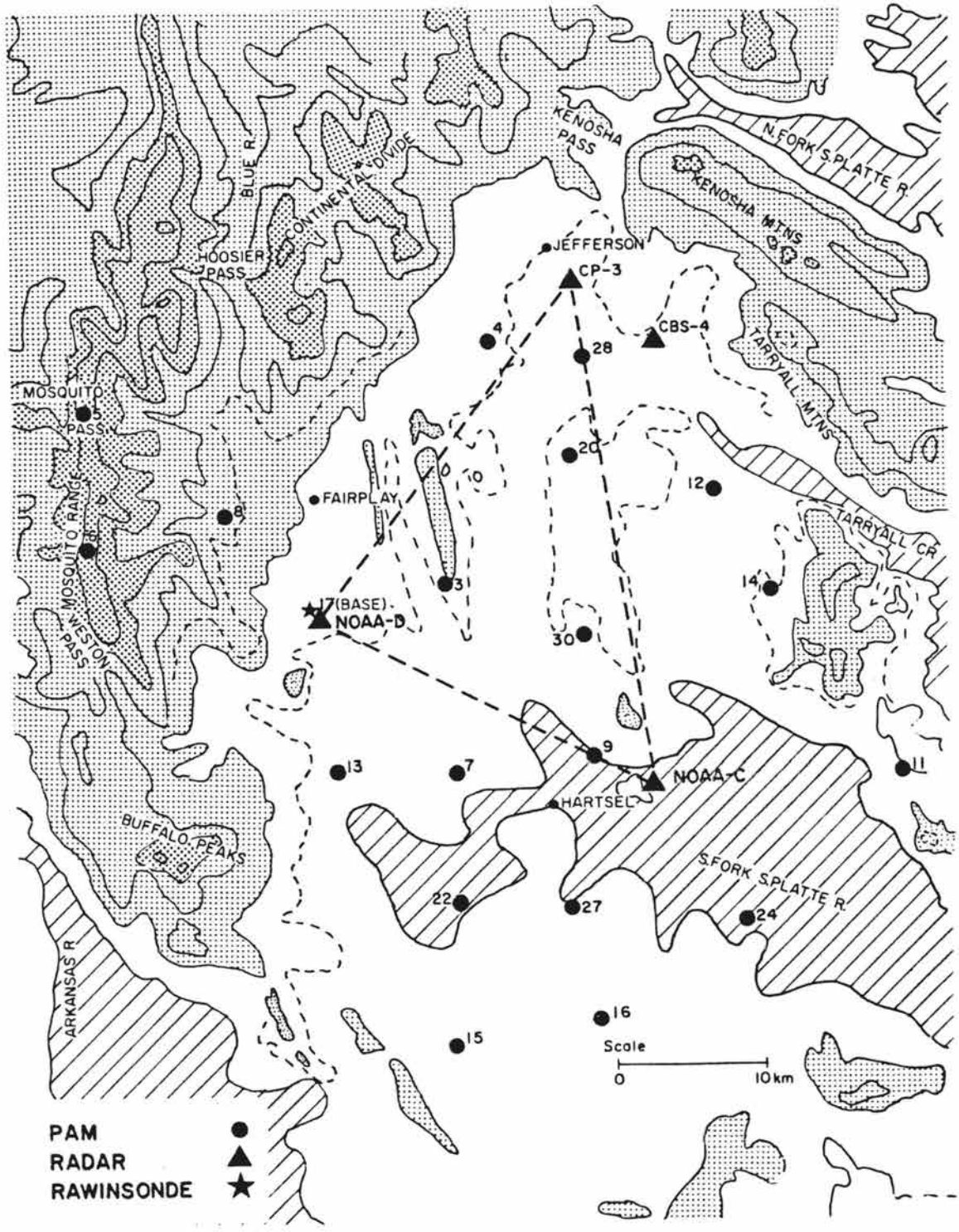

Fig. 3.1. Instrumentation employed during the 1977 South Park Area Cumulus Experiment (SPACE). Terrain below 9,000 ft (2745 m) is hatched, terrain above 10,000 ft (3048 m) is lightly shaded, and terrain above 12,000 ft (3657 m) is darkly shaded.

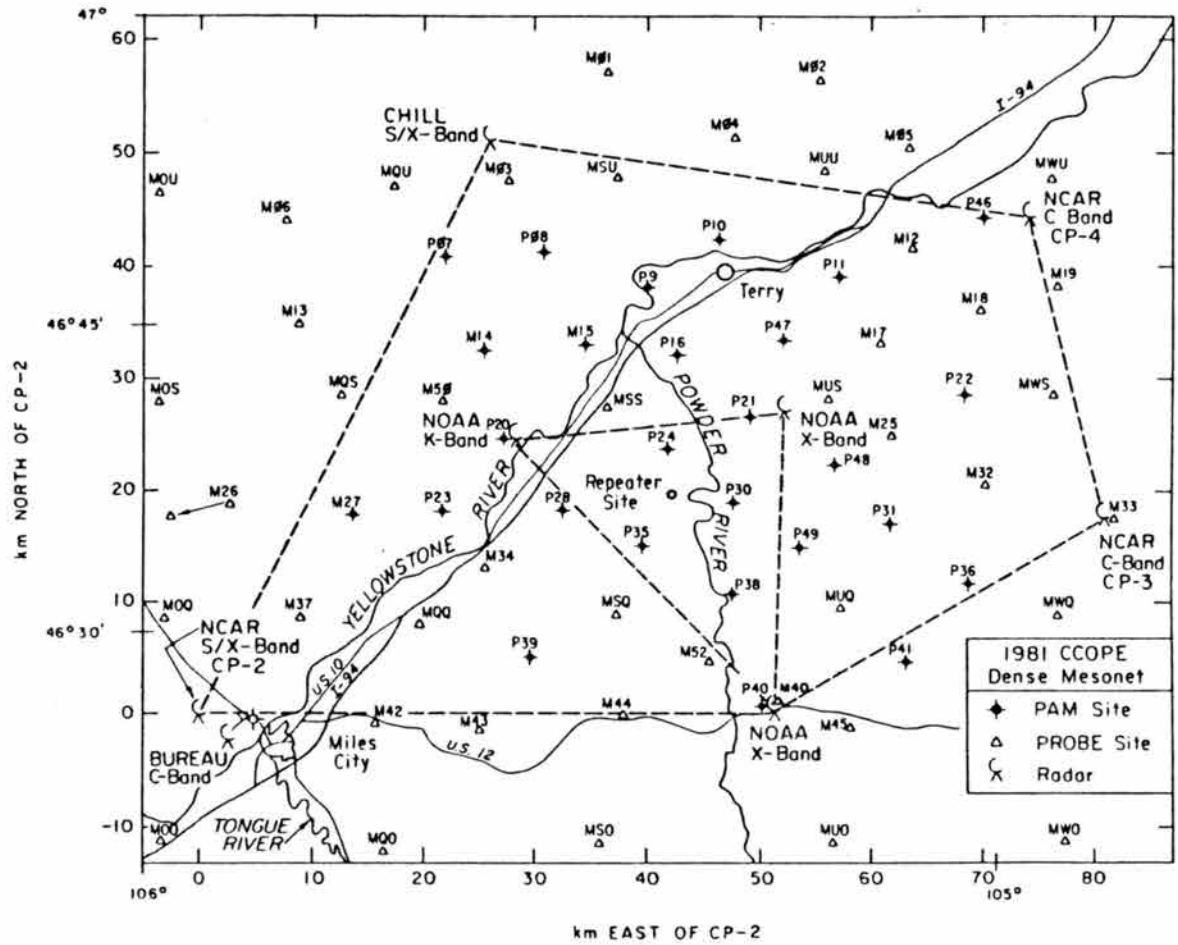

Fig. 3.2. Instrumentation employed during the 1981 Cooperative Convective Precipitation Experiment (CCOPE).

them at longer 5 min intervals. Characteristics of PAM and PROBE stations are detailed in Brock and Govind (1977) and in Harrison et al. (1979), respectively. Rawinsonde data consisting of temperature, humidity and horizontal wind were acquired in both field programs by the RD-65A automatic tracking system. Doppler radar data consisting of reflectivity factor, mean radial velocity and in some cases variance of the velocity spectrum were acquired by up to 3 Doppler radars in SPACE and up to 7 radars in CCOPE. Characteristics of each radar unit and their sampling characteristics are given in Appendix B. Table 3.1 presents information on quality and content of data used in the case studies.

TABLE 3.1 SUMMARY OF OBSERVATIONAL DATA

	Data Quality		Data Coverage	
Case[1]	Doppler	Mesonet	Doppler	Mesonet
6/22/76(s)	good	good	good	good
7/22/76(s)	good	good	good	good
7/25/76(s)	good	none	good	none
7/19/77(s)	fair	fair	fair	fair
7/20/77(s)	poor	good	fair	good
7/21/77(s)	none	good	none	good
7/26/77(c)	good	good	fair	good
8/4/77(c)	good	good	fair	good
6/12/81(c)	good	poor	good	poor
8/1/81(c)	good	good	good	good
8/2/81(s)	good	good	good	good

[1] These are classified as complete case studies (c) or supporting case studies (s).

Data from individual Doppler radars were edited to eliminate bad values, unfolded to correct aliased radial velocities, and then interpolated onto a Cartesian grid. Radial velocity data from two or more radars were then combined to produce estimates of horizontal motion (u,v) and horizontal divergence. In all cases to be presented, vertical

motion was obtained by integrating the anelastic mass continuity equation downward from echo top. The top boundary condition was set to the estimated divergence at the uppermost level, multiplied by one-half the vertical grid increment.

The derived vertical velocity data have not been corrected in any way to force a zero boundary condition at the surface (z = 0). While the mass balance scheme of O'Brien (1970) has been applied by Ray et al. (1980), such a procedure was not utilized in this study because accurate sampling of winds over the lowest kilometer, where downdrafts may be quite intense (see Section 2), was often not available. It is felt that mass balancing would have unrealistically diminished downdrafts at the lowest 1-2 km.

Data quality in all four cases labeled c in Table 3.1 is considered to be sufficiently good to depict general downdraft patterns, even at low levels. Downdraft magnitudes presented in Section 4 are believed to lie within 2-5 m/s (~50%) of true values in most cases. In all cases to be presented, comparison of Doppler-derived downdraft patterns with measurements from other platforms such as surface mesonet showed excellent qualitative agreement.

3.2 Description of the Cloud Model

The numerical modeling portion of this study employs the CSU cloud model as described and documented in Cotton and Tripoli (1978), Tripoli and Cotton (1980, 1982) and Cotton et al. (1982). Successful model applications have included simulations of marine cumulus congestus clouds (Cotton and Tripoli, 1978), investigations on the relation between cumulonimbus intensity and cloud/mesoscale forcing (Tripoli and Cotton, 1980), investigations on mechanisms of communication between

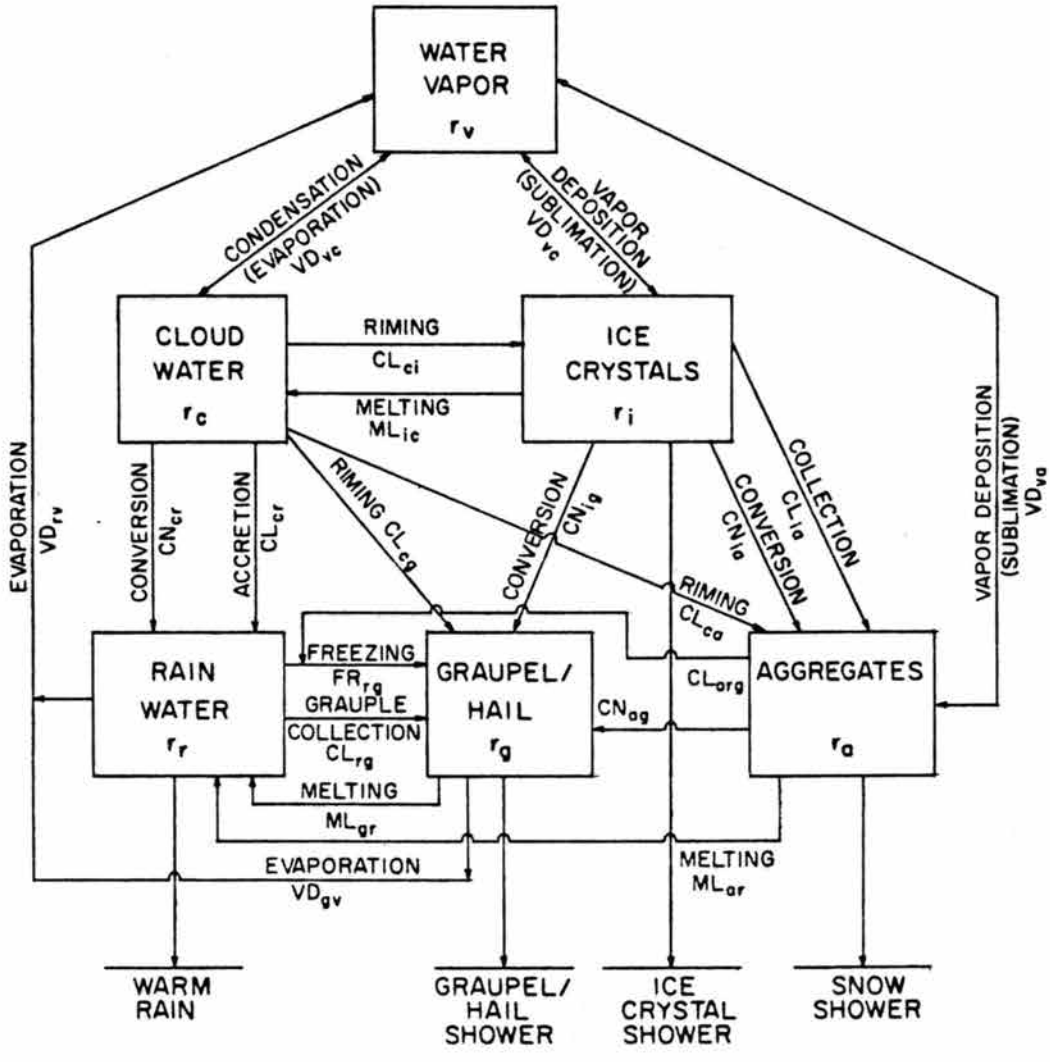

Fig. 3.3. Schematic illustration of microphysical processes parameterized in the CSU Cloud model. From Cotton et al. (1985).

boundary layer processes and convective cloud seeding response (Levy and Cotton, 1984), and simulations of wintertime orographic clouds (Cotton et al., 1982). General aspects of the model are described in this subsection, and details on model equations and parameterizations are given in Appendix C.

Both 2-D (slab symmetric) and 3-D versions of the cloud model were exercised in this study. The model contains a full set of non-hydrostatic compressible dynamic equations, a thermodynamic energy equation, and a set of microphysics equations for water- and ice-phase cloud and precipitation. Predicted variables include three velocity components, ice-liquid potential temperature (Tripoli and Cotton, 1981), dry air density, and mixing ratio of total condensate, rainwater, ice crystals, graupel and aggregates. Subgrid-scale turbulent processes (fluxes) are parameterized using an eddy-viscosity type first-order closure scheme.

Fig. 3.3 illustrates the microphysical processes included in the model. Both raindrop and graupel particles are assumed to follow Marshall-Palmer (1948) exponential distributions. Rainwater microphysical processes are parameterized using an autoconversion formulation in which raindrops spontaneously form when cloud water concentration exceeds a specified threshold. Raindrops may then grow by parameterized accretion processes. Ice crystals form by nucleation processes and grow by vapor deposition and/or riming of cloud water. Aggregates (clusters of ice crystals) are initiated from ice crystals which attain a critical collision/sticking rate determined by their size, concentration, mixing ratio and collection efficiency. Aggregate growth then occurs primarily by riming of cloud water, by collection of

ice crystals, and secondarily by vapor deposition. Graupel particles form by freezing of raindrops, conversion from aggregates which have undergone riming, and conversion from snow crystals whose growth rate exceeds a specified critical value. Graupel growth occurs from riming of cloud water, from collection of raindrops and aggregates, and secondarily from vapor deposition.

Raindrop evaporation is calculated by integrating over the raindrop distribution the rate of evaporation of a single drop. This formulation which makes use of diffusion theory adjusted for drop motion yields an expression which is highly dependent on drop radius (see Eq. C.17 in Appendix C). Melting of ice particles closely follows the formulation of Wisner et al. (1972) in which heat required to melt ice is derived from heat conduction from air and cloud/rain water, and from latent heat liberated by condensation of water vapor onto the ice particle. Additional melting can be produced by ice particle collection of cloud and rain water having temperatures greater than zero Celsius. Melting rates also exhibit a strong dependence on ice particle size and a weak dependence on wet-bulb temperature when $T > 273.16$ K. Evaporation of cloud water is assumed to occur instantly when ambient water vapor mixing ratios fall below saturation values. Ice crystal melting to cloud water similarly occurs when temperature exceeds 273.16 K. Further details on melting and evaporation are given in Appendix C.

The model equations were integrated on a Cartesian grid which varied from case to case as shown in Table 3.2 and Fig. 3.4. Constant horizontal grid spacing of 750-1000 m, and variable vertical grid spacing corresponding to hydrostatic pressure increments of 25-30 mb, yielded typical domain sizes of 45 km squared in the horizontal and 25

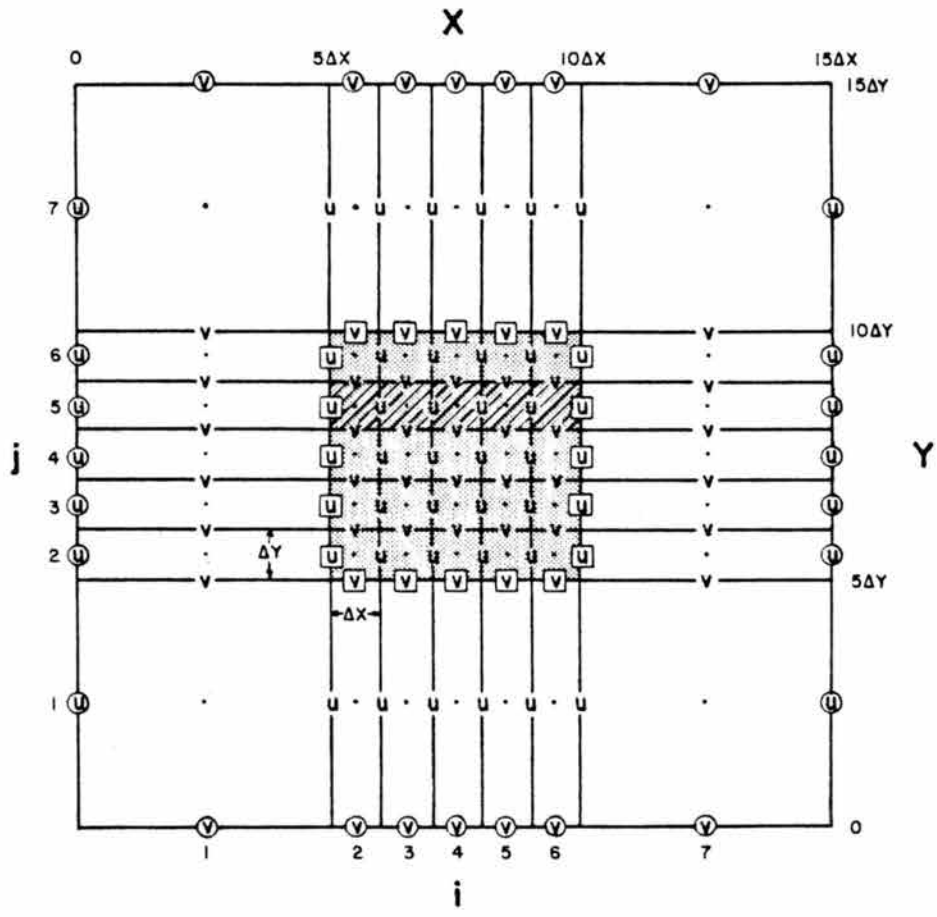

Fig. 3.4. Diagram showing cloud model grid configuration. The simulation domain is given by the shaded region and the MCR by the unshaded region. Scalar variables and w are located at points depicted by dots while u and v are shown at their given locations. From Tripoli and Cotton (1982).

km in the vertical. Kinematic and thermodynamic/microphysical variables are staggered as shown in Fig. 3.4. Model boundary conditions utilize a wall on the top and a mesoscale compensating equation [MCR - see Tripoli and Cotton (1982) and Fig. 3.4] along the lateral walls. The MCR was included to provide a larger-scale balance adjustment to circulations generated within the interior model domain depicted in Fig. 3.4. Lateral boundaries of the fine-mesh domain additionally incorporate the Orlanski (1976) radiation boundary

TABLE 3.2 CLOUD MODEL DETAILS FOR EACH CASE

Case	Dimension	$\Delta x_{1,2}$(km)	Δz or Δp	Types of Domain Size (km)	Experiments*
7/26/77	2	0.75	25 mb	42.75x25	A,R,G,N
7/26/77	3	0.75	25 mb	41.25x41.25x25	A,R
8/4/77	3	0.75	25 mb	41.25x41.25x25	A
8/1/81	3	1.0	30 mb	53x53x25	A

* Experimental types are defined according to the level of microphysics: N - no precipitation, R - rain and cloud water only, G - graupel, rain, cloud water and ice crystals, A - aggregates, graupel, rain and cloud water, ice crystals.

condition to allow propagation of gravity waves through the fine mesh/MCR walls. At the bottom boundary frictional effects are included, but values of thermodynamic variables were extrapolated linearly from predicted values at the first two grid levels above.

In all simulations, input initial conditions were derived from a proximity sounding considered representative of the observed storm's environmental conditions. Lower sounding levels were usually adjusted using surface data and in some cases aircraft data. In all experiments cloud circulations were initiated by prescribed symmetric convergence

focused on the cloud scale (see Tripoli and Cotton, 1980) generally confined to the boundary layer. Profiles of vertical motion through the center of the 4-6 km wide perturbation assumed Gaussian shapes in the 3-D experiments and triangular shapes in the 2-D experiments. Maximum induced vertical motion of ~ 2 m s^{-1} occurred near the vertical midpoint of the perturbation.

Because the model contains the compressible momentum equations, a time-split scheme (Klemp and Wilhelmson, 1978; Tripoli and Cotton, 1980) is utilized in the finite-difference representation. Long time steps of 4-6 s on the non-acoustic terms use the leap frog scheme with an Asselin Filter to prevent diverging solutions, while small time steps of 0.5 s applied to acoustic terms use the implicit Crank-Nicholson scheme on w and forward stepping on u and v. Space differencing is accomplished by a fourth-order quadratic conservative method in which model variables are distributed as shown in Fig. 3.4.

The CSU cloud model is considered to be ideally suited for this downdraft investigation because of its ability to simulate ice and water phase precipitation. Although small scale (500-1000 m) downdrafts cannot be simulated with the coarse model resolution (see Table 3.2), larger-scale low-level precipitating downdrafts, midlevel cloud-edge downdrafts, and downdrafts resulting from updraft equilibrium overshoot, as described in Section 2 and Fig. 2.2, can be investigated in detail. In the following sections the model is applied to examine the general structure and evolution of downdrafts forming in environments ranging from low instability and low shear to high instability and high shear. Experimental design in these cases is based on case study analyses, from which model output and observational analysis comparison can be made.

The model is also exercised to examine the sensitivity of downdraft structure on such things as melting of ice-phase precipitation, mean precipitation size and static stability.

4. DOWNDRAFT KINEMATIC STRUCTURE, DYNAMICS AND THERMODYNAMICS

In this section observational analyses and three-dimensional cloud model results from several contrasting cases are presented to illustrate general features of downdrafts associated with precipitating convection. Observational results consist of analyses of multiple Doppler radar data, surface mesonet data and aircraft data. These are supplemented with observational results borrowed from other case studies, and with three-dimensional cloud model results run on three of the observational case studies.

As shown in Figs. 4.1 to 4.3, the case studies examine precipitating cumulonimbi (Cb) forming in High Plains and mountain environments ranging from moist to dry and from low shear to high shear so that generalizations on downdraft structure may be drawn. Observed storm structure for the primary and supporting cases listed in Table 4.1 ranges from short-lived multicellular storms to longer-lived supercell storms.

For convenience, the cases listed in Table 4.1 have been categorized into three classes, low, moderate and high shear, where shear is defined as the magnitude of the vector difference between the surface and 3 km AGL winds. A height of 3 km was chosen here because cloud model studies (e.g., Weisman and Klemp, 1982) indicate that wind shear at low levels is more influential than at high levels. Although this classification is somewhat arbitrary, observational studies (Marwitz, 1972a,b,c; Chisholm and Renick, 1972) and numerical cloud

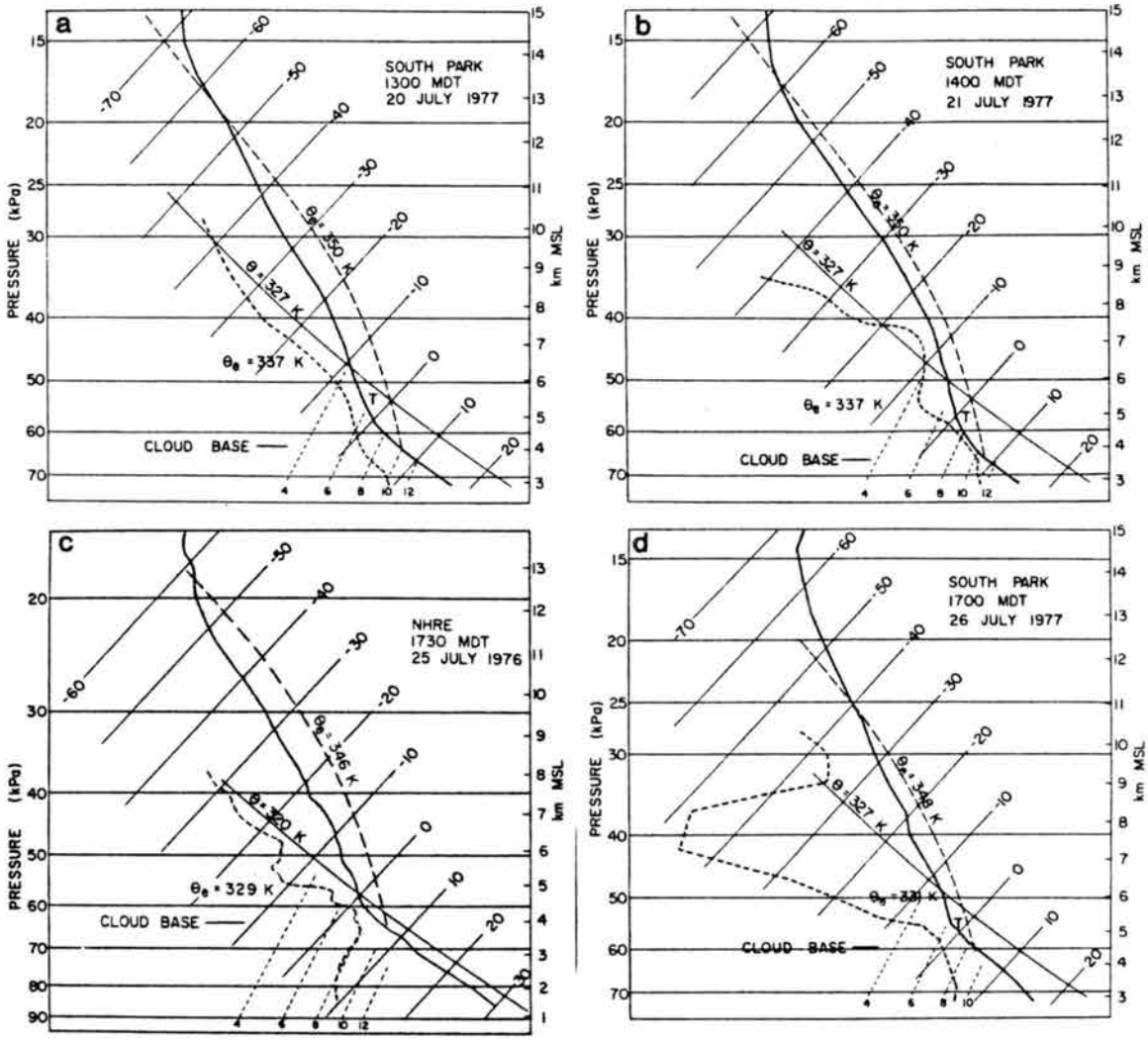

Fig. 4.1 Representative environmental soundings plotted on Skew-T, log-p diagrams for individual case studies. Unmixed parcel paths ascending unmixed from cloud base are denoted by long-dashed lines. The θ_e value at the level of minimum θ_e is included in each sounding.

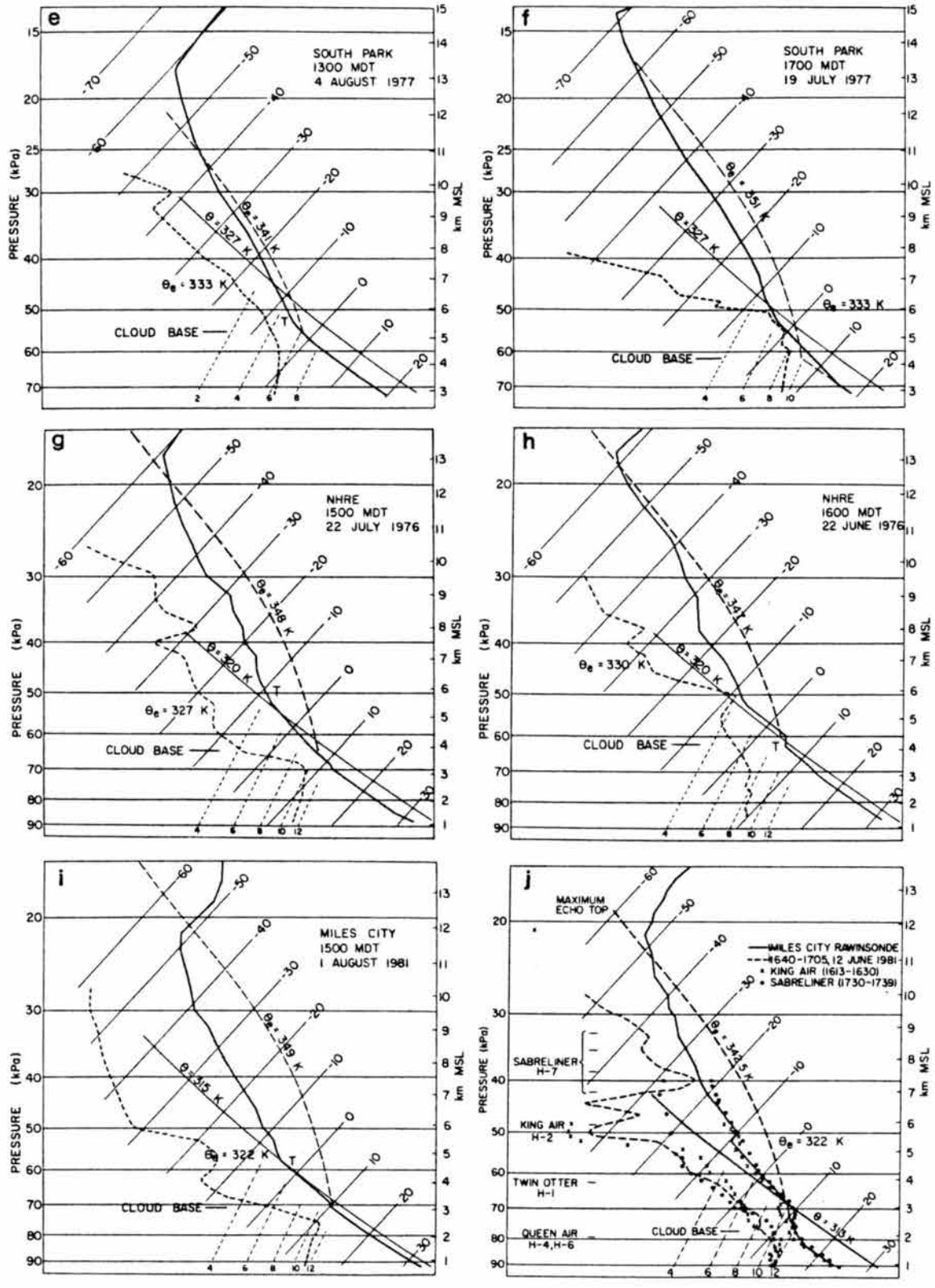

Fig. 4.1. Continued.

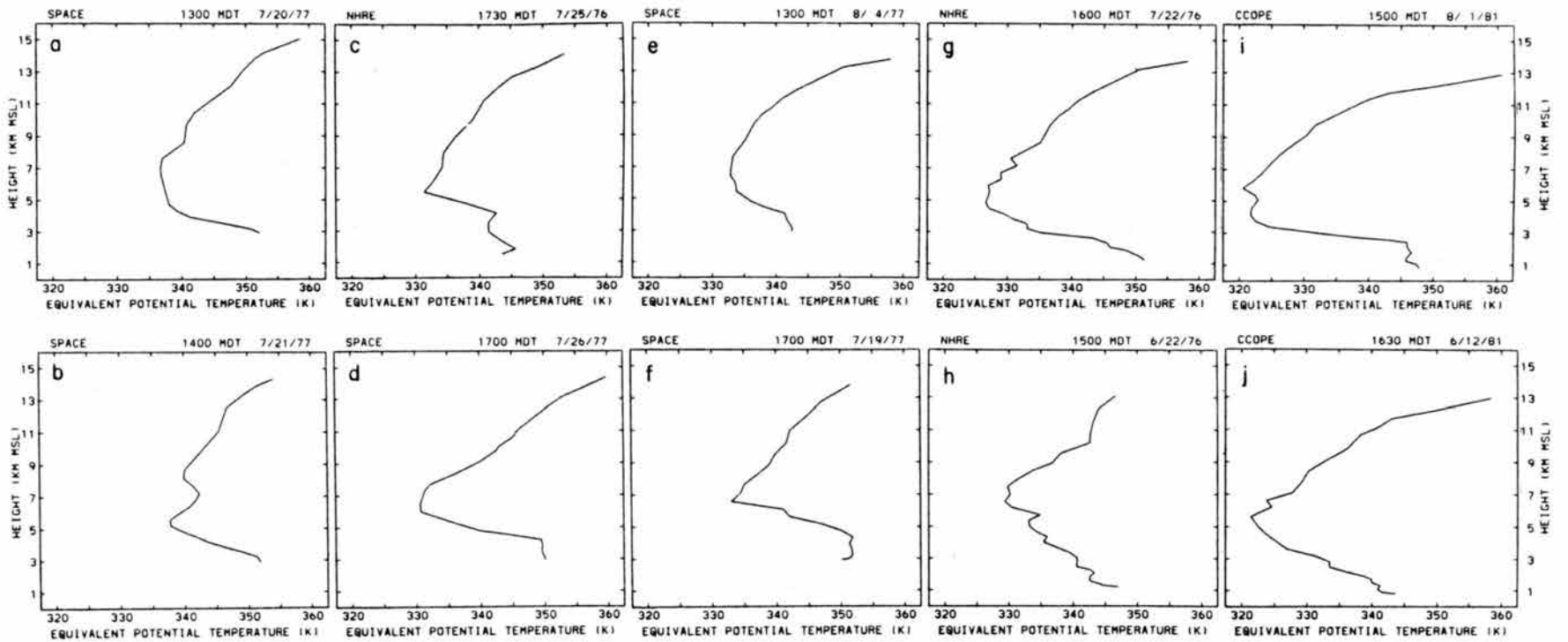

Fig. 4.2. Vertical profiles of equivalent potential temperature derived from the soundings in Fig. 4.1.

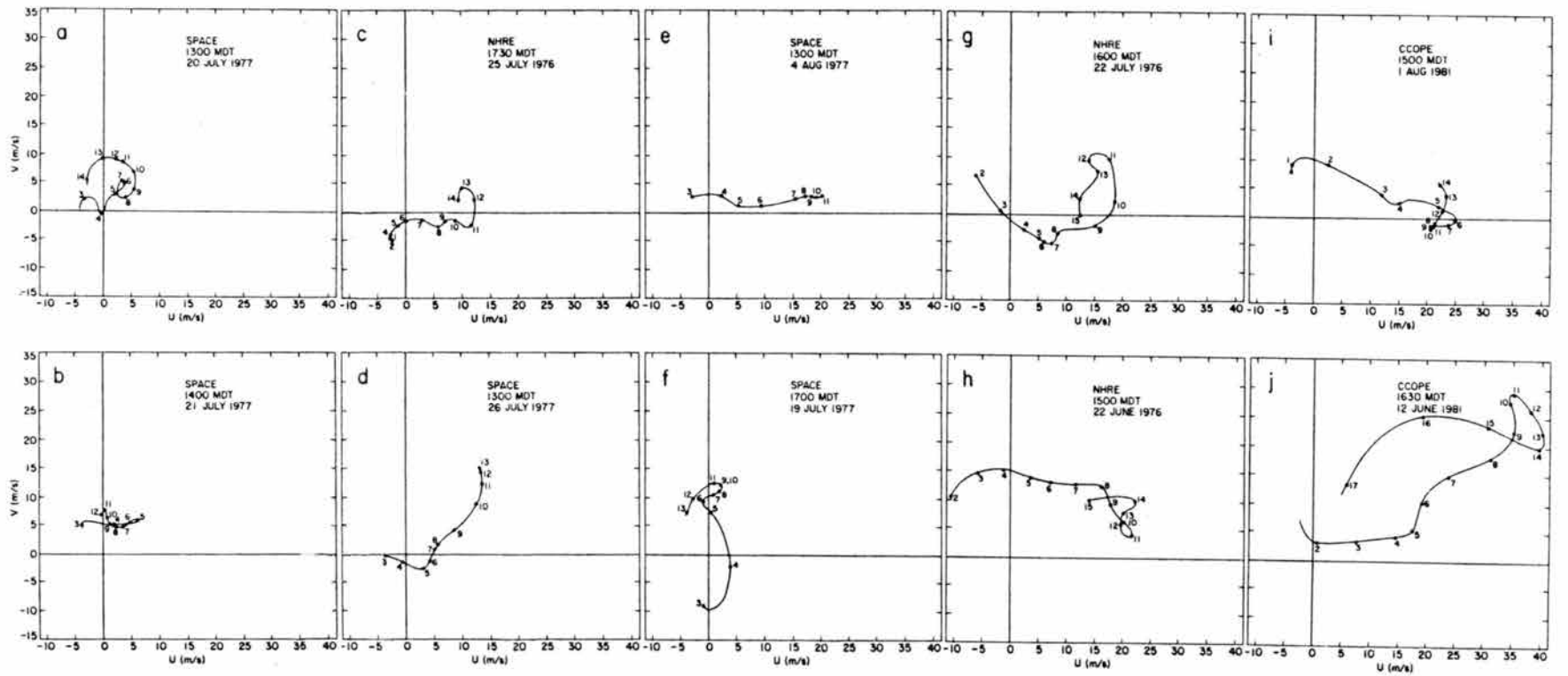

Fig. 4.3. Hodographs of environmental winds corresponding to the soundings in Fig. 4.1. Numbers beside dots on each curve give height in km MSL.

TABLE 4.1. Case study storm and environmental characteristics

Date	0-3 km AGL shear ($m\ s^{-1}$ per 3 km)	0-6 km AGL shear ($m\ s^{-1}$ per 6 km)	CAPE (m^2/s^2)	Ri	Surface r_v ($g\ kg^{-1}$)	Estimated Cloud base height (km) AGL	Parcel θ'_{max} (K)	W_{max} (m/s)	W_{min} (m/s)	Storm Characteristics[2]
7/25/76	3	2.5	1090	347	9.0	2.4	4.0	~15	-7	m/c
7/20/77	8	5.5	990	64	10.5	1.0	4.0	~25	-5 to -10	m/c
7/26/77	8	5.2	460	35	9.0	1.5	3.0	~15	-8	m/c
7/21/77	8.5	6.0	750	42	11.0	0.8	2.5	-	-	m/c
8/4/77	12.5	8.4	340	10	6.5	2.2	2.0	10	-10	m/c, W
6/22/76	15	6.8	1200	52	9.0	2.6	7.0	~30	-10 to -15	m/c
7/22/76	16	10.9	1530	26	11.0	2.4	6.0	~30	-10 to -15	m/c, A
6/12/81	17	15.6	1330	11	12.0	1.2	6.5	~20	-5	m/c
8/1/81	17	20	2340	11	11.5	2.3	9.0	~40	< -7	s/c,m/c,AW
7/19/77	18	13.4	900	10	9.5	1.3	3.5	~25	-5 to -10	s/c,m/c
8/2/81	22	20	2800	13	13.5	1.8	12.0	~50	< -10	s/c,m/c,A,W

[1] 0-6 km shear was obtained by subtracting an average atmospheric boundary layer wind from the 6 km AGL environmental wind.

[2] Storm characteristics are: m/c-multicell, s/c-supercell, A-large hail (2 cm), W-strong surface winds 20 $m\ s^{-1}$

modeling work by Weisman and Klemp (1982, 1984) suggest that general Cb structure is dependent on environmental wind shear magnitude at low to middle levels. Weisman and Klemp (1982) indicated that a bulk Richardson number, defined previously in Section 2.1,

$$Ri = \frac{CAPE}{\frac{1}{2}\bar{U}^2},$$

may differentiate steady long-lived convection from unsteady convection. Weisman and Klemp found that Ri values of ~ 50 separated steady convection from unsteady convection. This value translates to about 15 in this study because of different methods of computation used herein. Table 4.1 lists for each case values of environmental wind shear, CAPE, low-level moisture and R. Also included are quantities indicating bulk storm properties. Note that these storms exhibit peak updrafts in the interval 10-50 m s^{-1} and peak downdrafts in the interval 5-20 m s^{-1}.

In the following, information from four observational case studies, one low shear case (7/26), one moderate shear case (8/4) and two high shear cases (6/12 and 8/1) illustrates general aspects of mature storm downdraft structure, namely downdraft depth and intensity, relative location, origin of downdraft inflow, and downdraft dynamics and thermodynamics. The most detailed and accurate information is provided by a low-shear case (7/26) in which details of precipitating downdrafts were analyzed and modeled. Subsequent subsections then extract additional information from other observations and model results to illustrate variations in downdraft structure and to provide a more general description of downdraft structure.

4.1 Low-Shear Environments

Precipitating convection forming in low-shear environments is easily studied because clouds typically move slowly, remain nonsevere and are small in size. Cloud model results discussed in Section 2 (e.g., Schlesinger, 1978) indicate that for no shear, low level precipitating downdrafts form within precipitation falling from weakening updrafts. Although no cases presented here occurred in an ideal environment void of shear, the shear vector magnitude over the lowest 3 km is less than 10 m s^{-1} in four of five cases (7/20, 7/21, 7/25, 7/26)* discussed in this section. Observed storm structure was multicellular in each case, and general structure ranged from relatively isolated convection (7/21, 7/25, 8/4) to larger-scale convective systems composed of closely-interacting storms arranged in lines (7/20) or in more circular clusters (7/26).

4.1.1 The 26 July 1977 case: Analysis of observations

Results from this combined observational-modeling study illustrate in this study most of the general aspects of downdraft flow structure, thermodynamics and dynamics for a variety of environments. Because of this and the fact that these observations are complete and quite accurate, aspects of this case are described in considerable detail.

In this low-shear case a group of moderately-intense Cb developed over South Park and adjacent areas, forming a well-defined region of cold downdraft outflow air about 80 min after first echoes appeared. Fig. 4.4 illustrates analyzed patterns observed at the surface for two time periods. Evidence of downdraft activity in the form of lower-

---

* Hereafter, case studies will be referred to the day and month in which they occurred. See Table 4.1.

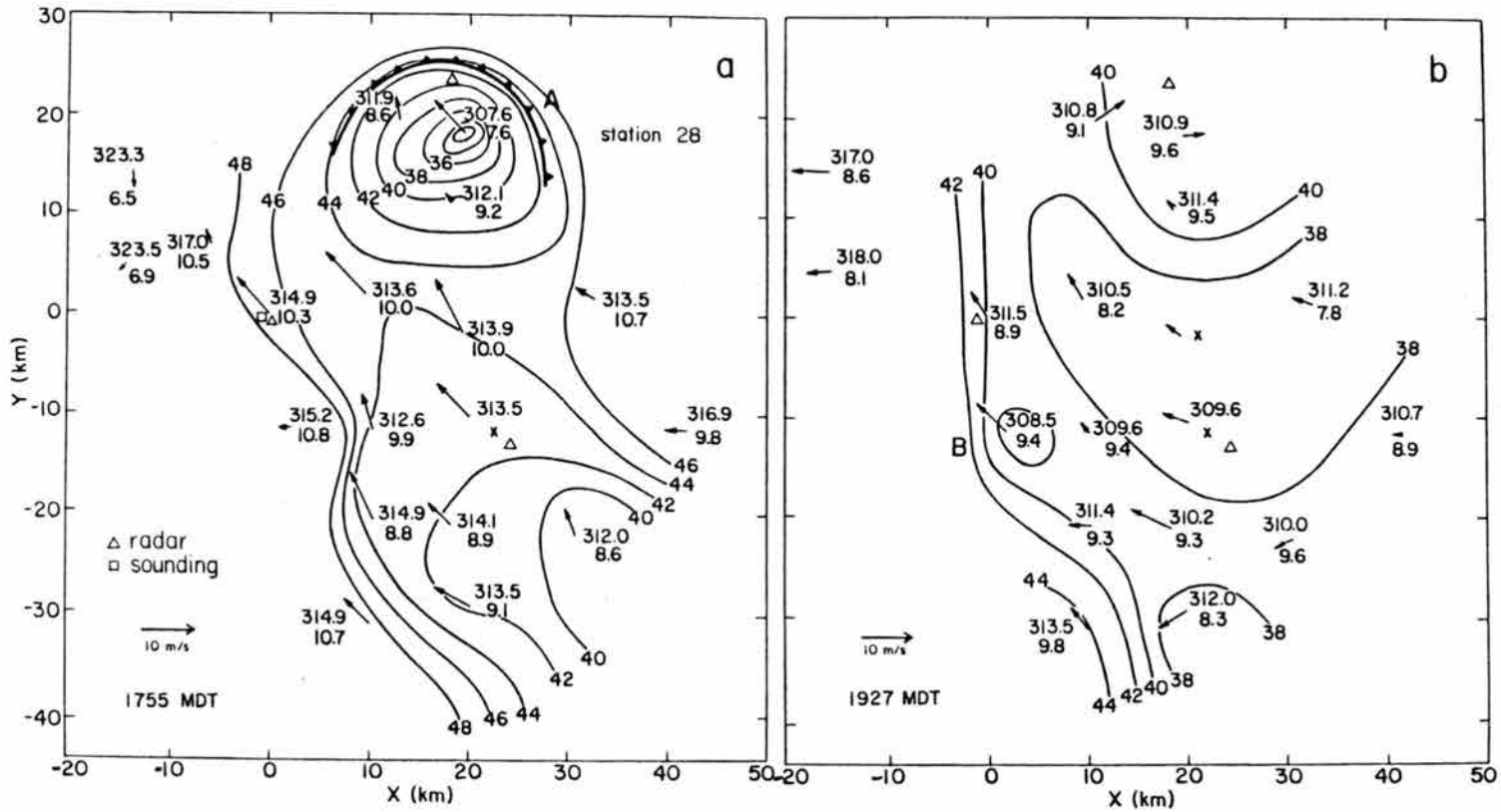

Fig. 4.4. Surface analyses for the 26 July 1977 case. Equivalent potential temperature (deg K minus 300) is contoured every 2 K. Station values of potential temperature (K) and water vapor mixing ratio (g kg-1) are shown beside each surface station.

valued θ_e air first appeared near 1715. Downdraft outflow produced by a relatively intense storm over northern South Park at 1755 (labeled A in Fig. 4.4a) was associated with a well-developed downdraft circulation described in detail in the following discussion. Weaker downdrafts associated with intermediate-valued θ_e air (Fig 4.4a) correspond to weaker showers located over the central and southeastern portions of South Park during the 1715-1755 time period. Another individual storm examined in detail for this case (storm B, position indicated in Fig. 4.4b) generated less substantial outflow than storm A, possibly because the PBL had been modified by outflow air from previous downdraft activity.

A representative environmental sounding presented in Fig. 4.1d was constructed from the 1300 MDT sounding released from the point (0,0) indicated in Fig. 4.4, modified with surface observations in the vicinity of the storm. Subcloud layers exhibit relatively moist conditions as opposed to middle levels which are quite dry. A nearly dry adiabatic layer extends from the surface to ~ 55 kPa (550 mb), above which a nearly moist adiabatic temperature profile is found. This transition (labeled T in Fig. 4.1) from dry adiabatic to moist adiabatic stratification near 55 kPa has theoretical significance. Only weak buoyant-driven downdrafts would be expected above 55 kPa within the moist adiabatic layer because adiabatic warming produced by downward parcel displacements would likely exceed cooling by evaporation and/or sublimation (see Fig 2.14 and the assiciated discussion) provided that evaporation of precipitation into the dry layer does not change this moist-adiabatic stratification. This notion is supported by calculations presented below. More significant downdraft activity is

likely in the nearly dry-adiabatic layer below. It will be shown in the following that most significant low-level downdraft activity in fact occurred below 55 kPa.

Individual cloud updraft/downdraft relative location of storms comprising the larger-scale storm complex varied depending on location relative to the low-level cold outflow pool. Fig. 4.5 portrays the evolution of maximum reflectivity factor, updrafts and downdrafts for storms A and B labeled in Fig 4.4. Although storm B briefly achieved greater intensity than A, storm A was more steady, produced more precipitation and generated more cold low-level outflow. Moreover, storm A propagated in a downshear direction along its self-generated outflow boundary, but storm B was constrained to propagate upshear along a mesoscale outflow boundary, formed by a number of clouds, shown in Fig. 4.4. In both storms, downdrafts exhibited peak values of ~ 8 m/s at the lowest analysis grid level at roughly 0.5 km AGL. Maximum values of low level downdraft mass flux furthermore lag maximum values of midlevel updraft mass flux in both storms.

Fig. 4.6 presents a plan view of analyzed reflectivity factor, updrafts and downdrafts at 2 km AGL for several analysis times of storms A and B. In storm A (Fig. 4.6a-d) an initial reflectivity cell split into two components (A_1 and A_2) which then exhibited diverging relative motion for the next 30 min. Contrary to the unsteady character of cell A_2 which dissipated rather quickly, cell A_1 exhibited a degree of steadiness in both reflectivity and kinematic structure for ~ 30 min. During and after the splitting process, downdrafts initially colocated with the reflectivity core of A_1 at 1738 migrated in a relative sense towards the upshear (west) flank along the reflectivity gradient by 1803

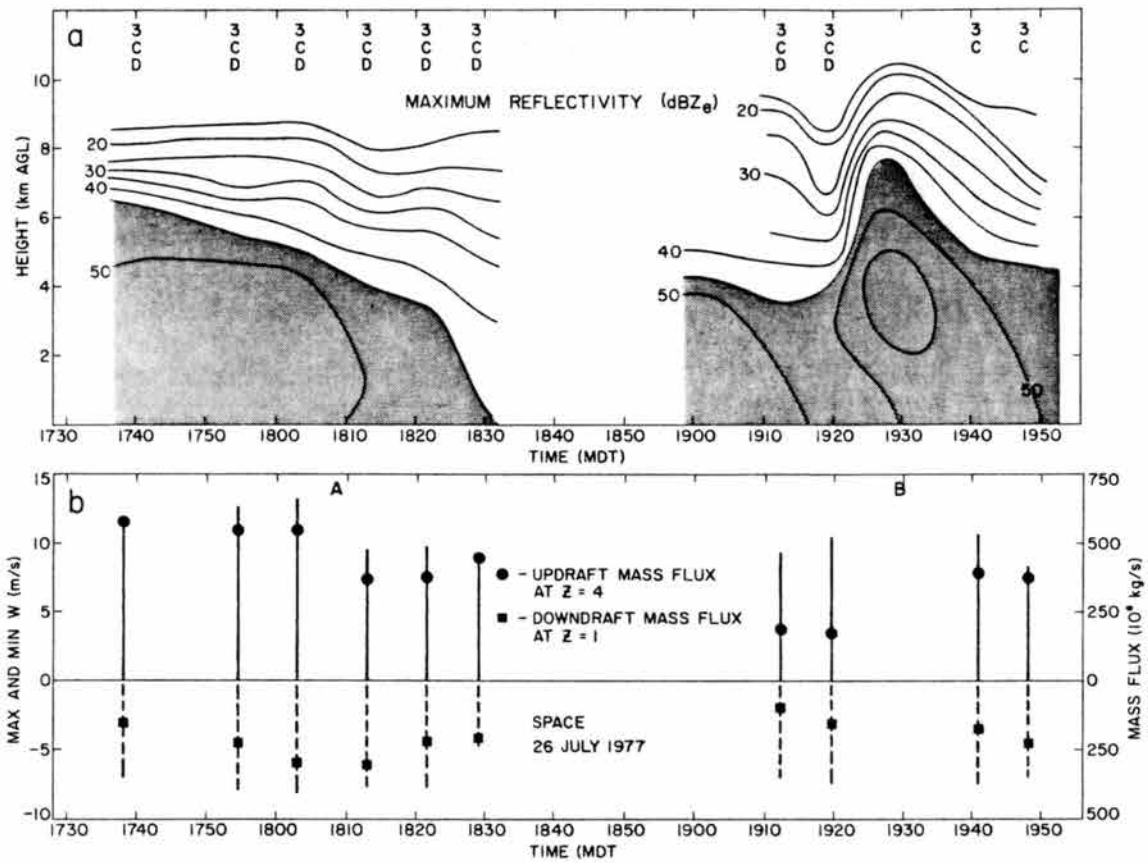

Fig. 4.5. (a) Time vs. height section of maximum reflectivity factor in dBZ_e. Symbols at the top denote Doppler radars used: 3 - CP-3, C - NOAA-C, D - NOAA-D. (b) Doppler analyzed maximum, minimum vertical motion (m s^{-1}) and vertical mass flux (10^6 kg s^{-1}) for storms A and B on 26 July 1977.

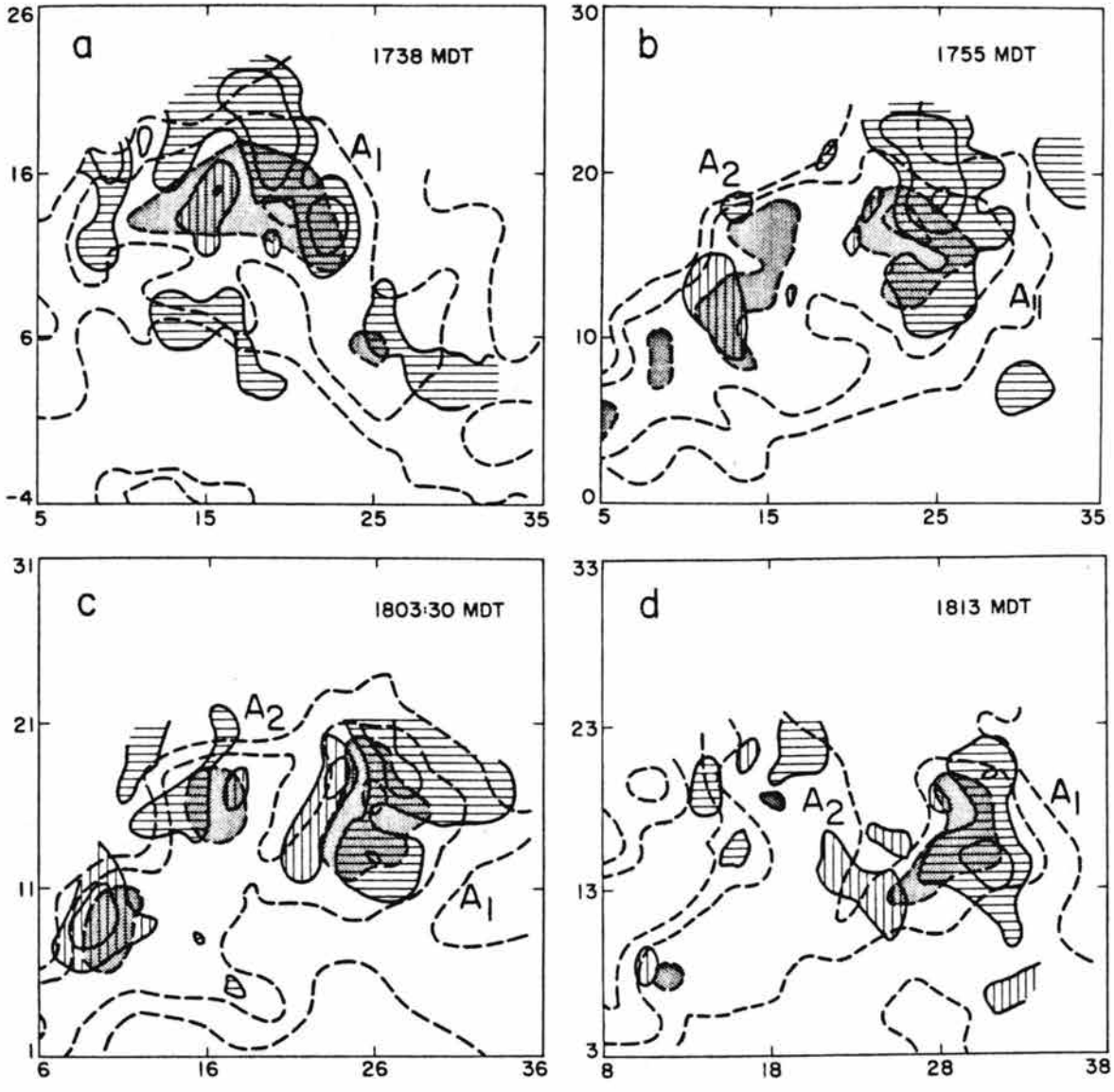

Fig. 4.6. Analyses at 2 km AGL of Doppler-derived vertical motion and measured radar reflectivity factor for storm A (a-d) and storm B (e-h) on 26 July 1977. Reflectivity (dashed lines) is analyzed every 10 dBZ_e beginning with 20 dBZ_e (greater than 40 dBZ_e is shaded). Vertical motion (solid line) is contoured every 2 m s^{-1}, with the zero contour deleted. Updrafts are indicated by horizontal hatching and downdrafts by vertical hatching.

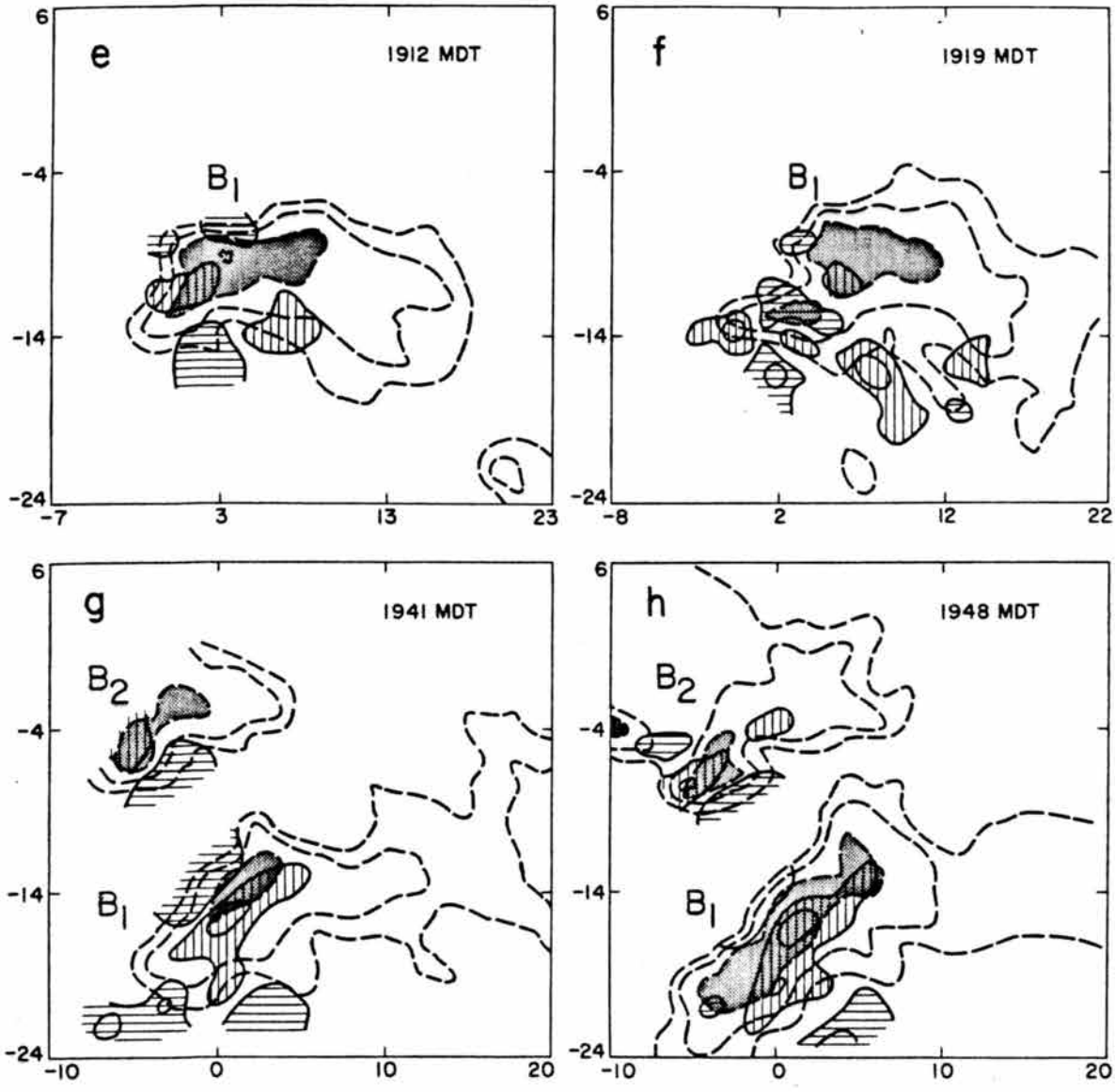

Fig. 4.6. Continued.

(Figs. 4b-4d). The patterns for cell A_2 in Figs. 4a-4d exhibit an opposite arrangement in which areas of weak downdraft are more typicaly located downshear from primary updrafts. Storm B_1, and another nearby cell B_2 (Fig 4.6e-h) exhibited yet another arrangement in which downdrafts, nearly coincident with reflectivity cores, were flanked by updrafts generally to the south and northwest. Such variation indicates that relative updraft-downdraft location is dependent on boundary layer convergence regions which, in this case, persistently initiated updrafts along the general upshear flank in cells A_2, B_1 and B_2. Only storm A_1 which propagated along its own gust front, and which was not influenced by mesoscale convergence zones, exhibited low-level downdrafts located within the upshear sector.

Vertical profiles of air mass flux* (calculated over the entire analysis domain) shown in Fig. 4.7 reveal similar shapes in updraft and downdraft profiles for both storms even though relative storm structure differed. Maximum updraft mass flux typically occurs at 3.5 km AGL, while downdraft fluxes peak at the lowest grid level of ~ 0.5 km AGL. The stormwide downdraft mass flux profiles represent several individual downdrafts and differ appreciably in shape from updraft flux profiles. The downdraft profiles all show significant increases in magnitude from near 4 km down to 0.5 km, the lowest analysis grid level. Such a vertical flux divergence is indicative of continuous horizontal inflow, most intense near the 2 km AGL level. The observed profiles in downdraft mass flux suggest that downdrafts in this case (independent of

---

* Air mass flux was computed by summing over a given updraft or downdraft area ($w>0$ or $w<0$, respectively) the product $\rho w_i A_i$ where $\rho(z)$ is density, $w_i(z)$ is vertical motion and A_i is a grid box area.

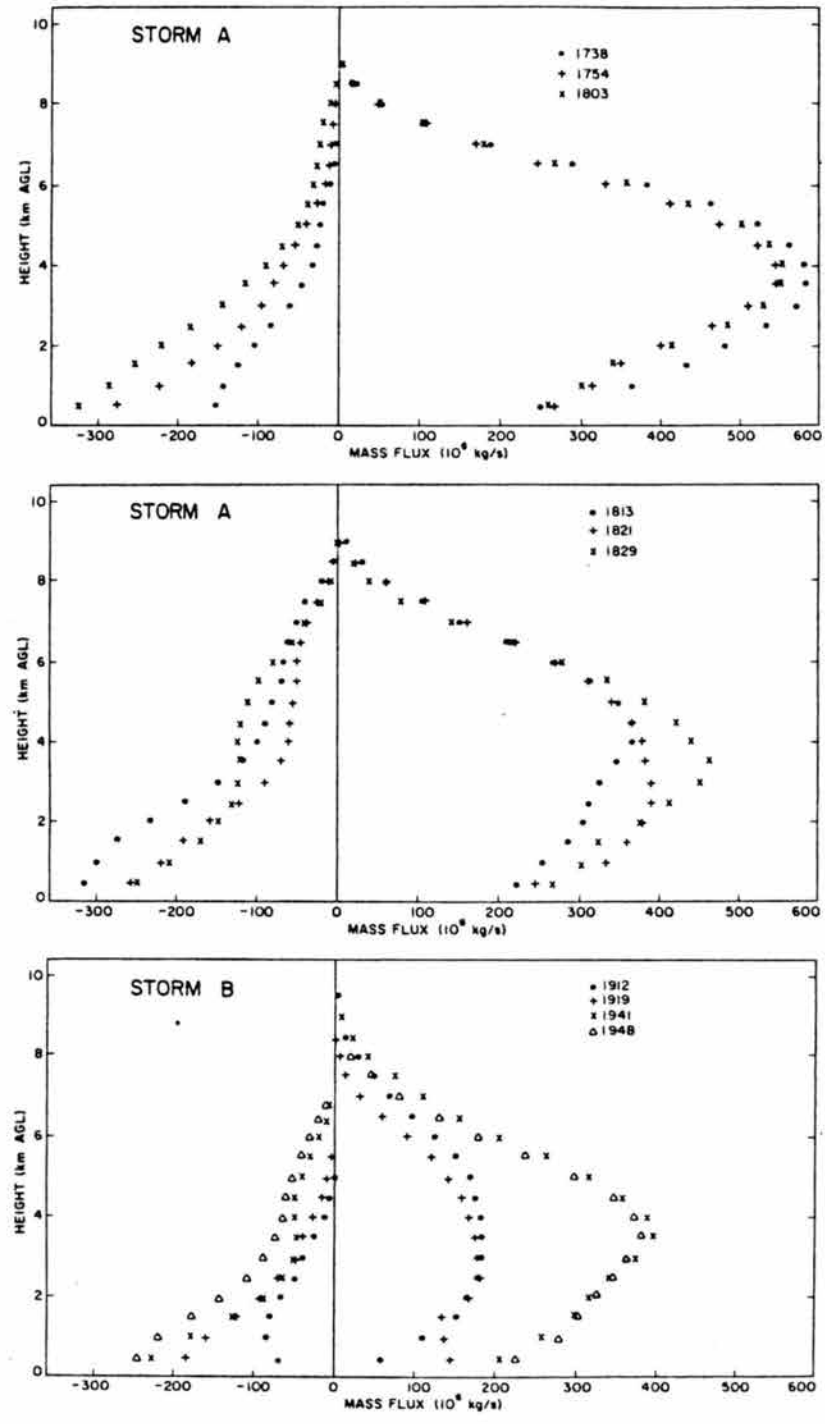

Fig. 4.7. Vertical mass flux profiles over a 30 km by 30 km domain in updrafts and downdrafts for 10 time periods of the 26 July 1977 case. Systematic and random errors in the Doppler-analyzed w (both are unknown-see Appendix A) produce the apparent discontinuity at the lowest grid level of ~ 0.5 km AGL.

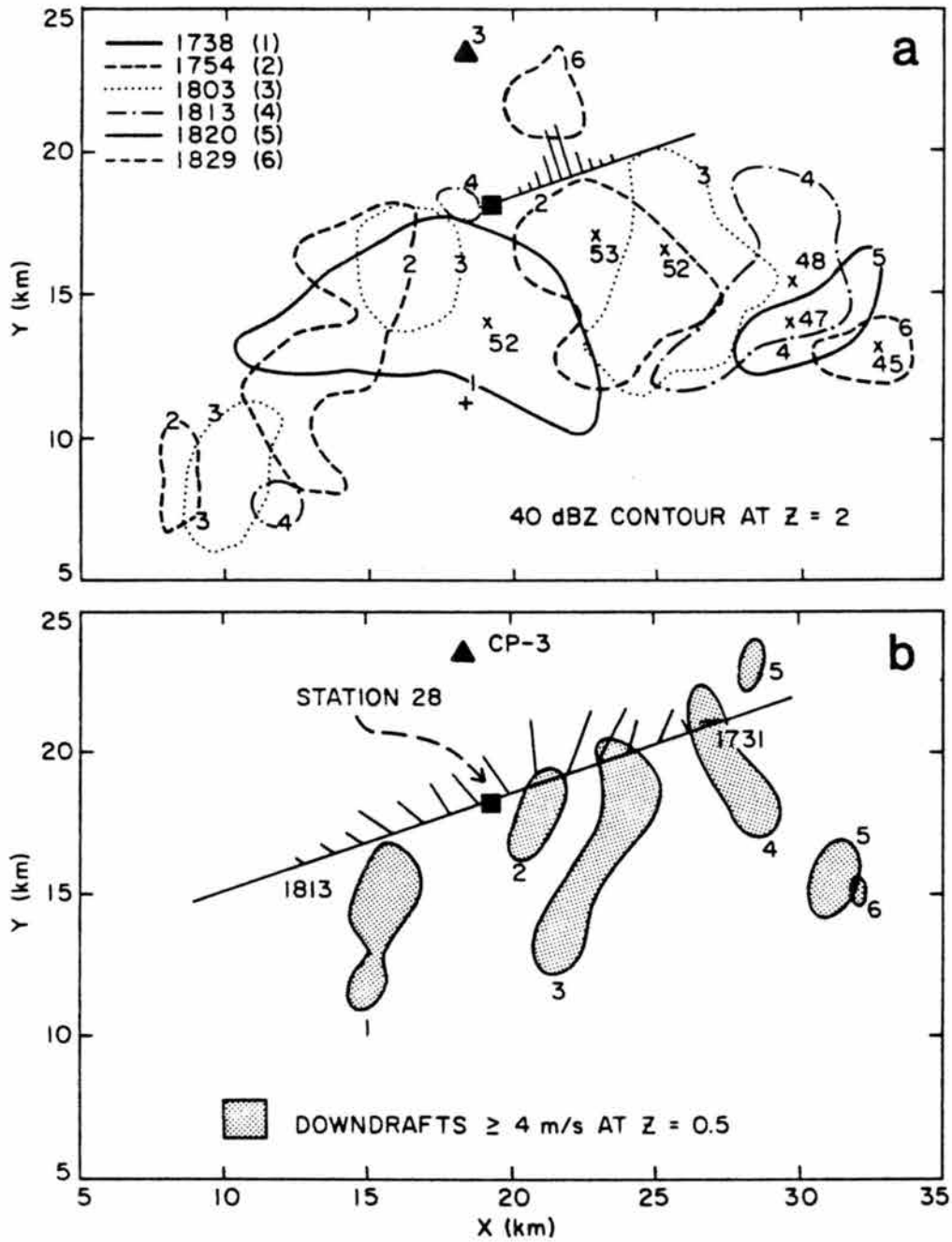

Fig. 4.8. Position of 40 dBZ_e contour at 2 km AGL (a) and $w = -4$ m s^{-1} contour (b) of storm A on 26 July 1977. Times correponding to labeled contours are given at the upper left. Locations of maximum labeled reflectivity (dBZ_e) are given by x symbols. Rainfall rates (maximum of 90 mm hr^{-1}) and winds (maximum of 13 m s^{-1}, represented by vectors emanating from the straight line) derived from station 28 are plotted in (a) and (b), respectively, by making a time to space conversion, based on the observed motion of the primary reflectivity cell. The relative location of plotted winds and rain rate is valid for 1754.

storm structure) were forced primarily at low levels. As noted earlier in Fig. 4.5, Fig. 4.7 illustrates that low-level downdraft mass flux values tend to increase with time as each storm develops.

A closer look at the downdraft structure within storm A is provided in Figs. 4.8-4.9. Fig. 4.8 illustrates the evolution of the splitting process in reflectivity and the relationship of downdrafts to reflectivity. Note that the downdraft and reflectivity core at 0.5 km AGL (Fig. 4.8) passed just south of PAM station 28, which measured a peak rainfall rate of 90 mm/hr (Fig. 4.8a), coincident with downdrafts overhead, and wind gusts to 13 m/s (plotted in Fig. 4.8b).

Characteristics of the surface outflow air associated with this downdraft are depicted in Fig. 4.9, a time series representation of saturation point (SP) derived from station 28. This time series indicates several processes occurring just prior to and during convection over South Park. In particular, cooling and slight drying from cloud shadowing and horizontal advection which occurred between 1500 and 1700 was followed by cooling at nearly constant θ_e from 1700 to 1740. This latter cooling trend from evaporation of light precipitation falling into the updraft inflow sector produces an apparently common pattern whenever precipitation falls into or through an air mass depth of nearly constant properties (Betts, 1984). Such a pattern has been termed an evaporation line (EL) structure by Betts (1984). The EL structure was followed by downward transport of lower-valued θ_e air within the downdraft (depicted in Fig. 4.8b) behind the gust front which passed over station 28 at 1738. This downdraft outflow air exhibited increasingly lower values of θ_e, reaching a minimum of 330 K within light precipitaion at 1754. Provided that θ_e is conserved, such a value

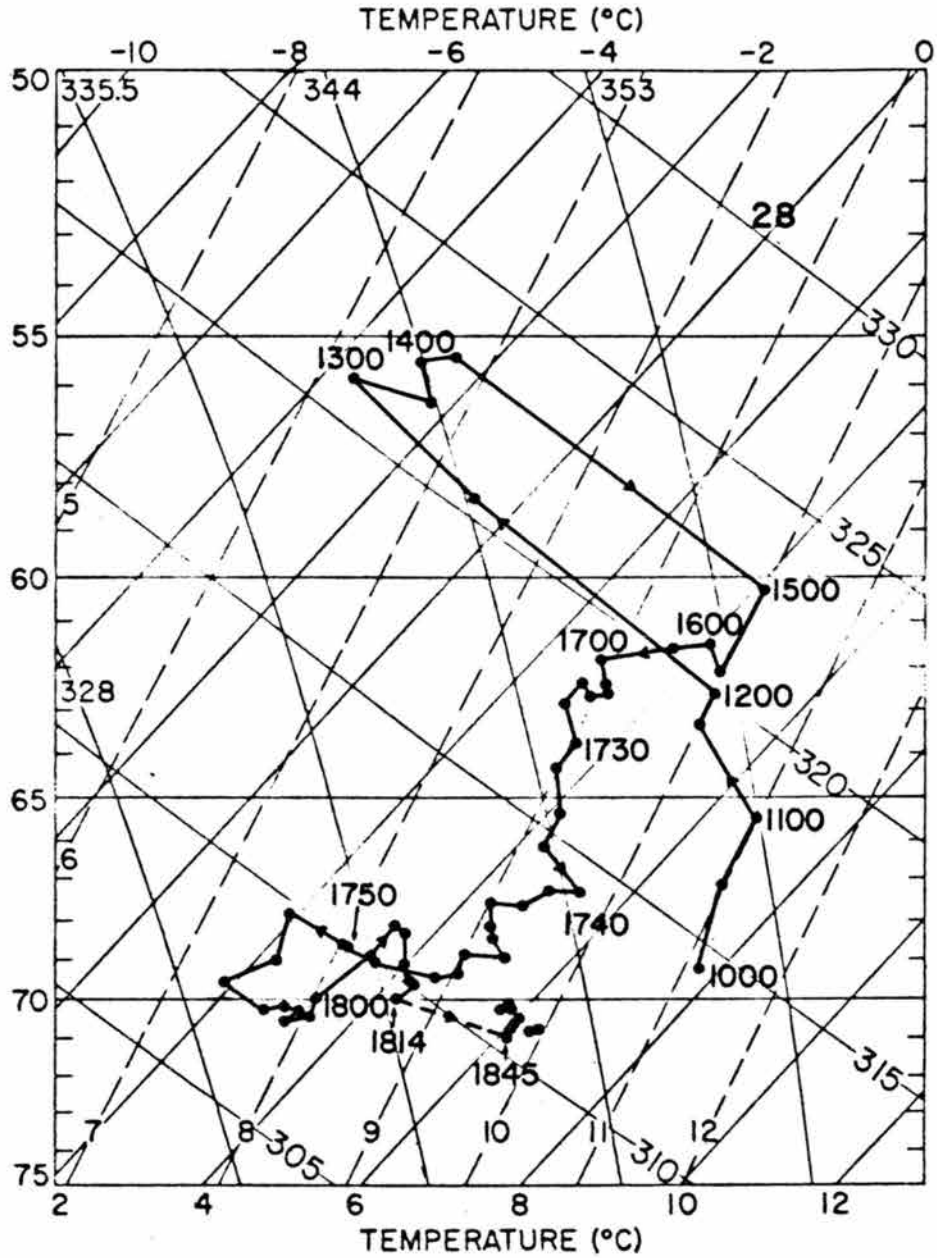

Fig. 4.9. Time series of saturation point (SP) from station 28, whose location near (20,20) is shown in Fig. 4.4a. Times in MDT are indicated, and individual points are plotted every half hour from 1000 to 1700, every 5 min from 1700 to 1740, every 1 min from 1740 to 1800, and every 2 min after 1800. Data is missing from the 1814-1845 time period.

indicates that this air descended ~ 3 km from near 50 kPa (see Fig. 4.2). Also note that the low-valued θ_e air occurred ~ 7 min after the maximum measured rainfall rate of 90 mm/hr. More will be said of this relation between rainfall and θ_e in Section 5.

Because storm A exhibited a fairly steady reflectivity and kinematic structure from 1738 to 1813, three analysis time periods (1738, 1754, 1803) were composited (relative to the motion of the reflectivity core of cell A_1-see Fig. 4.6) so that mean flow features could be examined. Fig. 4.10 displays a composite surface analysis, and Fig. 4.11 illustrates the composite Doppler fields at 3 levels, 0.5, 2.0 and 4.0 km AGL. The composite fields are in general similar to those of individual analysis times from which the composite was made. Storm-relative flow at the surface (Fig. 4.10) is primarily easterly ahead of and behind the gust front, behind which a nearly circular pool of cold air exists (see also Fig. 4.4). Only relatively small areas of low-valued θ_e air (θ_e<336) are analyzed, indicating that relatively small quantities of air originating at this level (~3 km AGL) descended in an unmixed fashion to the surface. The Doppler analysis at 0.5 km AGL (Fig. 4.11a) indicates that the cold surface outflow air is fed by a 6 m/s downdraft (PR) whose core lay 2 km east of the coldest surface air. Figs. 4.11a-c show that this downdraft decreases in magnitude with height, topping at about 4.0 km where only small pockets of weak downdraft are visible. Convergent flow into the downdraft is easterly at low levels, gradually shifting to northwesterly near 3-4 km. This turning of downdraft inflow with increasing height closely parallels the behavior of environmental winds which back with height (see Fig. 4.3d).

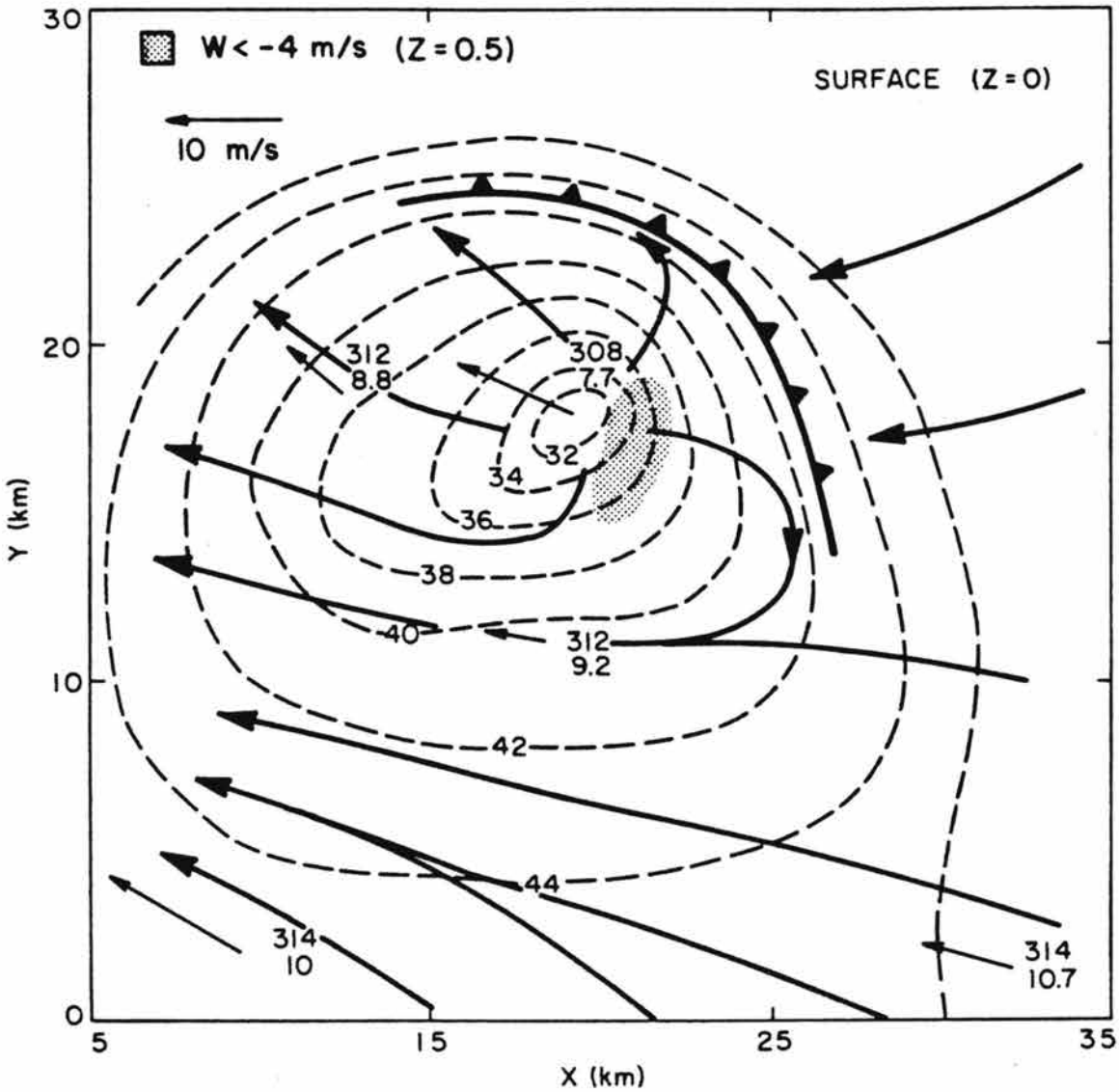

Fig. 4.10. Surface analysis in the vicinity of storm A (7/26). Dashed lines are θ_e contours, and thick lines are storm-relative streamlines. Individual surface station values of (θ, r_v) are plotted. The stippled region denotes analyzed downdraft ($w < -4$ m s^{-1}) obtained from the composite Doppler fields.

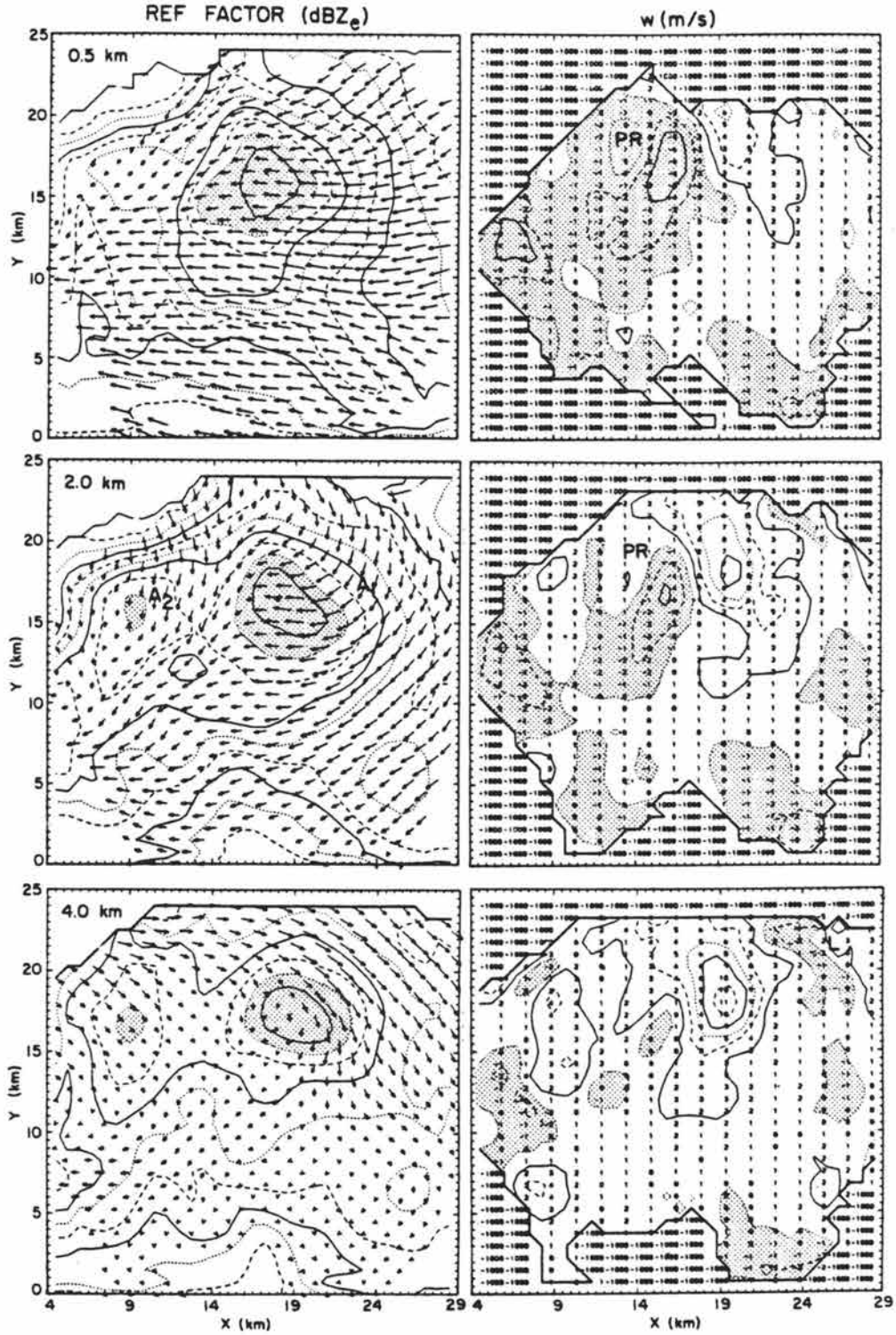

Fig. 4.11. Mean horizontal flow field composites at 0.5, 2.0 and 4.0 km AGL, based on triple Doppler radar analyses from the 1738, 1754 and 1803 scans. The left panels portray reflectivity factor, contoured every 5 dBZ (greater than 40 dBZ_e stippled); and the right panels give vertical velocity contoured every 2 m s^{-1}, with w < 0 stippled.

A second downdraft (L) independent from the previous and most prominent within the downshear wake at midlevels appears near (24,20) in Fig. 4.11. This downdraft, which may be categorized as a midlevel cloud edge downdraft (defined as L in Table 2.1 and Fig. 2.2) evidently has properties which differ substantially from those of the precipitation-associated downdraft PR. This downdraft also appears in the cloud model simulation run on this case and is discussed further in the following subsection on model results.

Flow within an east-west vertical section through the downdraft core at y = 18 is depicted in Fig. 4.12. The most obvious steady-state features are the downdraft location along the upshear reflectivity gradient and the prominent airflow into the downdraft from the downshear (right) updraft inflow sector. Another weaker low-level downdraft visible near x = 11 resides downshear from the weaker updraft region of storm A_2 which earlier had split as shown in Fig. 4.6. The elevated downdraft region near x = 25 represents a mixture of two closely-connected downdrafts, the overshooting downdraft and the cloud-edge wake downdraft mentioned above which appears more clearly in the 1754 Doppler analysis shown in Fig. 4.13. Examination of Doppler data from successive time periods (1738,1754,1803) not shown indicates that downdraft PR was initiated within high reflectivity at low levels (~ 1 km AGL). This downdraft then developed upwards to a 3-4 km height while migrating towards its steady-state position along the upshear reflectivity gradient.

Flow patterns for an individual analysis at 1754 presented in Fig. 4.13 show a structure similar to that of the composite in Fig. 4.12. Downdraft L, however, is more prominent at this time than in the

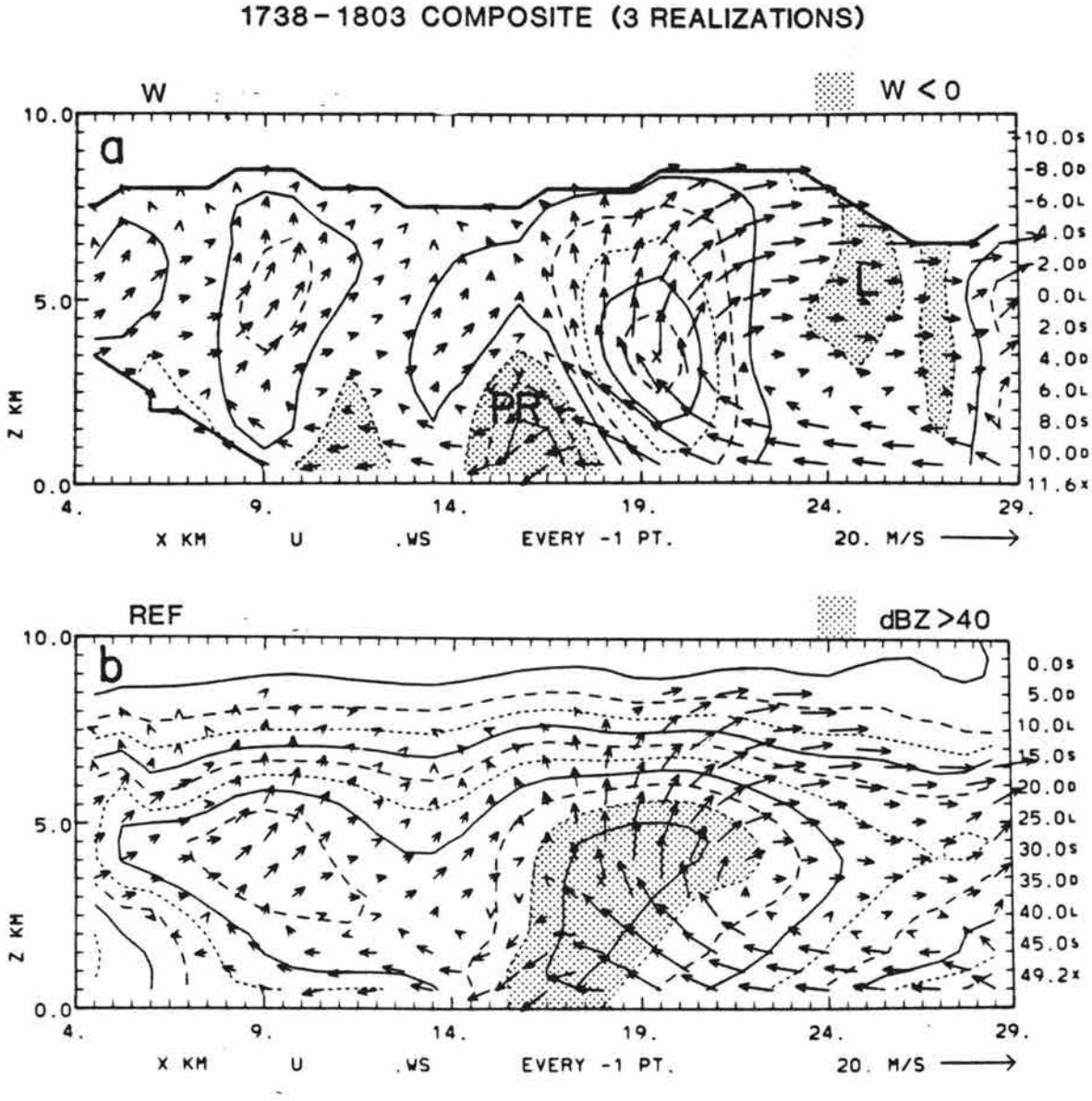

Fig. 4.12. Composite flow as in Fig. 4.11 along an east-west vertical plane at y = 18 km. Vertical motion is analyzed every 2 m s^{-1} in (a) and reflectivity is anayzed every 5 dBZ_e in (b).

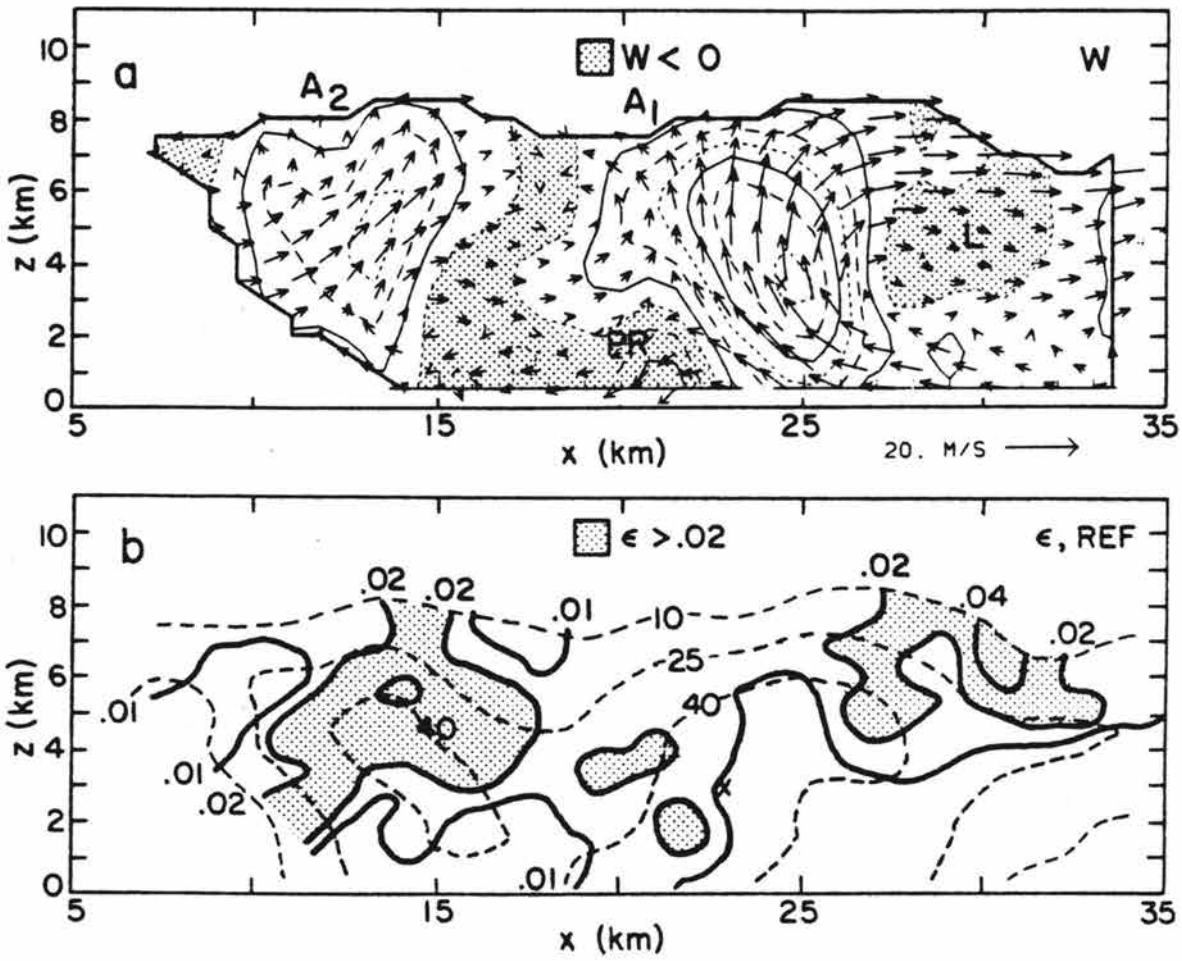

Fig. 4.13. Triple Doppler analysis at 1754 within an east-west vertical plane along y = 18. The top panel gives analyzed vertical motion contoured every 2 m s^{-1} and the bottom panel portrays analyzed reflectivity with 10, 25, and 40 dBZ_e contours given by dashed lines, and analyzed Doppler radar-derived turbulent kinetic energy dissipation estimates of .01, .02 and 0.4 m^2 s^{-3} given by solid lines.

composite. Values of radar-derived turbulent kinetic energy (TKE) dissipation (ε) are also presented in Fig. 4.13 to illustrate the degree of turbulence in updraft and downdraft circulations. See Knupp and Cotton (1982b) for a discussion of the physical significance of ε. These ε overlays illustrate several points. First, the low-level downdraft PR is associated with moderate values of ε, comparable to those present along the updraft fringes at mid to upper levels. One implication of this is that turbulent mixing produced by buoyant generation of TKE may be occurring between low θ_e air entering the northern storm flank at 2-3 km AGL, and high θ_e boundary layer air approaching from the downshear (east) sector. The moderately high ε values coincide with low-valued θ_e air at the surface, indicating that such mixing is indeed occurring. This turbulent mixing process appears to proceed well inside the reflectivity core where updraft air and downdraft air approach. Other patterns not shown here also suggest that cooling from mixing between cloud and environment may contribute to the observed downdraft strength since highest ε values are initiated fairly close to the cloud edge. However, comparision of updraft and ε magnitudes in cells A_1 and A_2 suggests that mixing is partly responsible for reduced updraft strength and greater ε in A_2. In contrast, the nearly turbulent-free updraft core of A_1, suggests less substantial mixing between updraft and environmental air.

Mass flux profiles through downdraft PR and through the weaker midlevel downdraft (L) downshear of the primary updraft, each identified in Figs. 4.11-4.13, are presented in Fig. 4.14. These profiles differ from those drawn in Fig. 4.7 in that we have now focused on <u>individual</u> downdrafts which may comprise a cloud system. The flux profile through

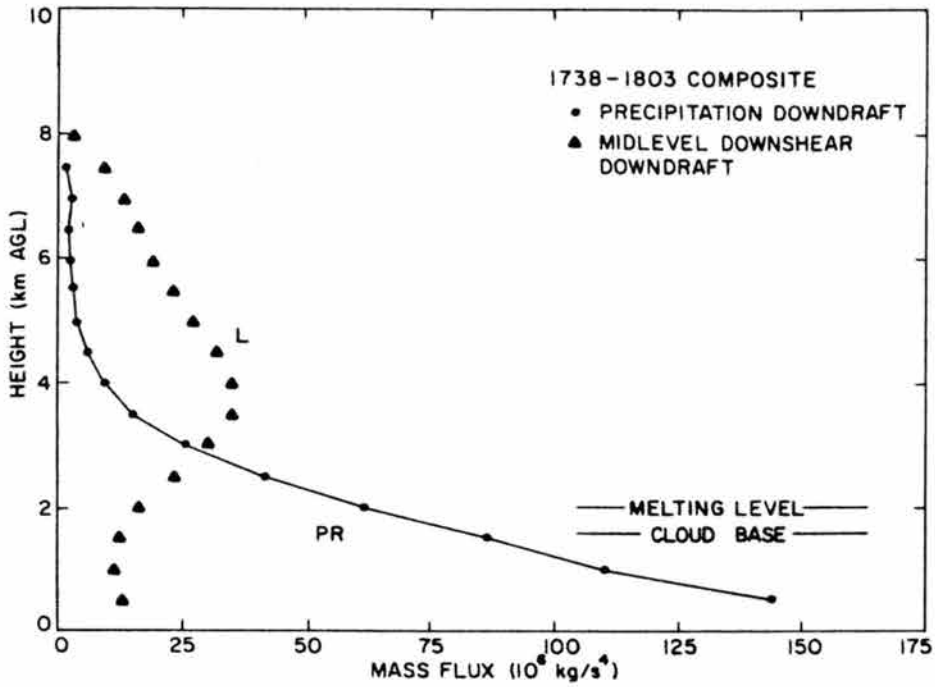

Fig. 4.14. Vertical mass flux profiles from composite data through downdrafts PR and L (labeled in Figs. 4.11, 4.12, 4.13).

downdraft PR suggests that precipitation forcing at levels below 2 km is very strong. In particular, it is inferred that very rapid cooling and negative buoyancy is generated within the unstable layer below 2.5 km by melting and evaporation (the 0 C level is at 2.1 km). It is hypothesized that such strong cooling then expands downdraft areas and accelerates existing downdrafts penetrating into this low layer. More detailed calculations on the thermodynamics and dynamics of this process appear in subsequent sections.

The flux profile through downdraft L, which is independent of PR, appears to be the result of several effects: (i) an updraft overshoot past the equilibrium level at upper levels as was suggested in Fig. 4.12; (ii) mixing of cloud and environmental air within the wake region downshear of the updraft, as observed by Heymsfield et al. (1978) and modeled by Cotton and Tripoli (1978); (iii) cooling by sublimation of

precipitaion falling into subsaturated air flowing into the downshear wake region; and (iv) vertical pressure gradient forces associated with localized mass compensation from the updraft mass flux which peaks near 3.5 km (Fig. 4.7). One may consider downdraft L to be a precipitation-induced downdraft which undergoes limited descent because of two effects: (i) greater static stability at middle levels (see Fig. 4.1d), and (ii) limited cooling rates from sublimation of graupel, aggregates, and ice crystals which probably produce the 25-40 dBZ_e reflectivity within downdraft L (see Figs. 4.12 and 4.13).

Some details of the mixing process are elucidated by referring to observations made within the downshear flank of a storm (7/25) of similar size and similar environmental wind shear (see Table 4.1). Aircraft measurements of θ_e and Doppler winds composited by Dye et al. (1982) indicate that the region immediately downshear from the updraft is composed of weak to moderate downdraft intensities, reduced updraft intensity and air possessing θ_e values (<340 K) indicative of mixing between undiluted updraft air ($\theta_e \simeq 346$) and subsaturated environmental air ($\theta_e < 336$). Model results for the 7/26 case discussed below display θ_e patterns within the downshear flank similar to these, indicating that evaporational cooling of cloud and of precipitation falling into the downshear wake provides primary forcing.

A number of air parcel trajectories were calculated using data from three time periods (1738, 1755, 1804) to determine the origin of low-level downdraft air. Fig. 4.15 displays some selected trajectories which can be divided into 2 classes, those originating within the northern flank above the PBL within the 1.5 to 3.0 km AGL level, defined herein as midlevel trajectories (trajectories 1 and 2), and those which

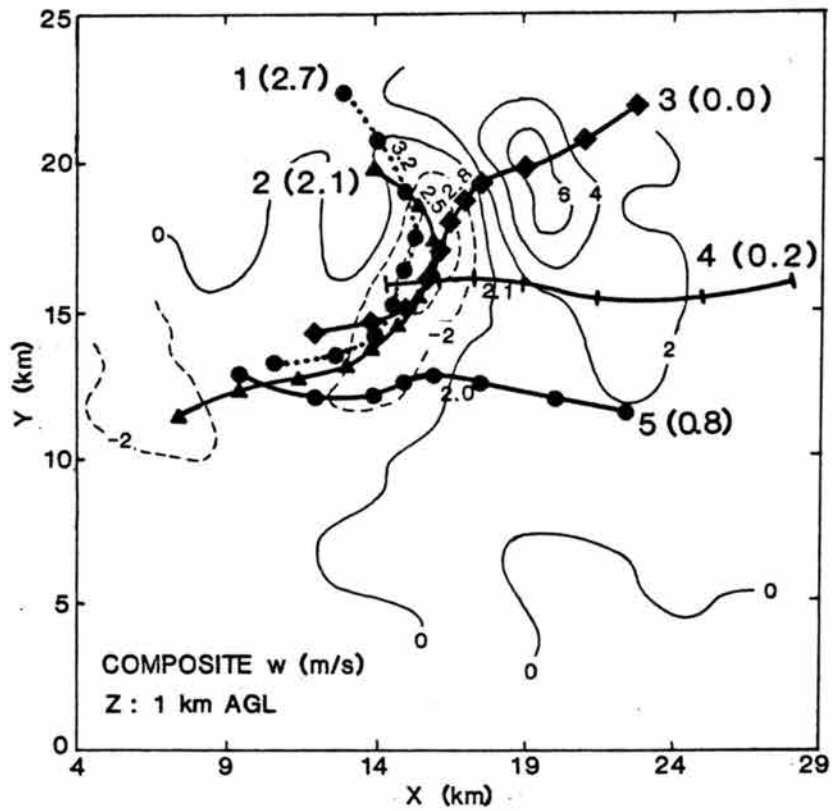

Fig. 4.15. Plots of five selected trajectories computed from individual scans at 1738, 1754 and 1803. Each trajectory is labeled with an identification number and starting level in kilometers. Tick marks along each trajectory are drawn every 4 min from initial time. Vertical motion is taken from the 1738-1803 composite at 1 km AGL and is contoured every 2 m s^{-1}, with dashed lines indicating negative values. Other numbers along each trajectory indicate the maximum height attained along the path.

originating at levels below ~ 1.5 km AGL, defined as up-down trajectories (trajectories 3, 4 and 5). The fact that these trajectories converge in both direction and speed indicates the convergent nature of the downdraft above 0.5 - 1.0 km AGL.

Most of the computed trajectories ending within the low-level core downdraft originated from the updraft inflow flank located downshear from the downdraft. It will be shown that these up-down trajectories ascended over the gust front before descending as downdrafts within heavy precipitation. Although not obvious in Fig. 4.15, midlevel trajectories originating above the PBL typically descended more slowly at rates of 1-3 ms^{-1}, reaching the surface several km behind (upshear) the core downdraft. The trajectory analyses indicate that the maximum level of origin of downdraft air reaching the surface was ~ 3 km AGL, consistent with surface θ_e analyses (Fig. 4.10) which showed a minimum θ_e correspondng to 3 km AGL undisturbed environmental air.

Values of parameters along trajectories 2 and 4 given in Fig. 4.16 illustrate the contrasting nature of each trajectory type. The upper panels give quantities obtained or inferred from the Doppler radar analysis, while the lower panels present estimated acceleration terms of a truncated form of the vertical equation of motion given as

$$\frac{d\bar{w}}{dt} = -\frac{1}{\rho}\frac{\partial p'}{\partial z} + g\left(\frac{\theta_v'}{\theta_{v_o}} - r_T\right), \qquad (4.1)$$

(a) (b) (c) (d)

The acceleration components (a), (c) and (d) were obtained diagnostically from observed quantities by using expressions for melting and evaporation of precipitation along computed trajectories. The

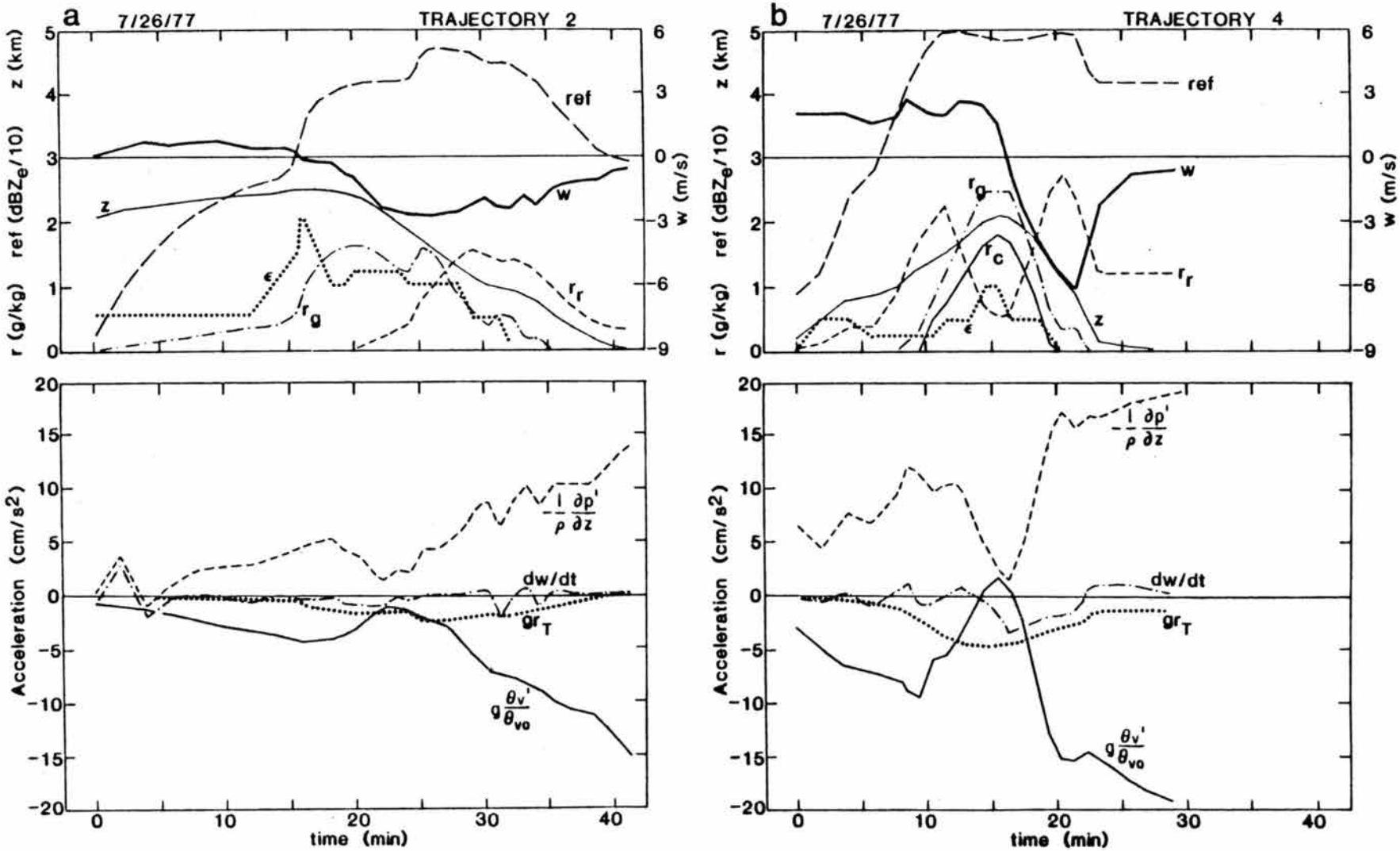

Fig. 4.16. Values along trajectories 2 and 4 plotted in Fig. 4.15. Starting times correspond to number labels given in Fig. 4.15.

pressure gradient term (b) was then solved as a residual. Further details on the diagnostic model are given in Appendix C.

Trajectory 2 (Fig. 4.16a) originating near 2.2 km initially rises, encounters increasing reflectivity and turbulence (ε) within the reflectivity gradient and then descends at rates of ~ 2 m s^{-1} within high reflectivity. The increase in ε along the reflectivity gradient may represent TKE generation from mixing between modified cloud and subsaturated environmental air alluded to above. Values of ε remain at moderate levels betwee 1 and 2 km AGL and then taper to low values near the surface. Accelerations along this path are generally very small. Thermal buoyancy and loading provide primary downward forcing throughout and are primarily opposed (nearly hydrostatically) by pressure gradient forces. Most of the negative buoyancy is provided by sublimation of graupel and evaporation of rain. Graupel and rainwater mixing ratios depicted in the upper panel of Fig. 4.16a were determined from assumed distributions of rain and graupel which vary only in height (see Appendix C). Vertical profiles of temperature and water vapor mixing raio along this path indicate descent which approaches a moist adiabat near 30 min at a level of 64 kPa or 1 km AGL. Such a profile can occur only under slow descent speeds within relatively high precipitation content as was the case here.

The behavior along up-down trajectory 4, which has a path approximately along the plane of Fig. 4.12, differs appreciably from the previous. Air originating near the surface rises 2 km within the lower regions of the primary updraft, encounters high turbulence within moderate reflectivity near the summit, and then descends within the downdraft core up to 6 m s^{-1} within 40-50 dBZ_e echo. Turbulence

intensity (ε) near the top of this trajectory indicates that appreciable mixing occurs presumably between this high θ_e boundary-layer air and low-valued θ_e air approaching the reflectivity core along midlevel trajectories from the north. (Turbulent mixing is not included in the diagnostic calculations.) Greater levels of turbulence were encountered at the summit along trajectory 4 (see Fig. 4.15), located closer to the midlevel downdraft inflow.

Considerable amounts of condensate in all forms are encountered along the apex of trajectory 4. Air rising from near the surface is initially negatively buoyant from evaporational cooling of rain falling into the updraft inflow flank (see Fig. 4.12). Increasing negative buoyancy along the up segment is produced primarily by melting within the melting zone between 1 and 2 km AGL. Only a short segment along this path experiences positive buoyancy above cloud base due to cloud condensation, which may in fact be underestimated if initial temperatures were warmer than inferred. Negative buoyancy is very quickly produced by melting and evaporation within heavy preipitation along the down segment. Condensate loading is relatively large and important near the downdraft top. Pressure gradient forces, obtained as a residual from the vertical equation of motion (4.1), are instrumental in forcing negatively-buoyant air upwards along the up branch. Although not the case here, negative pressure gradient forces along other up-down trajectories (e.g., 3) act to force positively-buoyant air down into the melting zone. Such patterns support the inference that negative pressure perturbations exist below the 273 K level, as was suggested by the accelerating nature of the downdraft between 1 and 4 km seen in the Doppler analyses. Inferred pressure forces along up-down trajectories

are instrumental in forcing negatively buoyant air upwards below cloud base and then forcing positively buoyant air downwards from above cloud base. This type of trajectory will appear again for other cases, and its dynamics are further elucidated using cloud model results presented in the next subsection.

Total cooling and contributions to this cooling by precipitation melting and evaporation listed in Table 4.2 indicate that the cooling contribution by graupel melting varies from 13% along the midlevel trajectory 2 to 60% along the up-down trajectory 4. Cooling by melting along up-down trajectories 3 and 4 is greater than along trajectory 2 because parcels spend a greater time within the melting zone along the up and down branches in the former. Melting within heavy precipitation along the ascending branch of up-down trajectories such as 4 may in fact provide sufficient negative buoyancy when combined with loading to drive air downwards along the down branch. Vertical profiles of cooling rates by evaporation and melting are given later in Section 6 for several idealized cases. These cooling rates, obtained by calculating cooling from melting and evaporation of precipitation (3.6 g/kg) released from just above the melting level, indicate a melting contribution of 40% for the 7/26 case.

TABLE 4.2. Accumulated cooling from evaporation and melting along trajectories plotted in Fig. 4.16.

Trajectory	Rain evaporation (RVAP-K)	Graupel sublimation (GVAP-K)	Graupel melting (GMELT-K)	Total (K)
2	-4.3	-1.2	-0.8	-6.3
3	-2.1	-0.1	-1.8	-4.0
4	-1.9	-0.1	-2.9	-4.9

4.1.2 The 26 July 1977 case: Cloud model results

A three-dimensional simulation initialized in a homogeneous environment with the observed sounding (Fig. 4.1d) reproduced many of the observed storm features. As shown in Fig. 4.17, updrafts and downdrafts exhibited initial maximum values of 26 m s^{-1} and -11 m s^{-1}, respectively, which were considerably greater than subsequent, more typical maxima of ~ 15 m s^{-1} for updrafts and -8 m s^{-1} for downdrafts. Four downdraft types defined previously in Fig. 2.4 and in Table 2.1 are portrayed in the time-height section of Fig. 4.17. The first (L_1) is a cloud edge downdraft of 8 m s^{-1} magnitude associated with the developing cloud. This downdraft was distributed almost symmetrically around the cloud/updraft edge during the cloud growth stage. A second downdraft region (OS) centered near 8-9 km level occurred at the time of maximum updraft. This downdraft also attained 8 m s^{-1} speeds and was forced by negative buoyancy and pressure forces described in more detail below. A third downdraft region occurring at lower levels was composed of two closely-interacting downdrafts, L_2 and PR. It will be shown below that downdraft L_2 which first appeared near 2.5 km within the downshear flank, was partly forced by wake entrainment effects described previously in Sections 2.2.2 and 4.1.1. Precipitation effects then generated and supported downdrafts L_2 and PR, whose structures are detailed in the following paragraphs.

Fig. 4.18 illustrates midlevel patterns at 2760 s, ~ 600 s after maximum updraft intensity was attained. General flow structure and cloud size appear qualitatively similar to observed patterns. The plume of intermediate-valued θ_e (Fig. 4.18b), associated temperature reductions (Fig. 4.18d), and reduced updraft extending downshear (east)

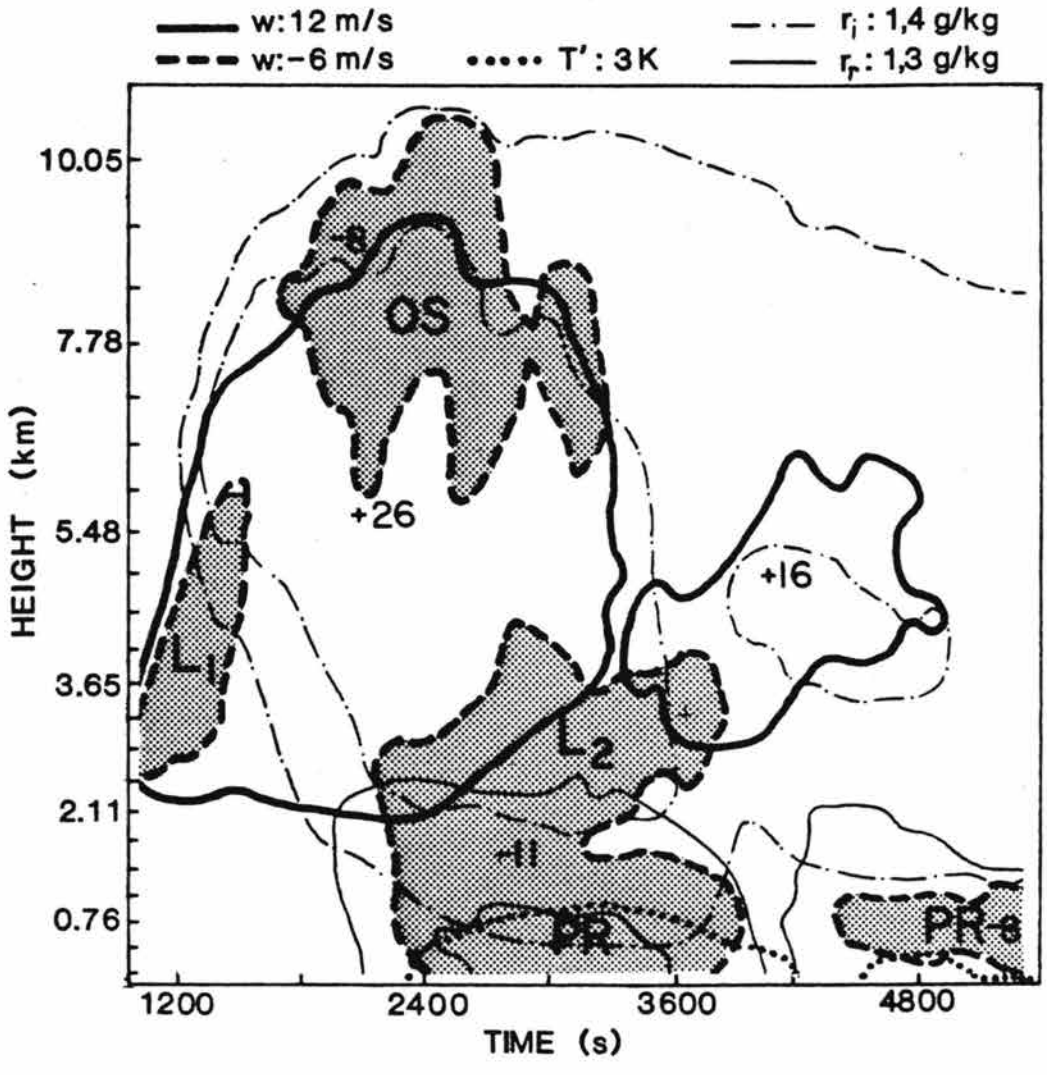

Fig. 4.17. Time vs. height section of selected analyzed quantities from a three-dimensional simulation using the envionment of 26 July as input conditions. Letters refer to downdraft types defined in the text.

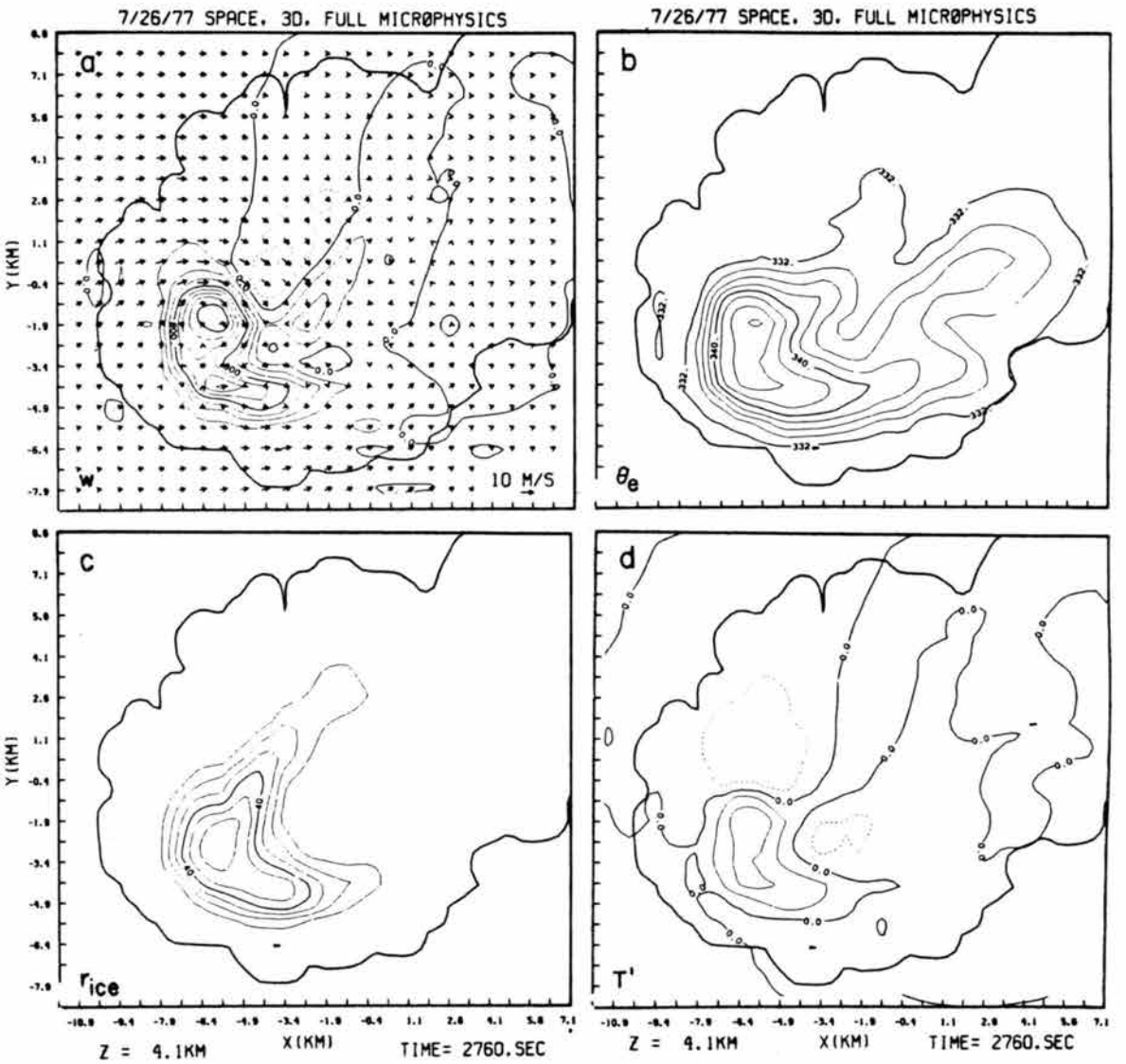

Fig. 4.18. Patterns through a midlevel downdraft L_2 at 4.1 km during the latter developing downdraft stages at 2760 s simulation time. Contour intervals of analyzed fields are as follows: (a) w every 2 m s^{-1}, (b) θ_e every 2K, (c) ice precipitation mixing ratio every 2 g kg^{-1}, (d) T' every 1 K.

from the updraft core is indicative of mixing occurring within the downshear flank in a manner similar to that depicted in Fig. 2.7. Downdrafts at this time were most active in the lowest 3 km. The precipitation field at 4.1 km (Fig. 4.18c) deserves attention here because of its importance in driving downdrafts at low levels. This relationship is discussed in detail in Section 5. In particular, the axis extending from the main core towards the northeast is colocated with downdraft L_2, within which very strong downward flux of precipitation occurs. This northeastward extension is a manifestation of the environmental wind shear (Fig. 4. d) which acts to tilt the updraft towards the northeast above middle levels. Precipitation falling from the weakened updraft then forms the midlevel extension portrayed in Fig. 4.18c. It is primarily this feed that initiated and maintained downdrafts at lower levels.

Characteristics of model-generated downdraft types indicated previously in Fig. 4.17 appear in Figs. 4.19-4.21. A vertical east-west section along y = 0.4 which cuts through the northern storm flank (Fig. 4.18) is shown in Fig. 4.19. The most substantial downdraft within this plane is OS, associated with negative buoyancy produced by updraft equilibrium overshoot. This downdraft region actually extends above the updraft and cloud top, and exhibits relatively warm temperatures in its upper and lower regions. Warm air within the upper regions of OS, with probable origins within or above the tropopause, is forced downwards by pressure forces. The other warm air region in the lower part of OS has boundary layer origins and represents the initial thermal equilibrium overshoot of downdraft OS. Patterns within this downdraft, similar to those analyzed in detail by Schlesinger (1984b), exhibit characteristics

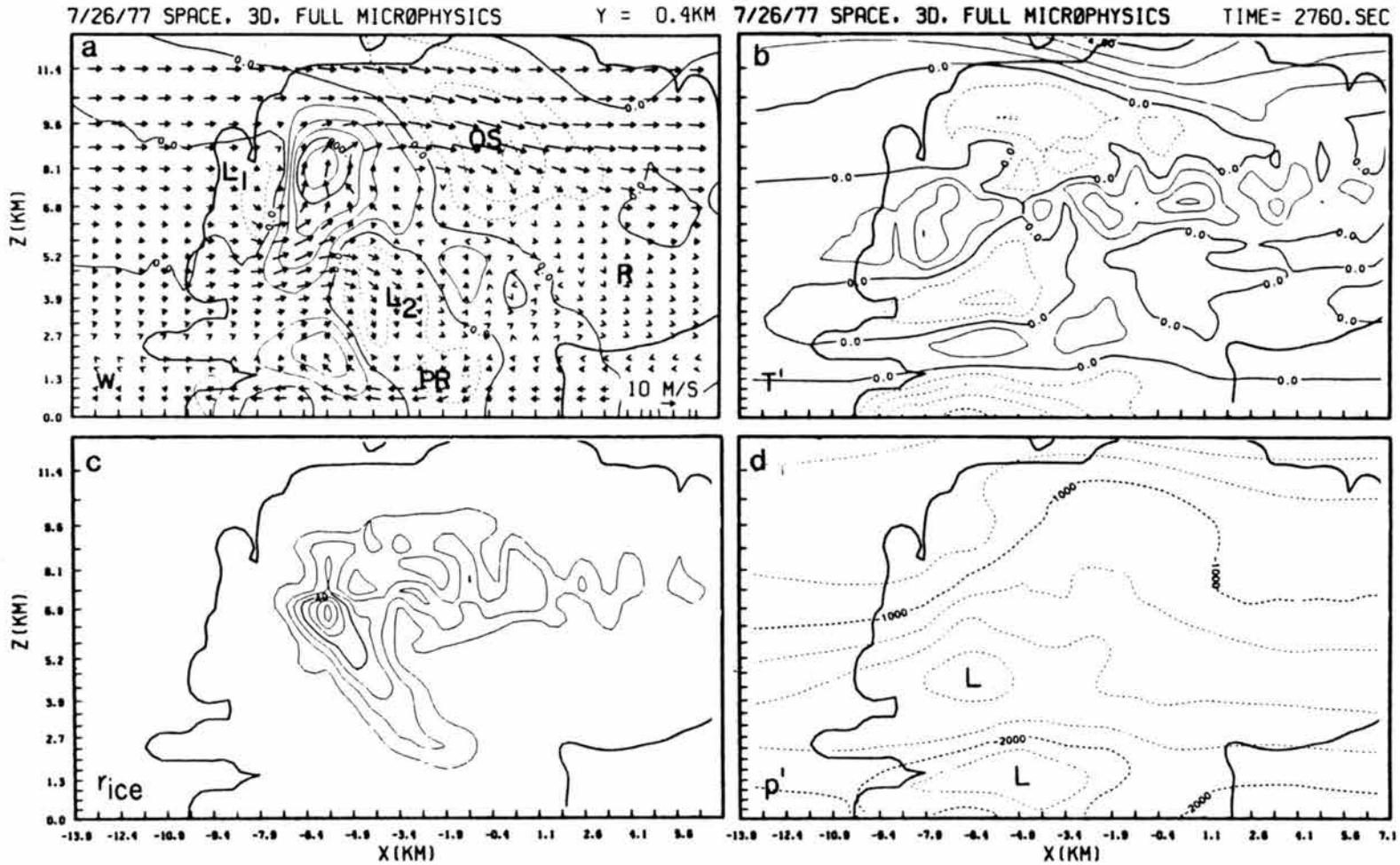

Fig. 4.19. Cloud model patterns at 2760 s within an east-west vertical plane along y = 0.4 km in Fig. 4.18, illustrating several downdraft types. Contours of analyzed fields are the same as in Fig. 4.18 except in (d) where p' contours are drawn every 25 Pa.

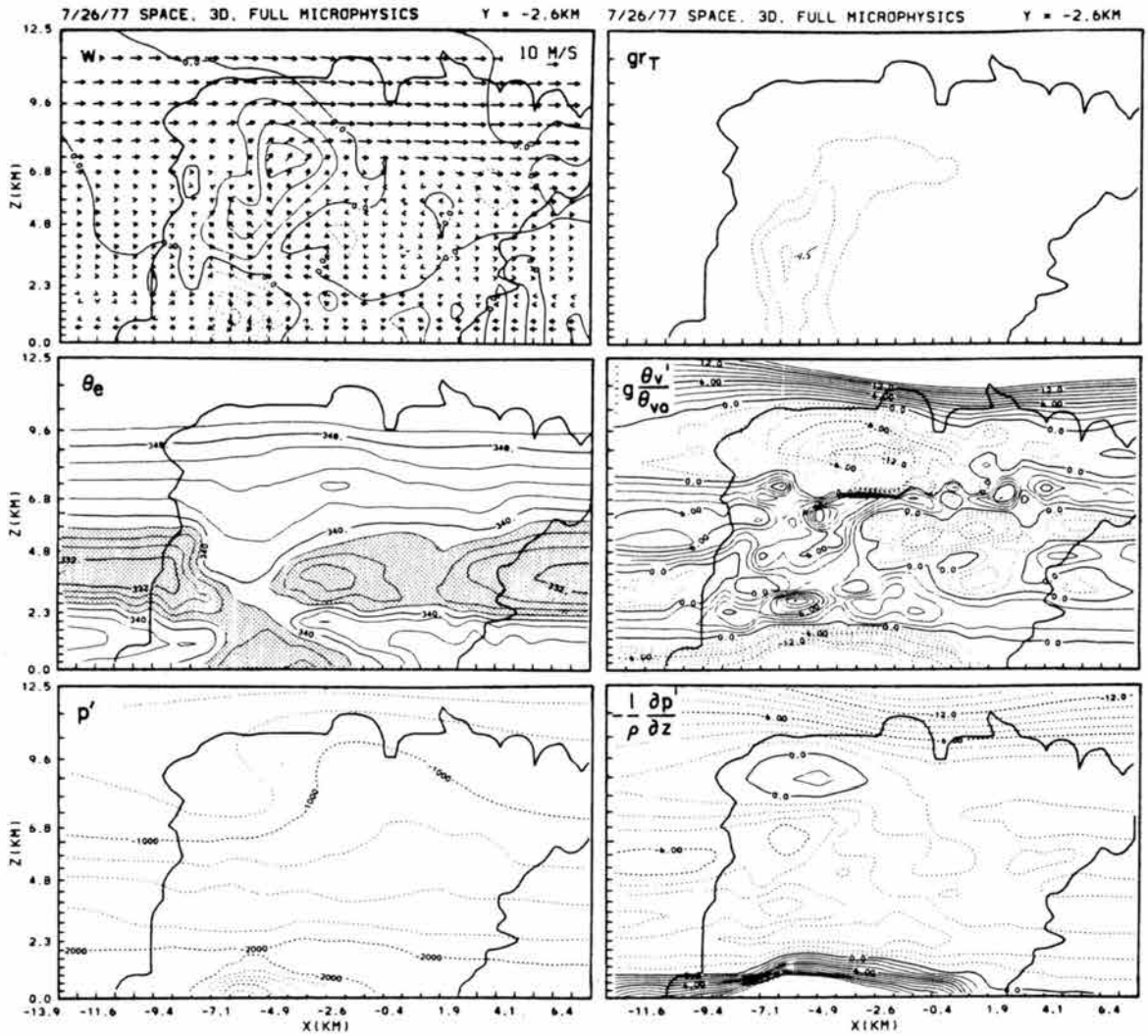

Fig. 4.20. Cloud model patterns along an east-west vertical section through the mature downdraft core at 3360 simulation time. Contours of analyzed fields are as follows: (a) w every 2 m s^{-1}, (b) θ_e every 2 K, (c) p' every 25 Pa, (d)-(f) selected acceleration components contoured every 0.015 m s^{-2}.

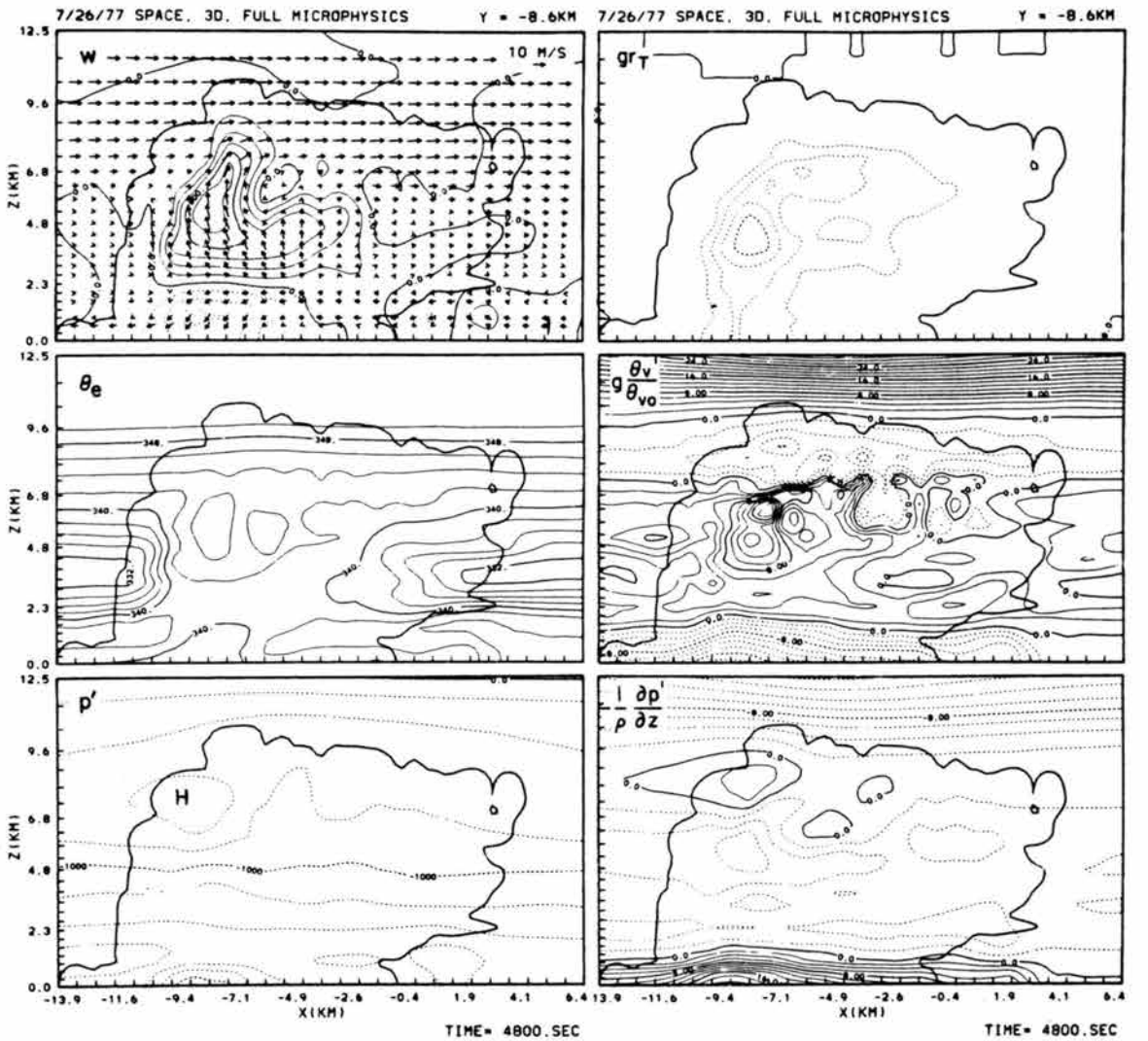

Fig. 4.21. Same as Fig. 4.20, except at 4800 s simulation time. Acceleration components are contoured every 0.02 m s^{-2}.

which differ appreciably from downdraft PR. Magnitudes within downdraft OS closely paralleled relative updraft intensity and were strongest (8-9 m/s) near 2400 s, after which maximum values subsided to ~ 5 m/s near the updraft parcel equilibrium level of 8 km. Examination of overshooting downdrafts in other cloud model simulations conducted in this study indicate that OS downdraft magnitudes and fluxes are proportional to updraft fluxes near the parcel equilibrium level.

Also present within the vertical plane of Fig. 4.19 are weak regions of subsidence (R) which flank the cloud, particularly downshear. Stronger cloud-edge downdrafts are located upshear at high levels (L_1) and along the downshear flank at low middle levels (L_2). Downdrafts such as L_1 are typically produced (in the model) by slight negative buoyancy produced by sublimation or evaporation along cloud edge (supported by aircraft measurements summarized in Section 2.2), or by negative vertical pressure gradient forces, the case for L_1. This positive thermal behavior within elevated downdrafts occurs frequently in cloud model simulations (see also Section 2.4.3) and indicates that downdraft development from levels above ~ 4 km, as Lemon and Doswell (1979) have envisioned for supercell storms, is unlikely. Because these downdrafts often occur within stable upper levels outside significant cloud and precipitation water, positive buoyancy is quickly produced upon descent which is approximately dry adiabatic outside of regions having significant cloud water or precipitation contents.

Downdraft L_2, also depicted in Fig. 4.19 and located at lower midlevels was more intense and persistent, being prominent during the intense updraft stages from 1800 s to 3000 s. (The low-level updraft is located to the south of this east-west vertical plane.) This downdraft

appears northeast of the updraft within precipitation and low-valued θ_e air at 4.1 km AGL (see Figs. 4.18 and 4.19) and is similar in size and strength to the analyzed midlevel downdraft portrayed in the observational results of Fig. 4.13. In contrast to the relative warmness of L_1, portions of downdraft L_2 exhibit negative thermal buoyancy (Figs. 4.19 and 4.20), accomplished by sublimation of ice-phase precipitation falling into this region. Lower regions of L_2 are warm ($T' > 0$) because cooling rates from sublimation are slower than adiabatic warming rates of air being forced downward by loading. Analyses of quantities along a trajectory passing through L_2 are presented below. All elevated downdrafts (L_1,L_2,OS) decreased significantly in intensity and coverage after ~ 3000 s (Fig. 4.17), contrary to the low-level precipitation downdraft which exhibited maximum values within 30% of the absolute maximum of ~ 12 m/s occurring at 2800 s near 1.8 km.

Characteristics of the simulated downdraft PR are illustrated in Figs. 4.19 - 4.21. Although this downdraft was weakly coupled with downdraft L_2 at and before 2760 s, later analyses at 3360 s and 4800 s (Figs. 4.20 and 4.21) indicate a more independent structure isolated to the lowest 2-3 km AGL. This downdraft is directly associated with the precipitation core extending within and below the primary updraft. At 3360 s, a tongue of low-valued θ_e air (Fig. 4.20b) extends from the downdraft core to the upshear (left) cloud edge. At this time the primary updraft feed is becoming established within the downshear (east) cloud sector. Low-valued θ_e air initially entered the downdraft within the downshear cloud sector (see Figs. 4.18, 4.19) during the developing downdraft stages (discussed in detail in Section 5.2) when L_2 and PR

were closely coupled (Fig.4.19a). This midlevel "feed" was subsequently cut off shortly before 3360 s when updraft inflow was established in the downshear sector above the downdraft-generated gust front as shown in Fig. 4.20a. The upshear "feed" to the downdraft weakened with time, being negligible by 4800 s when very little low-valued θ_e existed at low levels (Fig. 4.21b). Trajectory analyses indicate that only small amounts of air entered the downdraft core from the upshear flank. Observations presented previously indicated a more pronounced upshear downdraft inflow which exhibited a sustained midlevel downdraft feed from the northern flank. Absence of this weak downdraft region in the modeled patterns may be due to the precipitation parameterization, which apparently fails to produce large regions of relatively light precipitation trailing the main core as was observed. Such a failure may be related to the lack of model generated precipitation in the form of aggregates having low fall speeds which would naturally trail the main precipitation region.

At 3360 s and 4800 s low-level maximum downdraft speeds occurred near the 0.8 km level within heaviest precipitation. In the upper regions of this downdraft ($z \gtrsim 1.8$ km) pressure forces and loading accelerate air downwards (Figs. 4.20 and 4.21). Negative buoyancy interestingly exists below 2 km, the melting level in this case. Therefore, above 2 km only loading and pressure forces act to accelerate downdraft air downwards. Below 0.8 km, however, pressure forces exceed total buoyancy forces and vertically decelerate and horizontally accelerate downdraft air. More detailed calculations presented in Section 6 indicate that melting accounts for ~ 2/3 total cooling in the 1-2 km AGL layer. Except for positive pressure perturbations located

within the low-level downdraft and at upper regions along the updraft upshear flank, the p' field is relatively featureless.

The equilibrium maximum height of the "steady-state" low-level downdraft (PR, Fig. 4.21a) is located near 2.3 km, significantly lower than it was in the developing stage. Such a height is near the transition between dry and moist adiabatic temperature structure indicated by the letter T in Fig. 4.1d. Results in subsequent subsections will indicate a similar relationship between downdraft tops and the environmental sounding T level, thus suggesting that such a value would have utility in a parametric model.

Fig. 4.22 presents calculated downdraft air-parcel trajectories around 2760 s and 4800 s. In the developing and early mature stages (2760 s) trajectories passing through the downdraft core originate from the northern semicircle over the lowest 3-4 km. The southern semicircle lacks midlevel downdraft trajectories because environmental winds backed with height, thus forcing relative inflow from the left or north flank. Some of these trajectories such as 4 and 15 are up-down types originating within the PBL, while other midlevel trajectories (3,5,17) begin from above the PBL. Midlevel trajectories which dominate the initial downdraft stages (Fig. 4.22a) for this simulation (discussed further in Section 5.2) were later dominated by up-down trajectories (Fig. 4.22b) originating within the downshear flank during the latter mature storm stage. Only a small fraction of the computed trajectories (e.g., 5,14) entered the downdraft directly from the upshear or rear flank.

Values along selected trajectories (3, 16, and 17) are presented in Fig. 4.23. Trajectory 3 (Fig. 4.23a) is one typical of a lower midlevel

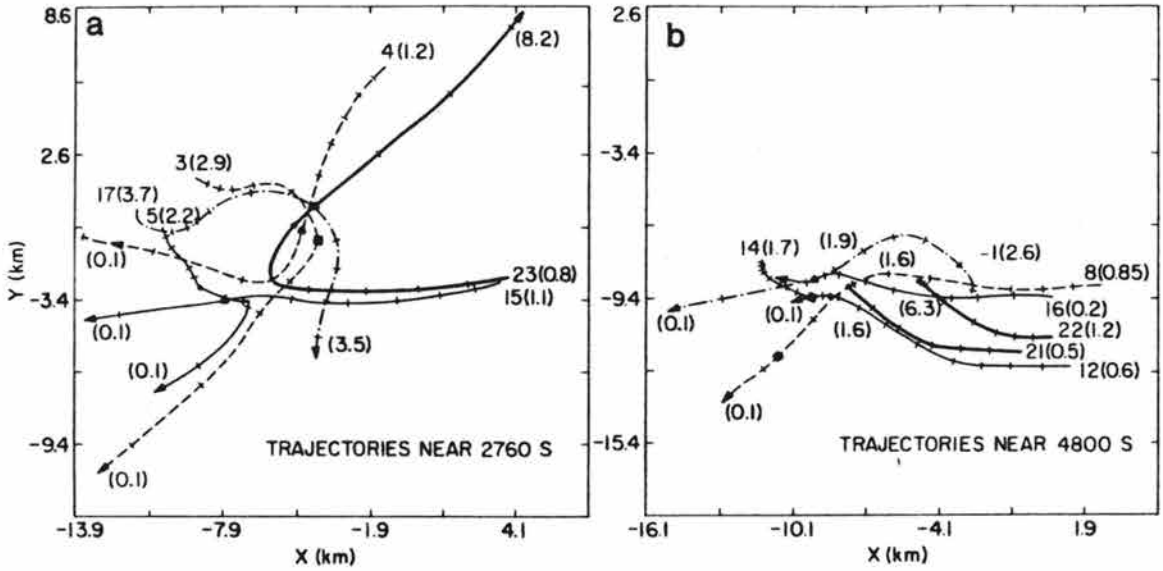

Fig. 4.22. Paths of selected time-dependent trajectories from the 7/26 cloud model simulation centered around the 2760 s and 4800 s times. Tick marks are drawn every 4 min. Numbers near the start and end of each represent trajectory indentification number and level of origin (km). Filled-in squares, triangles and circles portray parcel position at the time indicated in each parcel.

trajectory originating within low-valued θ_e air at 2.5-3.0 km. Its path (Fig. 4.22a) is essentially opposite to that depicted in the Browning (1964) model (Fig. 2.4) because winds back rather than veer with height in the 7/26 case. An air parcel traveling this path initially subsides at rates up to 0.4 m s^{-1} before decreased downward-directed pressure forces combine with positive buoyancy to provide lifting and associated dry adiabatic cooling very near the storm flank. As a result, the parcel undergoes a period of negative buoyancy associated with horizontal accelerations produced by low perturbation pressure (p') located at midlevels within the northern flank (see Fig. 4.19d). Significant ice-phase precipitation falling from above is encountered within this flank and loading combines with negative buoyancy to produce downward accelerations. Positive buoyancy which is temporarily established in the upper downdraft portions (due to the relatively high

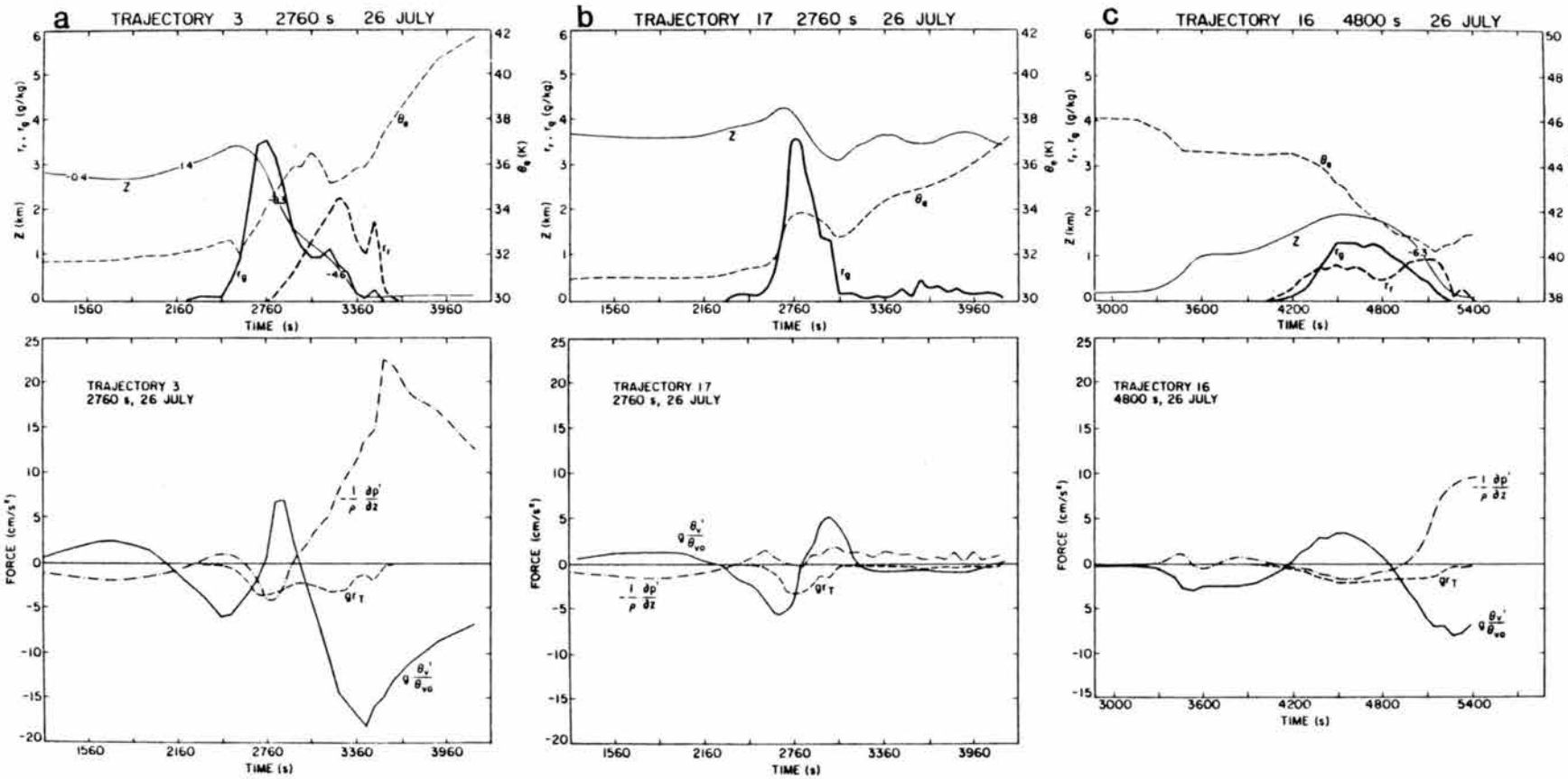

Fig. 4.23. Values of parameters and acceleration components along selected trajectories from model output of the 7/26 case. The left column contains θ_e, mixing ratios of rain and graupel, and height. Values along the z curve denote vertical motion in m s-1. The left column presents values of acceleration components loading, thermal buoyancy and the vertical perturbation pressure gradient force.

initial θ of this parcel) is countered by negative pressure forces and loading. Cooling by evaporation and melting below 2 km quickly return the parcel to negative buoyancy within the more unstable boundary layer. Note that θ_e increases ~ 4 K as air descends within the downdraft, indicating the presence of mixing between downdraft and environment. Although this may be regarded as artificial model diffusion, observations presented earlier suggest that similar mixing processes occur within the downdraft. In this cloud model case mixing proceeds primarily within the downshear wake as indicated in the analysis of Fig. 4.18 and in the schematic of Fig. 2.7.

The initial behavior of trajectory 17 (Fig. 4.23b) is generally similar to the initial behavior along trajectory 3. In this case, however, total descent within the downdraft zone is much smaller (~ 1 km) for three possible reasons. Firstly, this parcel originates at higher levels within a nearly moist adiabatic layer. It therefore possesses a greater θ and hence requires greater rates of cooling to overcome the positively buoyant tendency produced by descent. Secondly, this parcel moves at greater relative horizontal speeds through the downdraft region and simply descends ~0.5 km after passing through the downdraft zone. Such a behavior indicates that total <u>downdraft vertical displacement</u> is a function of the ratio of vertical to horizontal flow over the downdraft width. This phenomenon is more common for high shear environments as we shall see in following subsections. Finally, another factor which prevented parcels higher than 3 km from reaching the surface is that they were further removed from pressure forcing produced by rapid onset of negative buoyancy of parcels entering the lowest 2 km. This process is discussed in detail in Sections 5.2 and 5.3.

The behavior along trajectory 16 during a latter storm stage (Fig. 4.23c) is representative of parcels entering the up-down downdraft branch within the downshear flank. Trajectory 16 originates very near the surface and exhibits two distinct periods of rising motion, the initial one (near 3400 s) being over the gust front and the second more gradual one being associated with p' forces very near the storm.* Ascent along the up segment of this up-down branch occurs under negative buoyancy, in agreement with the observations. Positive buoyancy generated by latent heating above this parcel's SP is countered by loading and negative p' forces. Mixing with lower-valued θ_e air provides the cooling necessary for loading to overcome buoyant forces. Fastest descent again occurs near 1 km where significant negative buoyancy produced by evaporation and melting is supplemented with loading to drive air downwards. The behavior along up-down trajectories 4 and 15 is similar to that along 16, except negative buoyancy along the up-branch is absent in 4 and 15 due to scarcity of precipitation and associated evaporational cooling within the downshear inflow sector at earlier stages.

The cloud model results from this case illustrate all downdraft types defined earlier. Distinct structural, dynamic and thermodynamic differences in each type are obvious. For this particular case the low-level precipitating downdraft is most extensive, intense and long-

---

* The lower panel of Fig. 4.23c is somewhat inconsistent with the height (z) curve of the top panel. It is believed that the thermal buoyancy term is too negative because θ_v of the environment is probably lower than intial θ_{v_o} because of evaporation of precipitation into the inflow flank. A more correct term would involve a "local" θ_v'.

lived. The overshooting downdraft is typically dependent on updraft properties, but apparently less dependent on microphysical properties.

4.2 Variations in Downdraft Structure

This section provides supplementary observational data on downdraft structure obtained from other low to moderate shear cases listed in Table 4.1. These supporting cases verify patterns observed in the previous section and clarify some of the relationships between low-level downdrafts and precipitation.

4.2.1 The 4 August 1977 (8/4) case

The moderate shear case of 8/4 provides both similarities and contrasts in downdraft structure. In this case strong downdrafts located primarily in the upshear cloud sector exhibited both primary downshear and secondary upshear inflows. A surface analysis for an early mature storm state at 1350 (Fig. 4.24) indicates strong divergent 10–15 m s^{-1} winds near and within high reflectivity. Outflow winds attained downburst intensity near 1350, when a radar-measured outflow wind around 300 m AGL was detected (see Fig. 4.24). Air at the surface across the outflow exhibited temperatures 4–8 K colder than ambient values ahead (east) of the storm. Variations in θ_e within this outflow crudely indicate variations in downdraft source level here, as in the 7/26 case. For example, low-valued θ_e air within the northern echo flank of Fig. 4.24 originated from the 2–3 km AGL level, while higher-valued θ_e air exceeding 340 K in the southern flank had probable origins within the boundary layer ahead of the storm. This in fact is the case, as Doppler analyses presented below will indicate.

The evolution of bulk storm properties portrayed in Figs. 4.25 and 4.26 indicates that this storm attained most intense levels between 1340

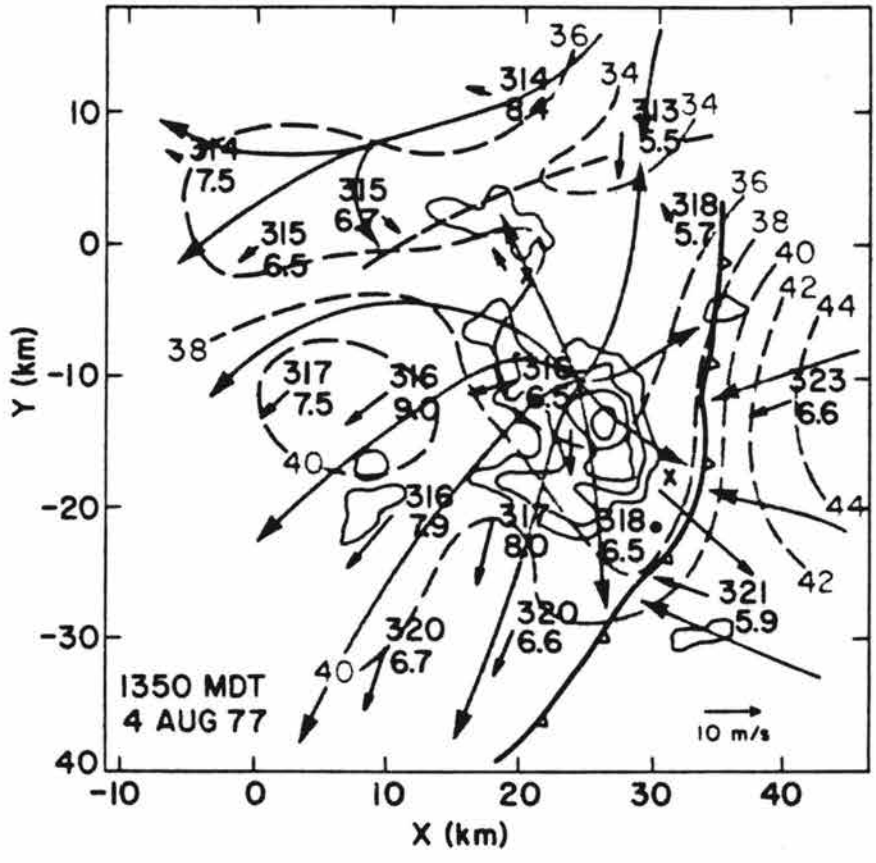

Fig. 4.24. Surface analysis as in Fig. 4.4, except solid contours represent radar reflectivity contoured every 10 dBZ_e, beginning at 20 dBZ_e.

and 1430. Note that development to intense reflectivity levels proceeded more slowly than did weakening from intense levels after 1430. Updraft and downdraft peak magnitudes (both ~ 10 m s^{-1}) and mass fluxes (Fig. 4.25b) are comparable, a unique feature of this storm when compared to others examined in this study. Individual updraft, downdraft and reflectivity cells demonstrated significant spatial and temporal fluctuations which are more apparent in patterns on horizontal planes for individual time periods (Fig. 4.26).

Fig. 4.26 illustrates the continuously-changing storm updraft, downdraft and reflectivity structure at four selected times during the mature to dissipating stages. In the earlier mature state (Fig.

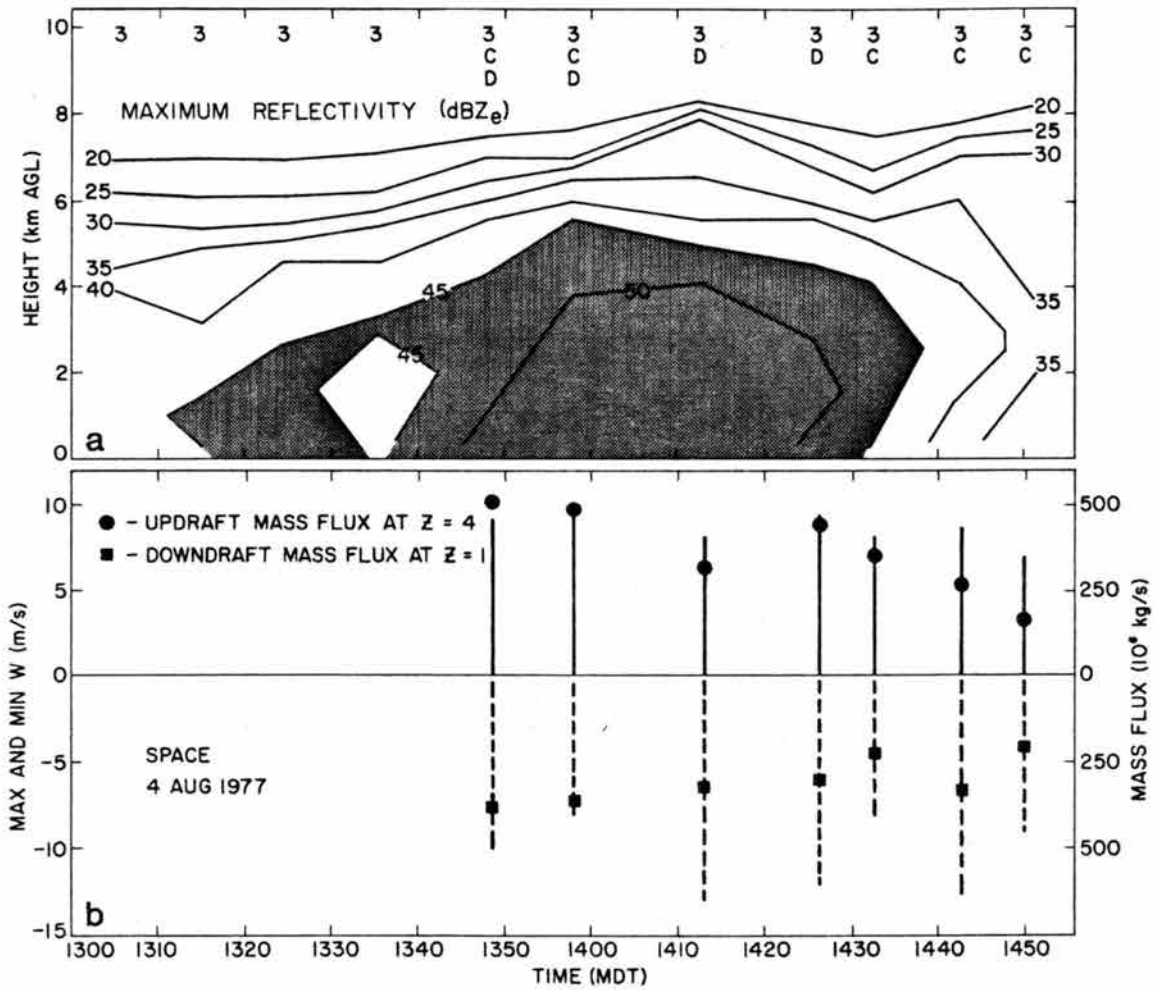

Fig. 4.25. Same as Fig. 4.5, except for the 8/4 SPACE case.

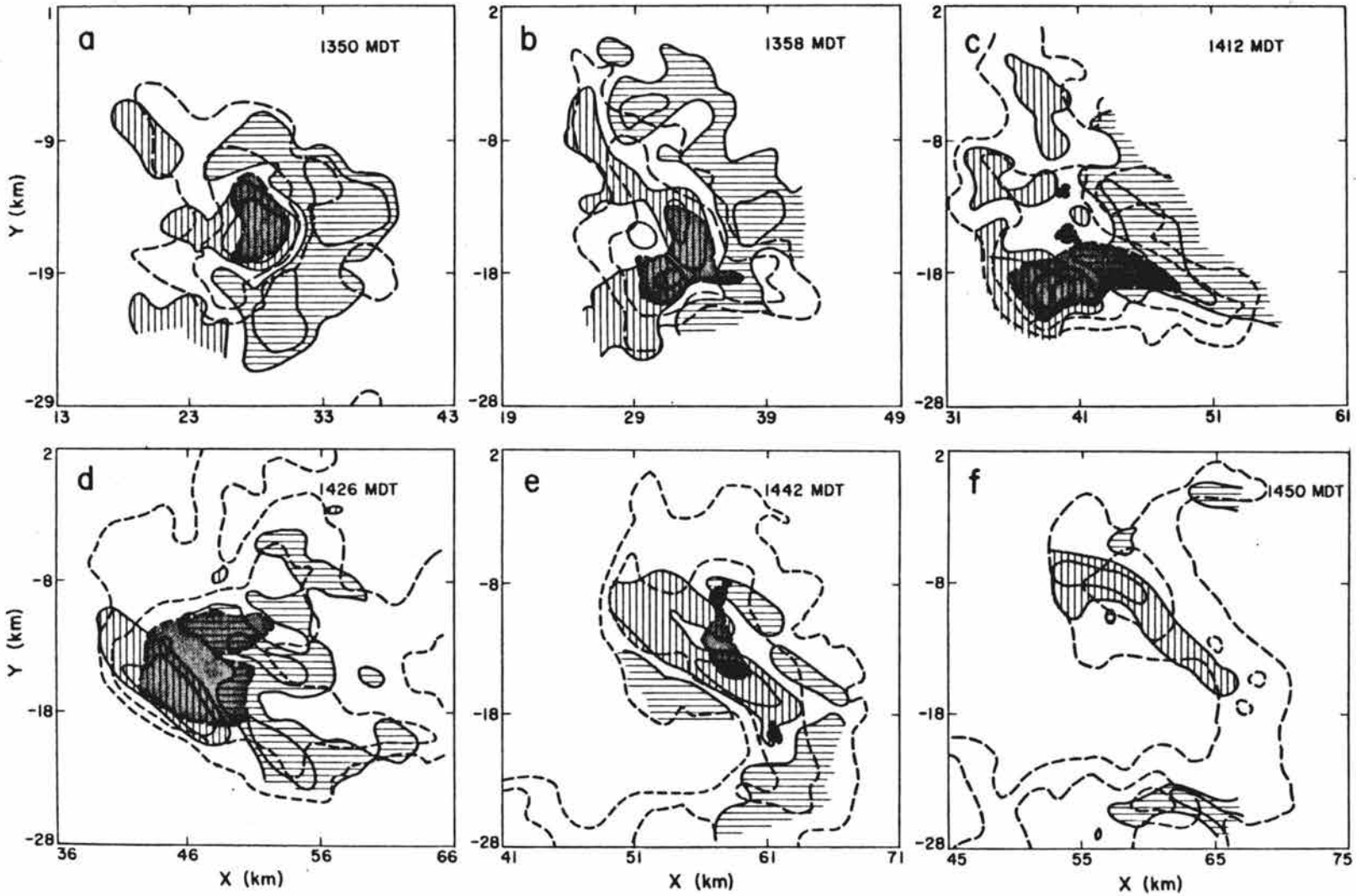

Fig. 4.26. Same as Fig. 4.6, except for the 8/4 SPACE case.

4.26a,b) downdraft regions, nearly colocated with highest reflectivity at low levels, were flanked by updrafts to the north, east and south. Areas of weaker and more uniform downdrafts were located below 3 km AGL to the west and northwest within weaker reflectivity. However, during the later mature phases the patterns were such that strongest downdrafts were located primarily along the upshear cloud sector within the reflectivity gradient (Fig. 4.26c-f).

Downdraft mass flux profiles (Fig. 4.27) and vertical gradients of these fluxes exhibit maxima at 1 km and 3 km AGL, respectively, with the latter approximately one kilometer higher than the previous case of 26 July. It is inferred that downdrafts reached higher levels in this case because a deeper and drier boundary layer present on 4 August promoted greater rates of evaportion. Temporal trends in mass flux indicate that downdraft mass flux magnitudes closely paralleled updraft mass flux magnitudes, suggesting that downdrafts are dependent on updrafts (and vice versa). Even though downdrafts displayed considerable temporal changes in relative location, bulk downdraft mass fluxes show a relatively consistent temporal behavior. Details of these contrasting downdraft spatial structures for an early mature stage (1350) and for a latter mature stage (1442) are given next.

A vertical east-west section through the downdraft core at 1350 is displayed in Fig. 4.28a. At this time the up-down downdraft inflow component in the downshear flank is more substantial than the upshear midlevel component entering at relatively high levels in this case. The dominant downshear branch originates within the updraft inflow sector, rises over the gust front and then descends up to 10 m s^{-1} within high reflectivity in a manner similar to that exhibited in the 7/26 case.

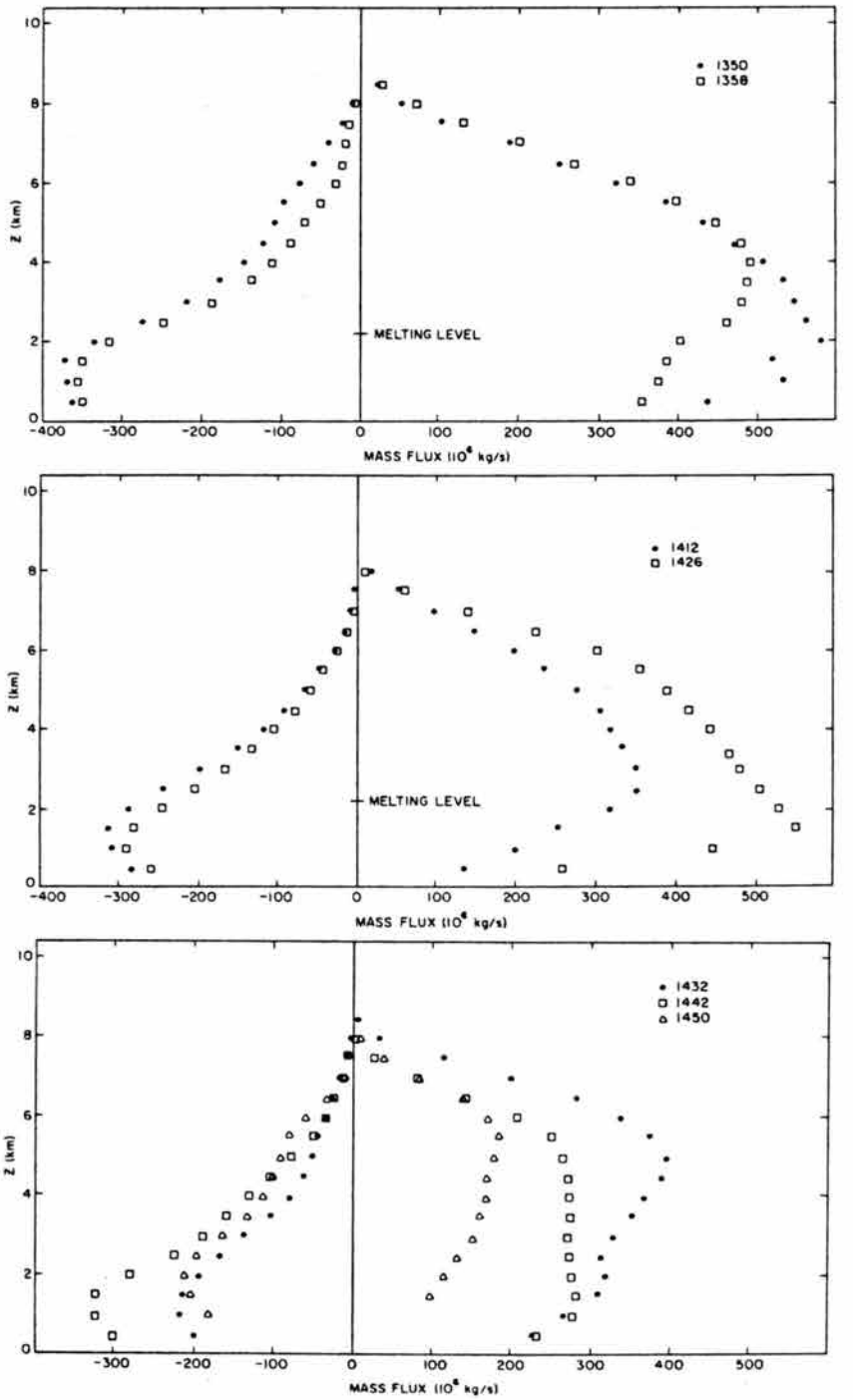

Fig. 4.27. Vertical mass flux profiles in updrafts and downdrafts for the 8/4 case.

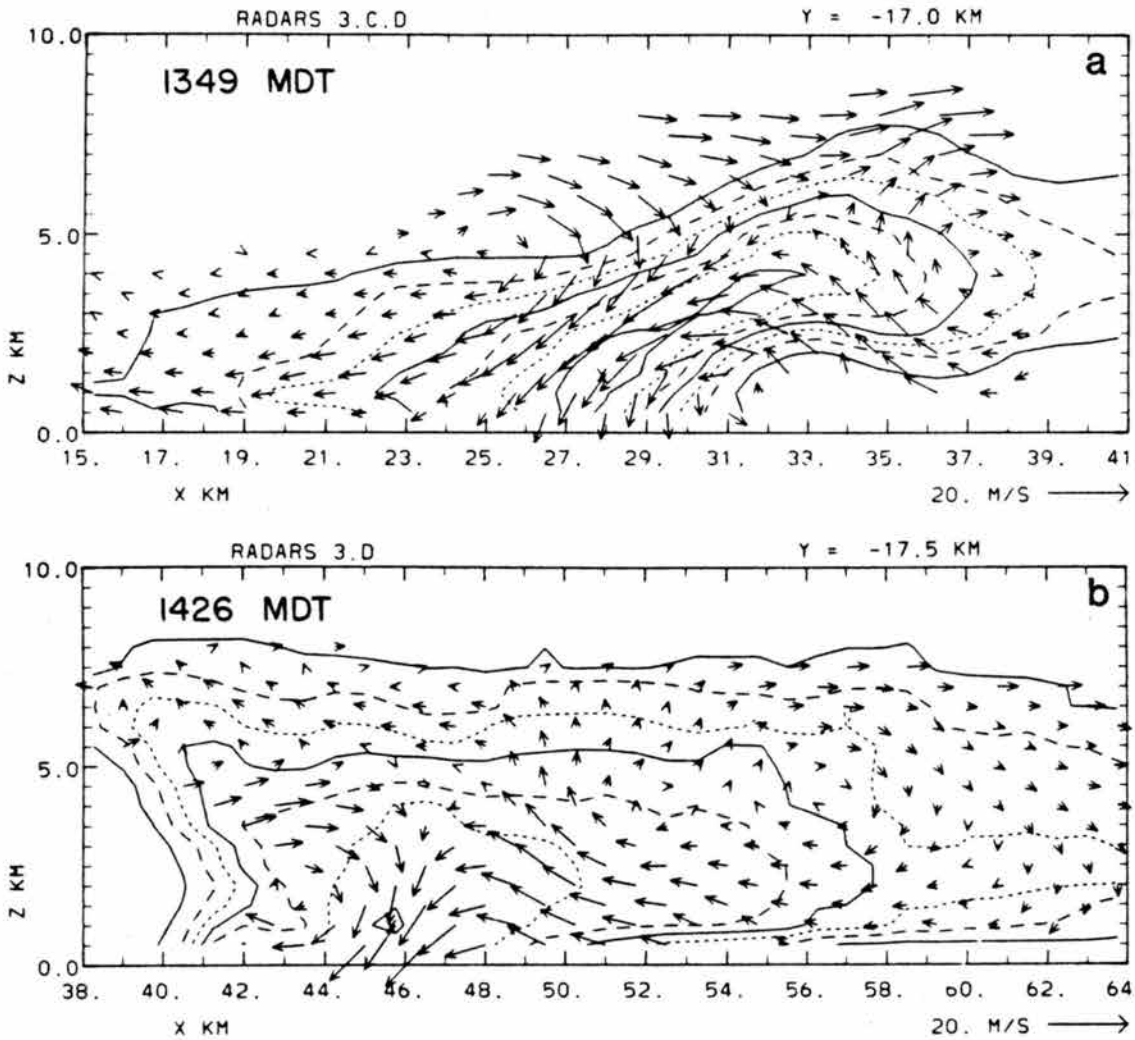

Fig. 4.28. East-west vertical section through the downdraft core at an early mature storm stage (1349) and at a late mature storm stage (1426). Reflectivity factor is analyzed every 5 dBZ_e beginning at 15 dBZ_e.

Air directly above this downdraft inflow is able to maintain ascent within weak updrafts. Note that air parcels moving along the up-down downdraft inflow branch would experience increasingly higher precipitation content prior to descending rapidly within relatively high reflectivity. Trajectory analyses presented below will demonstrate that precipitation effects (loading, evaporation and melting) exerted significant downward forcing in this case.

The upshear inflow branch to the downdraft at 1350, visible in Fig. 4.28a, enters the circulation at the 5-6 km level and merges with the primary low-level branch while reversing direction. This upper branch was much weaker but still visible in the Doppler analysis 8 1/2 min later. Reflectivity patterns at and before 1350 indicate a collapse in echo structure at 1350 from times previous. Because updraft parcel buoyancy was small in this case (Fig. 4.1d), it is inferred that precipitation and cloud condensate loading at upper levels combined with loading, evaporation and melting at lower levels to produce a transient 6 km deep downdraft at 1350. Air parcel trajectories constructed from the 1350 and 1358 time periods indicate that only small portions of 5 km downdraft air descended 2-4 km to intermediate levels or reascended in updrafts, suggestive of buoyancy oscillations.

Vertical sections through the downdraft core during the weakening stage at 1426 (Fig. 4.28b) and at other nearby times reveal a similar persistent structure. Downdraft inflow is apparent from both upshear (near 4 km) and downshear (near 1 km) directions. In both branches this downdraft inflow initially rises 1-4 km, the ascent being greater in the downshear sector, and then descends at rates up to 10 m s^{-1} within highest reflectivities of ~ 45 dBZ. As in the earlier mature stages,

highest reflectivity appears to correlate well with greatest downdraft speed. Contrary to earlier times, however, much greater proportions of downdraft core mass flux originate from the upshear inflow sector at 3-4 km, as downdraft trajectory analyses discussed next demonstrate. Moreover, the large area of weak downdraft located earlier along the western flank is now replaced by stronger core downdraft activity.

Air parcel trajectories computed using data around the early (1350, 1358) and late (1426,1432,1440,1450) time periods are presented in Fig. 4.29. Trajectories 1 and 2 for the early period (Fig. 4.29a) typify airflow which enters the downshear updraft inflow sector and rises up to 4 km before descending to the surface within high reflectivity. Up-down downdraft trajectories of this type were most common during this early time period and accounted for most of the mass flux passing through the core downdraft.

Figs. 4.30a and 4.31 illustrate thermodynamic and inferred dynamic processes along trajectory 1. Air originating near the surface rises over the gust front up to 5 m s^{-1}, encounters rapidly-increasing reflectivity and cloud water above its SP and then descends at speeds to 7.5 m s^{-1} within relatively high reflectivity (> 40 dBZ). Positive buoyancy (1 - 1.5 K) is attained above cloud base and is only partially compensated by loading, suggesting that downward-directed pressure gradient forces are operating here. Upon descent to lower subcloud levels, negative buoyancy is quickly reestablished in the unstable lowest 2 km. Endpoint values of (θ,r_v) along this and other up-down trajectories agree very well with surface station measurements of outflow air presented in Fig. 4.24. Similar relative patterns appeared along the up-down branch in the 7/26 case (Fig. 4.16b).

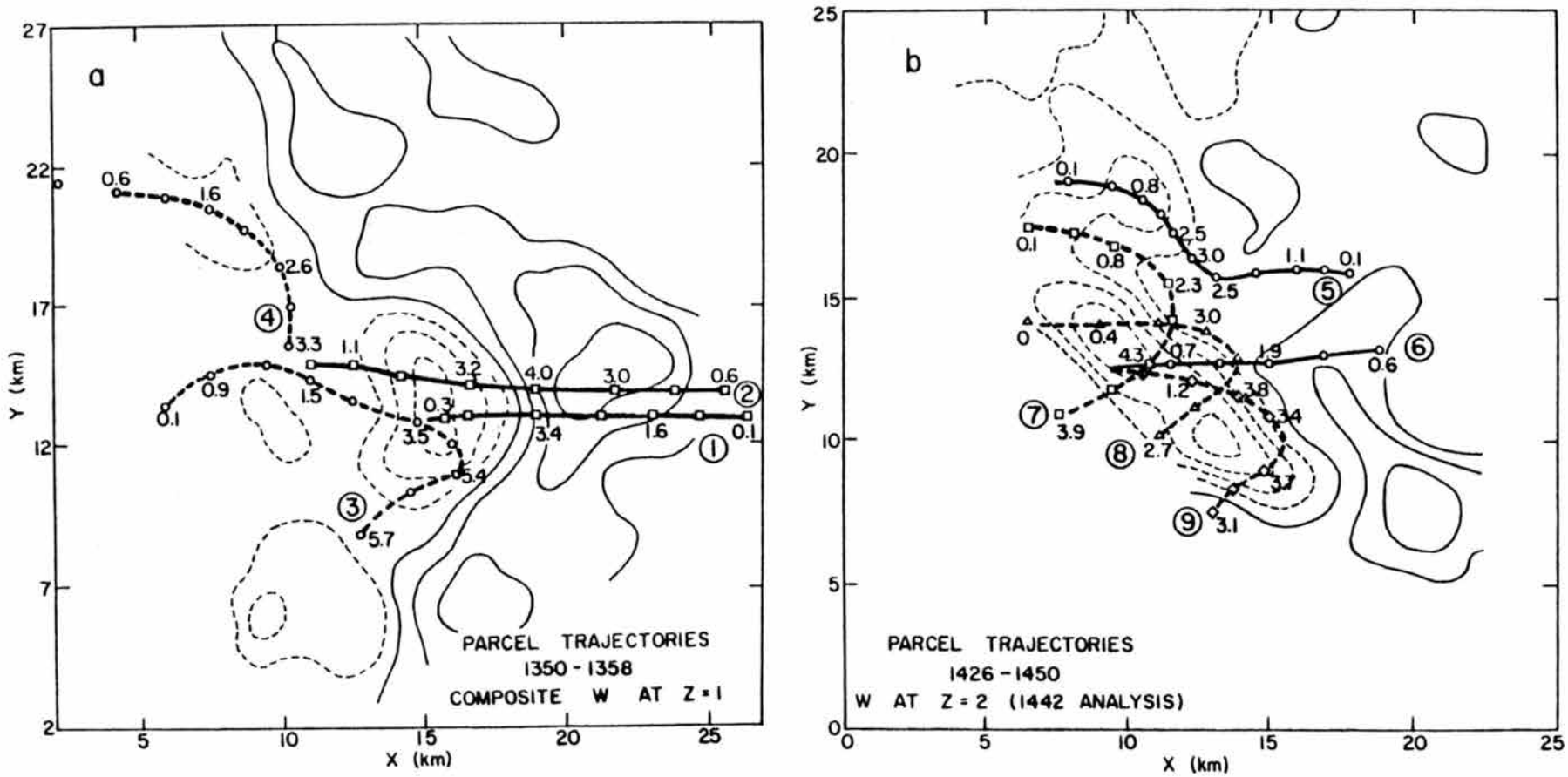

Fig. 4.29. Calculated downdraft air parcel trajectories for the 8/4 case using Doppler data from early mature storm stages (a) and dissipating storm stages (b). Vertical motion is contoured every 2 m s-1 (dashed lines indicate negative values). Marks along each trajectory appear every 4 min.

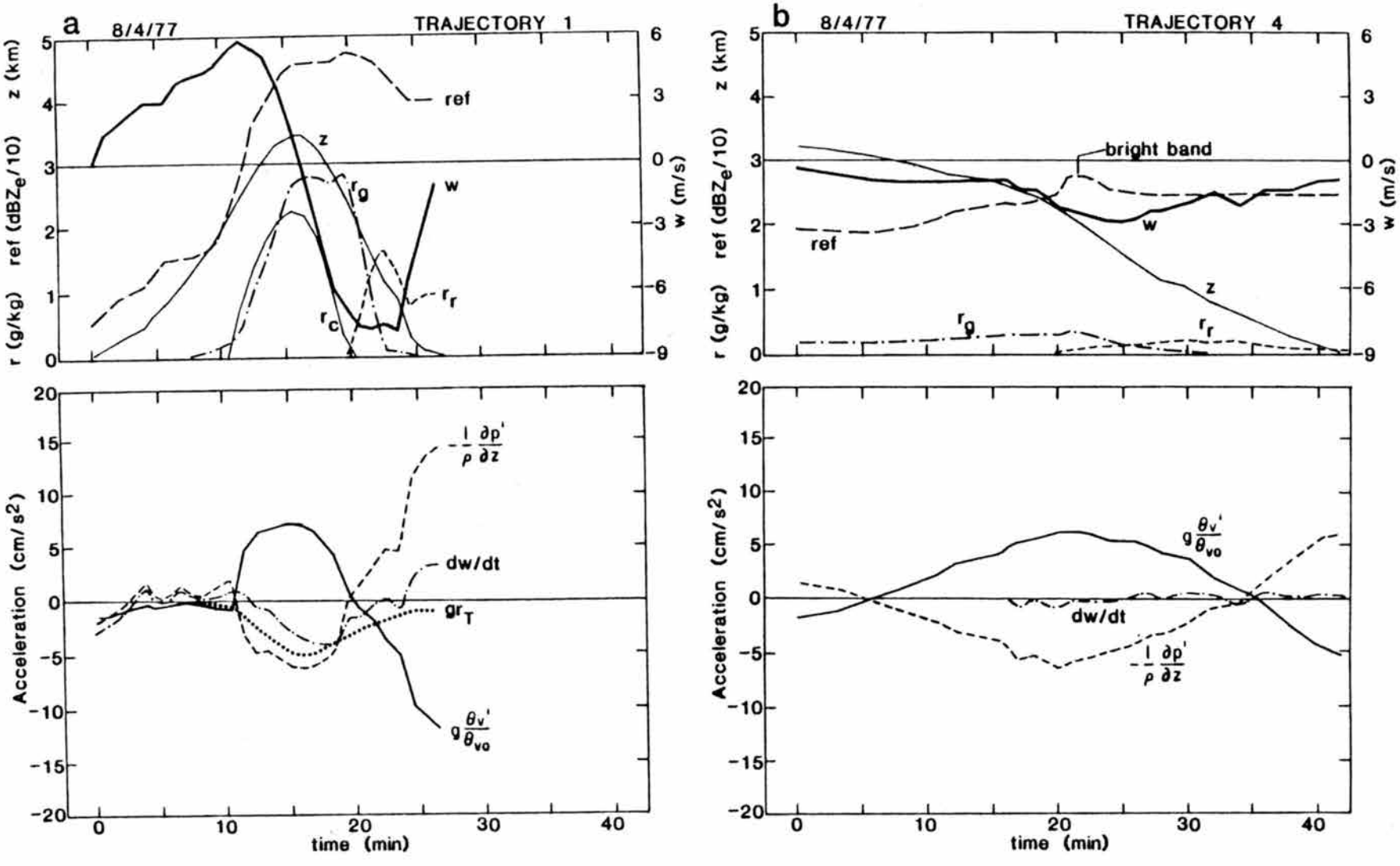

Fig. 4.30. Values along trajectories 1 and 4 plotted in Fig. 4.29a.

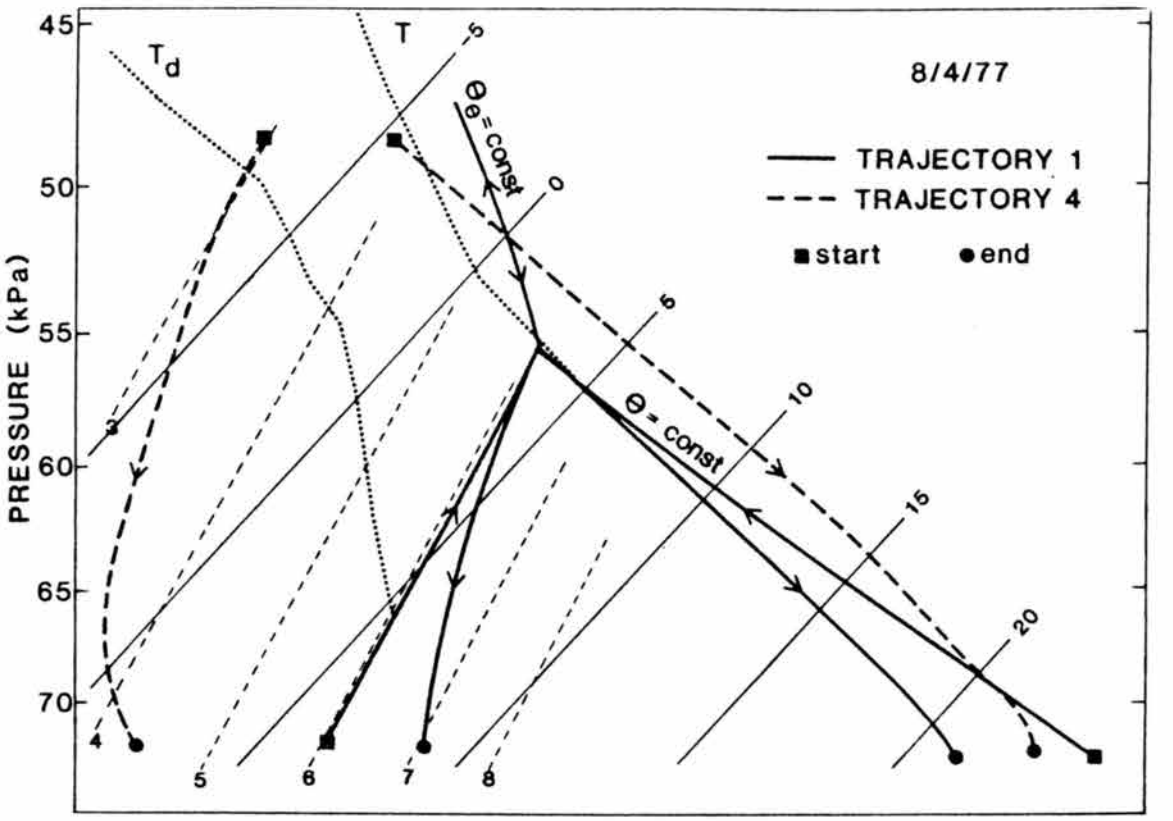

Fig. 4.31. Vertical profiles of temperature and mixing ratio along trajectories 1 and 4 (thin lines). Dotted lines represent 8/4 environmental sounding.

Only a small fraction of air entering the downdraft core from upper levels (5-6 km AGL) reached the surface as did trajectory 3 in Fig. 4.29. Because this air possessed relatively high θ, much of it either reascended to upper levels or descended 1-3 km to intermediate levels. Analysis of thermodynamic variables along trajectory 3 (not shown) indicate a large degree of positive buoyancy over much of its descent. Either this downdraft was overexaggerated in the Doppler analysis (a definite possibility) or greater cloud and precipitation water contents existed within it than were inferred.

The thermodynamic and kinematic nature of air parcels descending within weak reflectivity along the western flank (trajectory 4) is

portrayed in Figs. 4.30b and 4.31. Here, low-valued θ_e air originating near 3 km AGL descended monotonically at rates of 1-3 m/s within 20-25 dBZ echo over a relatively long time period. Figs. 4.30b and 4.31 indicate that negative buoyancy is established only in the lowest kilometer, above which positive buoyancy needs to be overcome by other means. Because loading effects are small here, inferred pressure forces provide this forcing provided that the Doppler derived downdraft speeds are not overexaggerated. The fact that low-valued θ_e air exists at the surface beneath this downdraft (Fig. 4.24) substantiates its qualitative structure, however. The behavior along this particular trajectory illustrates that cooling rates and loading within relatively weak echo (<30 dBZ) are small; therefore, descent rates are necessarily also minimal unless static stability is nearly dry adiabtic. Overall, the qualitative behavior along trajectories 1 and 4 is quite similar to those found for trajectories 2 and 4 in the 7/26 case.

Downdraft core trajectories for the late time period (Fig. 4.29b) reveal a different structure to the core downdraft as indicated above in Fig. 4.28 for the Doppler analyses. Although the up-down downdraft flow branch in the downshear sector is visible here (trajectories 5 and 6), the midlevel flow branch (trajectories 7,8,9) appears to be more pronounced during this time period. All three upshear-branch trajectories initially rise 0.5 to 1.2 km before descending up to 10-12 m s^{-1} within the primary downdraft.

Fig. 4.32b presents measured and calculated values along midlevel trajectory 8 in which relatively moist midlevel air from the 2.7 km level (see Fig. 4.1) rises 1.2 km, with 0.8 km of this ascent being saturated. Condensate loading along this trajectory increases rapidly

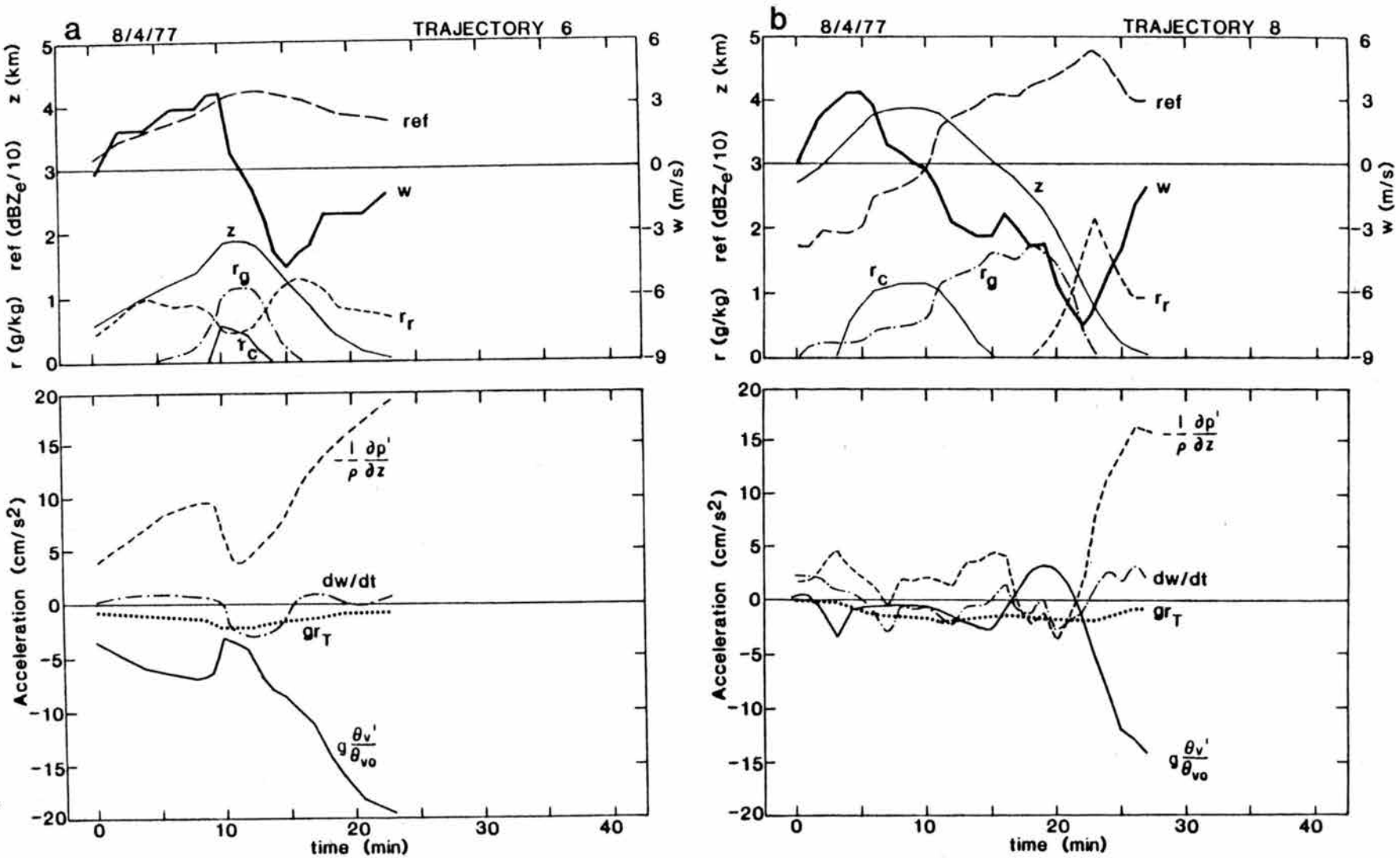

Fig. 4.32. Values along trajectories 6 and 8 plotted in Fig. 4.29b.

as liquid cloud water is condensed and as high reflectivity values (i.e., precipitation mixing ratios) are encountered along the ascending portion of this branch. Although a segment of the descending branch experiences positive total buoyancy ($gr_T + g \frac{\theta'_v}{\theta_{vo}}$) where the air is descending rapidly, most of the descent occurs under negative buoyancy. Note that fastest downward movement occurs within higher reflectivity just below the melting level where graupel melting is significant.

Values along up-down trajectory 6 originating at 0.6 km within the updraft inflow sector (Fig. 4.32a) exhibit similar features to those observed earlier along trajectory 1 with one exception. In this case the initially cooler parcel ascends within higher reflectivity only ~ 20 mb above its SP near 600 mb. Consequently, latent heating effects remain small and the parcel remains significantly negatively buoyant throughout. Forced uplifting from inferred pressure gradient forces is significant here. These patterns would change, however, if the initial negative buoyancy was closer to zero.

Results from a 3-D cloud model simulation revealed features only grossly similar to those observed. Although maximum updrafts of 17 ms^{-1} and maximum downdrafts of 11 ms^{-1} correspond fairly well with the observations, all features of the observed downdraft circulation were not reproduced in the simulation, possibly due to at least two effects: (i) inadequate representation of characteristic precipitation size in the precipitation parameterization and/or (ii) greater PBL moisture present in the model (6.5 g kg^{-1}) as opposed to the observations (6.0 g kg^{-1}). Fig. 4.33 portrays some model output fields through the low-level downdraft core at 4800 s. Because flow within this plane was relatively steady and two-dimensional, flow streamlines may also be

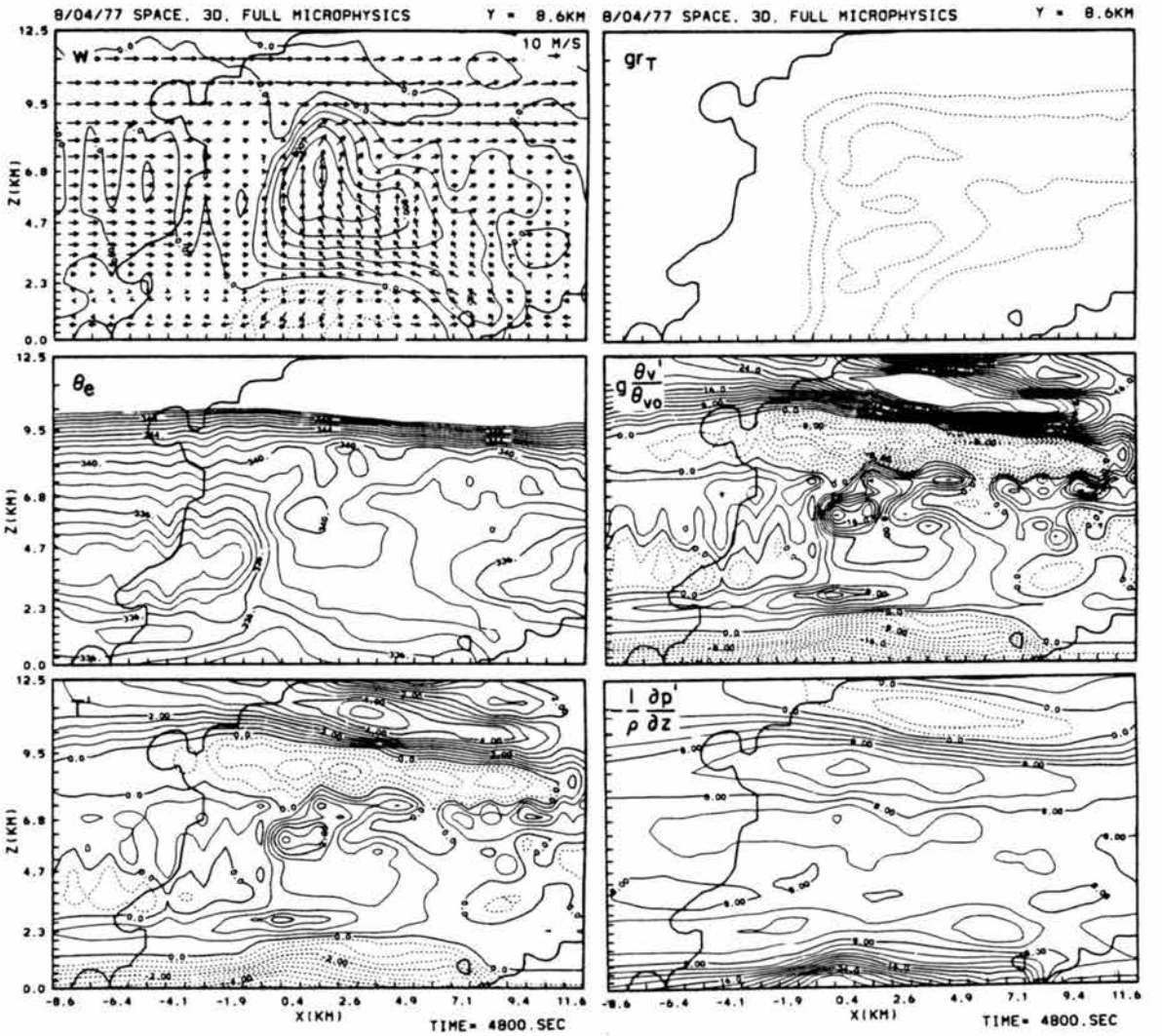

Fig. 4.33. Cloud model output from a simulation using the 8/4 sounding as input conditions. Contours of analyzed fields are as follows: (a) w every 2 m s^{-1}, (b) θ_e every 2 K, (c) T' every 0.5 K, (d)-(f) selected acceleration components every .02 m s^{-2}.

represented as air parcel trajectories. Flow patterns at this time indicate a low-level downdraft nearly colocated with precipitation and centered near 0.9 km AGL, just slightly upshear of the updraft above it. The dominant downdraft branch is anup-down type, similar to the observed structure. However, upshear midlevel downdraft inflow branches common in the latter stages of the observed storm did not appear throughout the course of this simulation.

Another difference between observed and modeled downdraft flow structure stands out by comparing Fig. 4.33 with Fig. 4.28. The simulated downdraft is about 2.3 km deep, nearly half that observed. Both observational and modeling results portray a similar process within the up-down downdraft feed: air forced over the gust front by pressure forces rises, encounters precipitation and then splits, part falling into downdraft and the other segment rising in updraft. The fact that a greater fraction continued to ascend in the simulation is thought to be a result of two effects: (i) greater potential buoyancy present in the model (6.5 g kg^{-1} surface moisture) compared to the observations (6 g kg^{-1})*, and (ii) the inference that smaller-sized precipitation particles existed in the real cloud than were parameterized in the model. The presence of smaller-sized precipitation is supported by the diagnostic model calculations discussed above which produced more consistent results when assumed characteristic precipitation sizes were reduced to 3/4 the standard values. Because small sizes produce increased rates of cooling by melting and evaporation, deeper downdrafts

---

* The cloud model simulation for this case was initialized in a more moist environmental PBL so that an initial cloud circulation could be initiated. A surface mixing ratio of 6 g kg^{-1} failed to generate a precipitating cloud.

would be expected for small-sized precipitation elements. Deeper downdrafts would also be expected for a dryer PBL since reduced updraft buoyancy would increase relative effects of condensate loading.

In combining the 8/4 and 7/26 observational and modeling results, it is hypothesized that the downshear up-down downdraft branch (when it exists) becomes increasingly influential when low-level total buoyancy [$g\ (\theta'_v/\theta_{vo} - r_T)$] within air parcels along this branch is reduced, provided that the pressure gradient force associated with the gust front, or the storm updraft, is sufficient to lift this negatively-buoyant air. Hence, there must be some limiting negative buoyancy at low levels which, if exceeded, would inhibit development or maintenance of the up-down branch. Such reductions in potential temperature (θ) can be accomplished by melting of ice-phase precipitation, by θ reductions from cloud shadowing and precipitation evaporation, or by relative storm movement into more stable air at low levels. The last mechanism may have been particularly important in the 8/4 case in which reduced potential positive updraft buoyancy was accomplished by storm movement into a drier PBL region. Perhaps even more effective is relative storm movement into cold outflow generated by other storms. Such a case occurred during CCOPE on 2 August 1981 in which two intense storms separated by ~50 km coexisted for several hours. The second storm travelled in the outflow wake of the first. A Doppler analysis shown in Fig. 4.34 indicates a well-developed and relatively deep up-down downdraft branch within the downshear updraft inflow sector, the intensity of which was augmented by ingestion of cold outflow air generated by the other preceding storm. Foote and Frank (1983) have also speculated that downdraft outflow air from nearby storms produced

up-down downdraft branches in an intense hailstorm (see branches F and G in Fig. 2.13).

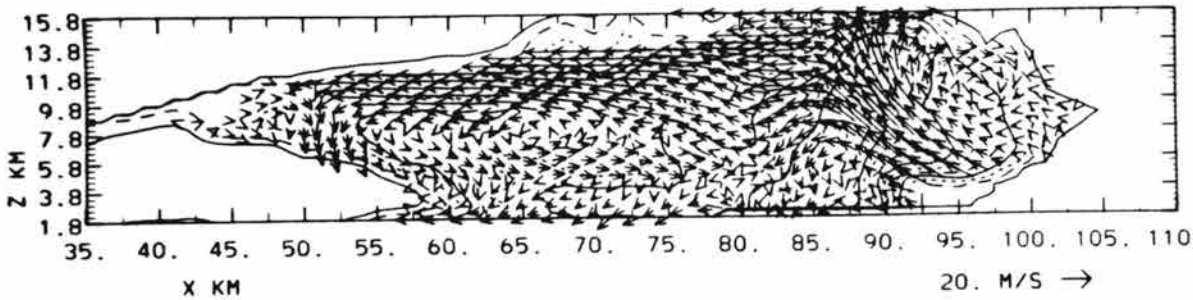

Fig. 4.34. Vertical east-west section through an intense segment of a CCOPE squall line at 2105 MDT, 2 August 1981. Analyzed contours are reflectivity factor contoured every 5 dBZ_e, beginning at 5 dBZ_e. Courtesy of Jerome Schmidt.

The 8/4 case exhibits similarities and differences from the previous 7/26 case. Downdraft flow branches (the up-down and midlevel) and behavior along these branches were similar in both cases. Observations from the 8/4 case, however, indicate deeper and stronger downdrafts even though static stability profiles were similar (see Fig. 4.1). It is surmised that stronger downdrafts were achieved in the 8/4 case because of several effects: (i) greater evaporation rates within a deeper and drier subcloud layer, (ii) smaller inferred characteristic precipitation sizes in the 8/4 case, assuming that smaller particles were produced by weaker updrafts and drier subcloud conditions, and (iii) updrafts and associated total buoyancy were weaker. Although precipitation rates and associated melting rates were probably smaller in the 8/4 case, simple calculations presented in Section 6 demonstrate that increased evaporation rates in drier subcloud layers exceed reduced cooling by melting as PBL moisture decreases.

4.2.2 The 20 July 1977 case

In this relatively unstable, moist and low-shear case heavily precipitating convection generated widespread low-level outflow and surface wind gusts up to 15 m s^{-1} over South Park. Surface analyses (Motallebi, 1982) indicate that strongest winds were associated with reflectivity cores, and that lowest-valued θ_e air was located west (upshear) of reflectivity cores within 20-30 dBZ_e echo.

The downdraft structure observed within individual cells is similar to that in the 7/26 case. Fig. 4.35 displays dual-Doppler derived flow patterns within moderately-intense convection at a relatively early time (1256). Weak downdraft activity prevailed at and below 2 km AGL (Fig. 4.35a) within the upshear reflectivity gradient to the rear of a north-south line of moderately-intense precipitating convection. Stronger downdraft cells were generally located within or just upshear from echo cores. An east-west vertical section through the core of the center-most cell (Fig. 4.35b) reveals a low-level downdraft about 3 km deep located primarily within highest reflectivity. Both up-down and midlevel flow branches converging into the downdraft and reflectivity core near (1,-7) exhibit a general structure and produce vertical excursions of parcels traveling along each branch that are strikingly similar to the 7/26 case. Although the upshear flow branch is more prominent at this time, later Doppler analyses during an intense, more mature stage at 1349 (Motallebi, 1982) indicate a more dominant downshear up-down branch feeding core downdrafts which were essentially colocated with high reflectivity. Such an increasing relative strength in the up-down branch at storm maturity is consistent with the observations and cloud model results from the 7/26 and 8/4 cases.

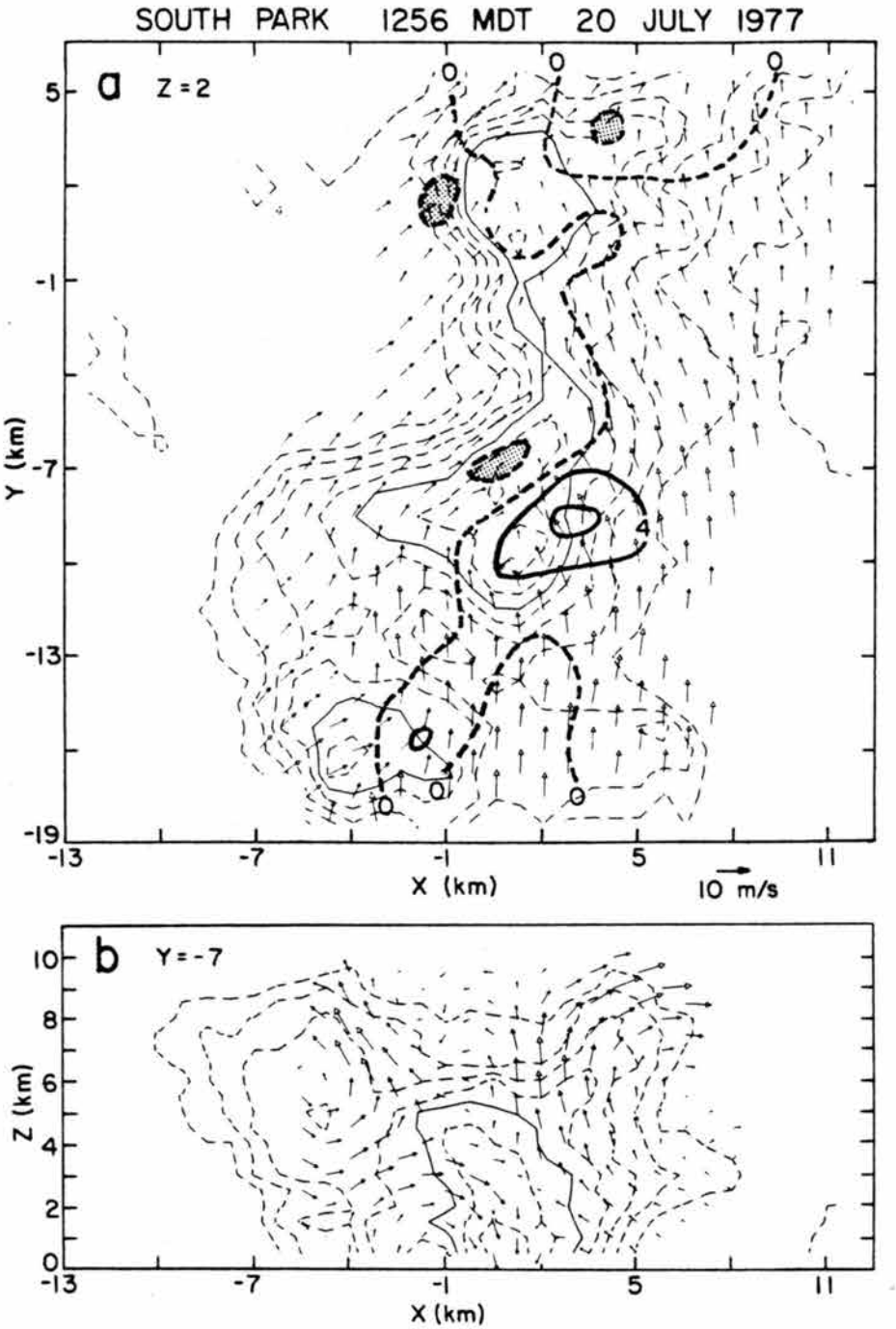

Fig. 4.35. Dual Doppler analysis at 1256 MDT on 20 July 1977. Storm-relative flow patterns are shown at 2 km AGL in (a), and in a vertical section along y = -7 through the downdraft core in (b). Reflectivity factor is analyzed every 5 dBZ_e beginning at 20 dBZ_e in both panels. In panel (a), thick lines are anayzed vertical motion contoured every 4 m s^{-1}. Shaded regions indicate w < 4 m s^{-1}.

4.3 Downdraft Structure in High Shear Cases

The structure of downdrafts within precipitating convection forming in moderate to high environmental wind shear exhibits characteristic spatial structures which differ from those in weaker shear conditions. In three cases presented below, mature storm precipitating downdrafts are more typically located downshear from updrafts. Although downshear downdrafts were also noted in two low shear cases (7/25 and 7/26), they were confined primarily to the midlevel wake region. The following subsections illustrate the spatial structure of downshear downdrafts and further reveal aspects of downdraft dynamics and thermodynamics.

4.3.1 The 12 June 1981 CCOPE case

This case is unique in that downdrafts were weak and downdraft outflow was virtually undetected by surface stations within 10 km of the reflectivity core. Fig. 4.36 portrays surface features and CP-2 radar echo patterns at 1630, a time of storm intensification. Storms of interest are those located along a line directly north of MLS, situated at the coordinate origin. Radar, aircraft and photographic data indicate that storms along this line formed above a boundary layer convergence zone (probably a quasi-stationary frontal zone) around 1530. All storms along the line attained intense levels from 1530 to 1630, but subsequent intense activity after 1630 was confined to the upshear portion as shown in Fig. 4.36. This convectively active upshear region is discussed in the following paragraphs.

General storm structure is classified as multicullular, in which new cells formed primarily on the extreme upshear or southwest flank. Aircraft measurements at cloud base indicated a rather steady updraft peaking at 5-8 m s^{-1} from 1640 to 1740, but analyzed Doppler patterns

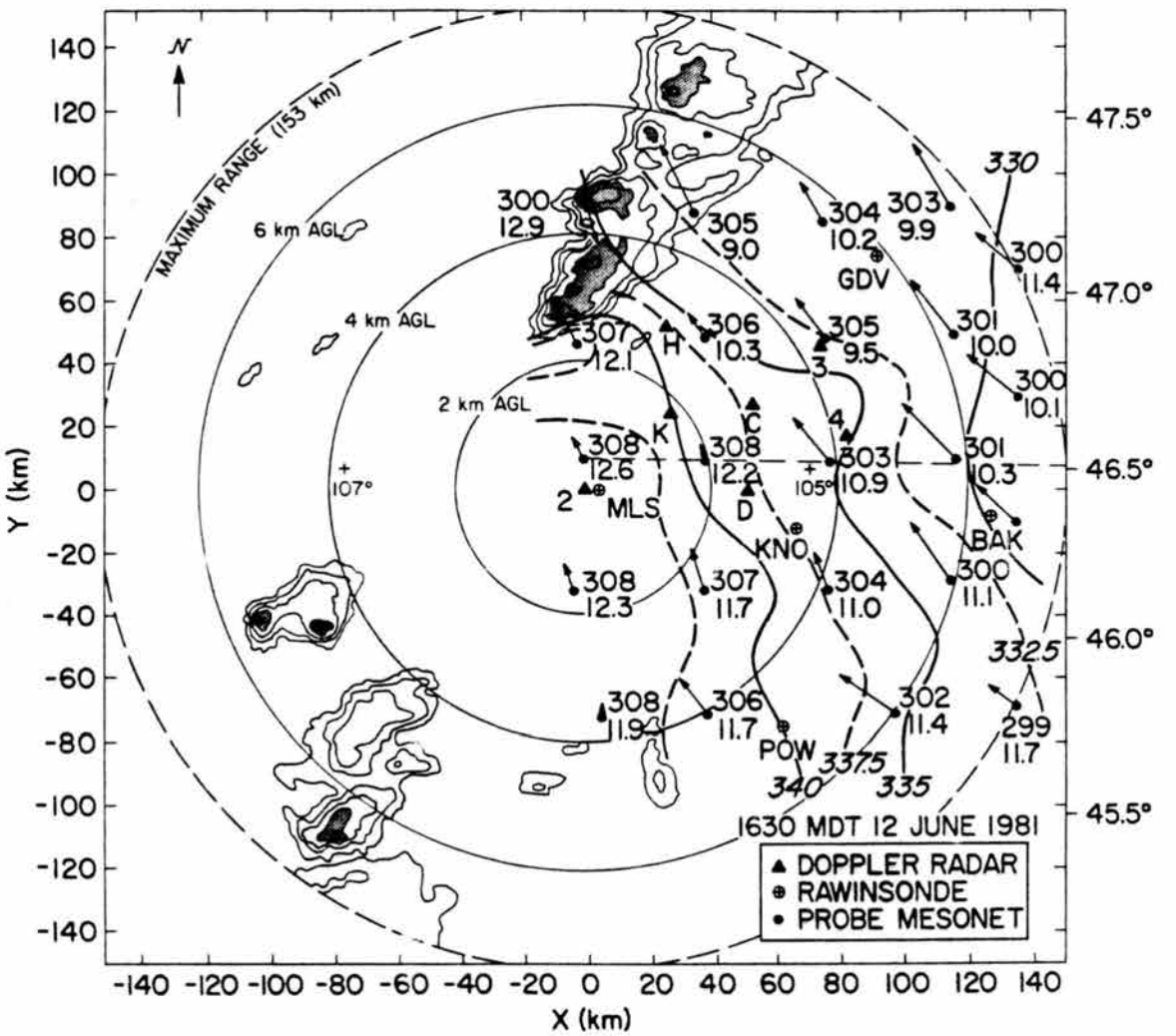

Fig. 4.36. Surface analysis over the CCOPE area on 12 June 1981. Contours are analysis of θ_e. Potential temperature (K) and water vapor mixing ratio (g/kg) are plotted for each station. Radar echoes from CP-2 (located at the origin) are contoured every 10 dBZ_e beginning at 10 dBZ_e (40 dBZ_e and greater is shaded).

show an increasingly unsteady and more cellular structure at higher levels.

Fig. 4.37 presents a time history of maximum raw reflectivity and maximum Doppler-analyzed updrafts downdrafts for 14 time periods. Greatest reflectivity typically found at lower levels exhibits three local maxima exceeding 65 dBZ_e near 1640, 1657 and 1720. Maximum updrafts just over 20 m s^{-1} at 1637 and 1717 slightly precede two of these reflectivity maxima. Maximum downdrafts located in the downshear sector near the 2.8 km level (subtract 0.8 km for height AGL) contrastingly show relatively low and uniform magnitudes ranging between 3 and 5 m s^{-1}.

Fig. 4.38, a plot of updraft and downdraft mass flux profiles for selected times, further exemplifies the scarcity of downdrafts within precipitating storm regions. Analyzed downdraft mass flux maxima reside near 2.8 km (MSL) just above cloud base and decrease with height to background values at 5.8 km. Downdraft profiles exhibit relatively small changes with time, as opposed to updrafts which change significantly in relative magnitude. It appears that downdrafts in this case were influenced by two stable layers, the first being the deep moist adiabatic layer located just above cloud base near 2.8 km and the second being a less significant inversion near 5.8 km (see Fig. 4.1j). Because stable layers act to damp downdraft activity, weak downdrafts would be expected within these regions (provided that the near environment is unaltered by precipitation evaportation), as was indeed observed. The impact of the 2.8 km stable layer on downdrafts is examined in further detail below.

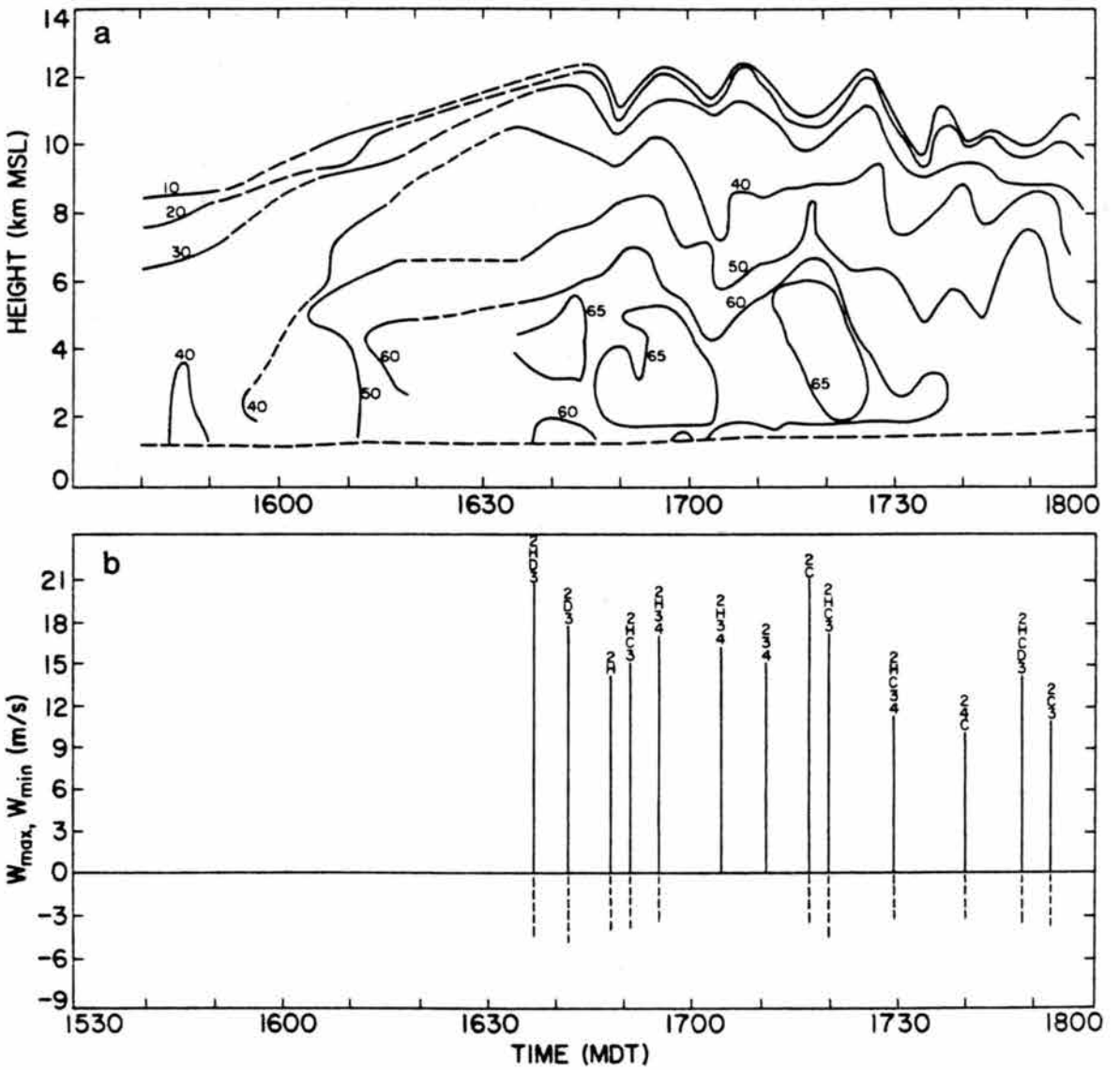

Fig. 4.37. (a) Time vs. height section of maximum raw radar reflectivity measured within the 6/12 storm. (b) Maximum and minimum multiple Doppler-derived vertical motion within the active storm portions. Letters and numbers at the top indicate radars (locations given in Fig. 4.36) used in the multiple Doppler synthesis.

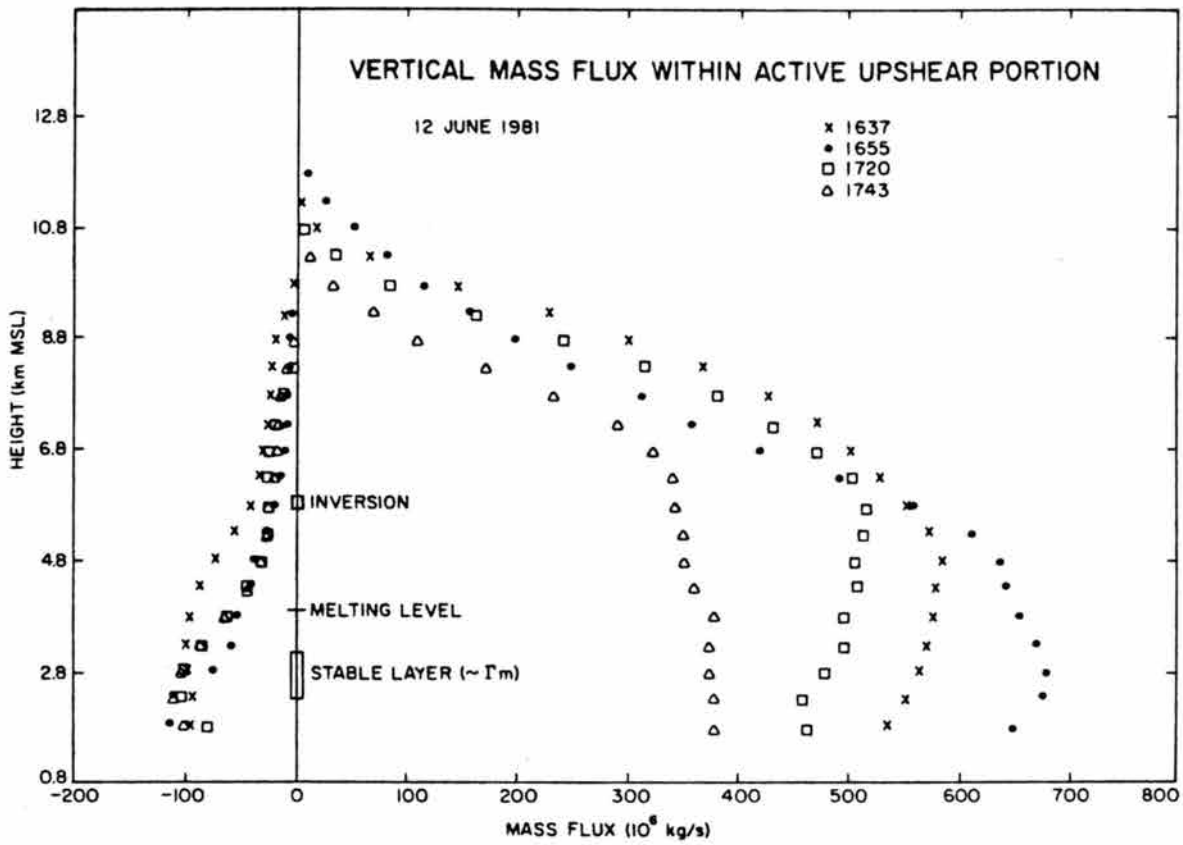

Fig. 4.38. Vertical profiles of Doppler-derived updraft and downdraft mass flux within the convectively-active upshear storm flank. Discontinuities in the profiles between the lowest level (1.8 km) and the surface (0.8 km) are due to accululated errors in w.

General storm structure during an intense storm stage at 1720 is illustrated in Fig. 4.39. At the surface relative easterly flow having θ_e > 340 K feeds updrafts along the upshear flank. Aircraft mappings (Fig. 4.39a) portray several updraft cells (within which θ_e > 340 K) within the updraft inflow sector, generally located south of highest reflectivity. The southwestward extension of weak updraft from the primary core corresponds to the cloud line associated with the boundary layer convergence zone. Only small pockets of downdraft were detected by cloud base aircraft in this region at 1720 and at other times, primarily because the updraft inflow sector was flown, and the

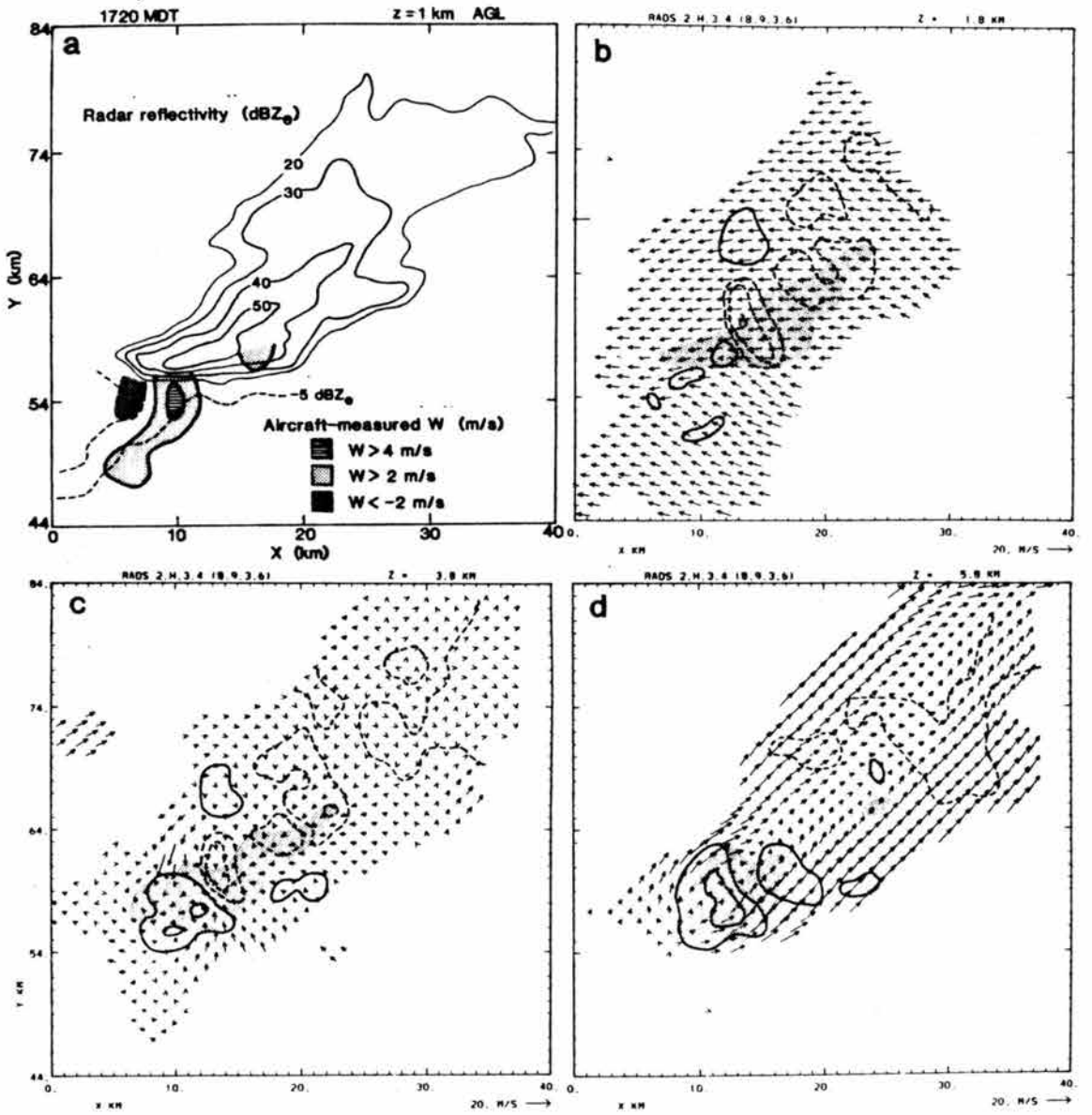

Fig. 4.39. (a) Aircraft analysis at 1.8 km. (b)-(d) Multiple Doppler analyses at 1.8, 3.8 and 5.8 km for the 1720 time period. Airflow is relative to the moving storm. Analyzed vertical motion (m/s) is contoured as follows: 0, -2, -4 are given by dashed lines, and 4,10 are represented by solid lines. Regions having reflectivity greater than 40 dBz_e are stippled.

precipitation core generally avoided. Variations in θ_e from updraft to downdraft were typically < 0.5 K.

The Doppler analysis at 1.8 km (Fig. 4.39b) indicates large regions of updraft within the upshear flank which only grossly reproduce aircraft-measured patterns. Analyzed downdrafts which extend downshear from updrafts exhibit several cells, the first located directly downshear from updrafts being most intense (~ 4 m s^{-1}).

At 3.8 km relative horizontal flow converges into the primary downdraft located directly downshear from the updraft. Weak northeasterly flow within this downdraft and within others further downshear is much weaker than easterly flow found at lower levels. Relative flow patterns higher up at 5.8 km maintain this trend in both updrafts and downdrafts. At 5.8 km downdrafts are considerably weaker and exist only within anvil precipitation extending downwind from the active convective zone. A well-defined wake zone is prominent here and at 3.8 km. A north-south vertical section through the downdraft core presented in Fig. 4.40 indicates a downdraft depth of about 4 km and a maximum speed of 4 m s^{-1} near 2.8 km. As shown here and in Fig. 4.39, horizontal inflow feeds the downdraft from the northeast at 3.8 km, from the northwest above 3.8 km and from the east below 2.8 km.

Doppler analyses at 3.8 km for several other times (1637, 1651, 1705 and 1730; see Fig. 4.41) exhibit similar patterns in horizontal and vertical flow structure. Downdrafts are generally located downshear from updrafts along the northern edge of moderately-high 40-50 dBZ echo. Vertical variation of horizontal flow within the downdraft regions is similar to that described above for the 1720 time period: generally west-northwesterly at 4.8-5.8 km and easterly below 3.8 km. Such a

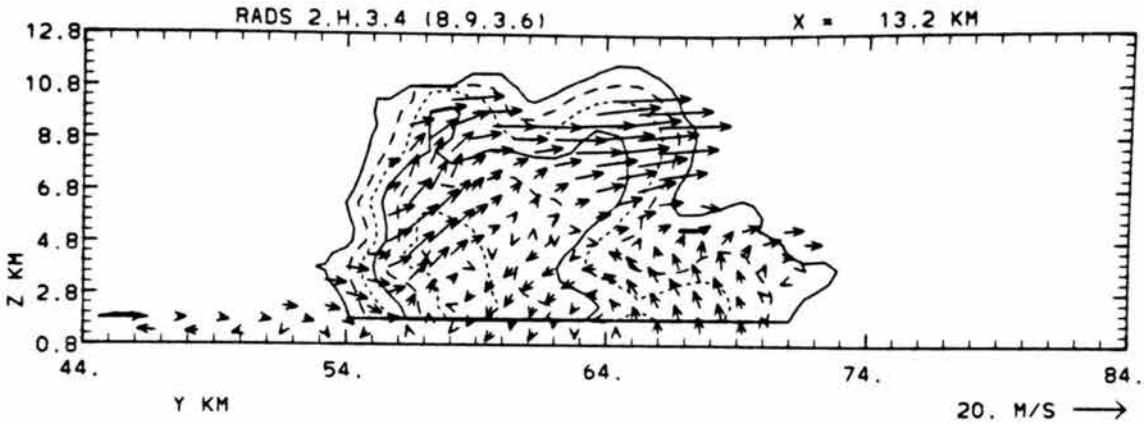

Fig. 4.40. Vertical section along x = 13.2 in Fig. 4.38. Flow is storm relative, and reflectivity factor is analyzed every 10 dBZ_e, beginning at 0 dBZ_e.

vertical shear of horizontal winds throughout the depth of the downdraft has a probable impact on vertical transport within downdrafts as will be demonstrated below.

A number of steady-state air parcel trajectories were constructed from the 1720 velocity data. Some selected trajectories are plotted in Fig. 4.42. Most parcels initialized within the downdraft between the 1.8 and 3.8 km levels moved through the downdraft region without descending to the surface. Some of these, such as trajectory U3 in Fig. 4.42 descended ~ 1 km while moving through the downdraft and then ascended to mid to upper levels within or along the fringes of the primary updraft. Other parcels like U4 entered the northern downdraft edge at 3.8 km and then recirculated within the wake region between updraft and downdraft before finally ascending to an equilibrium level of 7.2 km. Such trajectories would be expected to transport low-valued θ_e air into the wake region because this air probably originated from clear regions just outside the storm. Finally, trajectories entering the downdraft above 3.8 km from the northwest simply descended ~ 0.5 km.

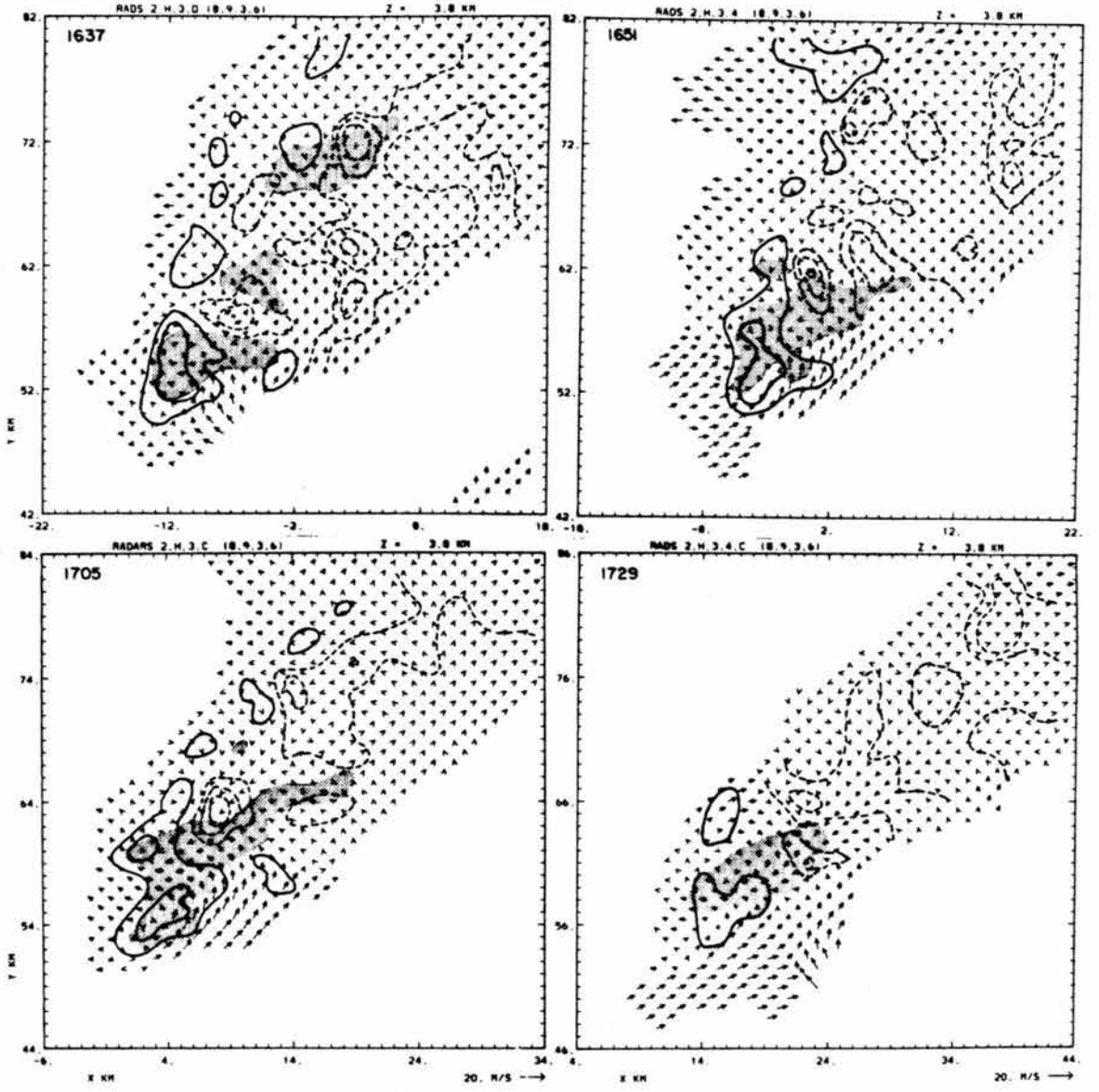

Fig. 4.41. Multiple Doppler analyses at the 3.8 km level for four selected times. Contours are identical to those in Fig. 4.39.

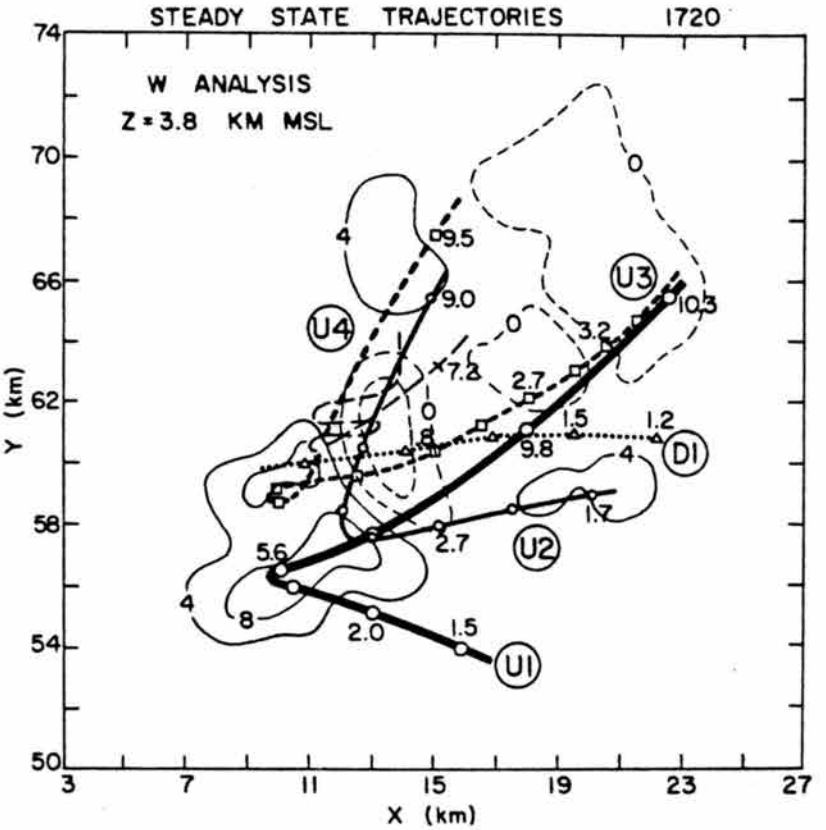

Fig. 4.42. Steady-state air parcel trajectories calculated from the 1720 analysis. Numbers beside tick marks (drawn every 4 min) represent height above MSL (the surface is 0.8 km above MSL). Contours depict analyzed vertical motion (m/s) at the 3.8 km level.

This behavior of trajectories descending only relatively small distances while passing through a much deeper downdraft region (4-5 km in this case) was alluded to above in the 7/26 case (Section 4.1). In both cases total parcel descent within downdraft regions (disregarding buoyancy forces for the moment) is controlled by the magnitude of relative winds within the downdraft, i.e., the instantaneous slope along a parcel path. This total descent can be expressed as

$$\Delta z = \frac{\bar{w}}{(\bar{u}^2 + \bar{v}^2)^{1/2}} \Delta s,$$

where the velocity components are averaged along the parcel path over the downdraft horizontal width Δs. In the 6/12 case strong easterly

flow at low levels near 1.8 km, and strong westerly flow at high downdraft levels near 5.8 km restricted downdraft parcel residence times so that downdraft parcels simply descended ~ 1 km to new (equilibrium) levels.

Only a few air parcels entering the far eastern edge of the primary downdraft at 1.8 - 2.8 km and the downdraft core below 1.8 km descended to the surface. This is consistent with the fact that little downdraft outflow entered the PBL, and that which did (Trajectory D1 in Fig. 4.42) possessed θ_e values typical of PBL air. Trajectories like D1 remain in easterly flow throughout and represent the up-down type discussed above. Thermodynamic values along D1 (not shown) reveal a behavior qualitatively similar to values along other up-down paths presented for previous cases. Here, parcel descent begins near maximum precipitation content just after condensation occurs. Thermal buoyancy and loading remain negative throughout, implying the presence of upward-directed pressure gradient forces as found in other cases.

Another calculation which provides insight on the weakness of downdrafts and lack of downdraft transport from midlevels is given in Fig. 4.43. Here, a hypothetical parcel is assumed to descend at maximum observed downdraft speeds indicated on the right within constant 50 dBZ echo. Kinematic model results indicate that positive buoyancy exists over much of this descent except near 66 kPa and below 84 kPa. The presence of the moist adiabatic layer centered near 73 kPa would actually induce significant deceleration as parcels enter this region and experience increasing positive buoyancy. Such a process explains the shape of downdraft mass flux profiles presented earlier in Fig. 4.38. A similar process may prevent downdrafts from originating much

higher than the midlevel inversion height (5.5 km) indicated in the environmental sounding (see Fig. 4.1j) and in Fig. 4.38.

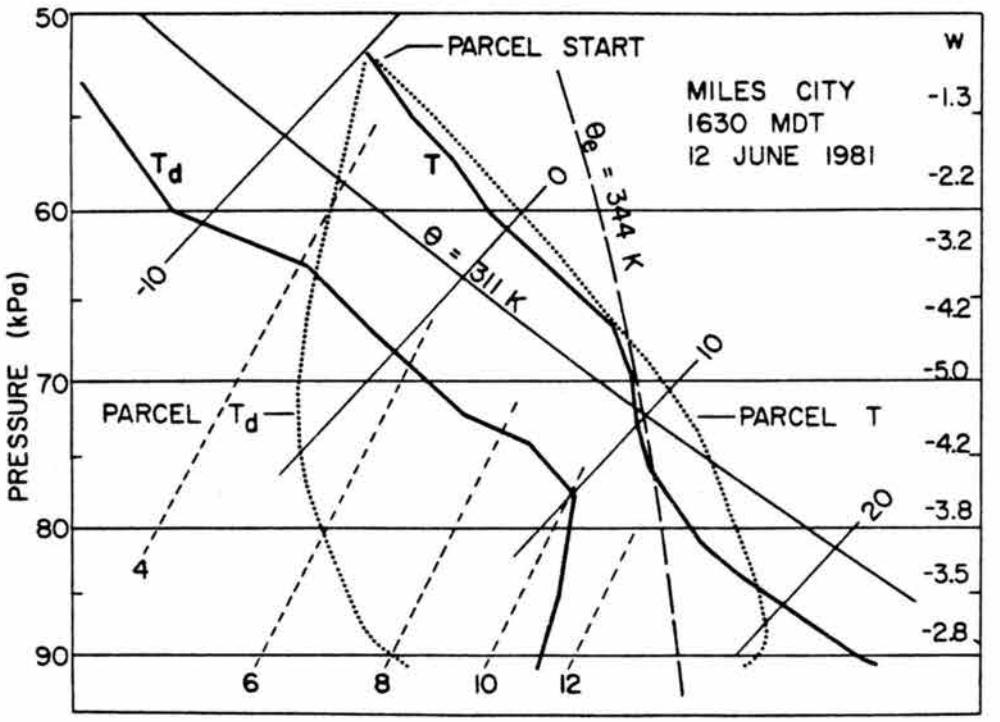

Fig. 4.43. Thermodynamic properties of a hypothetical downdraft parcel originating at 52 kPa and descending at speeds indicated on the far right within constant 50 dBZ_e echo. Heavy lines depict environmental temperature and dewpoint temperature, while thin lines portray parameters within the descending parcel as calculated from the diagnostic model described in Appendix C.

Results from this case indicate that stable layers, particularly deep ones, may act to dampen downdrafts depending on whether or not such stable layers are maintained very near the storm. Subsequent, more intense storm activity within the same region on this day generated stronger downdrafts and accomplished transport of low-valued θ_e air from midlevels (near 4 km) to the surface. This larger-scale storm complex (no Doppler data is available) assumed a more circular structure as opposed to the linear structure of the storm investigated in detail

here. It may be hypothesized that this second storm interacted differently with the environment to produce (weaker) relative midlevel flow patterns more conducive to deeper air parcel displacements within downdrafts as discussed above.

In summary, this case has furthermore substantiated that slopes of 3-D streamlines within downdraft regions exhibits a control on downdraft vertical transport. Downdrafts resided primarily within the downshear flank in this case because inferred mixing within the wake, and precipitation fallout and transport into the wake region of the downshear flank, provided continuous downdraft forcing at low levels. Similar structures appear in the next case study.

4.3.2 The 1 August 1981 CCOPE case

This unstable moderately high-shear case was selected because a series of three intense convective storm complexes over eastern Montana exhibited highly-contrasting downdraft structures. The nature of the differences between the second and third storms is examined in the following.

The first of two storms to be described was an intense and isolated supercell-type hailstorm (hailstones to baseball size) exhibiting peak Doppler-analyzed updrafts to 40 m s^{-1}. A surface analysis during this storm's intense stage (Fig. 4.44a) reveals a slightly reduced but relatively uniform and high-valued θ_e field near heavy precipitation. Diverging surface winds are located primarily northwest of heaviest precipitation. The fact that surface downdraft outflow θ_e remained high during this storm's evolution (90 min old at the time of this analysis) is surprising considering the degree of environmental static instability in the lowest 5 km (see Fig. 4.1). Only small amounts of evaporation

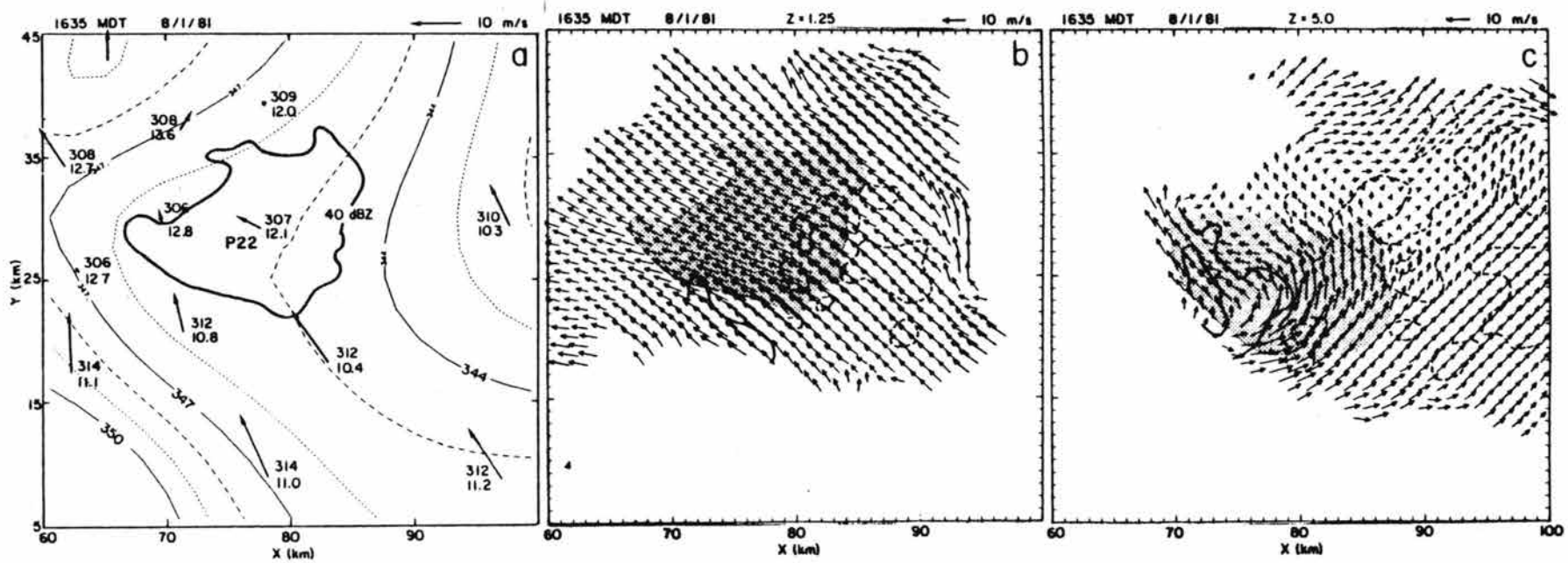

Fig 4.44. Surface and multiple Doppler radar analysis for storm A at 1635, 1 August 1981. (a) Objective analysis of θ_e, contoured every 1 K. Plotted station parameters are (θ, r_v), and station winds are ground relative. (b) Multiple Doppler analysis at 1.25 km MSL. Flow is storm relative, and vertical motion contours are drawn for -4, -2, 10, 20 m/s. Stippling denotes 40 dBZ echo. (c) Same as (b) except for 5.8 km MSL.

would theoretically be required to drive strong downdrafts in such an environment, as Betts (1984) has determined for this case.

Doppler analyses at 1.25 km MSL (subtract 0.8 km for height AGL) shown in Fig. 4.44b reveal a relatively uniform and strong (~ 20 m/s) east-southeasterly relative flow which exhibits weak divergence within and northwest of the precipitating region. Analyzed downdrafts located within the downshear (eastern) flank are weak and patchy. Significantly more horizontal wind structure is seen in the 5.0 km analysis (Fig. 4.44c), where analyzed downdrafts also exhibit a weak and nonuniform structure. Strong horizontal cyclonic flow into the southwest storm quadrant is apparently transporting significant amounts of low-valued θ_e air into the downshear wake above low-level precipitation, but downdrafts remain surprisingly weak. This and the fact that low-valued θ_e air does not reach the surface implies that rates of evaporation within this inflow branch are small, perhaps because precipitation probably consisted of large particles such as hailstones.

In combining the Doppler and surface analyses, the following scenario can be formulated. Precipitation produced within and adjacent to the strong updraft located within the upshear flank is transported from the updraft fringes basically downshear. Some of the larger precipitation particles fall out into strong midlevel inflow flanking the eastern updraft border, and are then transported northeastward to the low-level precipitation core. Because this precipitation is inferred to be large, cooling rates are small and hence little low-valued θ_e air descends within precipitation. Moreover, the strength of this inflow jet yields short residence times within favorable downdraft regions, and jump downdraft trajectories (i.e., those which descend a

fraction of the total downdraft depth) discussed in the previous subsection are inferred (no trajectories were calculated). Relatively weak up-down downdrafts are apparently produced at low levels within strong southeasterly flow. These downdrafts were then simply advected by southeasterly flow to the northwest flank where greatest surface divergence was measured.

A saturation point (SP) time series from station P22 located within high reflectivity at 1635 (Fig. 4.45a) indicates a prominent evaporation level (EL) structure from 1545 to 1640, during which θ fell by ~ 8 K and θ_e rose slightly. This structure, along with the presence of weak low-level divergence (Fig. 4.44a,b) implies that downdrafts reaching the surface were relatively shallow and characteristic of the up-down type with probable origins from the southeasterly PBL flow southeast of the storm.

A three-dimensional cloud model simulation initialized with the observed sounding (Fig. 4.1i) produced downdraft characteristics quite different from those observed. Although characteristic graupel sizes were doubled from the standard 0.1 cm size for this simulation (but still much smaller than characteristic sizes of the observed large hail), strong low-level downdrafts (up to 14 m/s) formed upon arrival of precipitation within the downshear flank at low levels. (This simulation is described more fully in Section 5.2.) Strong outflow and vertical transport of low-valued θ_e air from near 4 km were associated with these downdrafts. These results support the hypothesis that large particles, such as hail, generated small cooling rates and hence relatively weak downdrafts. This, combined with the strength of

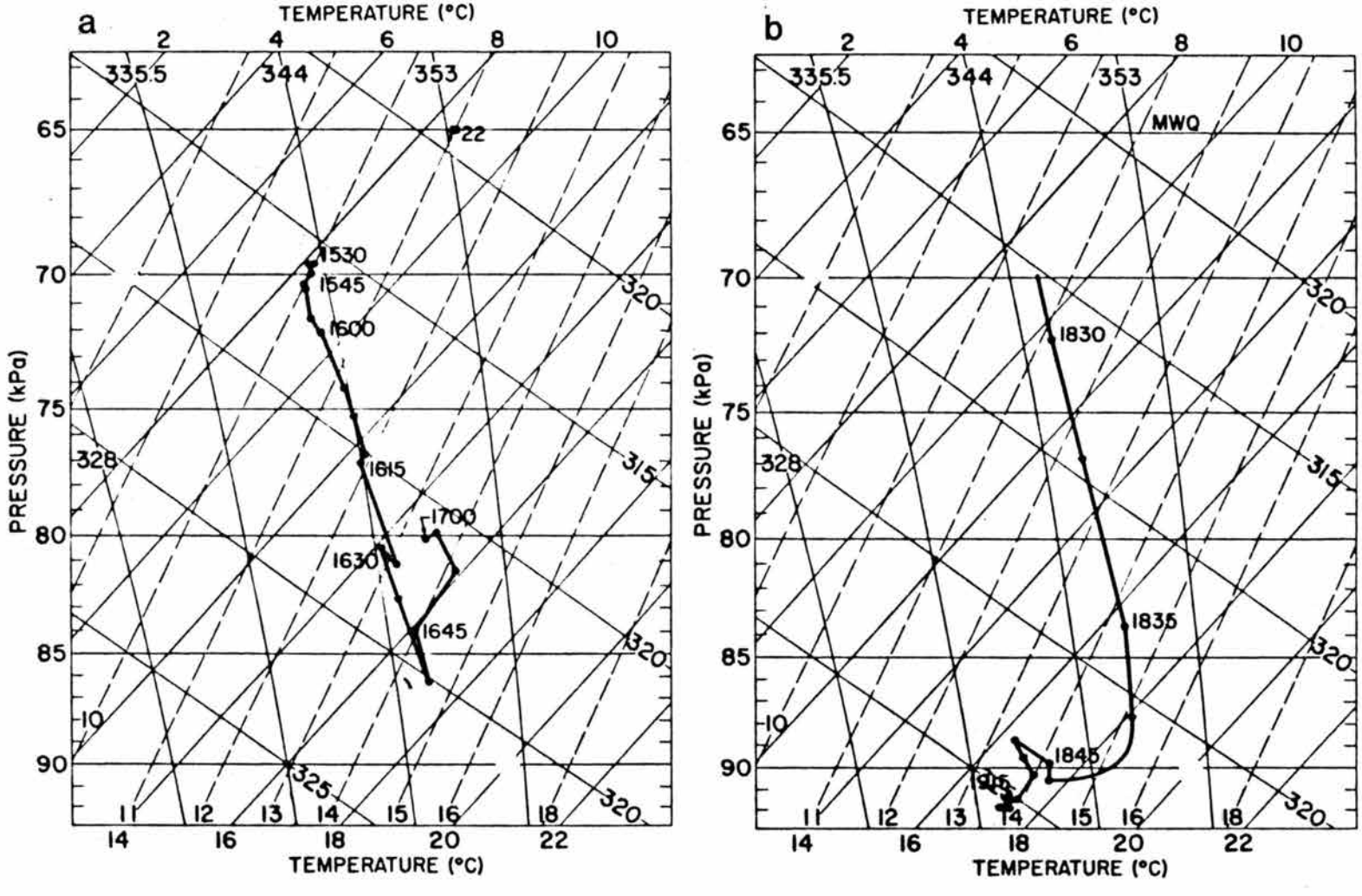

Fig. 4.45. Saturation point time series plots for stations P22 and MWQ. Points are plotted every 5 min.

horizontal flow through the downdraft region may explain the observed lack of low-valued θ_e transport to the surface.

The structure of a second storm observed two hours later exhibited completely different properties, including widespread downdrafts and low-valued θ_e air at the surface. Shown in Figs. 4.46 and 4.47, this

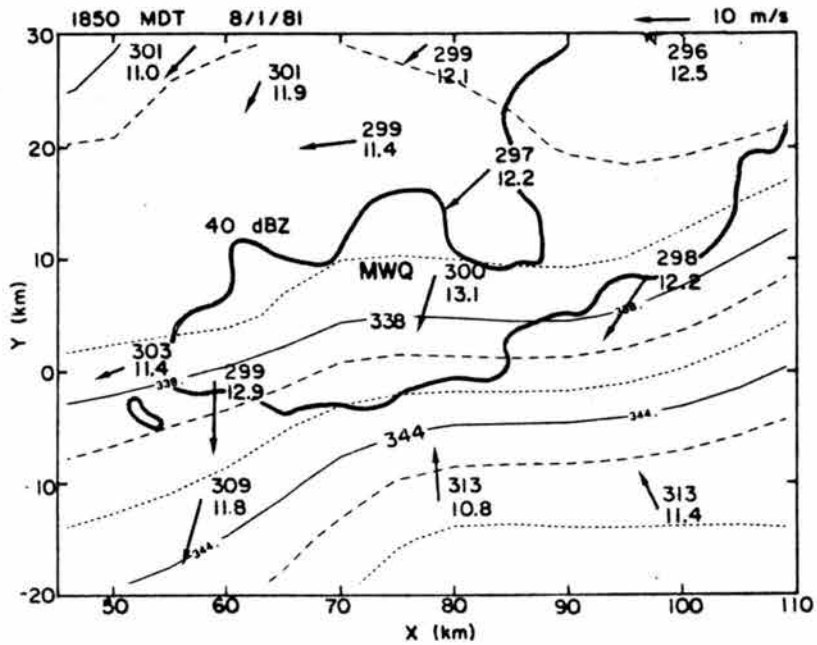

Fig. 4.46. Surface analysis as in Fig. 4.44a for storm B at 1850.

storm consisted of a line of cells, some containing updrafts greater than 30 m s^{-1}. This line extended west-southwestward from a developing larger-scale convective system and exhibited well-formed anvil cloud and precipitation extending upshear and downshear along the rear and forward flanks.

A surface analysis (Fig. 4.46) portrays large regions of low-valued θ_e air along the rear (north-northwestern) flank associated with divergent winds from downdrafts. The Doppler analysis at 2.75 km (the lowest level available) in Fig. 4.47a depicts strongest downdrafts of ~ 6 m s^{-1} associated with some of the reflectivity cores, particularly

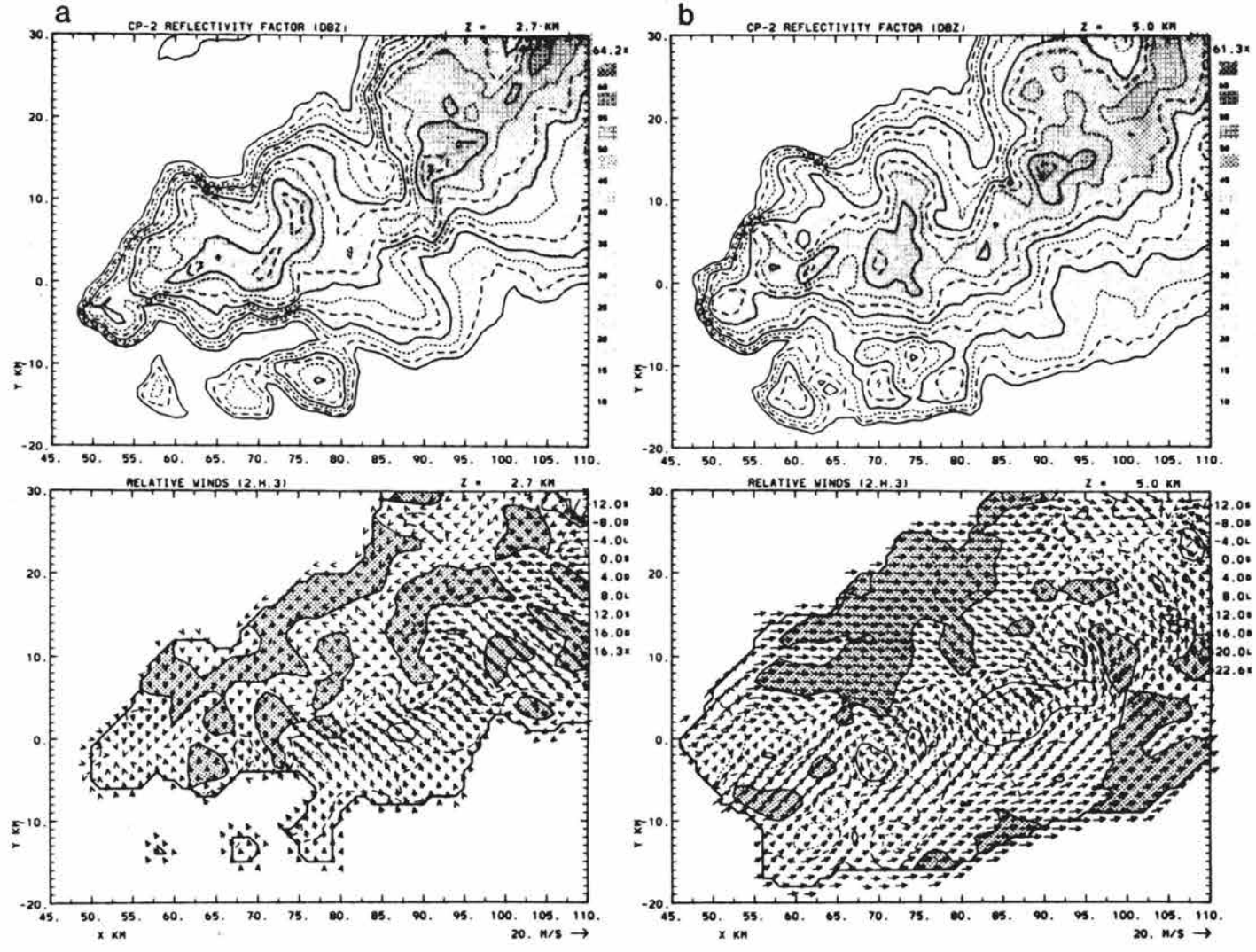

Fig. 4.47. Multiple Doppler radar analyses for storm B at levels of 2.75 and 5.0 km MSL. Upper panels give analyzed reflectivity factor contours every 5 dBZ_e, beginning at 10 dBZ_e. Lower panels show storm-relative flow and analyzed vertical motion, contoured every 4 m/s. Downdraft regions are stippled.

those regions associated with strongest surface divergence near the location (90,15). Weaker and more uniform downdraft activity is located along the rear reflectivity gradient. This broad downdraft area located along the rear storm flank is more widespread and associated with strong westerly inflow of low-valued θ_e air at 5.0 km (Fig. 4.47b). An east-west vertical section through this downdraft and an adjacent precipitation downdraft to the east (Fig. 4.48) reveals the shallow

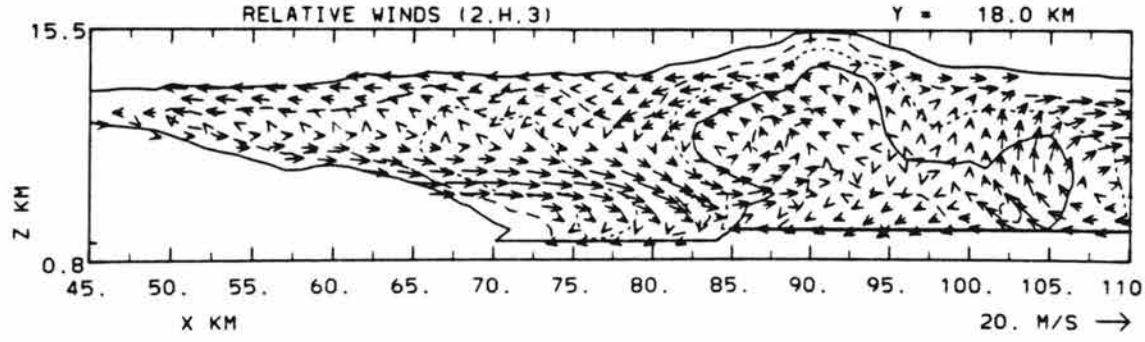

Fig. 4.48. Vertical east-west section along y = 18 in Fig. 4.46. Reflectivity factor is analyzed every 10 dBZ_e, beginning at 10 dBZ_e.

depth of this inflow jet and the extent of the rear flank anvil. Strong westerly relative flow entering the 4-5 km level encounters anvil precipitation and descends to the surface. Flow within the precipitating downdraft located near y = 95 (Fig. 4.48) appears to be of the up-down variety, entering from the southeast, rising within weak updraft and then descending into the precipitation core.

The structure of a SP time series from station MWQ (location given in Fig. 4.45b) indicates an initial EL structure persisting for ~ 5-10 min after gust front passage. This is followed by a quick leftward shift to a new EL around an average θ_e of 336K, typical of θ_e at the surface behind the line.

Updraft and downdraft mass flux profiles for each storm presented in Fig. 4.49 show a dominance of updrafts over downdrafts as was the

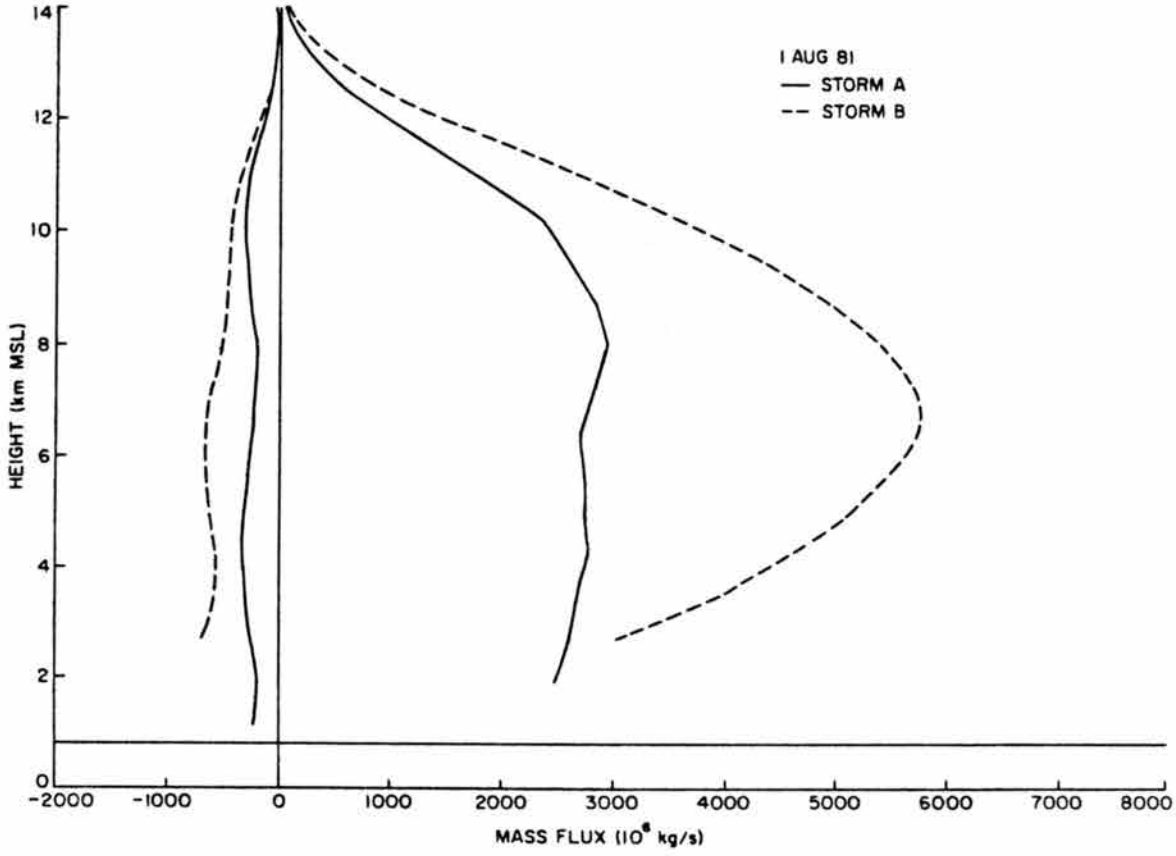

Fig. 4.49. Updraft and downdraft mass flux vertical profiles within storms A and B on 1 August 1981.

case for 6/12. Analyzed low-level downdraft activity within storm A is particularly low. Two minor peaks occurring near 4 and 10 km are inferred to be associated with cloud edge and overshooting downdrafts, respectively. The profile within B, however, indicates that downdraft fluxes peak at low levels and secondarily at middle levels near 6 km.

Differences in downdraft structure observed in each storm are attributed to variations in general storm kinematic structure. The following attributes are hypothesized to account for these differences.

a) Storm A contained a greater fraction of large particles (hail). Therefore, cooling rates by evaporation and melting were less.

b) Storm A exhibited stronger low-level relative flow which limited parcel residence times within potential downdraft cooling regions. Parcel excursions in downdrafts were therefore small.

c) Storm A lacked an extensive upshear anvil that was prevalent in B. As a consequence, rear flank downdrafts were absent and systematic downward transport of low θ_e air did not occur.

This case has brought out the potential importance of precipitation size in controlling cooling rates and downdraft magnitudes. A "rear-flank downdraft" driven by evaporation of anvil precipitation was also documented.

4.3.3 Other cases

Two well-documented moderate-shear cases occurring over northeastern Colorado during the 1976 National Hail Research Experiment are briefly described here. In each case convective activity possessing strong updrafts and downdrafts generated appreciable cold outflow at low levels.

In the moderate shear case of 22 June 1976 (Miller and Fankhauser, 1983), very large amounts of precipitation (rain and hail) and surface outflow winds up to 30 m s^{-1} were produced from a complex of intense thunderstorms. A representative sounding for this case (Fig. 4.1h) indicates a relatively deep boundary layer capped by an unstable and moist middle layer. The deep and nearly dry-adiabatic layer extending from the surface to near 50 kPa provided an environment ideal for deep

and relatively strong downdrafts which appeared in multiple Doppler radar analyses, and which were indicated by surface mesonet analyses.

Storm downdraft characteristics during an intense stage at 1625 are presented in Figs. 4.50 and 4.51. At the surface, outflow air 15-20 K

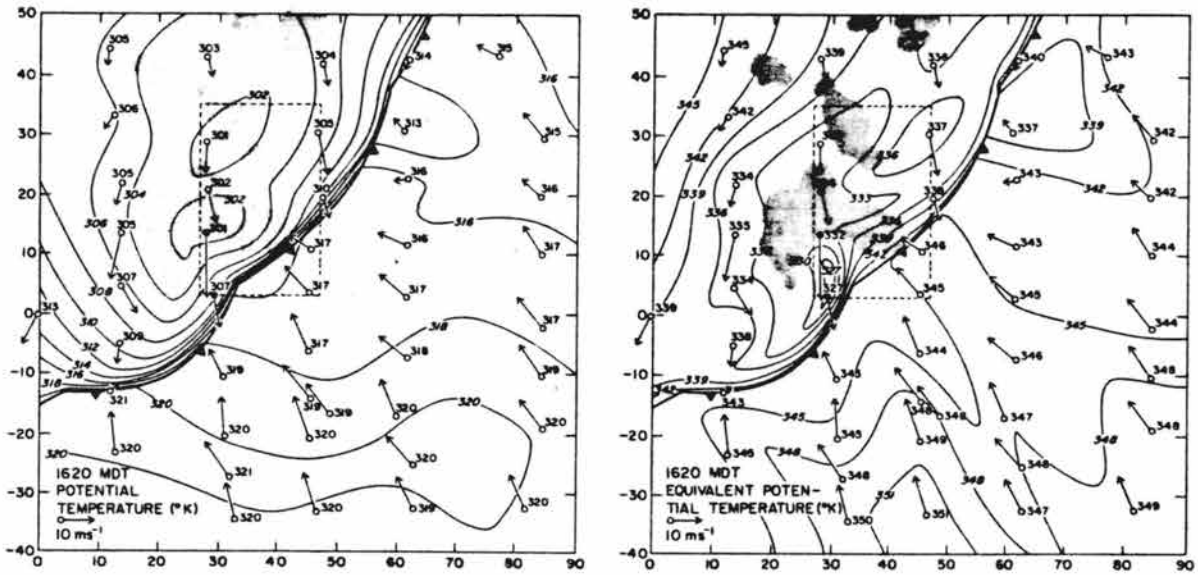

Fig. 4.50. Surface objective analyses of θ (left) and θ_e (right) at 1620 on 22 June 1976. Stippled regions indicate cloud base reflectivity factor of 35 dBZ_e or greater. Taken from Fankhauser (1982).

colder than undisturbed values was associated with downdrafts located within high reflectivity. Surface θ_e values of 333 K, typical of environmental values in the 4-7 km AGL layer (Fig. 4.2h) indicate that downdraft air descended quite large vertical distances in this case. A multiple Doppler radar analysis at 4 km MSL (2.6 km AGL) near cloud base (Fig. 4.51a) shows downdraft activity most pronounced within precipitation downstream from intense updrafts located along the southern flank. Note that horizontal flow associated with this downdraft region near (27,15) is largely convergent, a feature also noted at similar relative levels in previous cases. Similar horizontal flow patterns associated with weaker downdrafts were analyzed at 7 km

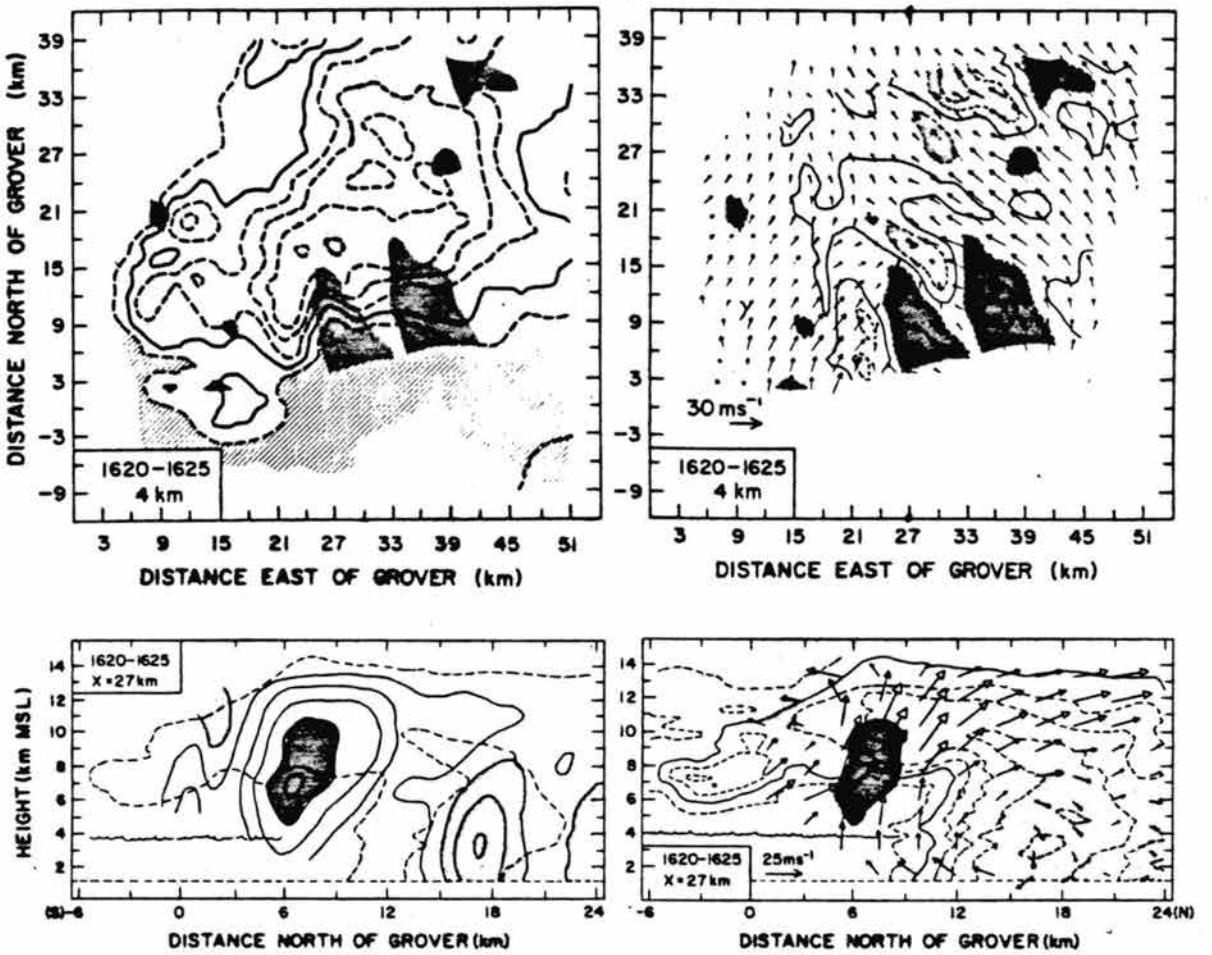

Fig. 4.51. Triple Doppler radar analyses at 1620, 22 June 1976 (NHRE). (a) Horizontal section at 4 km MSL (2.5 km AGL) showing reflectivity factor on the left (10 dBZ$_e$ intervals, 20 dBZ$_e$ solid) and analyzed vertical motion on the right (7.5 m/s intervals, zero contour solid). Dark shading denotes updraft > 7.5 m s^{-1}, light shading denotes downdradts < 0. (b) North-south vertical along x = 27 showing vertical motion on left and reflectivity factor on the right. Contour intervals are identical to those in (a), except that dark shading portrays updrafts > 30 m s^{-1}. Taken from Miller and Fankhauser (1984).

(MSL). Other analyzed downdrafts at 7 km were located downshear (east) from intense 30 m s^{-1} updrafts, rather than downstream (north, with respect to low-level flow) from updrafts. A similar structure with low-level downdrafts located downstream from updrafts, and midlevel downdrafts (separate from those at low levels) located downshear from updrafts was noted in the 7/26 case.

A vertical section through the downdraft core (Fig. 4.51b) shows a strong downdraft within the reflectivity core (analyzed speeds to 15 m s^{1-}) extending from the surface to ~ 8 km MSL. This upper-limiting height nearly matches the top of the unstable layer (Fig. 4.1) and is consistent with the surface θ_e analysis presented in Fig. 4.50. Comparison of Figs. 4.50 and 4.51 reveals that lowest surface θ_e was nearly colocated with the downdraft and reflectivity core.

Results from this case verify features inferred in previous cases. Precipitation-associated downdrafts up to ~ 15 m s^{-1} and total cooling of surface outflow air up to 19 K were particularly high in this case because of strong cooling rates (melting and evaporation) and significant loading occurring within very heavy precipitation in the presence of a deep low-level unstable layer. Interestingly, the patterns shown for this case differed appreciably from the 8/1 case A which exhibited similar environmental low-level thermodynamic structure (see Fig. 4.1). These differences may be attributed to differences in characteristic precipitation size in each case.

Another moderate shear case (7/22) similar in many respects to the previous 6/22 case is documented in Foote and Wade (1982), Foote and Frank (1983), and Heymsfield and Musil (1982). As in the 6/22 case, Doppler-analyzed downdrafts were nearly colocated with maximum

reflectivity. Surface analyses indicate total cooling within downdraft outflow of about 10 K. A representative environmental sounding presented in Fig. 4.19 shows a nearly dry adiabatic layer extending from the surface to 53 kPa. Strongest downdrafts would therefore be expected primarily below ~ 5 km.

Multiple Doppler radar analyses indicate that downdrafts were generally located within high reflectivity at low to middle levels downstream from powerful 30 m s^{-1} updrafts. A summary of downdraft trajectories computed from multiple radar data shown in Fig. 4.52 (see also Fig. 2.13) portrays several branches from low to middle levels converging into the low-level reflectivity core. Middle level (~ 6 km) trajectories B and C approach from the west and either enter the downdraft directly within westerly flow (C) or pass around the updraft to the south and east before entering the downdraft region. Other low-level trajectories (A,D) which represent up-down downdrafts enter the system near cloud base, ascend slightly within weak updraft and then descend to the surface within the primary downdraft. These trajectories, although generally similar to those constructed for the 7/26 case, apparently descend more quickly from higher levels because a deeper unstable layer existed in the 7/22 case.

4.4 Summary

In previous subsections downdraft structure within mature precipitating convection was elucidated with analyses of observational data (primarily Doppler radar) and cloud model results. Characteristics of two downdraft types defined in Section 2, the precipitation-associated low-level downdraft PR, and the cloud edge downdraft L located at midlevels, were discussed in considerable detail. For both

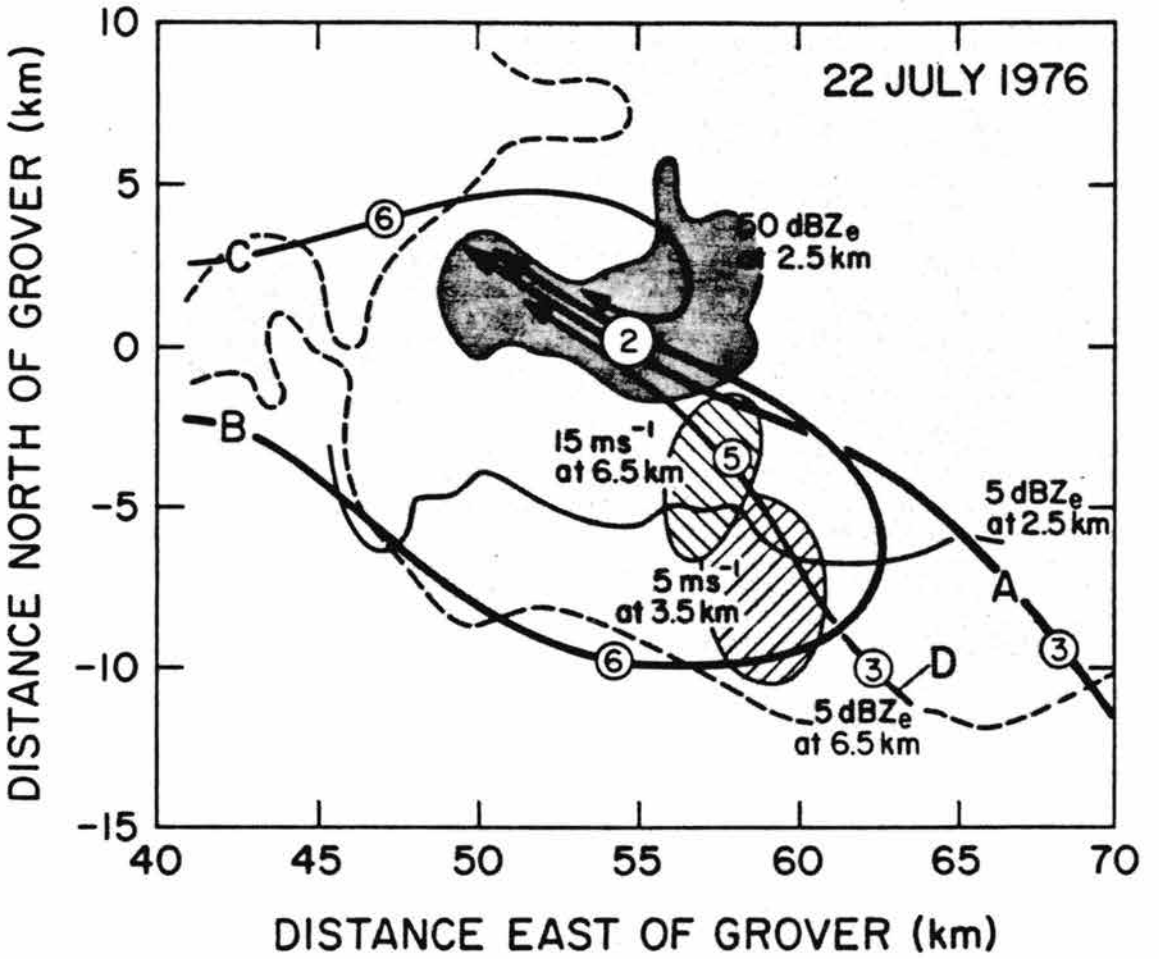

Fig. 4.52. Plan view indicating several downdraft trajectory branches for the 7/22/76 NHRE case. Paths A, B, C and D converge into the region of high reflectivity as they descend to low levels. Circled numbers denote approximate height in km MSL. (Subtract 1.5 km for height AGL). The updraft cores at 3.5 km and 6.5 km are hatched as shown. Taken from Foote and Frank (1983).

low- and high-shear cases the midlevel downdraft commonly appeared within the downshear flank wake region. In some cases (e.g., 7/22, 7/26 - see Fig. 4.53) this downdraft was independent of and totally removed from downdraft PR. Under higher shear conditions, however, midlevel downdrafts were observed directly above low-level downdrafts within the downshear flank. Evaporational cooling from mixing of subsaturated environmental air with cloud and precipitation serves as the primary forcing mechanism for the midlevel wake downdraft. Precipitation particles, particularly small ones, are effectively transported to the wake region by flow around updraft edges, and by fallout from weak updraft regions above.

The low-level downdraft PR is often composed of two general branches, one termed an up-down branch originating within the PBL, and the second a midlevel branch arriving from the relative upwind direction above the PBL. These are illustrated in Fig. 4.53 for the 7/26 case. Air mass fluxes associated with the up-down branch may be considerable during mature phases, possibly much larger than fluxes associated with the midlevel branch as in the 7/26 case. Air parcels traveling the up)-down branch usually originate within the downshear updraft inflow sector and may rise up to ~ 4 km before descending within the precipitation-laden primary downdraft region. Both Doppler analyses and cloud model results indicate that mixing occurs near the summit between air of this branch and lower-valued θ_e air flowing along the midlevel branch. Such mixing produces subsaturated, intermediate-valued θ_e air which in turn promotes increased evaporation rates along the descending portion of this branch. The relative magnitude of air mass flux along the up-down branch appears to be proportional to the stability of air

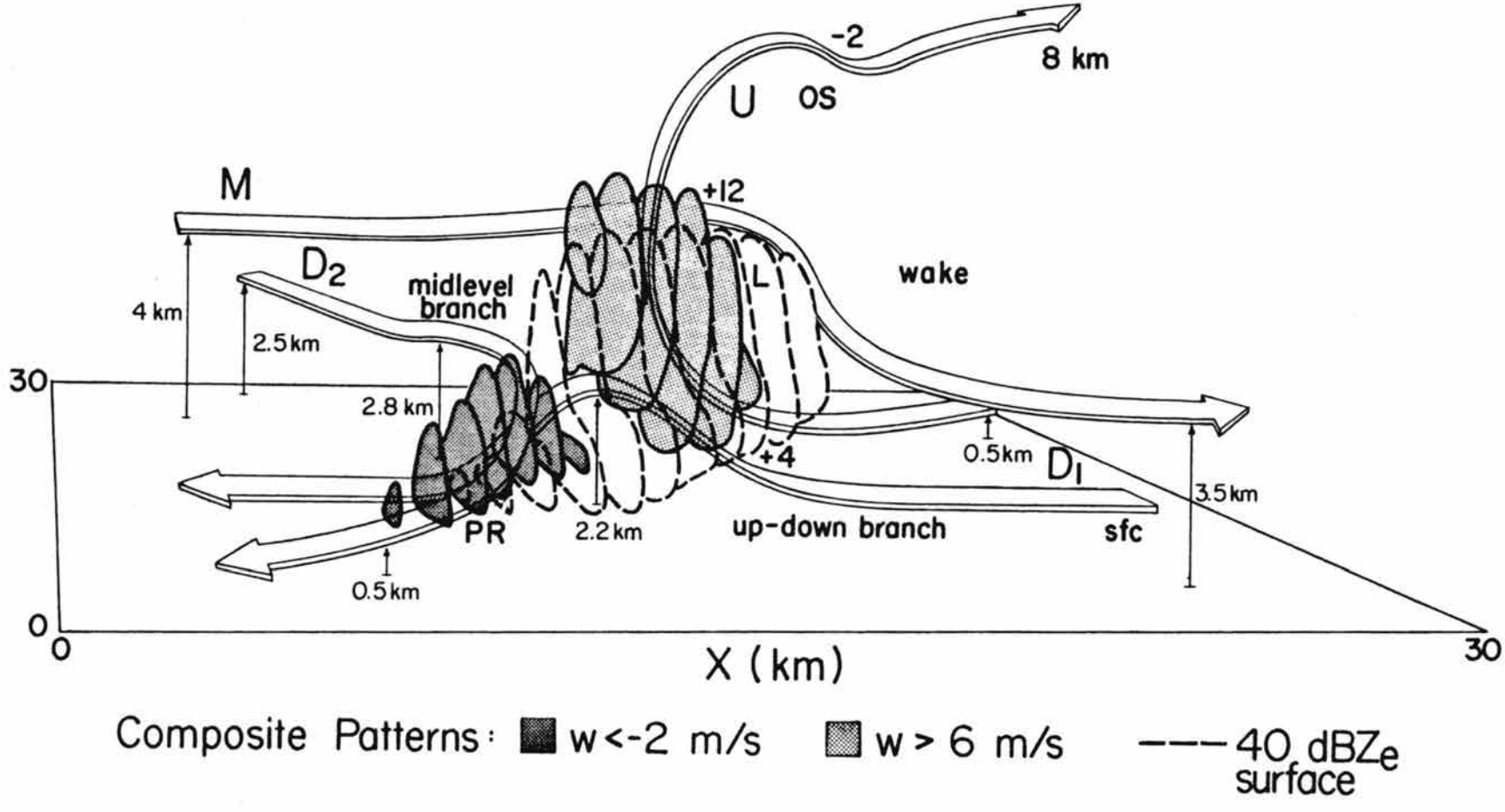

Fig. 4.53. Conceptual model of major downdraft flows (defined in text) within storm A on 7/26/77. Three-dimensional surfaces indicate three fields: reflectivity factor greater than 40 dBZ_e (dashed contours), updraft greater than 6 m s-1 (solid contours, light stippling) and downdraft less than -2 m s-1 (solid contours, heavy stippling).

entering this branch. Observational and modeling evidence indicates that stable air at low PBL levels may more effectively produce up-down type trajectories, primarily because "negative area" (negative potential energy) below the level of free convection of such parcels is larger. This downdraft branch therefore becomes more pronounced during mature storm stages when temperatures of the low-level inflow are reduced by one or more of several processes: (i) cloud shadowing, (ii) evaporation and/or melting of precipitation falling into the inflow sector, and (iii) ingestion of rain-cooled air downdraft produced by outflow air of other storms.

Flow along the midlevel branch transports low-valued θ_e air to regions near the up-down branch where mixing occurs, and more directly to the surface. Descent rates depend on static stability [or, more accurately, the difference level $\Delta\theta_v = \theta_v$ (midlevel) $- \theta_v$ (PBL) where θ_v is virtual potential temperature], of surrounding air at the origin level. For moderately stable conditions ($\Delta\theta_v \gtrsim 3$ K) descent rates tend to be small (1-3 m s^{-1}) as in the 7/26 and 8/4 cases. However, for unstable, nearly dry adiabatic lapse rates ($\Delta\theta_v \lesssim 2$ K), downdraft speeds may exceed 5 m s^{-1} (e.g., the 7/22 case). In general, greater stability of air feeding this branch produces slower descent rates. The upper-limiting height of air along this branch appears to be the T (transition) level where environmental temperature structure turns absolutely stable (see Fig. 4.1). This transition between updraft and downdraft flows is especially striking in the cloud model results.

General airflow and trajectory patterns within low-level downdrafts are convergent within the upper downdraft portions from ~ 0.8 km AGL upwards to near the T level. Because mass flux profiles typically

increase sharply below the melting level, the concept of distinct downdraft inflow levels (as defined above for convenience) is not strictly correct. Rather, downdraft inflow is continuous with height, particularly along the midlevel flow branch. The increasing downdraft mass flux to some point below cloud base (~ 0.8 km AGL) is a combination of increasing downdraft area and downdraft speed. Such patterns indicate that strong cooling from melting and evaporation within the unstable PBL draw air horizontally into the circulation via generation of low pressure perturbation. Such low pressure generation qualitatively comes about from vertical accelerations of parcels experiencing increasing negative buoyancy by melting and evaporation at low levels. Analysis of cloud model simulations during fully-developed, mature downdraft stages indicates relatively minor pressure perturbation reductions in the upper downdraft rgions near 2 km AGL. However, low pressure perturbations in model simulations during downdraft developing stages (Section 5) show much more substantial pressure reductions just below the melting level.

Another control on total descent within downdrafts, besides stability, is related to the ratio of vertical to horizontal flow speed over the downdraft width. Large horizontal speeds over the downdraft width generally inhibit significantly large parcel vertical excursions. Downdraft air simply jumps from one equilibrium level to another as demonstrated by the jump trajectory M in Fig. 4.53.

Total cooling along downdraft trajectories is determined by rates of evaporation and melting. Greatest local cooling rates exist within heavy precipitation usually below the melting level and particularly below cloud base where most unstable lapse rates exist. Melting

accounts for 10–60% total cooling along given downdraft trajectories, the fraction being greatest along up-down trajectories in which parcels typically reside within the melting zone for longer times. Precipitation evaporation becomes increasingly important along midlevel trajectories, which possess drier source air.

Dynamical processes along downdraft trajectories generally operate as follows. Along the up-down branch, upward-directed pressure gradient forces lift negatively-buoyant air above cloud base. Such pressure forces can be produced by two effects: (i) vertical pressure gradient forces associated with the low-level gust front, and (ii) vertical pressure gradient forces associated with (presumably) nonhydrostatic updraft effects. Air along up-down branches often achieves positive buoyancy some distance above cloud base, but relative motion transports the parcel outside the updraft to above the downdraft region, where downward-directed pressure forces exceed positive buoyancy. Below the melting level negative buoyancy is quickly reestablished and the parcels are accelerated downward to near the 0.8 km level. At this point upward-directed pressure forces (hydrostatic and dynamic) exceed total negative buoyancy, thus decelerating parcels during final descent. The behavior along midlevel branches is similar to that along the descending segment of the up-down branch, except initial positive buoyancy is often produced by adiabatic warming exceeding sublimational cooling within generally light precipitation.

These results clearly indicate that downdrafts are driven at low levels by precipitation effects: loading, and cooling by melting and evaporation. Entrainment-type flows into the cloudy and precipitating regions are regarded partly as effects of downdraft dynamical processes,

and are not the cause of the downdraft itself as originally hypothesized at the start of this investigation. Such inflows are driven partly by induced pressure reductions and partly by momentum transfer within downdrafts.

Downdraft structure, dynamics and thermodynamics described in this section apply to mature, fully-developed downdrafts within mature precipitating convection. The following section examines the structure and dynamics of developing downdrafts in which pressure forces are much greater than in mature downdrafts. Sections 5 and 6 further examine downdraft thermodynamics, in particular the role of melting, as a function of environmental conditions. Section 6 also establishes environmental controls influencing downdraft intensity and depth. Results of this section, Section 5, and Section 6 are then used in Section 7 to construct a generalized downdraft conceptual model.

5. DOWNDRAFT INITIATION

In the previous section mature storm downdraft structure was examined for a variety of storm types and environmental conditions. Additional insight on downdraft dynamics can be gained by examining the processes associated with early stages of downdraft formation. The following subsections examine observational evidence on downdraft formation from several appropriate case studies. Cloud model results are then described to elucidate dynamical processes involved, and finally, theoretical considerations and related calculations are addressed using observational and modeling results as a guideline.

5.1 Inferences from Observations

One signature of downdraft depth and intensity is the presence of low-valued θ_e surface air transported within downdrafts from levels above the PBL. Precipitation-associated downdrafts not associated with significantly-reduced θ_e air (when low-valued θ_e air exists above the PBL) may usually be regarded as shallow downdrafts confined primarily to the PBL*. In several case studies examined in this investigation, two of which will be discussed next, adjacent precipitating convection exhibited highly-contrasting surface θ_e patterns.

---

* This statement may not be universally true, particularly for storms which exhibit a well-defined up-down downdraft branch illustrated in the previous section. However, we note here that in the observations presented earlier, the presence of a strong up-down downdraft branch usually implies the presence of a midlevel branch which accomplishes vertical transport of low-valued midlevel θ_e to the surface.

A surface analysis for the 7/19 case (Fig. 5.1) reveals that only the southernmost storm (C11 - documented in Knupp and Cotton, 1982a,b) of a group systematically transported low-valued θ_e to the surface. A smaller but intense cell (C8) located 15 km north possessed comparable reflectivity but produced only very weak downdrafts and no θ_e reduction. On this day a large number of heavily-precipitating but relatively small cells were observed, but only two large and long-lived storms accomplished significant θ_e transport from midlevels (~ 3-4 km) to the surface (see Knupp, 1980). Some of the smaller cells produced transient and much weaker outflow. A similar pattern was noted in the 7/26 case (Section 4.1.1) in which largest and most intense precipitating convective cells exhibited strongest outflow and most substantial θ_e reductions (see Fig. 4.4) while less intense precipitating convection generated weaker downdraft outflow having smaller θ_e reductions.

The relationship between precipitation intensity and downdraft depth is further clarified in the following discussion of a storm (7/25) examined in considerable detail by Dye et al. (1980, 1982), by Dye and Martner (1982), and by Miller et al. (1982, 1984)*. Here, a relatively small precipitating convective storm was sampled by Doppler radar and aircraft over a one-hour period. Evolutionary characteristics of this storm's maximum reflectivity (Fig. 5.2) include a relatively slow growth in intensity to 60 dBZ_e and in height to 12 km. The 1920-1945 time period examined here encompasses initial and intermediate stages of this intense phase.

---

* The conclusions reached herein differ somewhat from those reached in these papers where it was concluded that low-level downdrafts were weak throughout.

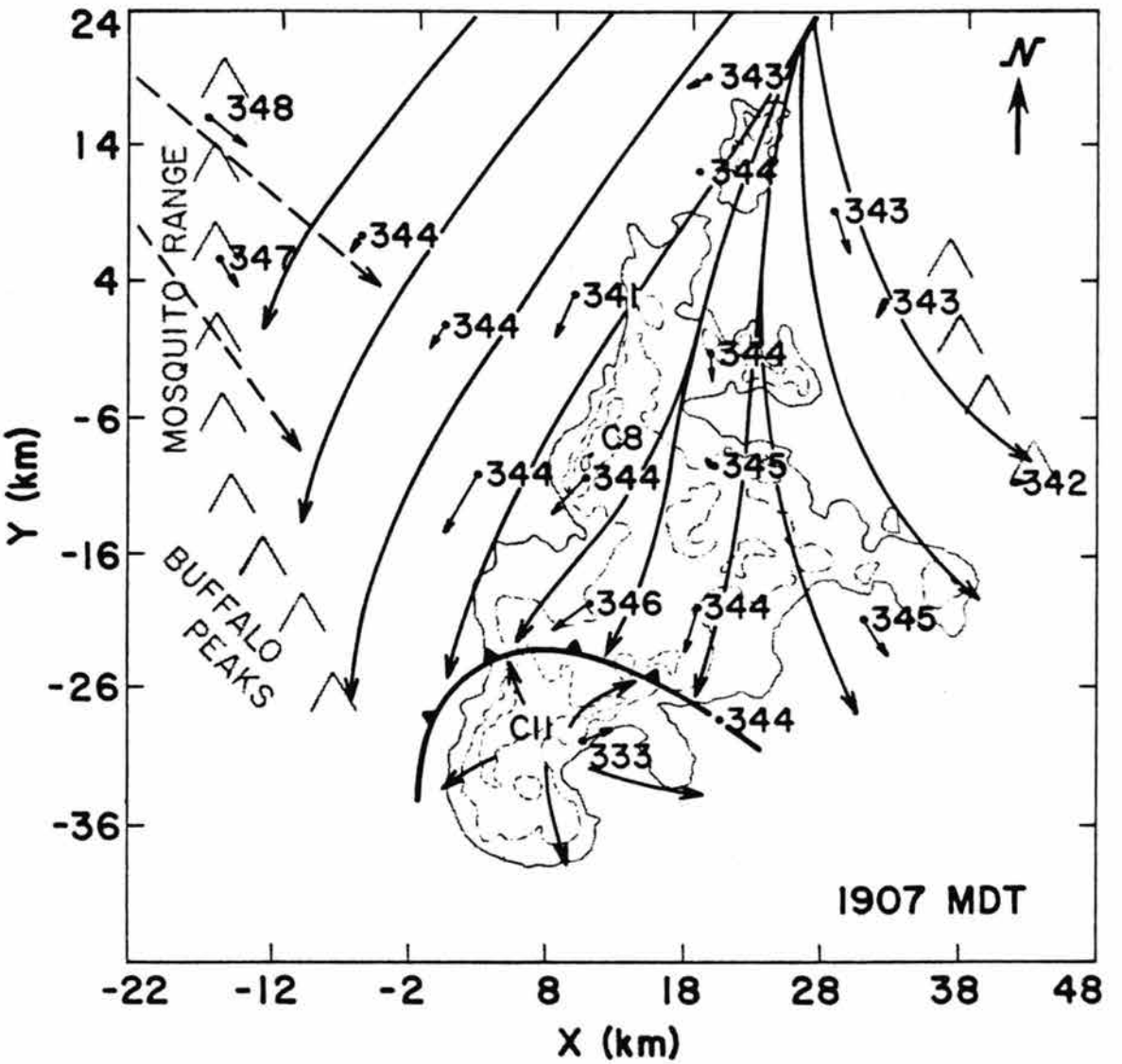

Fig. 5.1. Surface patterns over South Park at 1907, 19 July 1977. Plotted values are wind vectors (maximum vector 10 m s^{-1}) and θ_e. Radar echoes are from the 1.5° CP-3 PPI [location near 18,23)] and are contoured every 10 dBZ_e, beginning at 25 dBZ_e.

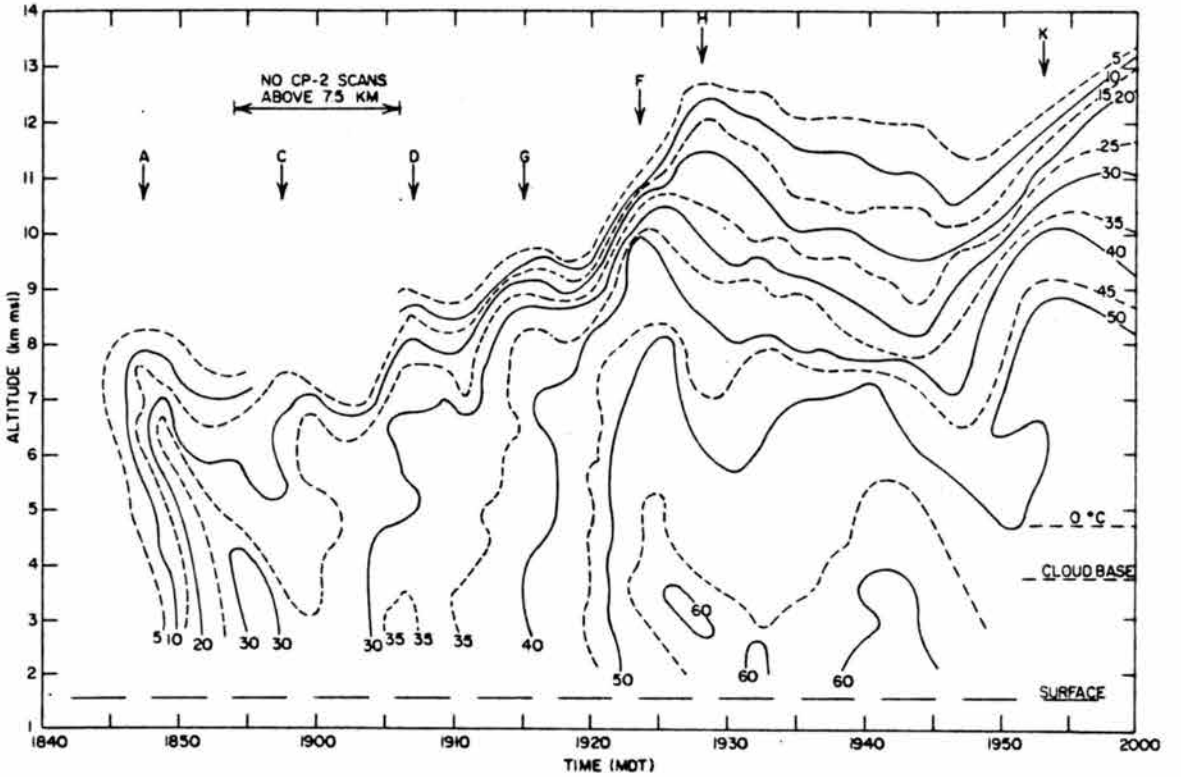

Fig. 5.2. Time vs. height plot of maximum reflectivity factor in an NHRE storm on 7/25/76. Taken from Dye et al. (1980).

The developmental stages of downdrafts at cloud base (z = 2.4 km AGL, T = 278 K) were fortuitously documented by three aircraft which penetrated the precipitation core near cloud base between 1923 and 1945, shortly after relatively heavy precipitation entered the subcloud layer (see Fig. 5.2). Two aircraft flying coordinated patterns shown in Fig. 5.3a detected only sporadic weak downdrafts within the precipitation core near 1928. Corresponding values of θ_e showed little variation ($\pm$ 1 K) from boundary layer values, thus substantiating that downdrafts were insignificant at and just above cloud base. However, small-scale penetrative type downdrafts were measured by other aircraft penetrating cloud at midlevels, several km above cloud base.

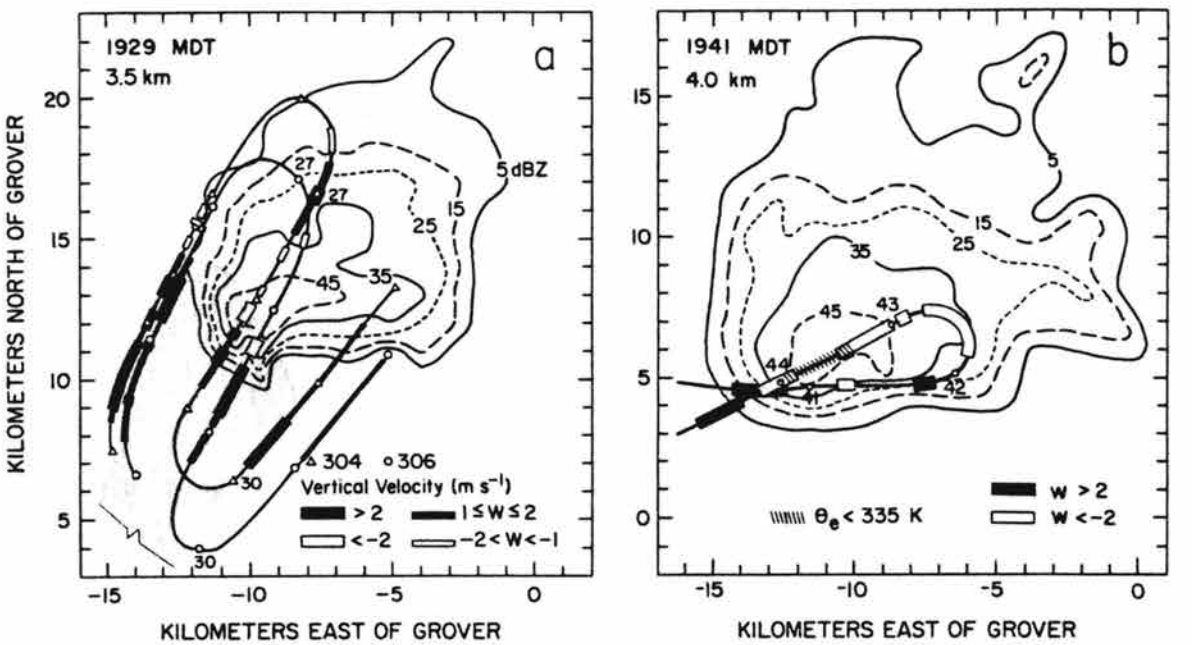

Fig. 5.3. Composite aircraft and radar mappings at the times and levels (MSL - subtract 1.5 km for AGL) indicted. Numbers beside each aircraft track refer to time past 1900. Reflectivity factor is labeled in dBZ_e. The lightly shaded area in (a) represents air having $\theta_e \geq 345.5$ K. Adapted from Dye et al. (1980).

By 1943, downdrafts and associated θ_e reductions at cloud base (Fig. 5.3b) had increased significantly in areal extent and intensity. As shown in Fig. 5.3b, 5 m s^{-1} peak downdrafts* and θ_e reductions up to 9 K from ambient values of 345 K were measured in this latter penetration. Apparently, downdrafts near and above cloud base formed shortly after 1928 and then became well established by 1943. A north-south vertical section of analyzed reflectivity through the core region (Fig. 5.4) implies the presence of low level downdrafts as early as

---

* In closely inspecting this aircraft data presented in Dye et al. (1980), an artificial trend in measured w was suggested. Upon removing this trend, pockets of 5 m/s downdrafts showed up in the time series from which Fig. 5.3b was made.

1936. The outward extension of low level reflectivity (marked A in Fig. 5.4) is indicative of strong low-level outflow winds driven by downdrafts (probably extending above cloud base) within the reflectivity core. (Similar signatures appear in Fig. 4.28 shown previously).

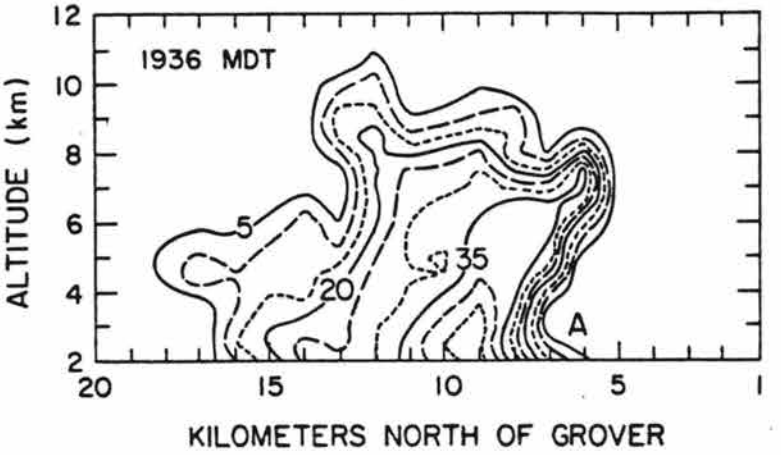

Fig. 5.4. Vertical north-south section near the reflectivity core of the 7/25 storm at 1936. Reflectivity factor contours are drawn every 5 dBZ_e, with selected contours labeled as shown. Taken from Dye et al., 1980).

Although weak downdraft activity existed below cloud base around 1920 as Doppler radar analyses indicate (Miller et al., 1984), significant downdraft activity apparently did not extend through cloud base until some time between 1928 and 1943, 10-20 min after heavy precipitation entered the subcloud layer. Hence, this appears to be another case in which some threshold in precipitation intensity and perhaps areal extent needs to be exceeded before downdrafts extend above cloud base.

The near simultaneous appearance of low-valued θ_e air and downdrafts within moderate to heavy precipitation indicates that low-valued θ_e air is ingested into the precipitation core by some mechanism such as pressure-induced horizontal accelerations. The process of evaporation of precipitation falling into a static subsaturated

environmental layer possessing low θ_e probably represents the most simple mechanism by which low-valued θ_e air and downdrafts coincide. This process, however, is probably absent in many low-shear cases described above. One example is provided by the 7/21 low-shear case in which vigorous downdrafts, inferred from 15 m s^{-1} outflow winds (Fig. 5.5) were colocated with heavy precipitation and low-valued θ_e air. A saturation point (SP) time series from station 15, situated close to the downdraft and precipitation core (Fig. 5.5), is presented in Fig. 5.6. This series indicates a dual evaporation line (EL) structure separated by a sharp reduction in θ_e associated with heavy rain. Each EL segment is produced by evaporation of precipitation within the PBL and within low-valued θ_e air originating within the 2-3 km AGL layer. This structure will be related to precipitation-induced pressure perturbations and associated horizontal inflow discussed next in conjunction with other Doppler-derived evidence.

Doppler radar observations from the 7/26 case considered in Section 4.1.1 captured the process of downdraft development and evolution within newly-formed precipitating regions. Analysis of patterns on horizontal planes indicated that a downdraft and associated precipitation zone developed in a semi-discrete fashion immediately adjacent to (north of) existing downdrafts and precipitation. Airflow patterns within an east to west vertical plane from three analyses within this developing downdraft core are displayed in Fig. 5.7. Downdrafts first formed at low levels (< 2 km) at 1738 and then developed upwards to some upper-limiting height, 3-4 km AGL in this case, by 1803. This development scenario is consistent with patterns in the 7/25 and 7/21 cases described previously. In combining these observations with previous

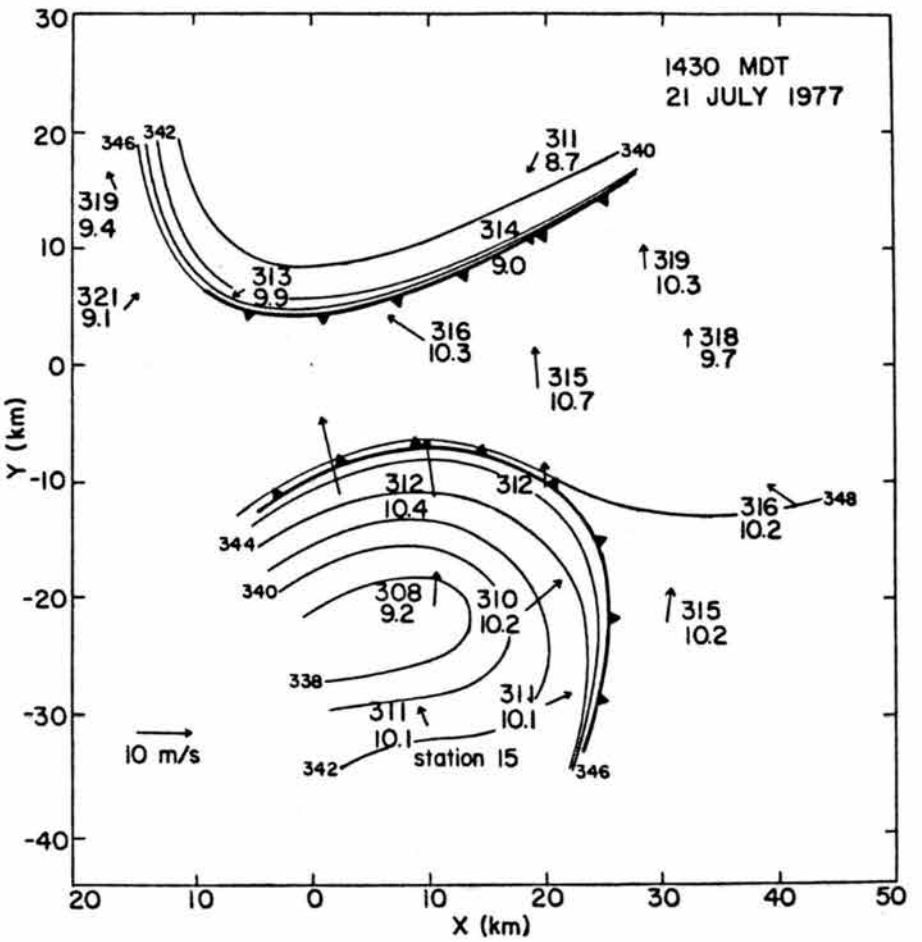

Fig. 5.5. Surface analysis over South Park at 1430 on 7/21/77. θ_e is analyzed every 2K. Plotted station parameters are potential temperature and mixing ratio.

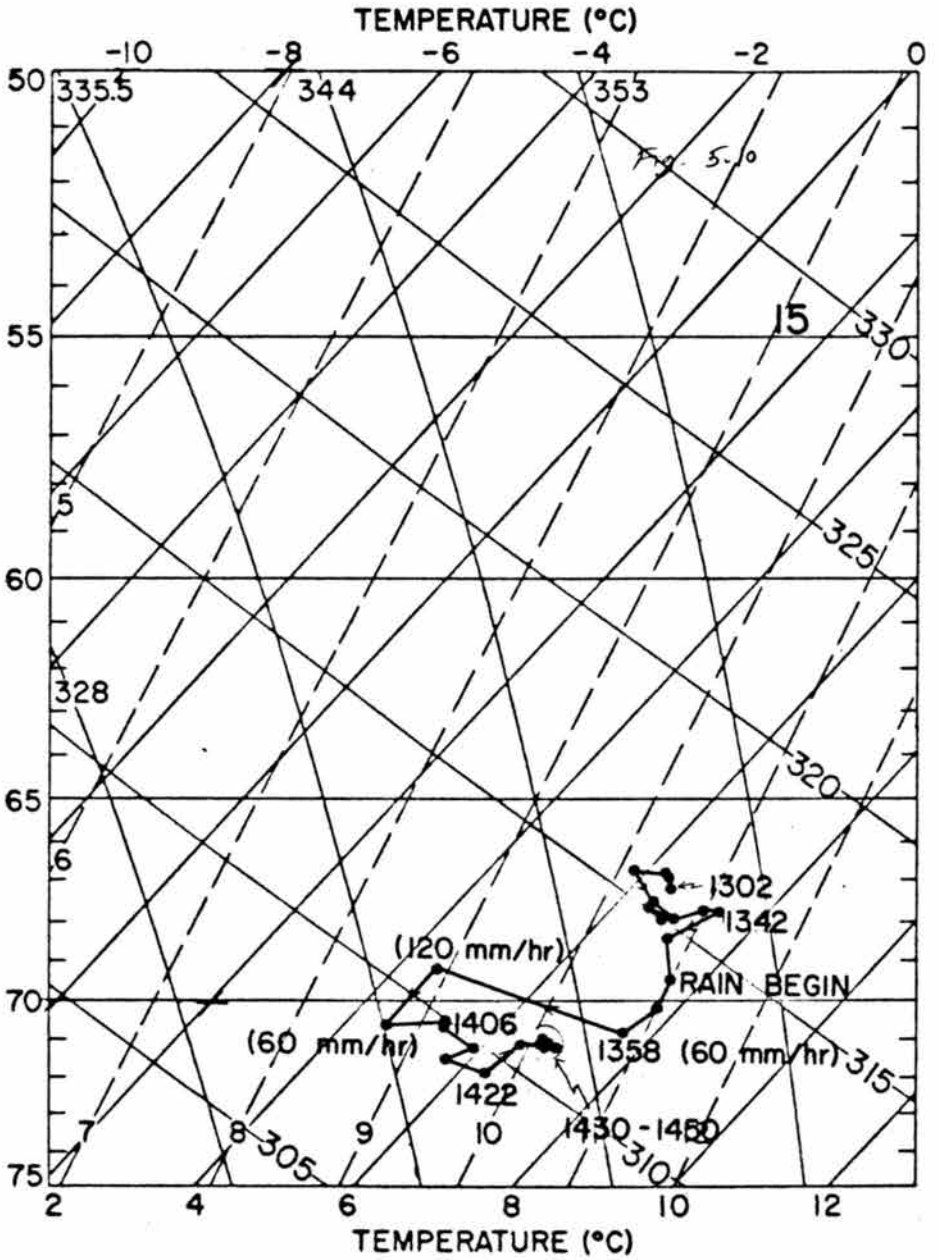

Fig. 5.6. Saturation point (SP) time series from surface station 15 (location given in Fig. 5.5). Points are plotted every 2 min from 1358 to 1406, and every 4 min otherwise.

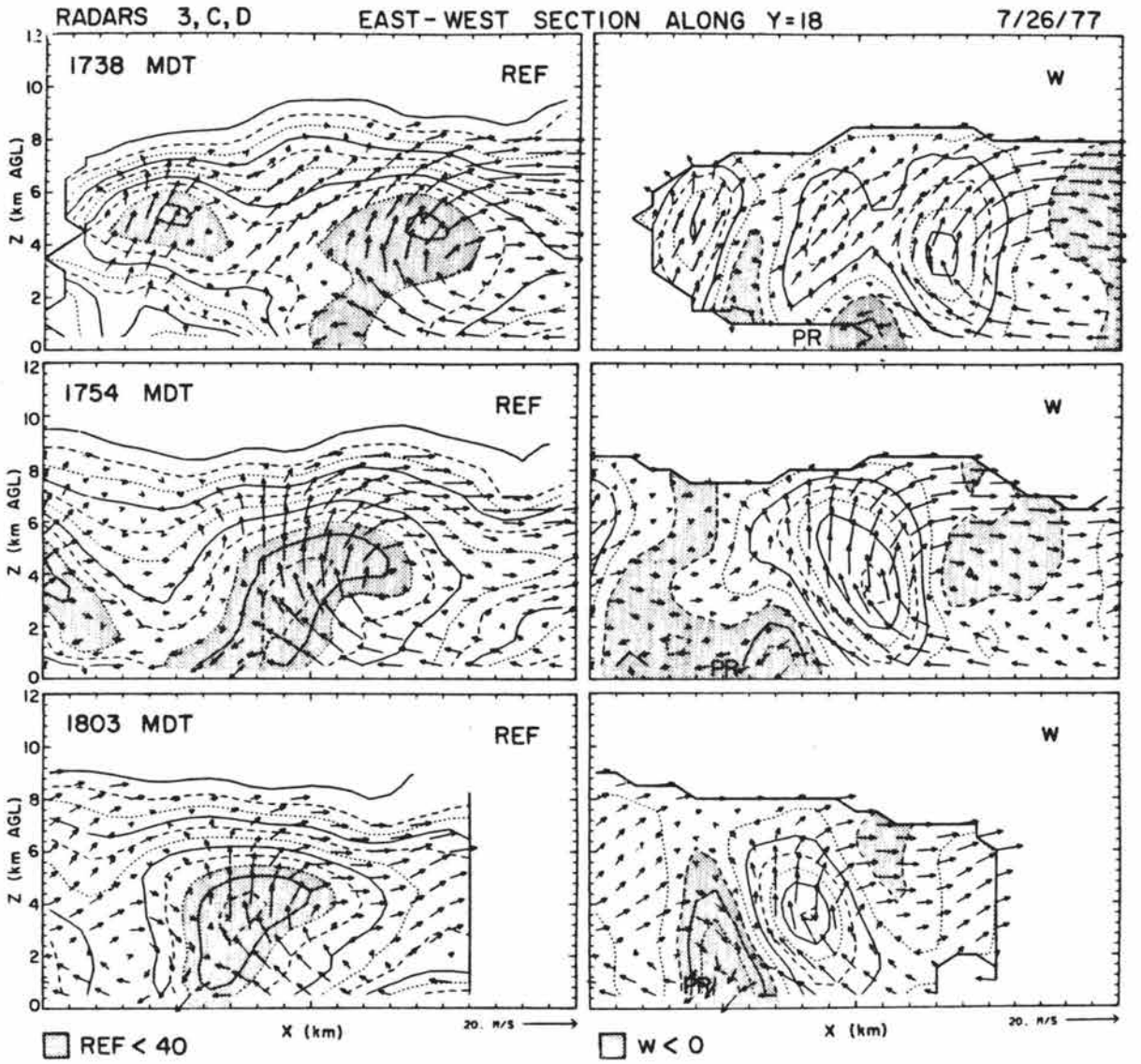

Fig. 5.7. Triple Doppler radar analyses at 1738, 1754 and 1803 for the 7/26 case. Vertical east-west sections are taken through the developing downdraft core. Top panels present reflectivity factor contoured every 5 dBZ, beginning at 0 dBZ_e. Bottom panels give vertical motion, contoured every 2 $m s^{-1}$, with negative values shaded. Airflow is storm relative.

information, it is inferred that cooling produced by melting and subcloud evaporational processes in the lowest 2 km produced weak downdrafts and an EL structure similar to that indicated in Fig. 5.6. As melting and evaporation proceed, increasing negative buoyancy at low levels produces greater downward accelerations and associated low pressure perturbations which in turn accelerate air horizontally and vertically, thereby incorporating lower-valued θ_e air into the downdraft circulation. This process, indicated in the schematic of Fig. 5.8, explains the observations previously presented in this and preceeding sections. If low environmental levels possess stable layers (as in the 6/12 case which lacked strong downdrafts), or if low-level cooling rates are small due to low precipitation rates and/or large particles (as in the 8/1 case) then such a process may not proceed.

The next section provides additional information on precipitation-induced pressure perturbations using results from three-dimensional cloud model simulations and gives an alternative model on the downdraft-initiation process.

5.2 Cloud Model Results

Cloud model simulations were conducted for three cases (7/26, 8/4, 8/1) described in Section 4. In each simulation clouds were initialized by imposing low-level convergence for a ten-minute time period, after which flow fields were allowed to relax to an equilibrium state (see Section 3). Because modeled clouds were initiated in a realistic manner, downdraft development within these clouds is considered to be natural within the limitations of the precipitation and turbulence parameterizations. Precipitating cloud downdraft initiation from two

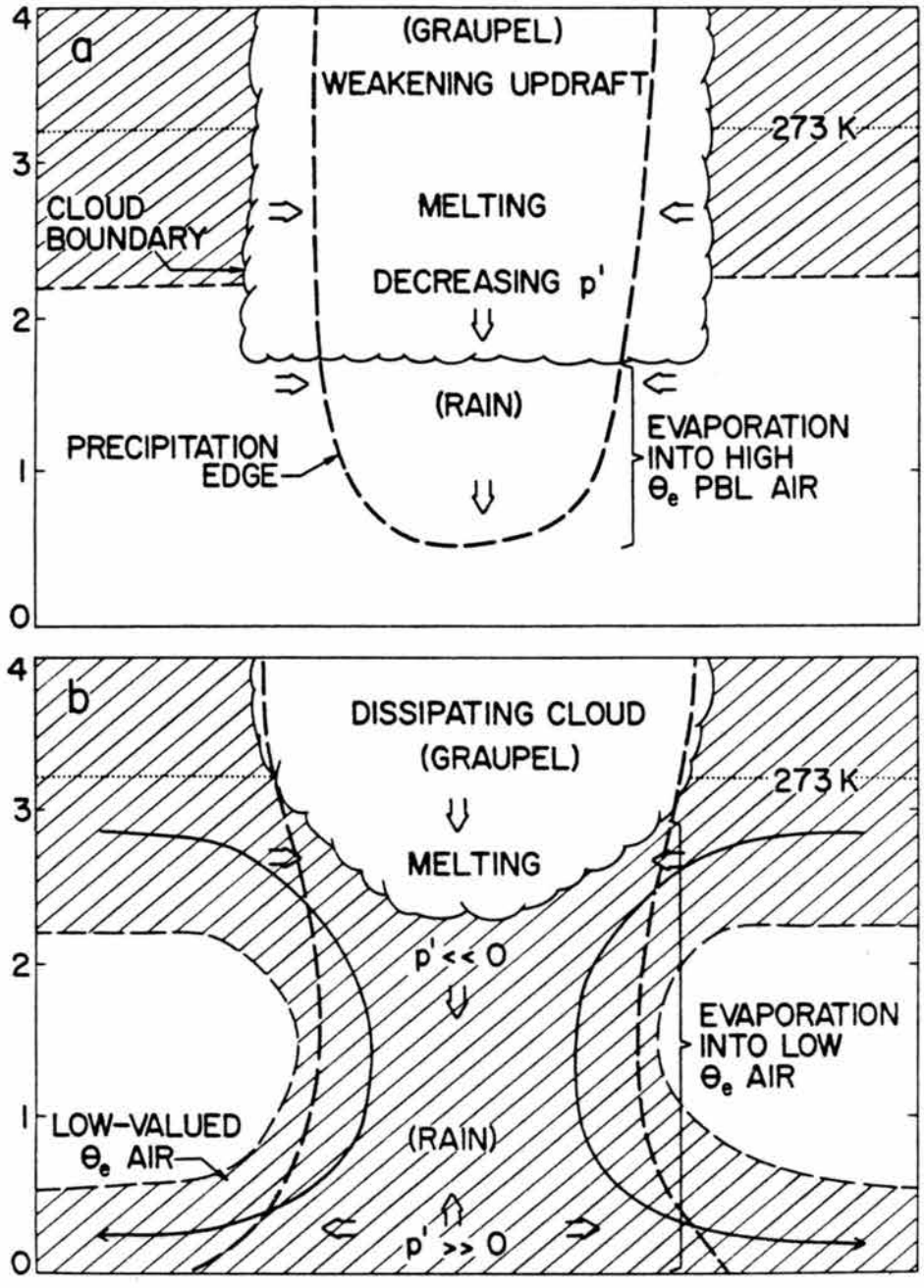

Fig. 5.8. Schematic illustrating downdraft initiation processes for no-shear conditions. Broad arrows represent air parcel accelerations.

simulations exhibiting contrasting environments (7/26 and 8/1) is described below.

In all three simulations, precipitation-associated downdrafts formed near cloud base within the wake region of the downshear flank, consistent with the schematic depiction of Fig. 2.7. Time-height sections for the 7/26 case (Fig. 4.17) and other analyses from all three simulations indicate that downdraft initiation (defined here as the point when $w \leq -2$ m s^{-1}) near the 1 km level followed precipitation arrival by 2-3 min. Downdrafts then quickly expand both upward and downward after initiation. Because precipitation represents a key ingredient to downdraft formation, the mechanism of precipitation transport to low levels requires consideration.

Precipitation transport is intimately connected with cloud microphysical processes and with flow structure as determined by environmental wind shear and associated flow around updrafts (see Fig. 2.7). Fig. 5.9 illustrates horizontal flow patterns and corresponding precipitation fields (precipitation loading can be equated with precipitation mixing ratio) at two levels (1.8 km and 4.1 km) at 2340 s for the 7/26 case. These patterns are similar to those at 1980 s when PR-type downdrafts emerged near 1 km. At 4.1 km, anticyclonic flow around the northern updraft border carried precipitation (primarily graupel) around the updraft edge into the downshear wake mixed region. Here, updrafts weakened from wake entrainment effects allowed precipitation descent to lower levels where downdrafts were produced. Precipitation within the lobe extending northeastward from the core originated from higher levels where graupel escaped the northeastward-tilted updraft. Thus, in this case, and in the 8/1 and 8/4 cases,

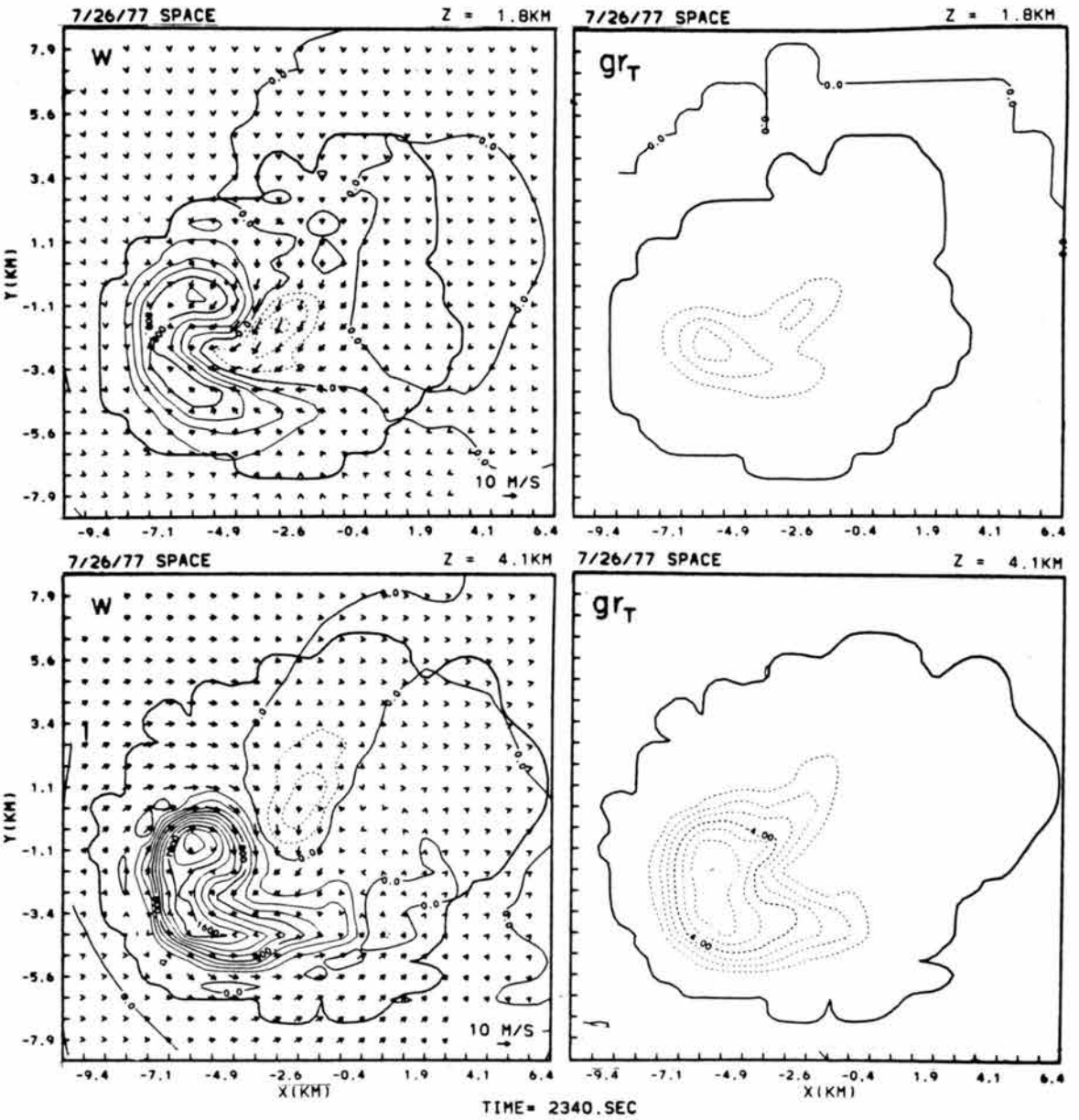

Fig. 5.9. Cloud model output fields on horizontal planes at 1.8 and 4.1 km at 2340 s during developing downdraft stages for the 7/26 case. Vertical motion, contoured every 2 m s^{-1}, appears on the left (negative contours are dashed), and total condensate fields or water loading, contoured every .01 m s^{-2}, appear on the right.

strong flow around the updraft at midlevels transported precipitation within the updraft edge and that falling into clear air from higher levels into the downshear wake where fallout to lower levels occurred. Provided that the updraft remains active, such a process can also maintain existing downshear-located downdrafts, as was noted in the 6/12 and 8/1 Doppler observations presented in Section 4.

Fig. 5.10 displays a sequence of patterns at the 2.8 km level for the more highly-sheared 8/1 simulation. Precipitation falling from higher levels into the downshear wake (in the manner just described) is directly associated with downdrafts which formed shortly after 1500 s. Other weaker downdrafts having ~ 3 m s^{-1} magnitudes were located along cloud edge outside of precipitation near the active updraft. These progressively weakened as the downshear-located downdraft intensified. The downshear downdraft attained a strong intensity by 2070 s when downdrafts were nearly colocated with precipitation. Small initial reductions in θ_e very quickly give way to appreciable θ_e decreases within the downshear wake. Note that the θ_e minimum is displaced downshear from the downdraft and precipitation cores, a feature also seen in the 7/26 case. The arrangement seen here provides another method by which surface precipitation may nearly coincide with downdrafts and low-valued θ_e air. In this case, as opposed to the scenario depicted in Fig. 5.8, precipitation falling into the subsaturated wake region generates negative buoyancy by loading and by cooling from melting and evaporation. This low θ_e air then descends within downdrafts and precipitation shortly after downdraft initiation.

Patterns of perturbation pressure (p') at the 2.8 km level (Fig. 5.10) exhibit a similar dependence on arrival of precipitation to low

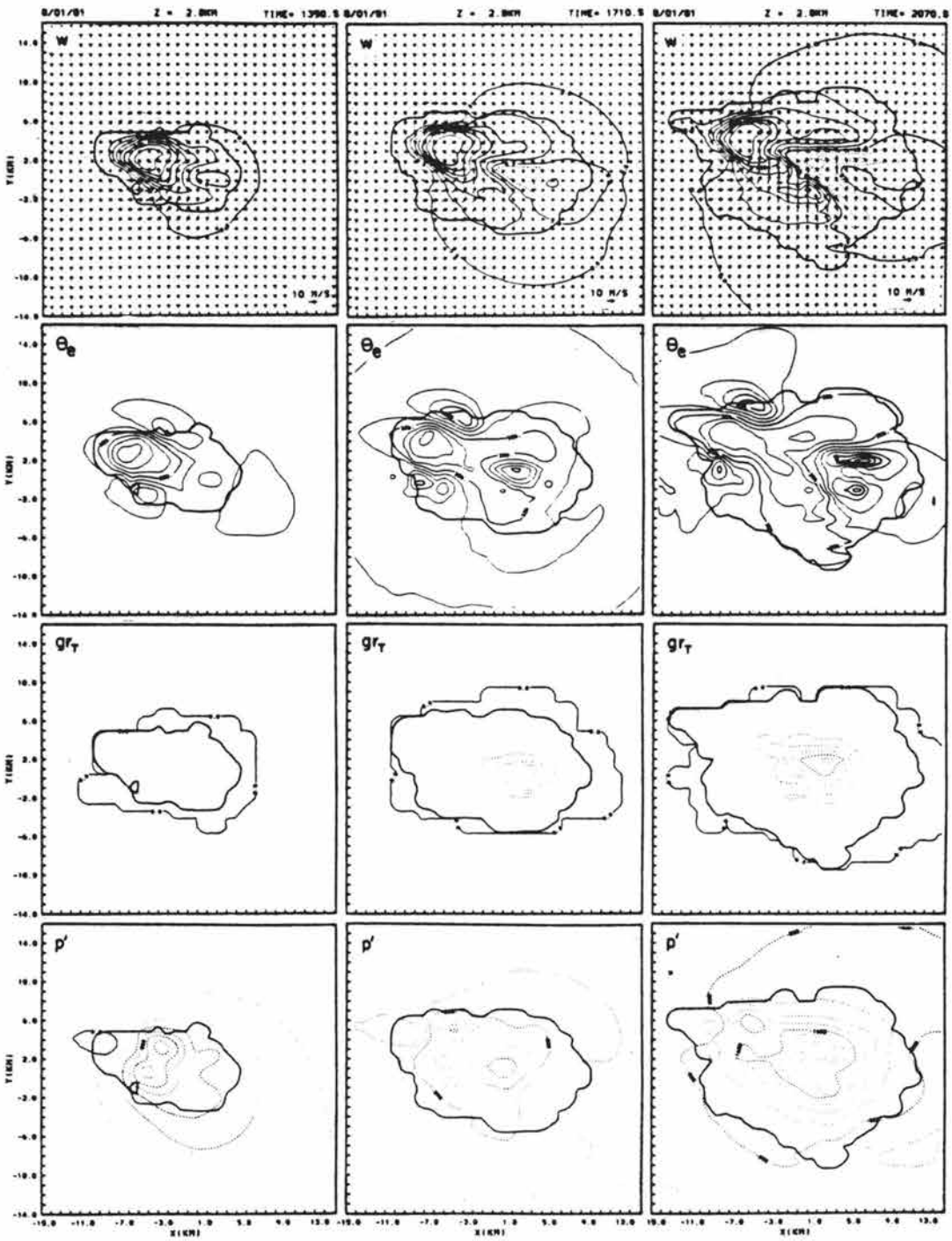

Fig. 5.10. Cloud model output on horizontal planes at 2.8 km during the developing downdraft stages (1350 s, 1710 s and 2070s) for the 8/1 case. Top panels give vertical motion contoured every 2 m s^{-1}; second row gives θ_e, contoured every 2K; third row presents total water buoyancy, contoured every .01 m s^{-2}; and fourth row is perturbation pressure, contoured every 20 Pa (0.2 mb). Dashed lines indicate negative values in all panels. The heavy solid line shown in all three panels denotes a total condensate mixing ratio of 0.01 g kg^{-1}.

levels. Lowest p' (~ -1.2 mb) is initially located within the downshear flank of the upshear-located updraft at 1350 s. However, as precipitation falls beneath the 2.8 km level into the downshear flank, a secondary p' minimum, nearly colocated with precipitation and associated downdrafts, emerges by 1710 s and becomes dominant (~ -1.6 mb) by 2070 s. This downdraft-associated p' minimum, which occurred ~ 10 min after precipitation arrival, subsequently declined in relative magnitude even though downdrafts continued to intensify. Similar relative (but less intense) patterns not shown here appeared in the 7/26 simulation.

Vertical east-west sections through the developing downdraft core, near the time of minimum p', are given in Fig. 5.11 for the 8/1 case and in Fig. 5.12 for the 7/26 case. Relative patterns of various fields are generally similar in each case, except magnitudes are larger in the 8/1 results. Developing downdrafts are located within precipitation downshear and partly beneath the primary updraft. Patterns of θ_e represent a time-integrated air parcel tracer and indicate descent from levels 2-4 km AGL. Lowest p' found in the upper regions of the downdraft core occur at 1.6 km AGL in the 7/26 case and at 2.6 km AGL in the 8/1 case. Both levels are approximately 0.6 km below the melting level. Although these p' reductions are partly produced by hydrostatic effects, simple calculations (Section 5.3) show that strong vertical variations in buoyancy and the attendant vertical accelerations <u>below</u> the level of minimum p' may account (nonhydrostatically) for much of the reduction. In both cases, negative p' magnitudes subsequently declined as the high p' cell (produced by dynamic and hydrostatic effects) worked upwards from the surface. The p' minimum at similar relative levels

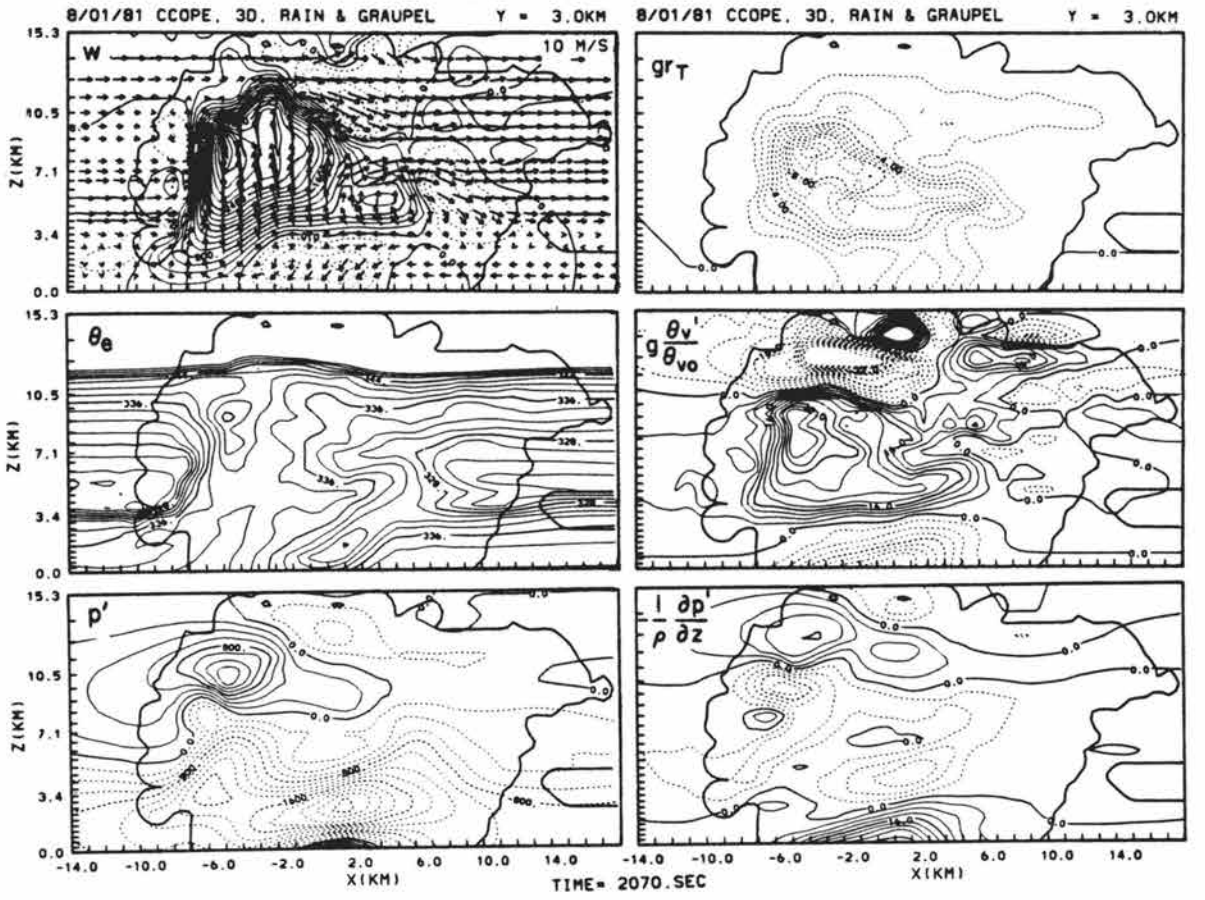

Fig. 5.11. Vertical east-west cross section near the low-level downdraft core of the 8/1 simulation at 2070 s, the time of minimum downdraft-associated pressure reduction. (a) Vertical velocity contoured every 2 m s^{-1}, (b) θ_e contoured every 2 K, (c) p' contoured every 20 Pa, (d) thermal buoyancy contoured every 0.04 m s^{-2}, (e) water buoyancy contoured every 0.01 m s^{-2}, and (f) vertical pressure forces contoured every 0.04 m s^{-2}.

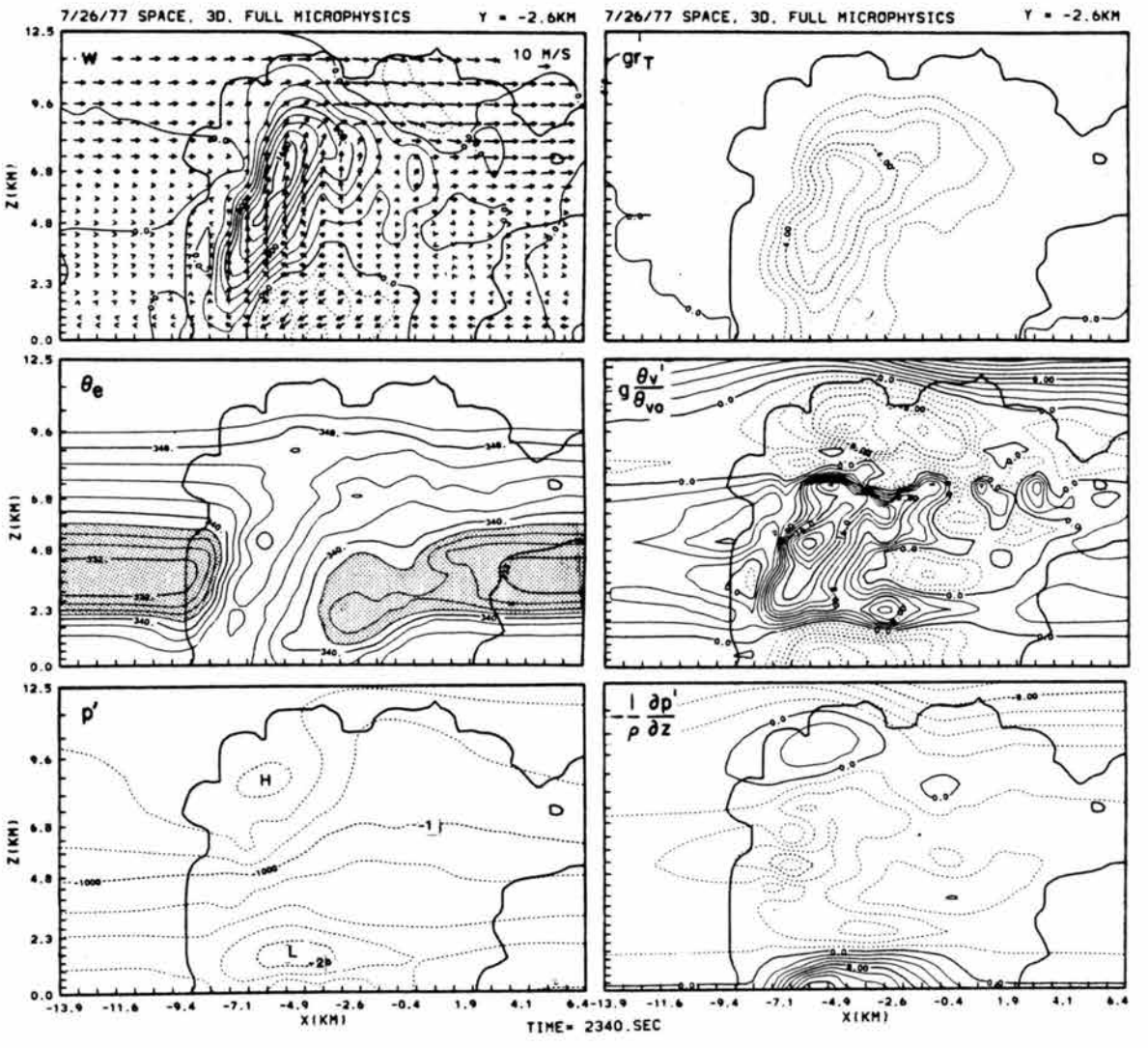

Fig. 5.12. Same as Fig. 5.11 for the 7/26 simulation at 2340 s. (a) Vertical velocity contoured every 2 m s^{-1}, (b) θ_e contoured every 2 K, (c) p' contoured every 25 Pa, (d) thermal buoyancy contoured every 0.02 m s^{-2}, (e) total water buoyancy contoured every 0.01 m s^{-2}, and (f) vertical pressure forces contoured every 0.02 m s^{-2}.

appears in mature downdrafts (Section 4) but with significantly weaker magnitudes. Reasons are given in the next subsection.

Patterns associated with developing downdrafts (Figs. 5.11 and 5.12) indicate a thermally buoyant structure (i.e., $g\ \theta_v'/\theta_{vo} > 0$) in the extreme upper downdraft regions above the PBL and melting level. Similar but less intense patterns were noted for mature downdrafts discussed in Section 4. This positive thermal buoyancy is produced by adiabatic warming which exceeds sublimational cooling within descending currents. During the developing downdraft stages, downward-directed pressure gradient forces produced by buoyant-related pressure reductions below, provide the primary forcing necessary to drive thermally-buoyant air downwards. During mature storm stages, condensate loading becomes more comparable to pressure forces. Initial downdrafts in the 7/26 and 8/4 cases were deeper and stronger (by 30-50%) than subsequent steady-state downdrafts. (The 8/1 simulation was terminated before downdrafts attained a steady state.)

Core downdraft trajectories constructed near the time of downdraft intensification in the 7/26 case revealed a uniform pattern in which most trajectories (of the 6 available) originated directly north of the updraft near the 2.5-3.0 km level. Such a strong directional bias and relatively high source level (for this case) appears to be related to circulations associated with the wake entrainment flow, and to initially large magnitude p' reductions associated with cloud development and downdraft initiation. Subsequent mature downdrafts generally exhibited lower source levels (see Fig. 4.22). Values along trajectories close in time to downdraft development (e.g., trajectory 3 shown in Fig. 4.23) show initial downdraft descent under significant positive thermal

buoyancy (countered by pressure and loading forces), consistent with the instantaneous picture presented in Figs. 5.11 and 5.12.

5.3 Theoretical Considerations

The pressure perturbation associated with developing downdrafts discussed in the previous subsection owes its origin to very rapid production of negative buoyancy from strong cooling by precipitation melting and evaporation at low levels. The nature of this negative pressure perturbation is illustrated in the pressure analysis and related discussion given below.

Pressure pertubations within and adjacent to convective clouds have been examined by Rotunno and Klemp (1982), by Klemp and Rotunno (1983) and by Schlesinger (1984a). These authors have outlined the derivation of a diagnostic Poisson equation for perturbation pressure which is formed by combining the equation of motion

$$\frac{d\vec{V}}{dt} = -c_p \bar{\theta} \nabla \pi' + B \vec{k} + \vec{S}, \tag{5.1}$$

with the anelastic mass continuity equation

$$\nabla \cdot \rho \vec{V} = 0, \tag{5.2}$$

where π' (the perturbation Exner function), B (buoyancy) and $\vec{S}$ (eddy stress) are defined as

$$\pi' = (p'/p_o)^{R/c_p},$$

$$B = g\left(\frac{\theta_v'}{\theta_{vo}} - r_T\right),$$

$$\vec{S} = \nabla(u_i'' u_j'').$$

Upon taking the divergence of (5.1) and applying (5.2), a diagnostic pressure equation may be written as

$$C_p \nabla \cdot (\bar{\rho}\,\bar{\theta}\,\nabla \pi') = \underbrace{\frac{\partial}{\partial z}(\bar{\rho}B)}_{F_b} \underbrace{- \nabla \cdot (\bar{\rho}\vec{V}' \cdot \nabla \vec{V}')}_{F_{dyn}} + \nabla \cdot (\bar{\rho}\vec{S}'), \qquad (5.3)$$

where F_b represents pressure forcing by vertical gradients of buoyancy and F_{dyn} represents dynamic forcing. The dynamic forcing term can be expanded into (following Klemp and Rotunno, 1983)

$$F_{dyn} = -\bar{\rho}\left[\left(\frac{\partial u}{\partial x}\right)^2 + \left(\frac{\partial v}{\partial y}\right)^2 + \left(\frac{\partial w}{\partial z}\right)^2 - \frac{d^2}{dz^2}\ln\bar{\rho}w^2\right]$$

(fluid extension)

$$\underbrace{-2\bar{\rho}\,\frac{\partial v}{\partial x}\,\frac{\partial u}{\partial y}}_{\text{(curvature)}} \qquad \underbrace{-2\bar{\rho}\left[\frac{\partial u}{\partial z}\,\frac{\partial w}{\partial x} + \frac{\partial v}{\partial z}\,\frac{\partial w}{\partial y}\right]}_{\text{(shear)}}. \qquad (5.4)$$

Dynamically-forced pressure perturbations are produced by fluid extension such as flow impinging on an obstacle, by curvature in the flow, and by fluid shear interactions between cloud updrafts and ambient flow. These terms have received the attention of the above-listed authors. Klemp and Rotunno (1983) in particular determined that the pressure distribution at low levels within a simulated tornadic storm was largely dynamically induced primarily by flow curvature and extension effects.

The behavior of F_b in Eq. (5.3) is particularly interesting because it is principally this mechanism which leads to pressure reductions referred to in previous subsections. This mechanism is now examined for an incompressible atmosphere in which F_b in (5.3) can be written as

$$F_b = \bar{\rho}\frac{\partial B}{\partial z} = \bar{\rho}\frac{\partial}{\partial z}\left(\frac{\theta_v'}{\theta_{vo}} - r_T\right) = \bar{\rho}\frac{\partial}{\partial z}\left[\frac{\theta'}{\theta_o}\left(\frac{1 + 0.61\, r_v'}{1 + 0.61\, r_{vo}}\right) - r_T\right]. \qquad (5.5)$$

Examination of cloud model output indicates that vertical variations in θ'/θ_o usually overshadow vertical variations in r_v' and r_T. Therefore, (5.5) can be simplified to

$$F_b \simeq \frac{\bar{\rho}}{\theta_o}\frac{\partial \theta'}{\partial z} = \frac{\bar{\rho}}{\theta_o}\frac{\partial}{\partial z}(\theta - \theta_o) \simeq \frac{\bar{\rho}}{\theta_o}\frac{\partial}{\partial z}\ln\theta \qquad (5.6)$$

for heights within the PBL and just above where $\theta_o \simeq$ const.

Changes in θ along a parcel trajectory through a developing downdraft, initially produced by evaporation and melting of precipitation falling into the subcloud layer, are described by the thermodynamic equation

$$\frac{d}{dt}\ln\theta = \left[L_{lv}VD_{rv} + L_{iv}VD_{gv} + L_{il}ML_{gr}\right]\frac{1}{c_pT} \qquad (5.7)$$

where expressions for evaporation $[VD_{rv} = (\frac{dr_r}{dt})_{evap}]$, sublimation $[VD_{gv} = (\frac{dr_g}{dt})_{sub}]$ and melting $[ML_{gr} = (\frac{dr_g}{dt})_{melt}]$ are given by Eqs. C.17, C.18 and C. 21, respectively, in Appendix C. Eq. (5.7) can be written to match Eq. (5.6) by taking the vertical gradient of (5.7) and then integrating over some short time period to get

$$\frac{\partial \ln\theta}{\partial z} = \frac{\partial}{\partial z}\int \frac{d\ln\theta}{dt}\, dt$$

$$= \int \frac{1}{c_pT}\left[L_{vl}\frac{\partial}{\partial z}VD_{rv} + L_{vi}\frac{\partial}{\partial z}VD_{gv} + L_{il}\frac{\partial}{\partial z}ML_{gr}\right]dt$$

$$
\begin{aligned}
&\overset{E_a}{} \qquad\qquad \overset{E_b}{} \\
&= E_1\Big[G(T,p)(S-1)\frac{\partial r_r}{\partial z} + r_r(S-1)f(T)\frac{\partial T}{\partial z} \\
&\qquad\qquad \overset{E_c}{} \\
&\qquad + r_r\, G(T,p)\,\frac{\partial}{\partial z}(S-1) \\
&\qquad\qquad \overset{S_a}{} \qquad\qquad \overset{S_b}{} \\
&+ G(T,p)K_{3g}\,\frac{\partial}{\partial z}(S-1) + K_{3g}(S_i-1)f(T)\frac{\partial T}{\partial Z} \\
&\qquad\qquad\qquad \overset{S_c}{} \\
&\qquad + (S_1-1)G(T,p)(Ar_g^{1/3} + B)\frac{\partial r_g}{\partial z}. \\
&\qquad\quad \overset{M_a}{} \\
&+ L_{il}^{-1}\, M_1(Ar_g^{-1/3} + B)\,\frac{\partial r_g}{\partial z} \\
&\qquad\qquad\quad \overset{M_b}{} \qquad\qquad \overset{M_c}{} \\
&\qquad + K_{3g}L_{il}[K\,\frac{\partial T}{\partial z} + D_v L_{vl}\rho\,\frac{\partial r_v}{\partial z}]
\end{aligned}
\tag{5.8}
$$

In Eq. (5.8), subscripted E, M and S labels refer to evaporation, sublimation and melting terms (3 each), S is relative humidity, r_r, r_g and r_v are mixing ratios of rain, graupel and water vapor, and E_1, M_1, f(T), A and B are defined by the following:

$$E_1 = 0.5 + 0.349\left(\frac{g\rho_o}{\mu^2}\right)^{1/2}\rho_w^{-3/4}\,R_m^{-5/4},$$

$$M_1 = K(T-T_f) + D_v L_{vl}\rho_o[r_v - r_{vs}(T_f)],$$

$$f(T) = \frac{2T\varepsilon L^2/KR + T^3L/\varepsilon D_v e_s - T^4R/\varepsilon D_v e_s}{(\varepsilon L^2/KR + RT^3/\varepsilon D_v e_s)^2},$$

$$A = \frac{2}{3}[4.3/(\pi^2 \rho_g^3 D_g^6)]^{1/3} \quad ,$$

$$B = 0.793\left[\frac{1}{\mu^{1/2}}\left(\frac{g\pi\rho_g D_g^3}{\rho C_D}\right)^{1/2}\right]^{1/2}\left[\frac{\rho_o^{1/2}}{\pi^{2/3}\rho_g D_g^2}\right] \quad .$$

Other symbols are defined in Table C.1 of Appendix C.

Magnitudes of individual terms in (5.8) were calculated within the melting zone beneath cloud base (shown schematically in Fig. 5.13b)

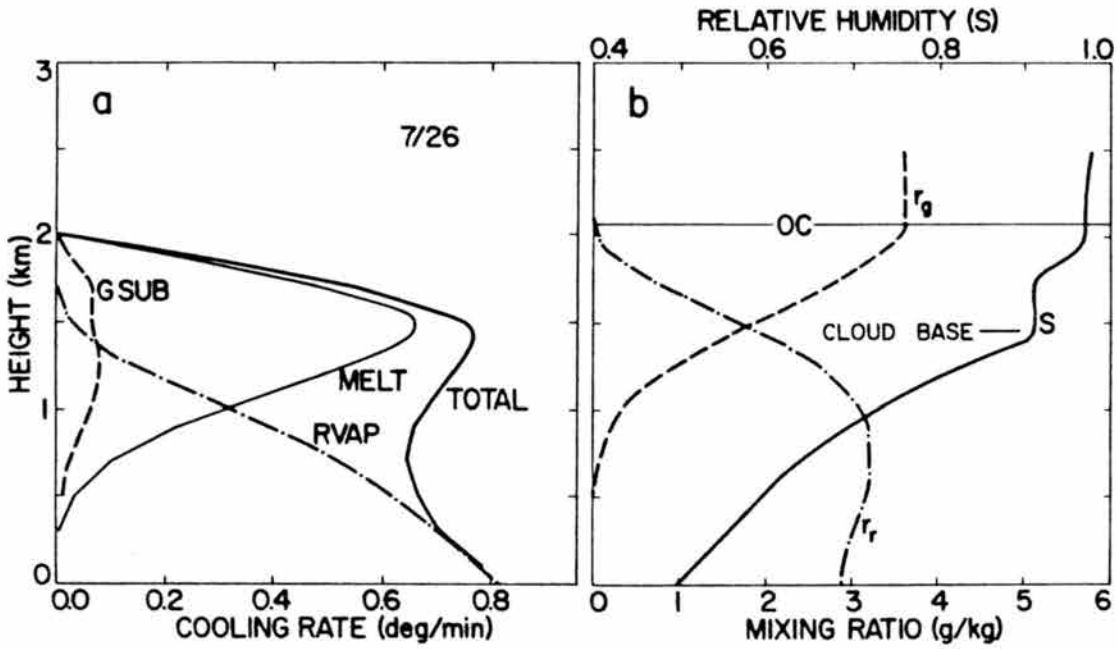

Fig. 5.13. (a) Profiles of cooling rates from sublimation of graupel (GSUB), evaporation of rain (RVAP), melting of graupel (MELT) and the sum of all three (TOTAL). These quantities were computed by simulating the fall of graupel below the melting level and cloud base. (b) Profiles of relative humidity used in the calculations of (a) and resulting profiles of graupel and rain mixing ratios r_g and r_r.

using two sets of assumed values which represent moist and dry subcloud layers. Table 5.1 presents these assumed values along with the term magnitudes. For both moist and dry subcloud layers the dominant terms are E_b, S_b and M_b. Also note that M_b is largest and nearly equal to E_b in the moist case, while E_b is nearly 50% larger than M_b in the dry

case. Note that if the melting level is located in a saturated environment above cloud base, E_b and S_b disappear and melting effects dominate. Retaining only the primary terms in (5.8) which force negative p' we have for a general case

$$-p' \sim \nabla^2\pi' \sim \frac{\partial \ln\theta}{\partial z} \simeq E_1\overline{r_r}(S-1)f(T)\,\frac{\partial T}{\partial z} + K_{3g}L_{il}^{-1}K\,\frac{\partial T}{\partial z} + (S-1)f(T)\,\frac{\partial T}{\partial z}. \qquad (5.9)$$

Cooling and associated pressure forcing are thus governed by several effects: temperature and its vertical gradient,

TABLE 5.1. Magnitudes of individual terms in Eq. (5.8) for dry and moist subcloud layers (10^{-10})

	E_a	E_b	E_c	S_a	S_b	S_c	M_a	M_b	M_c	S
Dry[1]	.15	3.1	.22	.11	1.6	-2.1	-7.2	2.1	.12	0.4
Moist[2]	.20	4.1	.44	.22	2.2	-2.9	-3.8	4.3	.49	0.6

[1] $\overline{r_v} = 6$, $\overline{r_g} = 2$, $\frac{\partial \overline{r_g}}{\partial z} = 1\ \text{km}^{-1}$, $\frac{\partial \overline{r_r}}{\partial z} = -1\ \text{km}^{-1}$, $\frac{\partial r_v}{\partial z} = 0.25\ \text{km}^{-1}$

[2] All values are double those in 1 above.

relative humidity, largeness of precipitation mixing ratios r_r and r_g, and smallness of precipitation size. Strongest pressure forcing associated with accelerating downdrafts is therefore produced within a warm and dry adiabatic subcloud layer of low relative humidity by precipitation of high mixing ratio and small characteristic size. Although all these conditions are usually not satisfied simultaneously because of natural balances between boundary layer dryness and

precipitation mixing ratio, such ideal conditions often exist along the High Plains Front Range area. A number of Doppler radar observations taken during the 1982 JAWS experiment (e.g., Roberts and Wilson, 1984; Kessinger et al., 1984; Fujita and Wakimoto, 1983) portray strongly convergent and sometimes rotational flow within downdrafts just beneath the base of clouds forming above relatively deep and dry boundary layers. Such patterns which also appear more moderately in Section 4 are indicative of low perturbation pressure produced according to (5.9).

Melting effects, in particular, are quite large and can produce a very sudden onset of cooling below the melting level as demonstrated in Fig. 5.13a. Here, evaporation and sublimation were obtained (using the same melting and evaporation equations as in the analysis above, and applying these to the 7/26 environment) by simulating the release of 3.6 g kg^{-1} graupel at the 2.3 km level and then calculating cooling rates produced by evaporation and melting at each level.* Strongest vertical gradients in cooling (and therefore negative buoyancy) are largest just below 2 km by virtue of melting effects. This region centered near 1.8 km would therefore experience greatest pressure reductions according to (5.9). Comparison with 7/26 model results in which minimum p' were found within developing downdrafts near 1.6 km (Fig. 5.12) reveals good agreement. Results of similar calculations for rain only indicate more gradual vertical cooling gradients below cloud base. Smaller pressure reductions would thus be expected when rain only exists, other factors being unchanged.

---

* Here, we have assumed that the environment remains motionless (despite generation of negative buoyancy) during the time precipitation falls at terminal speed (7.5 m s^{-1}) from the top level to the surface.

Reexamination of the model results presented in Figs. 5.11 and 5.12 reveals that downdraft-associated p' minima reside very close to strongest vertical gradients in $g\ \theta_v'/\theta_{vo}$ for both 7/26 and 8/1 cases, in good agreement with theoretical expectations. Although hydrostatically-induced p' would exhibit similar trends, magnitudes would generally be much smaller than the p' minima shown in Figs. 5.11 and 5.12. Larger p' reductions generated in the 8/1 simulation can furthermore be explained theoretically: stronger vertical gradients in $g\ \theta_v'/\theta_{vo}$ and associated higher magnitude pressure reductions were produced within a vertical interval having drier air, greater temperature, greater static instability and higher precipitation content. All these factors are ideal ingredients as mentioned above.

The p' minimum at this relative level also appears in mature downdrafts, but exhibits much weaker magnitudes. Such reduction in relative magnitudes has several possible explanations: (a) the dynamic pressure head produced at the downdraft base by flow impinging on the surface (Eq. 5.4) develops to higher levels and masks the negative p' contribution produced by buoyancy effects; (b) vertical advective processes alter the initial thermal structure by initially transporting higher-valued θ air from above cloud base, thereby stabilizing the layer most favorable for p' reduction (this is probably a transient state); (c) development of the cold outflow pool, approximately one kilometer deep (see Figs. 5.11 and 5.12) produces an effect similar to (b) in that local negative buoyancy is effectively decreased within the outflow depth; (d) subsequent precipitation intensity is reduced and hence melting and evaporation rates responsible for rapid onset of negative buoyancy are diminshed.

In this section the structure and dynamics of developing downdrafts have been investigated. The schematic model in Fig. 5.14 illustrates processes associated with downdraft initiation within a vigorous and isolated precipitating convective cloud. Instantaneous flow shown on selected horizontal planes portrays divergent flow at low and high cloud levels. A vortex couplet and associated pressure patterns adjacent to the midlevel updraft are shown at midlevels, consistent with general patterns determined by Rotunno and Klemp (1982). A well-defined downshear wake region is depicted as a strongly-convergent zone at midlevels, also consistent with cloud model results presented herein and elsewhere.

The general flow patterns act to transport precipitation to the downshear flank at low to mid levels as shown. Diverging flow at upper levels is especially important in ejecting precipitation outside the cloud so that transport to low levels can initiate downdrafts there. Two contrasting hypothetical precipitation trajectories are represented by the heavy dotted lines a and b in Fig. 5.14. (No precipitation trajectories were actually calculated, but were inferred from distributions of precipitation and associated flow patterns.) The barrier path b falls from diverging outflow at upper levels and is carried to the downshear cloud sector by strong flow diverted around the flank of the updraft. A wake trajectory a also originatng from high levels is depicted to remain within the low-speed wake during its fall into the downshear midlevel wake region.

Precipitation is responsible for initiation of the low-level downdraft and associated downdraft-induced pressure perturbations. During initial stages, downdraft air originating primarily above the PBL

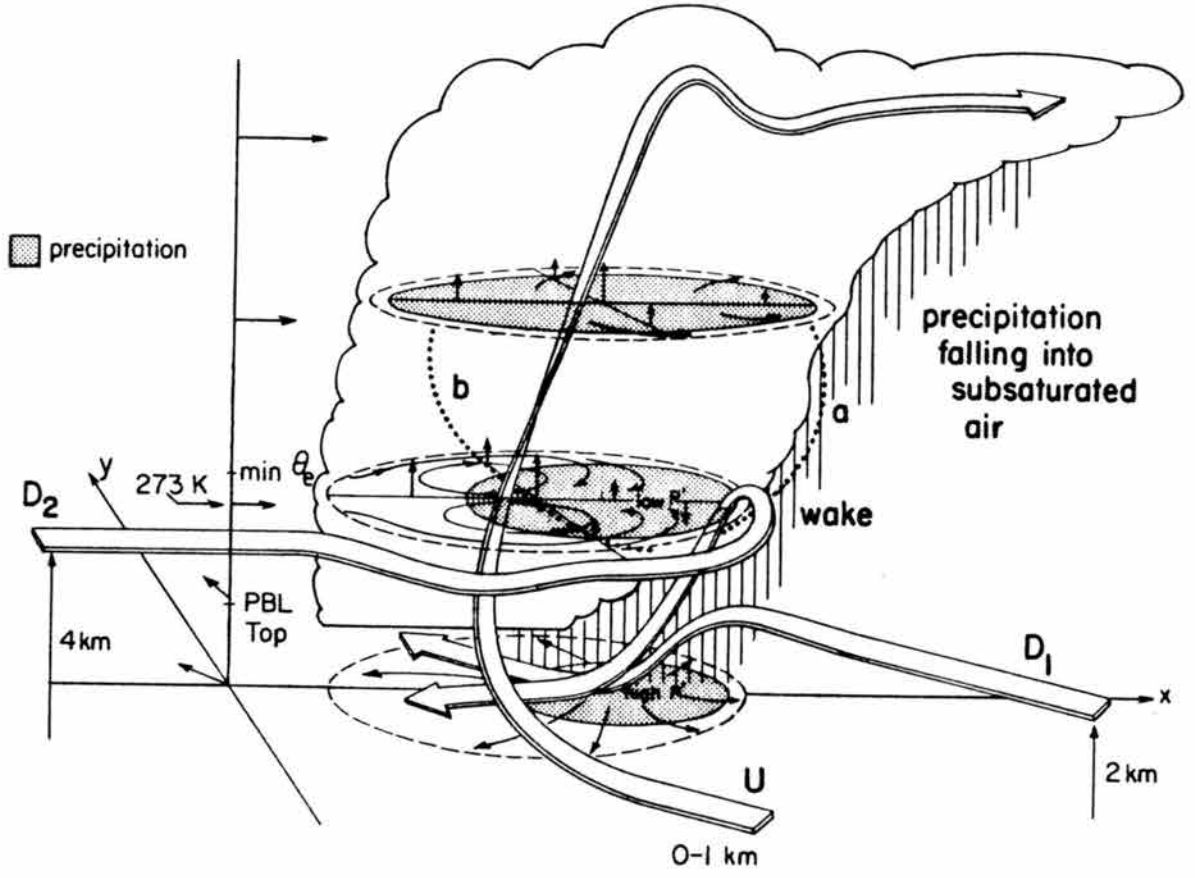

Fig. 5.14. Conceptual model illustrating downdraft initiation processes in sheared condions. Ribboned arrows denote trajectories of selected parcels. Streamlines of horizontal flow are shown in middle and upper planes. Stippled regions indicate location of precipitation on selected planes, and dotted lines portray paths of precipitation which is instrumental in initiating the downdraft.

follows midlevel-type paths. Up-down type paths become more common after the initial stages. Paths D_1 and D_2 represent highest and lowest midlevel branches. Cooling by evaporation and melting of precipitation induces low perturbation pressure, lowest in magnitude ~ 0.5 km below the melting level, approximately 10 min after precipitation arrives there. Pressure reductions associated with upper regions of downdrafts, inferred from observational results in Section 4, were found to be most pronounced for developing downdrafts because greatest vertical gradients in (negative) buoyancy occur during the developing stages. The perturbation pressure minimum is nearly colocated with the precipitation core itself and is governed by temperature and its vertical gradient, relative humidity along the inflow branches, largeness of precipitation mixing ratios, and the smallness of precipitation characteristic size. Although steep vertical gradients in negative buoyancy are particularly enhanced by melting effects, other microphysical factors not considered here are apparently important. These "other" factors are examined next.

6. CONTROLS ON DOWNDRAFT STRENGTH

Results from previous sections have indicated that downdraft structure and intensity are functions of precipitation and environmental characteristics, in agreement with early theoretical studies (e.g., Kamburova and Ludlam, 1966). The combination of microphysical and environmental characteristics determines vertical profiles of cooling rates which in turn influence downdraft depth, intensity and even downdraft initiation processes described in Sections 4 and 5. The following subsections examine these microphysical and environmental factors separately, elucidating primarily those effects which influence cooling rates and associated downdraft properties.

6.1 Precipitation Influences

The dependence of cooling rates and downdraft structure on precipitation characteristics, such as size and phase, was examined with the cloud model and with more elementary diagnostic calculations of cooling rates for predescribed precipitation characteristics. A series of sensitivity tests summarized in Table 6.1 were conducted with a two-dimensional version of the cloud model exercised in previous sections. For all runs the reference state was taken from the observed 7/26 sounding (Fig. 6.1), and clouds were initiated by imposing convergence over the boundary layer depth. Five experiments (15,14,16,8,12) were designed to examine sensitivity of low-level cooling and downdraft structure to imposed variations in precipitation parameterization. The remaining four experiments listed in Table 6.1 were included to examine

TABLE 6.1. Summary of two-dimensional cloud model sensitivity experiments initialized with the 7/26/77 South Park sounding or variations upon it.

No.	Experiment	W_{max} (m/s)	Low-level downdraft					Elevated downdraft	
			W_{min} (m/s)	Z (W_{min}) (km)	T'_{min} (K)	depth (km)	max r_r (g/kg)	W_{min} (m/s)	Z (W_{min}) km
4	Control-rain and ice	17	-11	0.8	-7.5	2.7	5.1	-8	3.7
15	Precip. size quartered	20	-13	0.8	-11.0	3.5	6.5	-11	8.5
14	Rain precip. only	21	-6	1.1	-5.0	2.9	4.5	-10	4.5
16	No evaporation/melting	16	-2	1.4	-0.4		0.3	-7	7.8
8	No melting	23	-6	0.8	-5.0	1.4	1.5	-8	7.8
12	No precip.	21	-1.5	0.8	-0.7		--	-10	4.5
1	Moist cloud layer ($T-T_d$ = 2K)	16	-9	1.1	-8.7		5.1	09	7.2
2	Dry cloud layer ($T-T_d$ = 30K)	22	-11	1.1	-9.9		5.2	-12	4.5
3	Deeper moisture in PBL	20	-10	0.8	N/A		6.1	-10	4.5
5	Adiabatic to 50 kPa	19	-12	0.8	-8.0		6.9	-9	4.1

the response of two-dimensional downdrafts to variations on the observed sounding as indicated in Fig. 6.1.

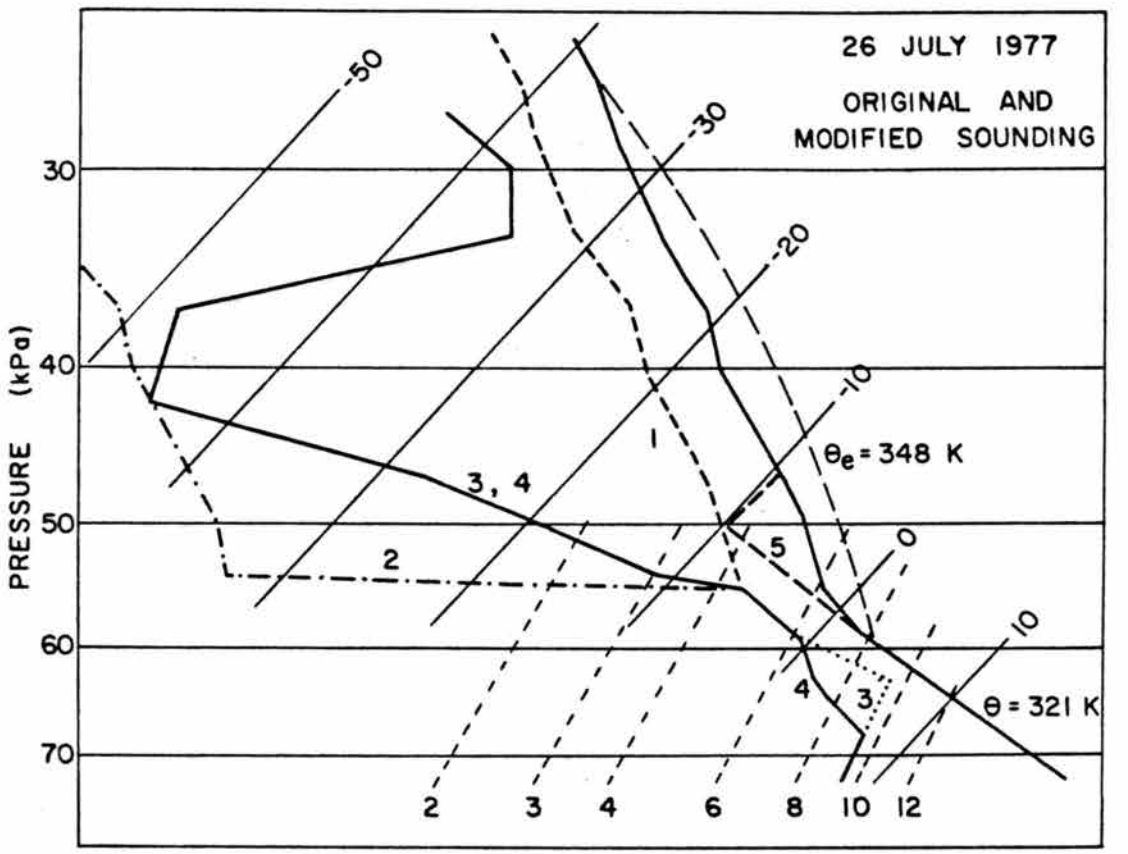

Fig. 6.1. Profiles of temperature and mixing ratio of the 7/26 sounding and variations made upon it for two-dimensional model sensitivity studies.

The precipitation variation experiments indicate that precipitation size may exert considerable influence on downdraft structure. By quartering characteristic precipitation size for both rain and graupel (Run 15), maximum downdraft magnitudes were increased over 2 m s^{-1}, low-level cooling was enlarged by 3.5 K and downdraft depth was heightened by 0.8 km. More importantly and somewhat suprisingly, the two-dimensional cloud circulation was significantly changed from the control case (4) as shown in Fig. 6.2. At 3600 s patterns in Run 15 (Fig. 6.2b) are dominated by a relatively steady and strong up-down

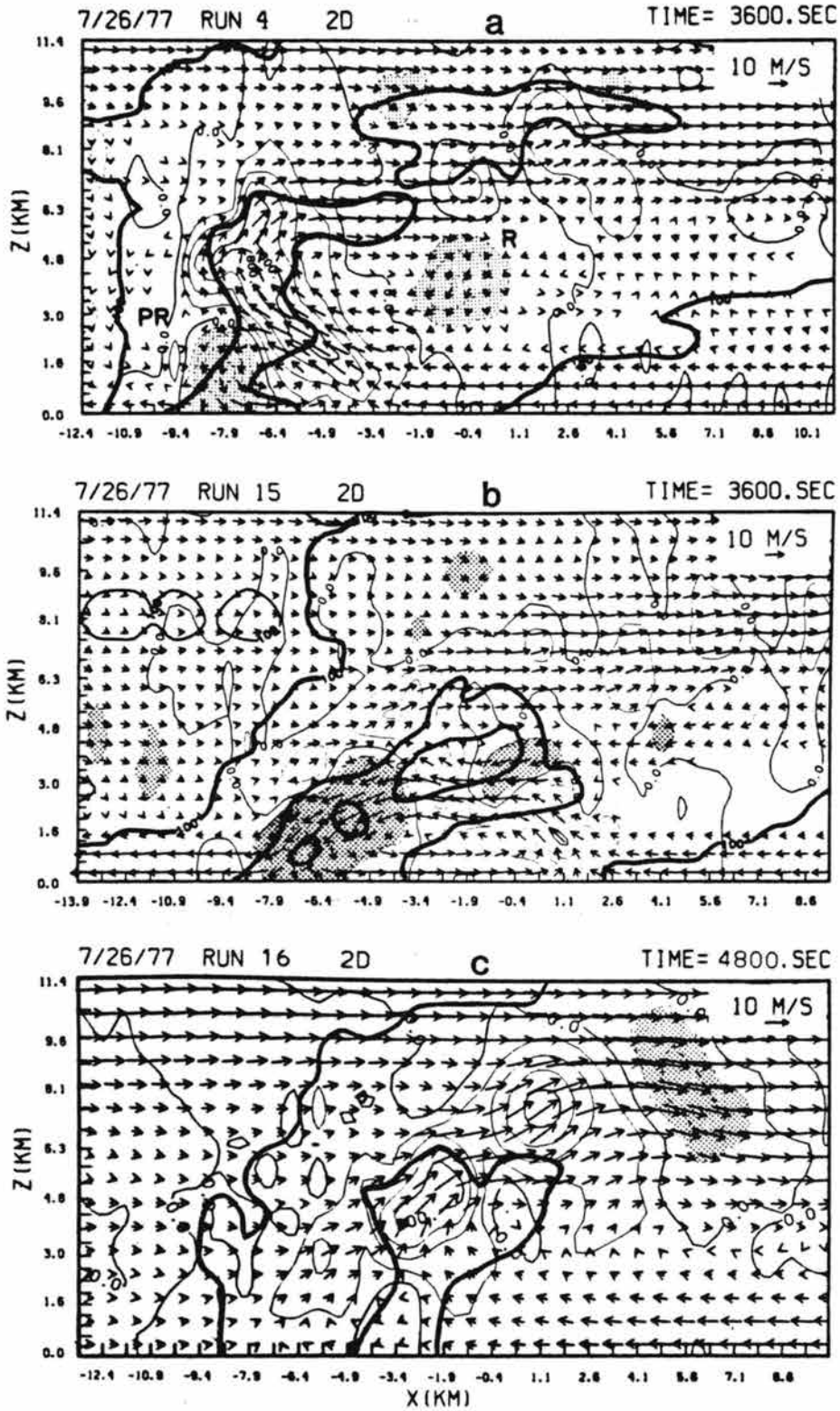

Fig. 6.2. Two-dimensional model results for selected runs at the indicated times. Heavy contours represent precipitation mixing ratios of ~0, 2 and 4 g kg^{-1}. Light lines denote analyzed vertical velocity, contoured every 2 m s^{-1}, with negative values stippled. Winds are approximately storm relative.

downdraft circulation. Patterns in the control case (Run 4, Fig. 6.2a) show a much less significant up-down downdraft circulation located beneath an upshear-tilted updraft which was virtually absent in the small precipitation experiment. This comparison, however, is complicated by non-linear effects present in the model equations.

Simulations with rain microphysics (no ice phase, Run 14) and with graupel and rain but no melting of graupel (Run 8) yielded similar statistical results (6 m s^{-1} downdrafts and low-level cooling of 5 K) but different flow structures. Experiments with no precipitation (cloud water only - Run 12) and with precipitation but no melting or evaporation (Run 16) also produced similar results, each exhibiting very weak low-level downdrafts and virtually no low-level cooling. The no precipitation case (12) interestingly generated midlevel, cloud-edge downdrafts ~ 2 m s^{-1} greater than in the control simulation, results similar to those obtained by Levy and Cotton (1984) for three-dimensional experiments. One may infer that such an increase is related to increased cloud evaporation in the cloud only case (12) in which cloud water contents (greater than 6 g kg^{-1}) greatly exceed the ~ 2 g kg^{-1} values when precipitation is included. Results from Experiment 16 (Fig. 6.2c) are also enlightening because precipitation loading alone, without precipitation-induced cooling, did not initiate strong low-level downdrafts - only very weak downdrafts less than 2 m s^{-1} in magnitude developed within the PBL as shown in Fig. 6.2c.

Several conclusions can be drawn from these results. The first is that cooling is required to initiate strong low-level downdrafts, not a surprising or new finding. This cooling is most effective when melting of ice-phase precipitation is present in addition to evaporation. These

results can be extended to infer that only weak downdrafts at best would be produced outside of melting regions wherever saturated conditions exist. This is particularly true for moist adiabatic layers in which downward motions are very slow (e.g., 6/12) even when evaporation is operative. Thus downdraft initiation within cloud would proceed slowly unless melting provides cooling as indicated previously in Fig. 5.13.

Because two-dimensional simulations inadequately represent wake entrainment effects commonly associated with downdrafts and downdraft initiation, the results present above, although felt to be generally relevant, should be interpreted with caution. For example, 2-D results indicate a large difference in kinematic structure between rain only and full precipitation physics (rain-graupel) simulations. However, a similar comparison made in three dimensions failed to reproduce the 2-D results. Both rain only and rain-graupel simulations produced maximum downdrafts of ~ 12 m s^{-1}, but low-level cooling was 2 K greater (total of 7 K) in the rain-graupel simulation. (Results from this simulation were presented in Sections 4 and 5). Further analyses of these three-dimensional results revealed that the near equality in maximum downdraft speed for each simulation was related to the following properties of the precipitation parameterization:

(a) The rain only simulation had greater precipitation efficiency despite weaker updrafts, and therefore delivered greater rain mixing ratios to levels below cloud base (5.5 g kg^{-1} vs. 3.5 g kg^{-1} in the rain-graupel simulation). Loading and evaporational cooling were therefore greater in this simulation.

(b) Rain evaporation (in the rain simulation) was greater than graupel sublimation (in the rain-graupel simulation) above the 273 K level for two reasons, disregarding differences in total precipitation ratio. First, because characteristic rain size is 54% the characteristic graupel size in the model, rates of evaporation exceed rates of sublimation due to the inverse dependence of evaporation/sublimation on particle size (see Eqs. C.18 and C.19 in Appendix C). Secondly, for equal particle size, evaporation rates of water drops increasingly exceed sublimation rates of ice particles as temperature decreases from 273 K. These two effects combined with (a) above act to produce evaporational cooling rates nearly twice as great as sublimational cooling rates over a several km deep layer above the 273 K level.

Vertical profiles of cooling by rain evaporation, graupel sublimation and graupel melting from the three-dimensional results, accumulated and compiled at each level over the model horizontal domain, are shown in Fig. 6.3 after 4500 s simulation time. Comparison of total cooling profiles indicates that the rain-graupel simulation generates greater cooling (despite generating less precipitation) below 2.5 km by virtue of melting of ice phase precipitation. Above 2.5 km the rain only simulation generates cooling rates nearly twice as great as in the rain-graupel simulation, due to the reasons mentioned above. In the rain-graupel simulation, the 1 km level (1.1 km below the 273 K level) marks the point of equality in cooling by melting and evaporation, below which cooling is dominated by rain evaporation.

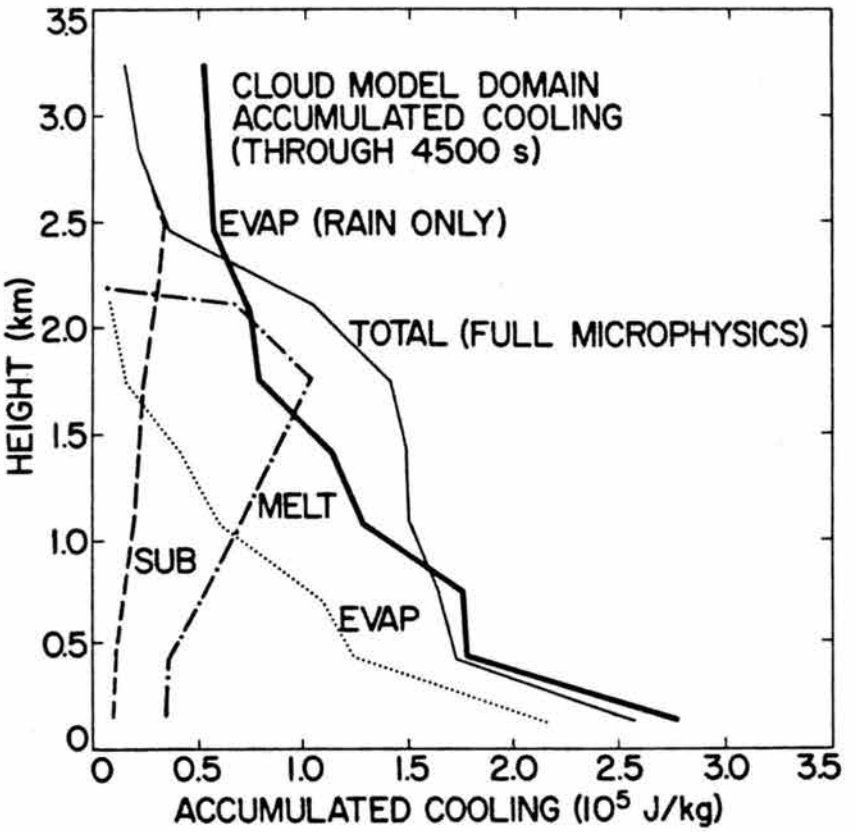

Fig. 6.3. Vertical profiles of total accumulated cooling from two three-dimensional simulations of the 7/26 case. The heavy solid line represents the cooling curve for a simulation with rain-only microphysical parameterization. The thin solid line is the total cooling curve for a corresponding simulation with parameterization of rain, graupel and aggregates included. Component cooling curves for this latter simulation are given by thin dashed lines.

Relative effects of melting and precipitation size were also estimated from more rudimentary calculations supplied by the diagnostic model, as was done in Fig. 5.13. For these calculations, 3.6 g kg^{-1} precipitation mixing ratio (all graupel or all rain) was allowed to fall near terminal velocity through a static environment (the 7/26 sounding) from the 2.3 km level to the surface, allowing evaporation and melting to occur during the fall. Fig. 6.4 presents cooling rate profiles from

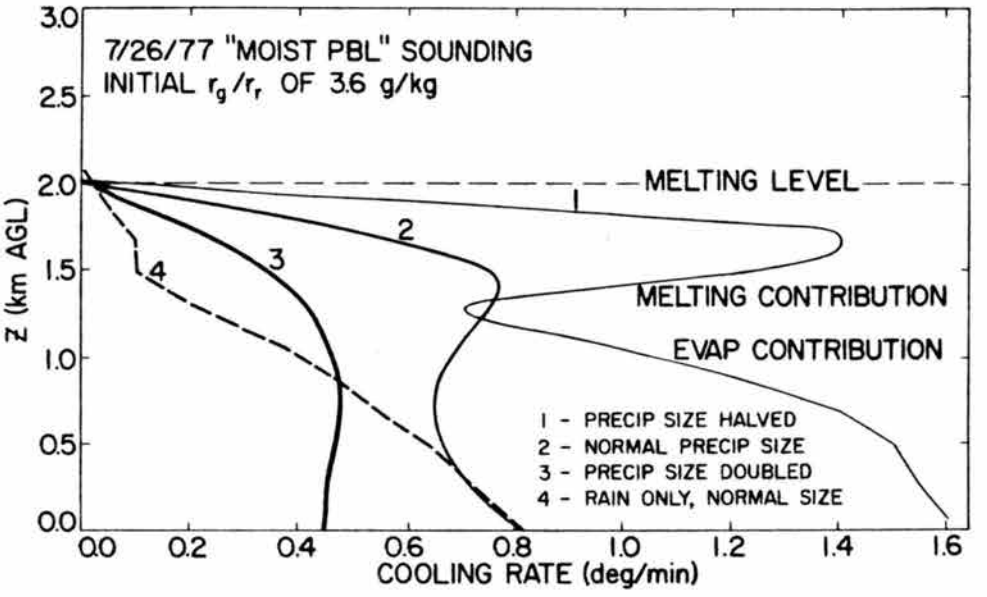

Fig. 6.4. Total cooling rate curves, similar to that in Fig. 5.13, obtained by simulating the release of precipitation (rain or graupel) from the 2.3 km level and computing rates of melting and evaporation. The 7/26 modified environment, as depicted in Fig. 5.13, is used in all four cases (curve 2 also appears in Fig. 5.13). The melting level is near the 0 C level in this case.

four experiments: initial graupel of normal, one-half, and twice the characteristic size of 1.0 mm; and initial rain of normal characteristic size (0.54 mm). Variations in precipitation size (both graupel and rain sizes are altered in identical ratios) produce significantly different cooling profiles. The curve (2) for initial graupel of normal size was previously shown, along with cooling components from melting, sublimation and evaporation in Fig. 5.13. When precipitation size is halved, very rapid melting over the 0.5 km layer below 273 K combines with large evaporation over the lowest kilometer to produce a sharp double-peaked profile labeled as curve 1. Doubling the precipitation size reduces both evaporation and melting, and distributes cooling by melting over a much deeper layer so that a nearly constant total cooling

profile is produced over the lowest 1.5 km. Finally, by introducing rain rather than graupel at the 2.3 km level, total cooling is reduced by ~ 50% in the absence of melting, and the resulting cooling profile displays a linear and less sudden increase in cooling with decreasing height. This difference is much more significant than that indicated by the (nonlinear) 3-D cloud model results presented in Fig. 6.3. It is concluded that downdraft strength and initiation potential, both functions of total cooling and vertical gradients in total cooling (Section 5.3), are highly dependent on precipitation phase and size.

6.2 Environmental Influences

The environment in which storms form acts as the ultimate control on storm structure. Environmental conditions such as wind shear, PBL characteristics, and stability and moisture profiles at cloud levels influence the characteristics and distribution of precipitation which, as seen in previous sections, determines the strength and location of low-level downdrafts. In the following, the environmental controls PBL characteristics and temperature and moisture profiles at cloud levels are considered. Wind shear effects will not be addressed here. The thermodynamic-related controls are divided into two classes depending on whether or not a significant stable layer exists above the PBL. Following the terminology of Fawbush and Miller (1954), the soundings associated with the contrasting environments can be categorized into:

(a) type I soundings, which possess a moist PBL capped by a strong stable layer (inversion) above which (usually) very dry and relatively unstable air is found;

(b) type II soundings, which have a PBL (moist to dry) not capped by an inversion.

Soundings of cases examined in this study (Fig. 4.1) are largely type II except for 6/12, and to a very weak degree, 8/1 and 7/22.

Observations from previous sections indicate that PBL depth (and related dryness) and downdraft strength are strongly related. The relationship is evident in Fig. 6.5, in which selected observations taken from Section 4 and elsewhere were combined to produce a plot of maximum measured downdraft strength (ranging from < 5 to > 15 m s^{-1}) as a function of PBL depth (ranging from 1.0 to 4.5 km). This plot

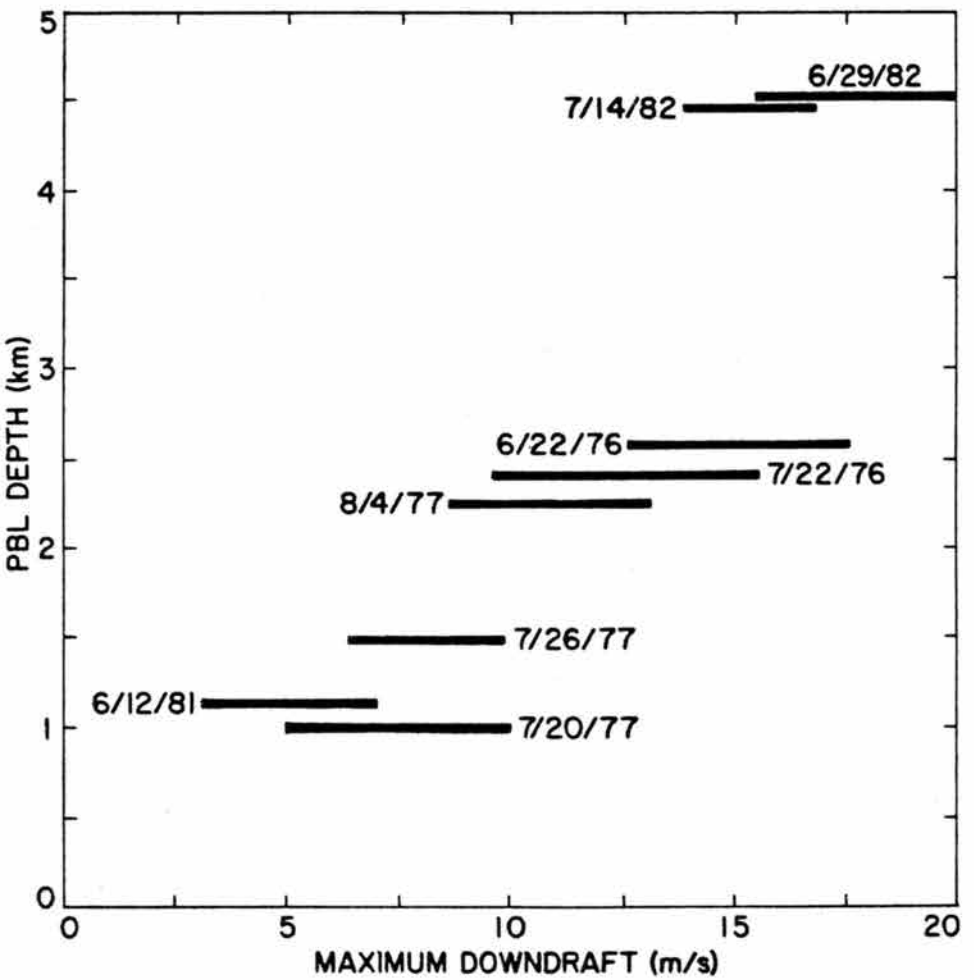

Fig. 6.5. Plot of maximum measured downdraft strength vs. planetary boundary layer (PBL) depth for 8 contrasting environments. Sources of data are: 6/29/82, Hjelmfelt (1984); 7/14/82, Rodi et al. (1983); 6/22/76, Miller and Fankhauser (1983); 7/22/76, Foote and Frank (1983).

indicates quite conclusively that strong downdrafts for type II soundings are generally associated with deep PBL. This relation is not linear because variations in precipitation characteristics such as mean size and mixing ratio strongly modulate downdraft intensity. For example, three cases in Fig. 6.5 (8/4, 7/22 and 6/22) appear close together even though individual storm and precipitation characteristics differed greatly. The 8/4 case exhibited weak updrafts, moderate precipitation rates and (inferred) small-sized precipitation, in contrast to the 6/22 storm which contained strong updrafts and very heavy precipitation consisting of hail and rain. Thus, the relation suggested in Fig. 6.5 contains a number of hidden precipitation-related factors, namely size and intensity. Its predictive value may be improved by considering also CAPE, echo intensity, etc. Development of downdrafts within this layer generally begins within the PBL; downdrafts then smoothly work upward to their maximum height.

Two 2-D sensitivity experiments listed in Table 6.1 were designed to test the sensitivity of low level downdrafts to changes in PBL depth and dryness. In Run 3 the PBL was moistened to greater heights as shown in Fig. 6.1. In agreement with expectations, resulting downdrafts were 1 m s^{-1} weaker (due to decreased evaporation in the PBL) than in the control Run 4 despite greater precipitation rates (~ 1 g kg^{-1}) in Run 3 which would tend to diminish this difference. In another experiment (Run 5) the dry adiabatic temperature profile was lifted from 58 kPa to 50 kPa (see Fig. 6.1). Resulting increases in downdraft strength of ~ 1 m s^{-1} were suprisingly small (although in the right direction) considering that 1.8 g kg^{-1} more rain was generated. Again, it should be remembered that the model response is nonlinear and somewhat

artificial due to the two-dimensionality of the simulation. However, these results are consistent with Fig. 6.5: deeper and drier PBL are more conducive to strong downdrafts, other factors being equal.

Thermodynamic processes associated with downdrafts existing in moist, shallow PBL as opposed to deep, dry PBL may be expected to exhibit large differences. Vertical profiles of rates of cooling by evaporation and melting were calculated for two contrasting type II soundings: the shallow PBL case of 7/21 and a deep PBL case (6/22/82) taken from Hjelmfelt (1984). Storms in both cases produced heavy rainfall and gusty surface winds which were especially strong in the 6/22/82 case. Fig. 6.6 illustrates profiles of cooling rates

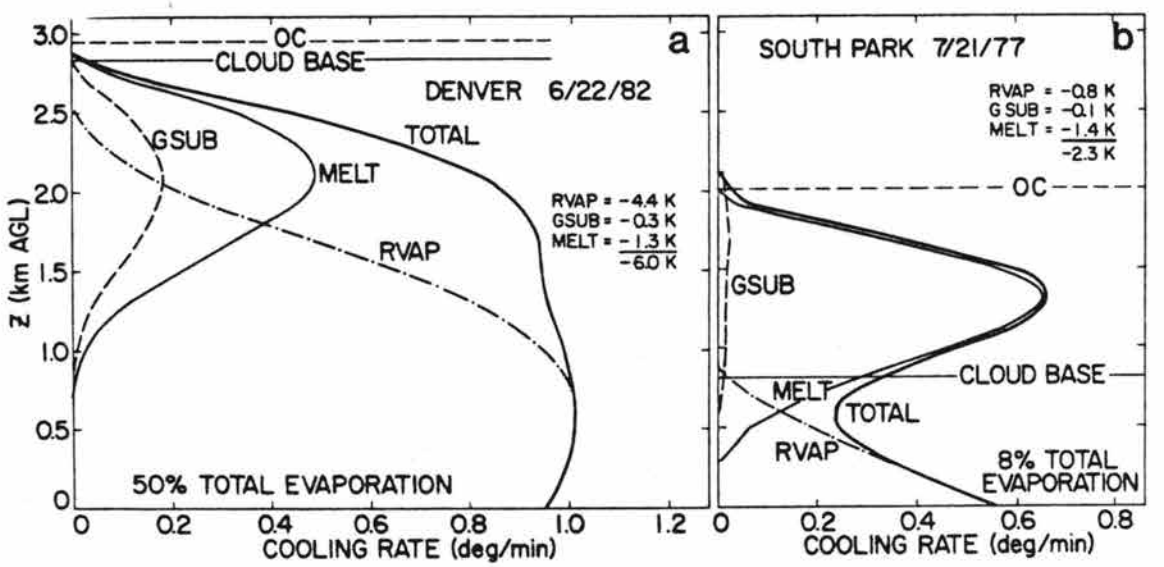

Fig. 6.6. Vertical profiles of cooling rates calculated as in Figs. 5.13 and 6.4 for (a) a deep, dry PBL (6/22/82), and (b) a shallow, moist PBL (7/21/77). Cloud base and melting level are shown for each case.

(calculated as in Fig. 6.4) by melting and evaporation resulting from the introduction of 3.6 g kg^{-1} graupel mixing ratio above the 273 K (0 C) level (within cloud) for each case. In the shallow PBL case the 273 K level residing 1.2 km above cloud base produces a double-peaked

structure in total cooling, 35% of which is achieved by rain evaporation. Greatest cooling due to melting actually occurs above cloud base. A completely different behavior is seen for the deep PBL case in which the 273 K level and cloud base nearly coincide. Here, Cloud base and melting level are shown for each case. significantly greater total cooling, 70% of which is accomplished by evaporation and sublimation, occurs below cloud base. Because melting and evaporation curves overlap, a double-peaked total cooling profile does not appear. In this dry case 50% of the initial precipitation is evaporated between cloud base and the surface, as opposed to 8% in the 7/21 case.

These calculations quantitatively explain the behavior indicated in Fig. 6.5. Differences between shallow PBL and deep PBL arise from greater total evaporation in the latter (melting effects were nearly equivalent) given similar precipitation conditions. In reality, precipitating convection forming above deep and dry mixed layers will generate lower precipitation rates. For extremely dry conditions (e.g., Brown et al., 1982) much of this precipitation undergoes nearly complete evaporation between the surface and cloud base, in which case the relative effects of evaporation/sublimation and melting are well approximated by

$$L_{vl}/L_{il} \simeq 7.5.$$

Static stability above the PBL constitutes a second environmental influence on downdraft structure. Effects of stability promote downdrafts wherever lapse rates are nearly dry adiabatic and inhibit downdrafts where lapse rates are moist adiabatic. In all soundings of cases examined in Section 4 (Fig. 4.1), a transition (T) level was defined as the point where environmental lapse rates change (sometimes

very gradually) from conditionally unstable (nearly dry adiabatic) to approximately absolutely stable. In most cases the T layer was found to represent the approximate maximum instantaneous downdraft height, as well as the greatest height from which surface downdraft air originated.

There are examples of severe storm environments in which downdraft strength and maximum height cannot be defined by procedures outlined above. A classic severe storm type I sounding shown in Fig. 6.7 indicates a strong stable layer separating moist PBL air of relatively low θ_v from potentially warmer and much drier air above the inversion height. Previous reasoning would predict relatively shallow and weak to moderate downdrafts within the PBL, virtually separated from downdrafts existing within the dry stable layer above the inversion, as in the 6/12 case described in Section 4.3. However, this environment supported widespread, intense storms which generated surface outflow winds of 30-40 m s^{-1}, large hail and tornadoes. Downdrafts above the inversion height within storms in such environments would certainly be very quickly damped by positive buoyancy upon reaching the inversion as demonstrated previously in Fig. 4.42. This inversion can be reduced or eliminated (i.e., the θ_v of the upper unstable dry layer reduced) by cooling from evaporation, sublimation and melting of precipitation falling outside of the cloud core into the highly subsaturated environment. Such a process was considered by Betts (1984) for the 8/1 case described in Section 4.3 (sounding in Fig. 4.1i). Betts estimated that evaporation of 0.6 g kg^{-1} precipitation within the unstable midlevel region of the 8/1 environment (Fig. 4.1) would sufficiently reduce the θ_v of this layer so that it matched the PBL θ_v, at which

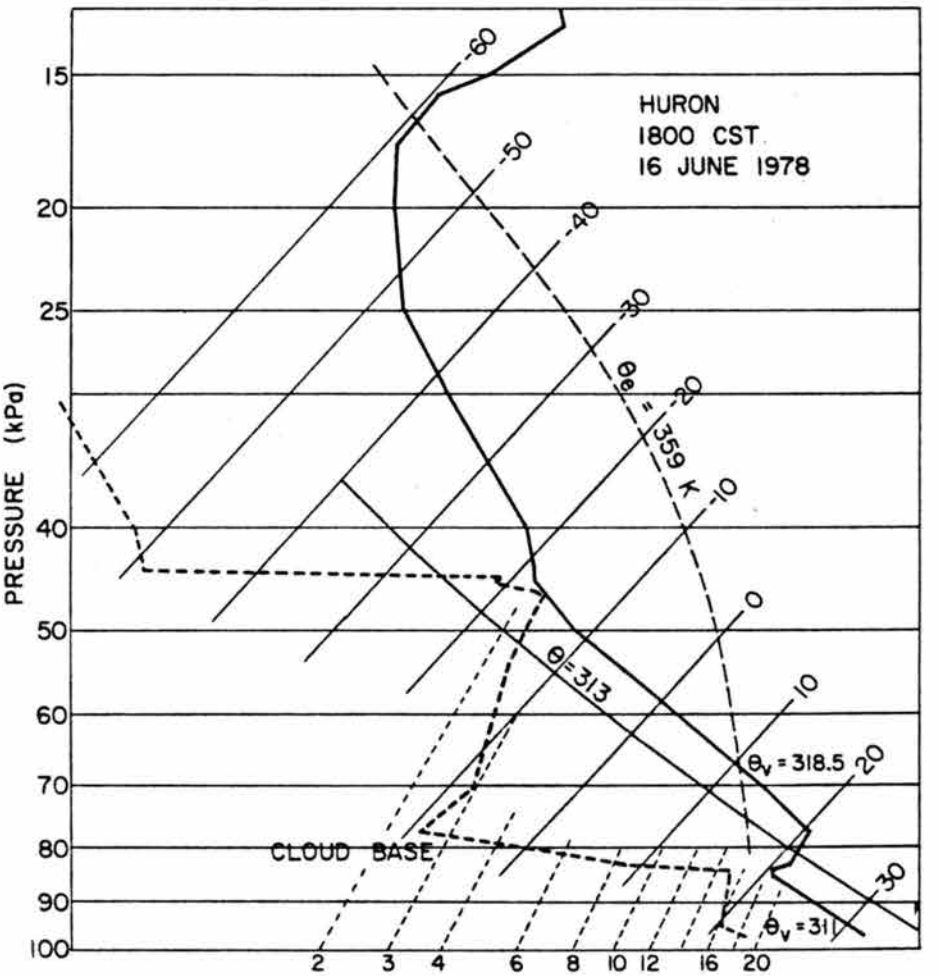

Fig. 6.7. Example of a type I severe storm sounding from Huron, South Dakota on 16 June 1978. Convective storms in the vicinity produced widespread damaging winds (estimates up to 40 m s^{-1}) in addition to tornadoes and large hail.

point deep, strong downdrafts would be produced upon further evaporation.

The sounding in Fig. 6.7 would be expected to undergo similar transformation by precipitation evaporation and melting in the layer between 80 and 50 kPa. In this case, however, much greater amounts of precipitation are required (~2.5 g kg^{-1}, melting effects included) to lower the θ_v of the upper, dry unstable layer so that it nearly matches the θ_v of the PBL. After this transformation (the processes of which are beyond the scope of this study) the thermodynamic structure would be similar to that of Type II soundings. It is obvious that the dryness of the elevated unstable layer is of critical importance. Such layers having greater moisture may not permit sufficient cooling by evaporation and hence would remain decoupled from the PBL, apparently the situation in the 6/12 case described in Section. 4.3.1.

For Type II environments (no inversion) the sensitivity of downdrafts to moist and dry middle layers was investigated in two 2-D simulations (Runs 1 and 2 in Table 6.1) on the 7/26 sounding (Fig. 6.1). The dry experiment ($T-T_d$ = 30 K above the PBL) produced stronger downdrafts at both midlevels (~3 m s^{-1}) and low levels (~2 m s^{-1}) than were generated by the moist case ($T-T_d$ = 2 K above the PBL). The greater relative strength at both levels for the dry case is a consequence of the greater total evaporation at the dry cloud levels. Results from simple diagnostic model experiments indicated a similar sensitivity to initial relative humidity. Greater total cooling is achieved for drier initial conditions because sublimational and evaporational cooling rates are greater throughout the entire downdraft descent. More conclusive results would require 3-D experiments (not

conducted in this investigation) which more accurately reproduce large-scale and systematic entrainment effects.

The dependence of downdraft structure and magnitude on wind shear cannot be evaluated here because controlled cloud model experiments with variation in wind shear were not conducted. It is expected that downdraft formation would proceed more quickly (as in 3-D simulations described by Klemp and Wilhemson, 1978a; Schlesinger, 1978) because entrainment effects would more quickly reduce updraft strength, and precipitation transport to the downshear wake would occur more quickly. However, effects of increasing wind shear on downdraft magnitude are unknown. For the time being, we can only speculate that increasing shear would produce weaker downdrafts as in the cloud model simulations of Klemp and Wilhelmson (1978a). In that study, downdrafts of lower magnitude resulted when vertical wind shear was increased, apparently because precipitation intensity over a given area was decreased.

7. GENERALIZED DOWNDRAFT CONCEPTUAL MODEL

Previous sections have disclosed the kinematic structure and dynamical, thermodynamical processes of mature downdrafts within precipitating convection. In this section these findings are integrated to produce a generalized mature storm low-level downdraft conceptual model.

General airflow and trajectory patterns within low-level downdrafts (regardless of location with respect to updrafts) are usually convergent from ~ 0.8 km upwards to downdraft top. Mass flux profiles typically increase rapidly with decreasing height as a result of strong buoyancy forcing below the melting level. Figure 7.1a illustrates several readily identifiable relative flow branches associated with an upshear-located downdraft. The environment in this case is assumed to have moderately-low wind shear in which relative environmental winds veer smoothly with height over the lowest 4 km as shown in Fig. 7.1c. A projection of these branches onto a vertical east-west plane (Fig. 7.1b) indicates processes along given trajectories and shows relationships between these branches and the assumed sounding (a type II sounding, defined in Section 6) plotted in Fig. 7.1c. This idealized sounding has a PBL ~ 2 km deep, a conditionally unstable layer between 2 and 4 km, and an absolutely stable structure above 4 km.

Downdraft branches comprising the low-level precipitation associated downdraft (Fig. 7.1a) can be categorized as 'midlevel,' those originating above the PBL, and 'up-down,' those originating within the

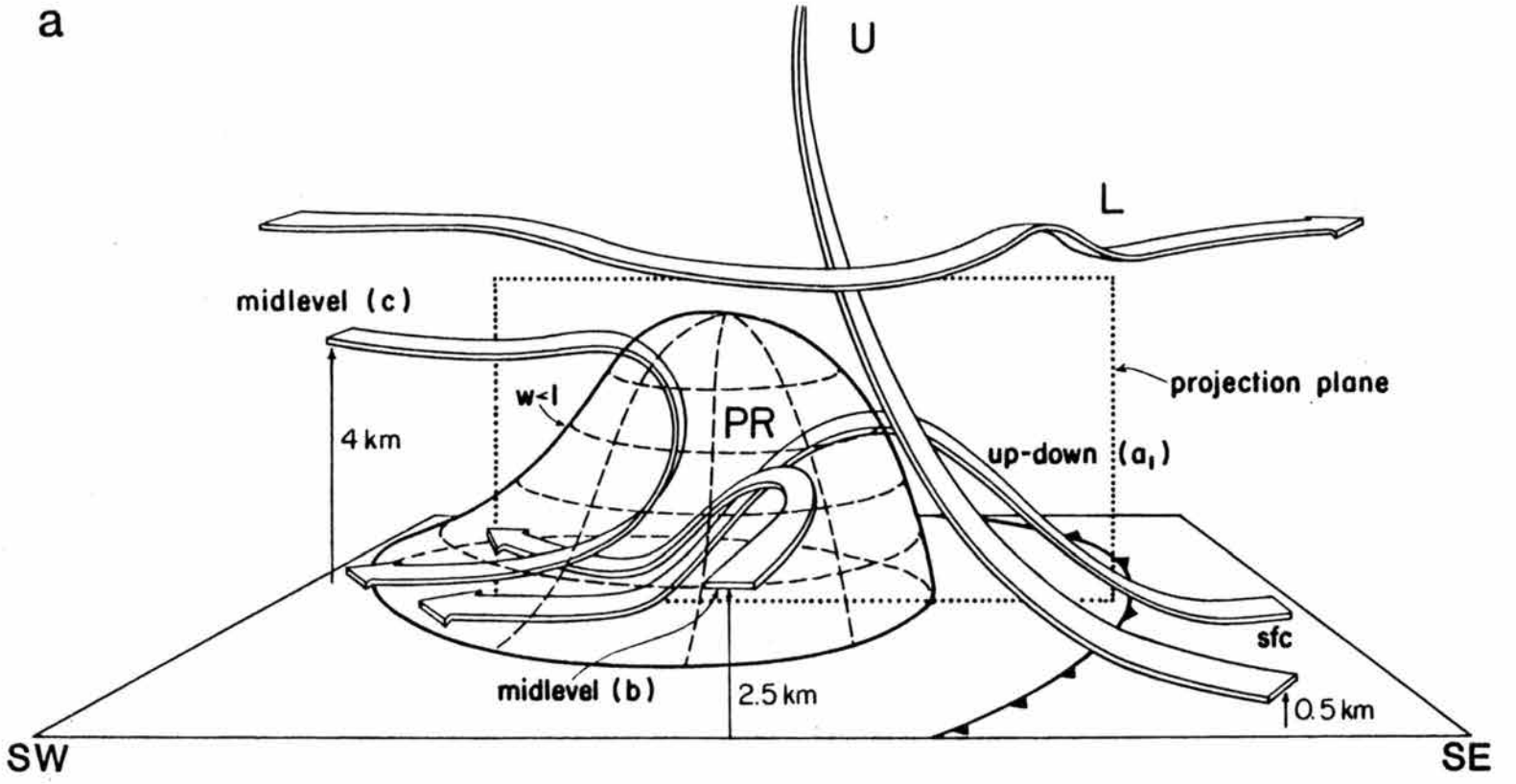

Fig. 7.1. (a) Schematic illustrating primary relative flow branches comprising the low-level precipitation-associated downdraft located along the upshear flank with respect to the updraft.

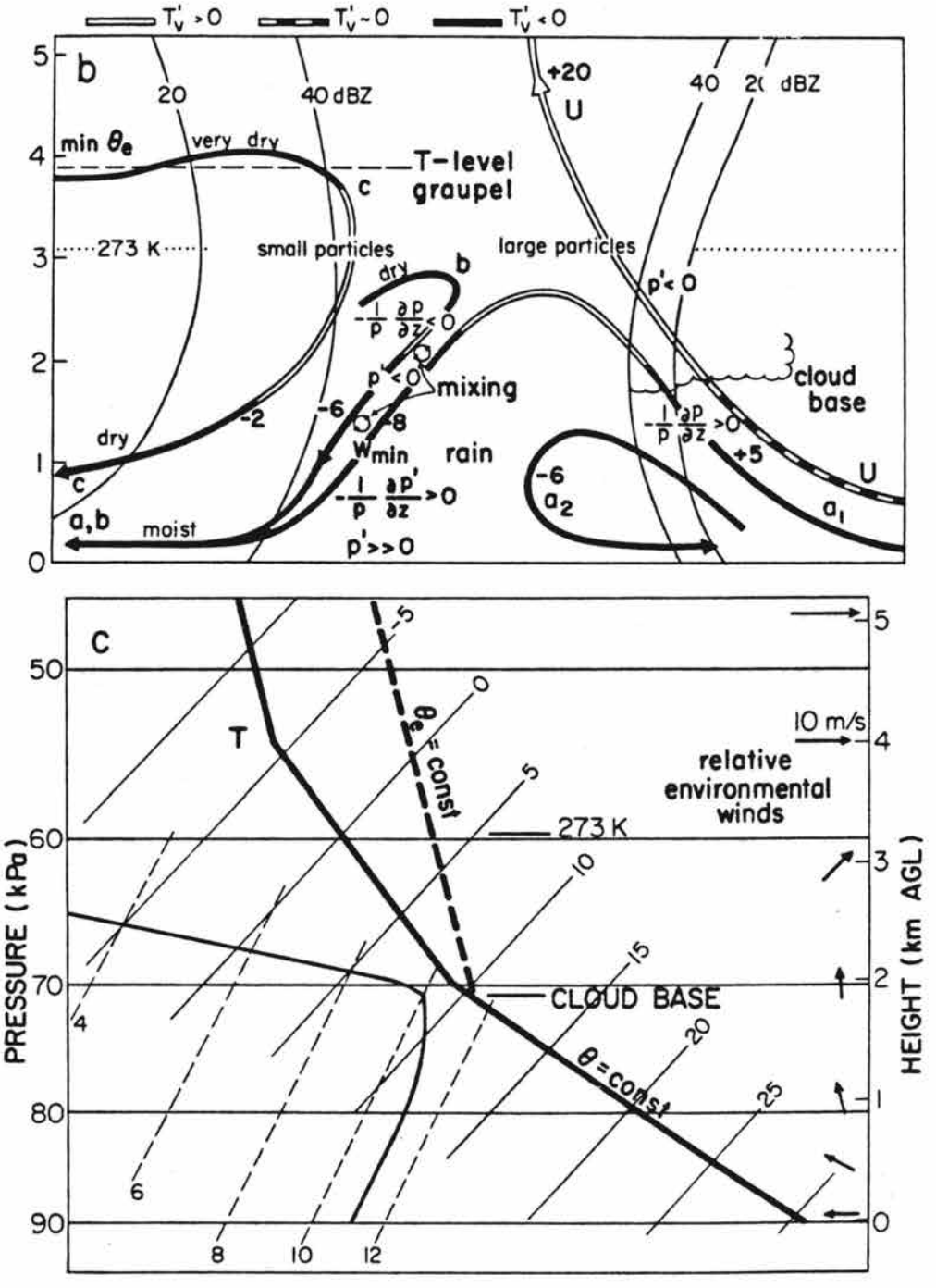

Fig. 7.1. (b) Projection of primary downdraft flow branches onto a vertical east-west plane. Physical processes along each branch are portrayed. (c) Sounding illustrating the relationship of downdraft properties to environmental structure.

PBL. The up-down branch (a) typically emerges during mature storm phases. Air parcels traveling the up-down branch usually originate within the downshear updraft inflow sector and may rise up to 4 km before descending within the precipitation-laden primary downdraft region. Two other downdraft branches (b and c) depicted in Fig. 7.1a,b represent midlevel trajectories originating within the 2-4 km AGL layer above the PBL from the southwestern quadrant. These trajectories are particularly pronounced during developing downdraft stages. Both trajectories exhibit a period of weak ascent before descending within precipitation, characteristics commonly found in both observations and model results. Flow along the midlevel branches transports low-valued θ_e air to regions near the up-down branch where mixing occurs (trajectory b), and more directly to the surface (trajectory c). Both Doppler analyses and cloud model results indicate that mixing occurs near the summit between moist air of the up-down branch and drier, lower-valued θ_e flowing along the midlevel branch b. Such mixing produces subsaturated, intermediate-valued θ_e air which promotes increased evaporation rates along the descending portion of up-down branch.

Dynamical processes along downdraft trajectories generally operate as follows. Along the up-down branch a in Fig. 7.1a,b, upward-directed pressure gradient forces lift negatively-buoyant PBL air above cloud base. This inflow air is rendered negatively buoyant by several processes, most notably evaporation of precipitation falling into the low-level inflow flank. Cloud shadowing and relative storm movement into more stable regions represent other such mechanisms. Pressure-gradient forces providing this lifting may be associated with the low-

level gust front, or with nonhydrostatic updraft-related dynamical processes (e.g., Rotunno and Klemp, 1982). This air often achieves positive buoyancy by some distance above cloud base, but relative horizontal motion transports the parcel outside the updraft to above the downdraft region, where one or more of the following processes may initiate downward acceleration: (i) a downward-directed pressure gradient force associated with downdraft dynamical/thermodynamical processes occurring at lower levels; (ii) a decrease in updraft-associated, upward-directed pressure gradient force as the parcel becomes further removed from the updraft base; (iii) increasing condensate loading as the parcel moves quasi-horizontally into the precipitation core; (iv) negative buoyancy produced by melting precipitation falling below the melting level; and (v) evaporational cooling of cloud and precipitation produced by turbulent mixing and organized inflow of dry air transported into the precipitation core by the midlevel branch. Below the melting level negative buoyancy is quickly reestablished by both melting and evaporation, and the parcels accelerate downward to near the 0.8 km level. At this point upward-directed (dynamic) pressure forces exceed total negative buoyancy, thus decelerating parcels during final descent. The behavior along midlevel branches is similar to that along the descending segment of the up-down branch, except initial positive buoyancy is produced by adiabatic warming exceeding sublimational and evaporational cooling within generally light precipitation.

Patterns of perturbation pressure (p') and associated pressure gradient forces therefore play an important role in downdraft structure, particularly during developing downdraft stages. The downdraft itself

exhibits a high-low p' couplet in which p' varies from -0.5 to -2.0 mb within the elevated low and up to +3 mb within the surface-based high. Three-dimensional cloud mode resls indicate that minimum p' are generally found ~ 0.6 km below the melting level approximately 10 min after precipitation (~ 2 g kg^{-1} or more) reaches the PBL. These pressure analyses support observational inferences presented in Section 4 and indicate that such pressure reductions are accomplished thermodynamically by very rapid cooling within adiabatic layers in and just above the PBL. Minima in p' subsequently decline to less than half original magnitude as the downdraft circulation reaches maturity. The induced pressure patterns are primarily related to downdraft processes and secondarily to storm-wide hydrostatic and dynamic effects. The buoyantly-produced low p' cell is produced by rapid increases in negative buoyancy by melting and evaporation within statically unstable low levels. The high p' cell is inferred to result primarily from dynamic effects (i.e., downdraft flow impinging on the surface) and secondarily from hydrostatic effects, consistent with the findings of Klemp and Rotunno (1983). An extension of the low p' region centered at 2 km near the updraft (Fig. 7.1b) is apparently produced by hydrostatic and positive buoyant accelerations within the updraft.

The relationship between downdrafts and negative p' as inferred herein differ from the interpretations of Klemp and Rotunno (1983) and of Wolfson (1983). In their high-resolution numerical simulations, Klemp and Rotunno (1983) postulated that a small scale "occlusion downdraft" (see Fig. 2.12) was forced primarily by an externally-produced vertical pressure gradient, generated mainly by a rotational wind field increasing in strength with decreasing height. Such rotation

or vorticity was produced by low-level tilting and was then rapidly amplfied by strong convergence at low levels. Wolfson (1983) similarly hypothesized that low-level rotation produced by tilting and subsequent stretching dynamically produced downburst activity as inferred from Doppler radar observations. This reduction, which apparently occurs on larger scales in Wolfson's (1983) data, may be explained in an alternative manner using the present results: downdraft processes may actually induce low pressure and hence amplify rotation by stretching of existing vorticity. Such a process may also explain the existence of rotating "microbursts" observed in several JAWS case studies mentioned at the end of Section 5.3.

Total cooling along downdraft branches (Fig. 7.1b) is provided by melting and evaporation of precipitation, and both these processes exhibit a direct dependence on precipitation concentration and an inverse dependence on precipitation size. Observations presented here and elsewhere indicate that downdrafts are often centered along the upshear reflectivity gradient. Because precipitation size exerts a dominating influence on measured reflectivity ($Z_e \sim nD^6$) such patterns may be related to horizontal gradients in precipitation size. Greatest cooling rates exist within heavy precipitation (consisting of smaller-sized particles further removed from the updraft) below the melting level, and particularly below cloud base where evaporation may augment melting. Melting accounts for 10-60% total cooling along given downdraft trajectories, the fraction being greatest along up-down trajectories in which parcels typically remain within the precipitation melting zone for longer periods. Precipitation evaporation is typically greater within drier air along midlevel trajectories.

The strength of low-level downdrafts depends on a number of factors: precipitation size and intensity, environmental dryness and stability at middle levels, and planetary boundary layer (PBL) characteristics such as depth and stability. The relative magnitude of air mass flux along the up-down branch appears to be proportional to the stability of air entering this branch. Observational and modeling evidence indicates that stable air at low PBL levels may more effectively produce up-down type trajectories. This downdraft branch therefore becomes more pronounced during mature storm stages when temperatures of the low-level inflow may be reduced. Observational evidence indicates that downdraft strength is proportional to PBL depth--deeper PBL generally are more conducive to stronger, deeper downdrafts, other factors remaining equal. Environmental dryness and stability above the PBL exert weaker controls on the strength of the midlevel branch. Two-dimensional model results show slight increases in downdraft strength under very dry conditions. Finally, precipitation characteristics (size in particular) probably dictate strongest controls on downdraft strength. Cloud model results and related calculations demonstrate considerable sensitivity to changes in precipitation size and phase. By reducing characteristic precipitation size by 50%, cooling rates increase by up to 100% and downdraft magnitudes are enhanced by 20-40%.

Descent rates along midlevel branches depend on static stability of environmental air at the origin level. Greater stability of air feeding such branches generally produces slower descent rates. The upper-limiting height of air along this branch appears to be the T (transition) level where the environmental temperature lapse rate turns

absolutely stable. For example, parcels b and c in Fig. 7.1 follow different paths because c originates in the upper regions of the conditionally unstable layer. Because its initial θ_v is 3.5 K greater than the PBL θ_v, total cooling on the order of 3.5 K needs to be attained before fast descent (under negatively-buoyant conditions) is possible. Parcels like c typically descend at rates of 1-3 m s^{-1} outside heaviest precipitation and reach the surface some distance behind (to the rear of) convective precipitation cores. This accounts for the frequent occurrence of lowest-valued θ_e air at the surface being located along the upshear sector (e.g., cases 7/26 and 8/4 examined herein, and cases examined by Lemon, 1976; Barnes, 1978a,b; and Ray et.al., 1981). Detailed calculations indicate that thermodynamic and kinematic characteristics along c-like trajectories appear to approach characteristics along trajectories within mesoscale downdrafts (Zipser, 1977; Leary and Houze, 1979b).

The structure of downdrafts located downshear from updrafts differs from that of upshear-located downdrafts. The magnitude of the shear vector appears to be the best parameter for differentiating relative downdraft location. In the cases examined herein, downdrafts exhibit an increasing tendency towards downshear location as wind shear increases. However, boundary layer convergence zones may also influence downdraft location. For example, when such convergent zones promote new cloud growth upshear from existing convection, downdraft activity is favored downshear within decaying convection as in the low-shear cases of 7/26 (Storm B) and 7/25. Another factor which influences relative downdraft location is the general storm structure. In particular, squall line

in this report) and to some extent in Klemp et al. (1981), and in cloud model simulations of tropical squall lines (i.e., Miller and Betts, 1977; Thorpe et.al., 1982). The present results have identified the structure and dynamical/thermodynamical processes acting along this branch. It has also identified the midlevel branch commonly recognized in many other studies (Browing, 1964; Foote and Frank, 1983; Klemp et al, 1981; and others). We have shown here that the maximum height attained by the midlevel branch is determined by stability, and that inflow to the midlevel branch is continuous (from its maximum height to the level of maximum downdraft near 0.8 km) rather than from one particular height interval as portrayed in Fig. 2.4.

A segment of the midlevel branch (i.e., branch c in Fig. 7.1) may be equated with the rear flank downdraft (RFD) defined and described in Section 2.3. In cases examined here, however, an upshear-located downdraft perhaps similar in some respects to the RFD, was identified in perhaps three cases, 7/26, 8/4 and 8/1. In each of these cases this upshear downdraft was weaker than precipitation core downdrafts, contrary to the speculations of Lemon and Doswell (1979), who inferred that the RFD originating at relatively high levels is typically much stronger than other downdrafts. Other calculations on precipitation cooling rates presented in Section 6 also indicate that RFD-type downdrafts originating near middle levels would be relatively weak outside of heavy precipitation unless nearly dry adiabatic stratification existed.

8. CONCLUSIONS

8.1 Primary Findings and Conclusions

This study has investigated kinematic, thermodynamic and dynamic aspects of downdrafts within precipitating convective clouds. The primary findings and conclusions are as follows:

(a) Four independent donwdraft types can be identified: (i) penetrative downdrafts, common to nonprecipitating clouds and upper regions of precipitating clouds; (ii) upper-level downdrafts resulting when updraft air surpasses an equilibrium level, cools upon further ascent and then descends to within several kilometers of cloud top; (iii) middle-level cloud-edge downdrafts, forced primarily by negative buoyancy associated with evaporation and melting of cloud and precipitation within and just outside cloud boundaries (most prominantly within the downshear cloud flank); and (iv) the low-level precipitation-associated downdraft forced at low levels by precipitation loading, evaporation and melting. This latter downdraft may attain relatively large scales, on the order of the horizontal dimension of precipitating regions at low levels. Such large scales provide a clear distinction from penetrative-type downdrafts of ~ 1 km maximum scale. Downdrafts of all types are relatively shallow when compared to updrafts. The low-level precipitation-associated downdraft, in particular, seldom exceeds a depth of 4 km. Maximum speeds in this downdraft typically occur just below one kilometer where greatest static instability usually exists.

(b) Although the low-level downdraft is vertically continuous, it is convenient to define two readily-identifiable general branches, one termed an up-down branch originating within the PBL, and the second a midlevel branch arriving from the relative upwind direction above the PBL. The midlevel branch is most pronounced during developing downdraft stages. The up-down downdraft branch contrastingly becomes more significant during mature storm stages when temperatures of the low-level inflow may be reduced.

(c) Downdraft descent rates depend on static stability of environmental air at the origin level, in agreement with the diagnostic model studies of Kamburova and Ludlam (1966). In general, greater stability of air feeding downdraft circulatons produces slower descent rates. The upper-limiting height of downdraft air reaching the surface appears to be the T (transition) level where environmental temperature structure turns absolutely stable (assuming that initial temperature perturbations are small).

(d) Low-level downdrafts are driven from low levels by melting and evaporation of precipitation. Loading at low levels and evaporational cooling associated with entrainment at midlevels appears to provide only secondary forcing, contrary to what was originally hypothesized. Greatest local negative buoyancy production occurs within heavy precipitation usually below the melting level and particularly below cloud base where most unstable lapse rates exist. Melting accounts for 10-60% total cooling along given downdraft trajectories, the fraction being greatest along up-down trajectories in which parcels remain within the precipitation melting zone for longer periods. In the High Plains cases examined here, the nearness of cloud base and the melting (273 K)

level produce an overlap in melting and evaporation cooling profiles, and thus concentrate cooling to the lowest 2-4 km. Such strong low-level forcing was related to buoyantly-produced pressure reductions which were strongest during developing downdraft stages (up to 2 mb) just below the 273 K level. The magnitude of buoyantly-produced pressure reductions is proportional to temperature and its vertical gradient, relative humidity and precipitation characteristics. Pressure forcing was found to draw air laterally into the downdraft circulation, and to extend the maximum downdraft height by forcing positively-buoyant air downwards from above. One may speculate that buoyant forcing within precipitation-associated downdrafts would be weaker in moist PBL environments at low elevations (where the melting level typically resides several kilometers above cloud base) because evaporation contributions to total cooling would be smaller.

(e) Finally, precipitation size and phase represent the most important downdraft intensity controlling factors. Although this aspect has been concluded elsewhere (e.g. Kamburova and Ludlam, 1966) it should be underscored here. For shallow PBL which typically exist over much of the U.S., melting of ice-phase precipitation represents the primary cooling source and therefore serves as a primary downdraft initiation mechanism. For all environments, strong cooling rates produced by evaporation and melting are highly dependent upon precipitation size. Knowledge of precipitation characteristiscs is thus required in order to accuratey simulate and/or parameterize precipitating convection, and in particular downdrafts. These precipitation parameters are probably influenced by: (i) variation of precipitation characteristics as a function of environmental parameters such as boundary layer mixing

ratio, potential updraft parcel buoyancy (or CAPE), and even wind shear; (ii) dependence of precipitation characteristics as a function of position within a given storm (this includes separating convective core precipitation from anvil precipitation), and (iii) temporal behavior of precipitation characteristics within a given storm.

Of the five conclusions listed and described above, three may be considered to be new findings in this study. The first is the recognition that several independent downdrafts [conclusion (a)] may exist simultaneously within precipitating convection. The second is the identification of (i) dynamical and thermodynamical processes active along up-down and midlevel downdraft branches, and (ii) the prominence of the up-down branch at storm maturity. Finally, we have established that strong dynamical processes associated with cooling by evaporation and melting at low levels can produce appreciable pressure reductions above the level of strong thermodynamic forcing and hence expand the downdraft region via pressure gradient forces. Hence, precipitation-associated downdrafts are driven at low levels.

8.2 Ambiguities and Unknowns

This study, like any other, has prompted new questions in addition to answering some of those originally posed in Section 2.5. One aspect not closely addressed above concerns the dependence of downdraft characteristics on wind shear. The observational results indicate that downdraft location moves to the downshear cloud flank under higher-shear conditions, but the response of other downdraft characteristics, such as lateral dimension, intensity and depth, to increasing wind shear remains unclear.

Because this study examined precipitating convection forming in High Plains environments, the results may not be applicable to other environments not considered, such as very moist environments typical of the southeastern U.S., and type I severe storm environments (with strong inversions capping the PBL) often found over the Great Plains. This latter environment, in particular, is intriguing because transformations by precipitation-induced cooling may be required to produce a modified environment capable of producing strong downdrafts. This will be a topic for future study.

Although one may apply the results presented in this and preceding sections to draw inferences on the structure and dynamics of downbursts (which presumably occur from strong downdrafts whose low-level outflow generates damaging winds), a complete discussion is beyond the scope of this study. However, results from previous sections can be summarized to briefy describe the diversity of conditions conducive for strong downdraft generation. Some possible mechanisms are:

(a) evaporation of precipitation into deep and dry PBL (Fig. 6.5);

(b) evaporation, melting and loading of excessive precipitation concentrations whose generation may be associated with strong updraft impulses and their subsequent collapse;

(c) introduction or generation of abnormally small precipitation particles within a given storm, which would promote higher rates of cooling by melting and evaporation;

(d) establishment of an up-down downdraft circulation in which the negative buoyancy of air feeding this branch is such that, when combined with pressure gradient forces which act to initially lift the air, allows a maximum downdraft speed as

air parcels moving through this branch exit the region of strong upward forcing [this mechanism may apply to long-lived downburst storms such as those documented by Fujita (1978), Fujita and Wakimoto (1981), and Johns and Hirt (1983)];

(e) small-scale microbursts produced when penetrative downdrafts forming at middle cloud levels are superimposed with global precipitation-associated downdrafts existing at low levels.

It is obvious that the above-listed mechanisms may span a wide variety of environmental and convective storm types.

Several recommendations for future research on downdrafts can be put forth: (a) Future cloud model experiments should examine downdraft formation and evolution under ideal type II environments having no shear and unidirectional or smoothly-varying vertical shear. Such experiments would establish a relation between downdrafts and wind shear, and would further elucidate the nature of downdraft-induced pressure perturbations. (b) Analyses of model results should additionally diagnose pressure fields so that dynamic and buoyant components can be resolved. (c) Simulations on type I environments should be conducted to examine the transformations necessary for production of strong and deep low-level downdrafts. (d) Future cloud model experiments should be designed to test the sensitivity of low to middle level downdrafts on turbulent entrainment. This naturally requires a high-level turbulence parameterization and relatively fine grid resolution. (e) Other downdraft types such as middle level cloud-edge downdrafts and large-scale subsidence regions ajacent to precipitating convection (see Fig. 2.2) need further study before convective cloud downdrafts can be parameterized accurately.

REFERENCES

Barnes, G. and M. Garstang, 1982: Subcloud layer energetics of precipitating convection. Mon. Wea. Rev., 110, 102-117.

Barnes, S.L., 1978a: Oklahoma thunderstorms on 29-30 April 1970. Part I: Morphology of a tornadic storm. Mon. Wea. Rev., 106, 673-684.

Barnes, S.L., 1978b: Oklahoma thunderstorms on 29-30 April 1970. Part II: Radar-observed merger of twin hook echoes. Mon. Wea. Rev., 106, 685-696.

Battan, L.J., 1975: Doppler radar observations of a hailstorm. J. Appl. Meteor., 14, 98-108.

Battan, L.J., 1980: Observations of two Colorado thunderstorms by means of a zenith-pointing Doppler radar. J. Appl. Meteor., 19, 580-592.

Battan, L.J. and J.B. Theiss, 1970: Measurements of vertical velocities in convective clouds by means of a pulsed Doppler radar. J. Atmos. Sci., 27, 293-298.

Betts, A.K., 1976: The thermodynamic transformation of the tropical subcloud layer by precipitation and downdrafts. J. Atmos. Sci., 33, 1008-1020.

Betts, A.K., R.W. Grover, and M.W. Moncrieff, 1976: Structure and motion of tropical squall lines over Venezuela, Quart. J. Roy. Meteor. Soc., 102, 395-404.

Betts, A.K., 1982a: Saturation point analysis of moist convective overturning. J. Atmos. Sci., 39, 1484-1505.

Betts, A.K., 1982b: Cloud thermodynamic models in saturation point coordinates. J. Atmos. Sci., 39, 2182-2191.

Betts, A.K., 1984: Boundary layer thermodynamics of a High Plains severe storm. Mon. Wea. Rev., 112.

Betts, A.K. and M.F. Silva Dias, 1979: Unsaturated downdraft thermodynamics in cumulonimbus. J. Atmos. Sci., 36, 1061-1071.

Bluestein, H.B., and C.R. Parks, 1983: A synoptic and photographic climatology of low-precipitation severe thunderstorms in the Southern Plains, Mon. Wea. Rev., 111, 2034-2046.

Boatman, J.F. and A.H. Auer, 1983: The role of cloud top entrainment in cumulus clouds. J. Atmos. Sci., 40, 1517-1534.

Bohne, A.R., and R.C. Srivastava, 1975: Random errors in wind and precipitation fall speed measurement by a triple Doppler radar system. Tech. Report No. 37, Lab. Atmos. Probing, Univ. of Chicago, 44 pp.

Braham, R.R., 1952: The water and energy budgets of the thunderstorm and their relation to thunderstorm development. J. Meteor., 9, 227-242.

Brock, F.V., and P.K. Govind, 1977: Portable automated mesonet in operation. J. Appl. Meteor., 16, 299-310.

Brown, J.M., 1979: Mesoscale unsaturated downdrafts driven by rainfall evaporation: A numerical study. J. Atmos. Sci., 36, 313-337.

Brown, J.M., K.R. Knupp, and F. Caracena, 1982: Destructive winds from shallow, high-based cumuli. Preprints 12th Conf. on Severe Local Storms, Amer. Meteor. Soc., 272-275.

Browning, K.A., 1964: Airflow and precipitation trajectories within severe local storms which travel to the right of the winds. J. Atmos. Sci., 21, 634-639.

Browning, K.A., 1977: The structure and mechanism of hailstorms. Meteor. Monogr., No. 38, Amer. Meteor. Soc., 1-39.

Browning, K.A., and F.H. Ludlam, 1962: Airflow in convective storms. Quart. J. Roy. Meteor. Soc., 88, 117-135.

Browning, K.A., J.C. Fankhauser, J.-P. Chalon, P.J. Eccles, R.G. Strauch, F.H. Merrem, D.J. Musil, E.L. May, and W.R. Sand, 1976: Structure of an evolving hailstorm, Part V: Synthesis and implications for hail growth and suppression. Mon. Wea. Rev., 104, 603-610.

Byers, H.R. and R.R. Braham, 1949: The Thunderstorm. U.S. Weather Bureau, Washington, D.C., 287 pp.

Chalon, J.-P., J.C. Fankhauser, and P.J. Eccles, 1976: Structure of an evolving hailstorm. Part I: General characteristics and cellular structure, Mon. Wea. Rev., 104, 564-575.

Chisholm, A.S., and J.H. Renick, 1972: The kinematics of multicell and supercell hailstorms. Alberta Hail Studies, Research Council of Alberta Hail Studies, Rep. 72-2, 24-32, 53 pp.

Clark, T.L., 1979: Numerical simulations with a three-dimensional cloud model: Lateral boundary condition experiments and multicellular storm simulations. J. Atmos. Sci., 36, 2191-2215.

Clark, T.L. and R. List, 1971: Dynamics of a falling particle zone. J. Atmos. Sci., 28, 718-727.

Cotton, W.R., and R.A. Anthes, 1985: The Dynamics of Clouds and Mesoscale Weather Systems. Part I: The Dynamics of Clouds, to be published by Academic Press.

Cotton, W.R., R.L. George, and K.R. Knupp, 1982: An intense, quasi-steady thunderstorm over mountanous terrain -- Part I: Evolution of the storm-initiating mesoscale circulation. J. Atmos. Sci., 39, 328-342.

Cotton, W.R., M.A. Stephens, T. Nehrkorn, and G.J. Tripoli, 1982: The Colorado State University three-dimensional cloud/mesoscale model - 1982. Part II: An ice phase parameterization. J. de Rech. Atmos., 16, 295-320.

Cotton, W.R., and G.J. Tripoli, 1978: Cumulus convection in shear flow-- Three dimensional numerical experiments. J. Atmos. Sci., 35, 1503-1521.

Cotton, W.R., G.J. Tripoli, and R.M. Rauber, 1985: Numerical simulation of the effects of varying ice crystal nucleation rates and aggregation processes on orographic snowfall. To be submitted to J. Clim. Appl. Meteor.

Das, P., 1964: Role of condensed water in the life cycle of a convective cloud. J. Atmos. Sci., 21, 404-418.

Das, P., and M.C. Subba Rao, 1972: The unsaturated downdraft. Ind. J. Meteor. Geophys., 23, 135-144.

Deardorff, J.W., 1980: Cloud top entrainment instability. J. Atmos. Sci., 37, 131-147.

Desai, B.N., and S. Mal, 1938: Thundersqualls of Bengal, Beiter. Geophys., 53, 285-304.

Douglas, R.H., 1964: Hail size distribution. Proc. Eleventh Radar Wea. Conf., Amer. Meteor. Soc., 146-149.

Doviak, R.J., D.S. Zrnic, and D.S. Sirmans, 1979: Doppler weather radar. Proc. IEEE, 67, 1522-1553.

Drazin, P.G. and L.N. Howard, 1964: Hydrodynamic stability and parallel flow of an inviscid fluid. Adv. Appl. Mech., 9, 1-89.

Dye, J.E., L.J. Miller, B.E. Martner, and Z. Levin, 1980: Dynamical-microphysical evolution of a convective storm. NCAR Tech. Note NCAR/TN-151+STR, 248 pp.

Dye, J.E., L.J. Miller, B.E. Martner, and Z. Levin, 1982: The 25 July 1976 case study: Environmental conditions, reflectivity structure, and evolution. Hailstorms of the Central High Plains, Vol. 2, Chap 21. The National Hail Research Experiment. C.A. Knight and P. Squires, Eds., Colorado Associated Univ. Press, Boulder, 197-209.

Dye, J.E., B.E. Martner and L.J. Miller, 1983: Dynamical-microphysical evolution of a convective storm in a weakly-sheared environment. Part I: Microphysical observations and interpretation. J. Atmos. Sci., 40, 2085-2096.

Emanuel, K.A., 1981: A similarity theory for unsaturated downdrafts within clouds. J. Atmos. Sci., 38, 1541-1557.

Fankhauser, J.C., 1976: Structure of an evolving hailstorm, Part II: Thermodynamic structure and airflow in the near environment. Mon. Wea. Rev., 104, 576-587.

Fankhauser, J.C., 1982: Hail Storms of the Central High Plains, Vol. 2, Part I: 22 June 1976 case study - a complex multicellular hail and rainstorm. Chap. 13: Large-scale influences, radar echo structure and mesoscale circulations. C. Knight and P. Squires, Eds., Colorado Assoc. Univ. Press., Boulder, 1-34.

Fankhauser, J.C., I.R. Paluch, W.A. Cooper, D.W. Breed, and R.E. Rinehart, 1982: Hailstorms of the Central High Plains, Vol. I: The National Hail Research Experiment. Air Motion and Thermodynamics, Chap. 6.4, C. Knight and P. Squires, Eds., Colo. Assoc. Univ. Press, 134-145.

Foote, G.B. and J.C. Fankhauser, 1973: Airflow and moisture budget beneath a Northeast Colorado hailstorm. J. Appl. Meteor., 12, 1330-1353.

Foote, G.B. and H.W. Frank, 1983: Case study of a hailstorm in Colorado. Part III: Airflow from triple-Doppler measurements. J. Atmos. Sci., 40, 686-707.

Foote, G.B., and C.G. Wade, 1982: Case study of a hailstorm in Colorado. Part I: Radar echo structure and evolution. J. Atmos. Sci., 39, 2828-2846.

Forbes, G.S., and R.M. Wakimoto, 1983: A concentrated outbreak of tornadoes, downbursts and microbursts, and implications regarding vortex classification. Mon. Wea. Rev., 111, 220-235.

Frank, H.W., and G.B. Foote, 1982: Hailstorms of the Central High Plains, Vol. 2, Part II, Chap. 18. The 22 July 1976 case study: Storm airflow, updraft structure, and mass flux from triple-Doppler measurements. C. Knight and P. Squires, Eds., Colorado Assoc. Univ. Press, Boulder, 131-162.

Fritsch, J.M., 1975: Cumulus dynamics: Local compensating subsidence and its implications for cumulus parameterization. Pure Appl. Geophys., 113, 851-867.

Fujita, T.T., 1959: Precipitation and cold air production in mesoscale thunderstorm systems. J. Meteor., 16, 454-466.

Fujita, T.T., 1974: Overshooting thunderheads observed from ATS and Learjet. SMRP Res. Paper No. 117, Dept. of Geophysical Science, Univ. of Chicago, 29 pp.

Fujita, T.T., 1978: Manual of downburst identification for project NIMROD. Satellite and Mesometeorology Paper No. 156, Dept. of Geophysical Science, Univ. of Chicago, 104 pp.

Fujita, T., 1981: Tornadoes and downbursts in the context of generalized planetary scales. J. Atmos. Sci., 38, 1511-1534

Fujita, T.T., and H.R. Byers, 1977: Spearhead echo and downburst in the crash of an airliner. Mon. Wea. Rev., 105, 129-146.

Fujita, T.T., and F. Caracena, 1977: An analysis of three weather-related aircraft accidents. Bull. Amer. Meteor. Soc., 58, 1164-1181.

Fujita, T. and R.M. Wakimoto, 1981: Five scales of airflow associated with a series of downbursts on 16 July 1980. Mon. Wea. Rev., 109, 1438-1456.

Gal-Chen, T., 1982: Errors in fixed and moving frame of references: Applications for conventional and Doppler radar analysis. J. Atmos. Sci., 39, 2279-2300.

Gamache, J.F. and R.A. Houze, 1982: Mesoscale air motion associated with a tropical squall line. Mon. Wea. Rev., 110, 118-135.

Girard, C. and R. List, 1975: Thermodynamics of falling precipitation zones. Pure Appl. Geophysics., 113, 1035-1053.

Goff, R.C., 1976: Vertical structure of thunderstorm outflow. Mon. Wea. Rev., 104, 1429-1440.

Hallett, J., R.I. Sax, D. Lamb, and A.S. Ramachandra Murty, 1978: Aircraft measurements of ice in Florida cumuli. Quart. J. Roy Meteor. Soc., 104, 631-651.

Haman, K.E., 1973: On the updraft-downdraft interaction in convective clouds. Acta Geophys. Pol., XXI, 215-253.

Haman, K.E. and M. Niewiadomski, 1980: Cold downdrafts in cumulonimbus clouds. Tellus, 32, 525-536.

Hane, C.E., 1973: The squall line thunderstorm: Numerical experimentation. J. Atmos. Sci., 30, 1672-1690.

Harris, F.I., 1977: The effects of evaporation at the base of ice precipitation layers: Theory and radar observations, J. Atmos. Sci., 34, 651-672.

Harrison, W.F., B.A. Silverman, and T.M. Engel, 1979: The HIPLEX mesonetwork: Design and description. Preprints, Seventh Conf. on Inadvertent and Planned Weather Modification, Banff, Alberta, Amer. Meteor. Soc., 112-113.

Heymsfield, A.J., D.N. Johnson, and J.E. Dye, 1978. Observations of moist adiabatic ascent in northeast Colorado cumulus congestus clouds. J. Atmos. Sci., 35, 1689-1703.

Heymsfield, A.J. and M.R. Hjelmfelt, 1981: Dynamical and microphysical observations in two Oklahoma squall lines. Part II: In situ measurements. Preprints, 20th Conf. Radar Meteor., AMS, 60-65.

Heymsfield, A.J. and D.J. Musil, 1982: Case study of a hailstorm in Colorado. Part II: Particle growth processes at midlevels deduced from in situ measurements. J. Atmos. Sci., 39, 2847-2866.

Heymsfield, G.M., 1981: Evolution of downdrafts and rotation in an Illinois thunderstorm. Mon. Wea. Rev., 109, 1969-1988.

Hjelmfelt, M.R., 1984: Radar and surface data analysis of a microburst in JAWS. Preprints, 22nd Conf. on Radar Meteor., Amer. Meteor. Soc., 64-69.

Holle, R.L., and M. Maier, 1980: Tornado formation from downdraft interaction in the FACE mesonetwork. Mon. Wea. Rev., 108, 1010-1028.

Holzworth, G.C., 1964: Estimates of mean maximum mixing depths in the contiguous United States, Mon. Wea. Rev., 92, 235-242.

Hookings, G.A., 1965: Precipitation maintained downdrafts. J. Appl. Meteor., 4, 190-195.

Houghton, H.G. and H.E. Cramer, 1951: A theory of entrainment in convective currents. J. Meteor., 8, 95-102.

Houze, R.A., Jr., 1977: Structure and dynamics of a tropical squall-line system. Mon. Wea. Rev., 105, 1541-1567.

Houze, R.A., and A.K. Betts, 1981: Convection in GATE, Rev. Geophys. Space Phys., 19, 541-576.

Houze, R.A., and P.V. Hobbs, 1982: Organization and structure of precipitating cloud systems, Advances in Geophysics, Vol. 24, Academic Press, 225-315.

Hoxit, L.R., C.F. Chappell and J.M. Fritsch, 1976: Formation of mesolows or pressure troughs in advance of cumulonimbus clouds. Mon. Wea. Rev., 104, 1419-1428.

Humphreys, W.J., 1914: The thunderstorm and its phenomena. Mon. Wea. Rev., 42, 348-380.

Johns, R.H. and W.D. Hirt, 1983: The derecho - A severe weather producing convective system. Preprints 13th Conf. Severe Local Storms, Amer. Meteor. Soc., 178-181.

Johnson, R.H. and M. Nichols, 1983: A composite analysis of the boundary layer accompanying a tropical squall line. Mon. Wea. Rev., 111, 308-319.

Jorgensen, D.P., 1984: Mesoscale and convective-scale characteristics of mature hurricanes. Ph.D. dissertation, Colorado State Univ., Ft. Collins, Colorado, 189 pp..

Kamburova, P.L., and F.H. Ludlam, 1966: Rainfall evaporation in thunderstorm downdrafts. Quart. J. Roy. Meteor. Soc., 92, 510-518.

Keller, V.W. and R.I. Sax, 1981: Microphysical development of a pulsating cumulus tower: A case study. Quart. J. Roy. Meteor. Soc., 107, 679-697.

Kitchen, M., and S.J. Caughey, 1981: Tethered balloon observations of the structure of small cumulus clouds. Quart. J. Roy. Meteor. Soc., 107, 853-874.

Klassen, G.P., and T.L. Clark, 1985: On the dynamics of a small cloud associated with the cloud-environment boundary: Two-dimensional simulations in no shear. Submitted to J. Atmos. Sci.

Klemp, J.B., R.B. Wilhelmson, and P. Ray, 1981: Observed and numerically simulated structure of a mature supercell thunderstorm. J. Atmos. Sci., 38, 1558-1580.

Klemp, J.B. and R. Rotunno, 1983: A study of the tornadic region within a supercell thunderstorm. J. Atmos. Sci., 40, 359-377.

Klemp, J.B. and R.B. Wilhelmson, 1978a: The simulation of three-dimensional convective storm dynamics. J. Atmos. Sci., 35, 1070-1096.

Klemp, J.B. and R.B. Wilhelmson, 1978b: Simulations of right- and left-moving storms produced through storm splitting. J. Atmos. Sci., 35, 1097-1110.

Knight, C.A., 1981: 13 June 1974 mature storm study: A small, isolated, steady state convective storm. NCAR Tech. Note 163+STR, 65 pp.

Knight, C.A., 1981: The Cooperative Convective Precipitation Experiment (CCOPE), 18 May - 7 August 1981. Bull. Amer. Meteor. Soc., 63, 386-398.

Knight, C.A., W.D. Hall, and P.M. Roskowski, 1983: Visual cloud histories related to first radar echo formation in notheast Colorado cumulus. J. Clim. Appl. Meteor., 22, 1022-1040.

Knupp, K.R., 1980: Observed characteristics of an intense, quasistationary thunderstorm complex over mountainous terrain. M.S. Thesis, Colorado State University, 196 pp.

Knupp, K.R., 1983a: Doppler radar analysis of the structure of a highly- sheared multicell convective storm. Preprints 21st Conf. Radar Meteorology, AMS, 64-69.

Knupp, K.R., 1983b: On the accuracy of convective storm wind fields determined by dual Doppler radar. Preprints, 21st Conf. on Radar Meteorology, Amer. Meteor. Soc., 542-546.

Knupp, K.R. and W.R. Cotton, 1982a: An intense, quasi-steady thunderstorm over mountainous terrain. Part II: Doppler radar observations of the storm morphological structure. J. Atmos. Sci., 39, 343-358.

Knupp, K.R. and W.R. Cotton, 1982b: An intense, quasi-steady thunderstorm over mountainous terrain. Part III: Doppler radar observations of the turbulent structure. J. Atmos. Sci., 39, 359-368.

Knupp, K.R., and W.R. Cotton, 1982c: Doppler radar case study of downdraft initiation and structure within a moderately-intense thunderstorm. 12th Conference on Severe Local Storms, 11-15 Jan 1982, San Antonio, Amer. Meteor. Soc.

Knupp, K.R. and W.R. Cotton, 1982d: Characteristics of downdrafts and turbulence within thunderstorms. Cloud Physics Conference, Nov. 15-18, 1982, Chicago, IL, Amer. Meteor. Soc.

Knupp, K.R., and W.R. Cotton, 1984: Precipitating convective cloud downdraft structure - A synthesis of observations and modeling, Proceedings of the 9th International Cloud Physics Conf., Tallinn, Estonian SSR, U.S.S.R.

Kropfli, R.A., and L.J. Miller, 1976: Kinematic structure and flux quantities in a convective storm from dual-Doppler radar observations. J. Atmos. Sci., 33, 520-529.

Krumm, W.R., 1954: On the cause of downdrafts from dry thunderstorms over the plateau area of the United States. Bull. Amer. Meteor. Soc., 35, 122-126.

Leary, C.A., 1980: Temperature and humidity profiles in mesoscale unsaturated downdrafts. J. Atmos. Sci., 37, 1005-1012.

Leary, C.A. and R.A. Houze, 1979a: The structure and evolution of convection in a tropical cloud cluster. J. Atmos. Sci., 36, 437-457.

Leary, C.A. and R.A. Houze, 1979: Melting and evaporation of hydrometeors in precipitation from the anvil clouds of deep tropical convection. J. Atmos. Sci., 36, 669-679.

Lemon, L.R., 1976: The flanking line, a severe thunderstorm intensification source. J. Atmos. Sci., 33, 686-694.

Lemon, R.L., and C.A. Doswell, III, 1979: Severe thunderstorm evolution and mesocyclone structure as related to tornadogenesis. Mon. Wea. Rev., 107, 1184-1197.

LeMone, M.A. and E.J. Zipser, 1980: Cumulonimbus vertical velocity events in GATE. Part I: Diameter, intensity and mass flux. J. Atmos. Sci., 37, 2444-2457.

Levy, G., and W.R. Cotton, 1984: A numerical investigation of mechanisms linking glaciation of the ice phase to the boundary layer. Submitted to J. Clim. Appl. Meteor., 23.

MacDonald, A.E., 1976: Gusty surface winds and high level thunderstorms, National Weather Service Western Region Technical Attachment No. 76-14, 5 pp.

MacPherson, J.I. and G.A. Isaac, 1977: Turbulent characteristics of some Canadian cumulus clouds. J. Appl. Meteor., 16, 81-90.

Maddox, R.A., 1980: Mesoscale convective complexes, Bull. Amer. Meteor. Soc., 61, 1374-1387.

Malkus, J.S., 1954: Some results of a trade cumulus cloud investigation. J. Meteor., 11, 220-237.

Malkus, J.S., 1955: On the formation and structure of downdrafts in cumulus clouds. J. Meteor., 12, 350-357.

Marwitz, J.D., 1972a: The structure and motion of severe hailstorms. Part I: Supercell storms, J. Appl. Meteor., 11, 166-179.

Marwitz, J.D., 1972b: The structure and motion of severe hailstorms. Part II: Multicell storms, J. Appl. Meteor., 11, 180-188.

Marwitz, J.D., 1972c: The structure and motion of severe hailstorms. Part III: Severely sheared storms, J. Appl. Meteor., 11, 189-201.

McCarthy, J., 1974: Field verification of the relationship between entrainment rate and cumulus cloud diameter. J. Atmos. Sci., 31, 1028-1039.

Miller, K.S., and M.M. Rochwarger, 1972: A covariance approach to moment estimation. IEEE Trans. on Inf. Theory, IT-18, 588-596.

Miller, L.J., J.E. Dye, and B.E. Martner, 1982: The 25 July 1976 case study: Airflow from Doppler radar observations and conceptual model of circulation. Hailstorms of the Central High Plains. Vol II: Case Studies of the National Hail Research Experiment. C.A. Knight and P. Squires, Eds., Colorado Associated Univ. Press, 229-245.

Miller, L.J., and J.C. Fankhauser, 1983: Radar echo structure, air motion and hail formation in a large stationary multicellular thunderstorm. J. Atmos. Sci.,40, 2399-2418.

Miller, L.J., J.E. Dye, and B.E. Martner, 1983: Dynamical microphysical evolution of a convective storm in a weakly-sheared environment. Part II: Airflow and precipitation trajectories from Doppler radar observations. J. Atmos. Sci., 40, 2097-2109.

Miller, L.J., and C.G. Mohr, 1983: The simple rectification to Cartesian space of folded radial velocities from Doppler radar sampling. Preprints, 21st Conf. on Radar Meteor., Amer. Meteor. Soc., 565-568.

Miller, M.J., 1978: The Hampstead storm: A numerical simulation of a quasi-stationary cumulonimbus system. Quart. J. Roy. Meteor. Soc., 104, 413-427.

Miller, M.J., and A.K. Betts, 1977: Traveling convective storms over Venezuela. Mon. Wea. Rev., 105, 833-848.

Mitchell, K.E. and J.B. Hovermale, 1977: A numerical investigation of the severe thunderstorm gust front. Mon. Wea. Rev., 105, 657-675.

Mohr, C.G., L.J. Miller, and R.L. Vaughan, 1981: An interactive software package for the rectification of radar data to three-dimensional Cartesian coordinates. Preprints, 20th Conf. on Radar Meteor., Amer. Meteor. Soc., 690-695.

Mohr, C.G., and L.J. Miller, 1983: CEDRIC - A software package for Cartesian space editing, synthesis and display of radar fields under interactive control. Preprints, 21st Conf. on Radar Meteor., Amer. Meteor. Soc., 569-574.

Moncrieff, M.W., and J.S.A. Green, 1972: The propagation and transfer properties of steady convective overturning in shear. Quart. J. Roy. Meteor. Soc., 98, 336-352.

Moncrieff, M.W., and M.J. Miller, 1976: The dynamics and simulation of tropical cumulonimbus and squall lines. Quart J. Roy. Met. Soc., 102, 373-394.

Motallebi, Nehzat, 1982: Doppler Radar Observation of the Evolution of Downdrafts in Convective Clouds. M.S. Thesis, Dept. of Atmospheric Science, Colorado State University, Fort Collins, CO 80523. (Atmospheric Science Paper No. 355).

Mueller, C.K. and P.H. Hildebrand, 1983: The structure of a microburst: As observed by ground-based and airborne Doppler radar. Preprints, 21st Conf. on Radar Meteorology, Amer. Meteor. Soc., 602-608.

Musil, D.J., W.R. Sand, and R.A. Schleusener, 1973: Analysis of data from T-28 aircraft penetrations of a Colorado hailstorm. J. Appl. Meteor., 12, 1364-1370.

Musil, D.J., E.L. May, P.L. Smith, and W.R. Sand, 1976: Structure of an evolving hailstorm, Part IV: Internal structure from penetrating aircraft. Mon. Wea. Rev., 104, 596-602.

Musil, D.J., P.L. Smith, J.R. Miller, J.H. Killinger and J.L. Halvorson, 1977: Characteristics of vertical velocities observed in T-28 penetrations of hailstorms. Preprints Sixth Conf. Weather Modification, Amer. Meteor. Soc., 166-169.

Musil, D.J., A.J. Heymsfield, and P.L. Smith, 1982: Characteristics of the weak echo region in an intense High Plains thunderstorms as determined by penetrating aircraft. Preprints Conf. of Cloud Physics, Amer. Meteor. Soc., 535-538.

Nelson, S.P., 1977: Rear flank downdraft: A hailstorm intensification mechanism. Preprints 10th Conf. Severe Local Storms, Amer. Meteor. Soc., 521-525.

Newton, C.W., 1950: Structure and mechanism of the prefrontal squall line. J. Meteor., 7, 210-222.

Newton, C.W., and J.C. Fankhauser, 1975: Movement and propagation of multicellular convective storms, Pure Appl. Geophys., 113, 747-764.

Newton, C.W., and H.R. Newton, 1959: Dynamical interactions between large convective clouds and environment with vertical shear. J. Meteor., 16, 483-496.

Normand, C.W.B., 1938: On stability from water vapor. Quart. J. Roy. Meteor. Soc., 64, 47-69.

Normand, C.W.B., 1946: Energy in the atmosphere. Quart. J. Roy. Meteor. Soc., 72, 145-167.

O'Brien, J.J., 1970: Alternative solutions to the classical vertical velocity problem. J. Appl. Meteor., 9, 197-203.

Ogura, Y., and M.T. Liou, 1980: The structure of a mid-latitude squall line: A case study. J. Atmos. Sci., 37, 553-567.

Orlanski, I., 1975: A rational subdivision of scales for atmospheric properties. Bull. Amer. Meteor. Soc., 56, 527-530.

Orlanski, I., 1976: A simple boundary condition for unbounded hyperbolic flows. J. Comput. Phys., 21, 251-269.

Orville, H.D. and F.J. Kopp, 1977: Numerical simulation of the life history of a hailstorm. J. Atmos. Sci., 34, 1596-1618.

Paluch, I.R., 1979: The entrainment mechanism in Colorado cumuli. J. Atmos. Sci., 36, 2462-2478.

Paluch, I.R., and C.A. Knight, 1984: Mixing and evolution of cloud droplet size spectra in a vigorous continental cumulus, J. Atmos. Sci., 41, 1801-1815.

Paluch, I.R., and D.W. Breed, 1984: A continental storm with a steady, adiabatic updraft and high concentrations of small ice particles: 6 July 1976 case study. J. Atmos. Sci., 41, 1008-1024.

Randall, D.A., 1980: Conditional instability of the first kind upside-down. J. Atmos. Sci., 37, 125-130.

Ray, P.S., B.C. Johnson, K.W. Johnson, J.S. Bradberry, J.J. Stephens, K.K. Wagner, R.B. Wilhelmson and J.B. Klemp, 1981: The morphology of several tornadic storms 20 May 1977. J. Atmos. Sci., 38, 1643-1663.

Ray, P.S., C.L. Ziegler, and W. Bumgarner, 1980: Single- and multiple Doppler radar observations of tornadic storms. Mon. Wea. Rev., 108, 1607-1625.

Raymond, D.J., 1981: Simulation of an air mass thunderstorm using the two-scale model. J. Atmos. Sci., 38, 2014-2020.

Rodi, A.R., K.L. Elmore, and W.P. Mahoney, 1983: Aircraft and Doppler air motion comparisons in a JAWS microburst. Preprints 21st Conf. Radar Meteor., Amer. Meteor. Soc.

Rotunno, R., and J.B. Klemp, 1982: The influence of shear-induced pressure gradients on thunderstorm motion. Mon. Wea. Rev., 110, 136-151.

Ryan, B.F. and J.C. Carstens, 1978: A comparison between a steady-state downdraft model and observations behind squall lines. J. Appl. Meteor., 17, 395-400.

Sinclair, P.C. and J.F.W. Purdom, 1983: The genesis and development of deep convective storms. Final Report for NOAA Grant NA80AA-D-00056, 44 pp.

Sloss, P.W., 1967: An empirical examination of cumulus entrainment. J. Appl. Meteor., 6, 878-881.

Sloss, P.W., and D. Atlas, 1968: Wind shear and reflectivity gradient effects on Doppler radar spectra. J. Atmos. Sci., 25, 1080-1089.

Squires, P., 1958: Penetrative downdraft in cumuli. Tellus, 10, 381-389.

Srivastava, R.C., 1967: A study of the effect of precipitation on cumulus dynamics. J. Atmos. Sci., 24, 36-45.

Srivastava, R.C., and D. Atlas, 1974: Effect of finite radar pulse volume on turbulence measurements. J. Appl. Meteor., 13, 472-480.

Stommel, H., 1947: Entrainment of air into a cumulus cloud, Part I. J. Appl. Meteor., 4, 91-94.

Stommel, H., 1951: Entrainment of air into a cumulus cloud II. J. Meteor., 8, 127-129.

Strauch, R.G. and F.H. Merrem, 1976: Structure of an evolving hailstorm. Part III: Internal structure from Doppler radar. Mon. Wea. Rev., 104, 588-595.

Takeda, T., 1966: Effect of the prevailing wind with vertical shear on the convective cloud accompanied with heavy rainfall. J. Meteor. Soc. Japan, 44, 129-143.

Takeda, T., 1971: Numerical simulation of a precipitating convective cloud: The formation of a long-lasting cloud. J. Atmos. Sci., 28, 350-376.

Thorpe, A.J. and M.J. Miller, 1978: Numerical simulations showing the role of downdraft in cumulonimbus motion and splitting. Quart. J. Roy. Meteor. Soc., 104, 873-893.

Thorpe, A.J., M.J. Miller, and M.W. Moncrieff, 1980: Dynamical models of two-dimensional downdrafts. Quart. J. Roy. Meteor. Soc., 106, 463-484.

Thorpe, A.J., M.J. Miller, and M.W. Moncrieff, 1982: Two-dimensional convection in non-constant shear: A model of mid-latitude squall lines. Quart. J. Roy. Meteor. Soc., 108, 739-762.

Tripoli, G.J. and W.R. Cotton, 1980: A numerical investigation of several factors contributing to the observed variable intensity of deep convection over South Florida. J. Appl. Meteor., 19, 1037-1063.

Tripoli, G.J. and W.R. Cotton, 1981: The use of ice-liquid water potential temperature as a thermodynamic variable in deep atmospheric models. Mon. Wea. Rev., 109, 1094-1102.

Tripoli, G.J., and W.R. Cotton, 1982: The Colorado State University three-dimensional cloud/mesoscale model - 1982. Part I: General theoretical framework and sensitivity experiments. J. de Rech. Atmos., 16, 185-220.

Wade, C.G. and G.B. Foote, 1982: Hailstorms of the Central High Plains, Vol. 2, Part II: 22 July 1976 case study: Low-level airflow and mesoscale influences, Chap.17. C. Knight and P. Squires, Eds., Colo. Assoc. Univ. Press, 115-130.

Wakimoto, R.M., 1982: The life cycle of thunderstorm gust fronts as viewed with Doppler radar and rawinsonde data. Mon. Wea. Rev., 110, 1050-1082.

Warner, J., 1955: The water content of cumuliform cloud. Tellus, 7, 449-457.

Warner, J., 1969: The microstructure of cumulus cloud. Part II. The effect on droplet size distribution of the cloud nucleus spectrum and updraft velocity. J. Atmos. Sci., 26, 1272-1282.

Warner, J., 1970: The microstructure of cumulus cloud. Part III. The nature of the updraft. J. Atmos. Sci., 27, 682-688.

Warner, J., 1975: Comments on "Field verification of the relationship between entrainment rate and cumulus cloud diameter." J. Atmos. Sci., 32, 995-996.

Warner, J., 1977: Time variation of updraft and water content in small cumulus clouds. J. Atmos. Sci., 34, 1306-1312.

Weaver, J.F. and S.P. Nelson, 1982: Multiscale aspects of thunderstorm gust fronts and their effects on subsequent storm development. Mon. Wea. Rev., 110, 707-718.

Weisman, M., and J. Klemp, 1982: The dependence of numerically simulated convective storms on vertical wind shear and buoyancy. Mon. Wea. Rev., 110, 504-520.

Weisman, M.L., and J.B. Klemp, 1984: The structure and classification of numerically simulated convective storms in directionally varying wind shears, Mon. Wea. Rev., 112.

Weisman, M.L., J.B. Klemp, and L.J. Miller, 1983: Modeling and Doppler analysis of the CCOPE August 2 supercell storm. Preprints, 13th Conf. on Severe Local Storms, Amer. Meteor. Soc., 223-226.

Wilhelmson, R.B. and C.S. Chen, 1982: A simulation of the development of successive cells along a cold outflow boundary. J. Atmos. Sci., 39. 1466-1483.

Wilhelmson, R.B. and J. Klemp, 1978: A numerical study of storm splitting that leads to long-lived storms. J. Atmos. Sci., 35, 1974-1986.

Wilhelmson, R.B. and J. Klemp, 1981: A three-dimensional numerical simulation of splitting severe storms on 3 April 1964. J. Atmos. Sci., 38, 1581-1600.

Willis, P.T., J. Hallett, and J.A. Jorden, 1982: The development of precipitation near the top of a marine cloud. Preprints on Cloud Physics, Amer. Meteor. Soc., 211-214.

Wilson, J.W. and T. Fujita, 1979: Vertical cross section through a rotating thunderstorm by Doppler radar. Preprints 11th Conf. Severe Local Storms, Amer. Meteor. Soc., 447-452.

Wilson, J.W., R.D. Roberts, C. Kessinger, and J. McCarthy, 1984: Microburst wind structure and evolution of Doppler radar for airport wind shear detection. J. Clim. Appl. Meteor., 23, 898-915.

Wiggert, V., R.I. Sax, and R.L. Holle, 1982: On the modification potential of Illinois summertime convective clouds, with comparisons to Florida and FACE observations. J. Appl. Meteor., 21, 1293-1322.

Wisner, C., H.D. Orville, and C. Myers, 1972: A numerical model of a hail-bearing cloud. J. Atmos. Sci., 29, 1160-1181.

Wolfson, M., 1983: Doppler radar observations of an Oklahoma downburst. Preprints, 21st Conf. on Radar Meteorology, Amer. Meteor. Soc., 590-595.

Xu, J.-L. and R.F. Reinking, 1982: Vertical continuity of microphysical processes and updrafts in supercooled portions of Florida cumuli. Preprints Conf. on Cloud Physics Conf., Amer. Meteor. Soc., 370-373.

Zipser, E.J., 1969: The role of organized unsaturated convective downdrafts in the structure and rapid decay of an equitorial disturbance. J. Appl. Meteor., 8, 799-814.

Zipser, E.J., 1977: Mesoscale and convective-scale downdrafts as distinct components of squall-line structure. Mon. Wea. Rev., 105, 1568-1598.

Zipser, E.J., and M.A. LeMone, 1980: Cumulonimbus vertical velocity events in GATE. Part II: Synthesis and model core structure. J. Atmos. Sci., 37, 2458-2469.

APPENDIX A. DOPPLER RADAR ACCURACY, REDUCTION AND SYNTHESIS

Wind fields derived from multiple Doppler radar contain errors due to (1) uncertainties in measurements of radial velocity, and (2) assumptions made in subsequent objective analysis and synthesis of the data. The following subsections outline data editing and synthesis procedures and present some details on accuracy and resolution of derived wind fields.

A.1 Radial Velocity Accuracy

Raw Doppler radar data are obtained at finite points along radials separated by roughly one degree in azimuth and elevation. Spacing of data points along the radial typically varies between 150 and 450 m. Sampling over a 0.8 - 1.2 degree pencil beam essentially acts as a low-pass filtering operation in which amplitudes with scales at smaller than the lateral beam dimension (Fig. A.1) are severely attenuated

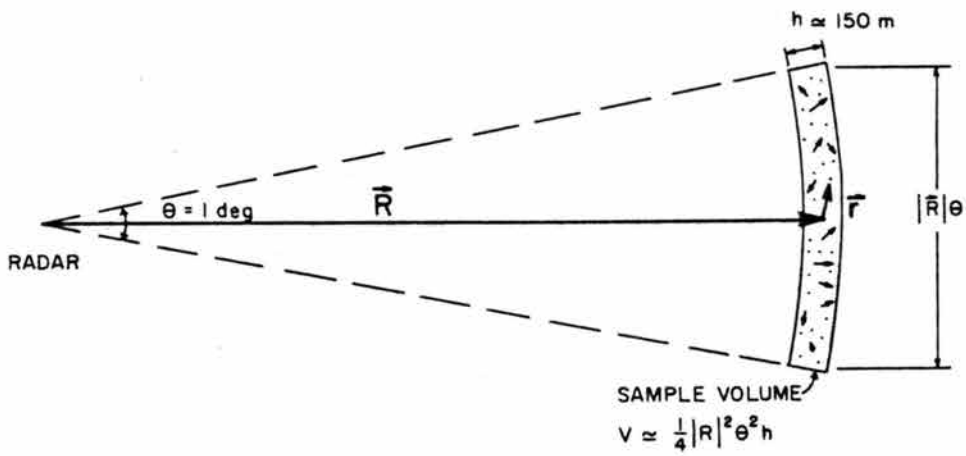

Fig. A.1. Schematic of a radar sampling volume.

(see Srivastava and Atlas, 1974). Because the lateral beam dimension increases linearly with range, minimum resolvable scales therefore also increase with range.

Measured radial velocity (V_R) is actually a filtered value weighted by radar reflectivity (Z) according to (see Doviak et al., 1979)

$$V_R(\vec{R}) = \frac{\int_{vol} V_R(\vec{r})\ I(\vec{R},\vec{r})\ Z(\vec{r})\ d\vec{r}}{\int_{vol} N(\vec{r})\ I(\vec{R},\vec{r})\ d\vec{r}} \quad , \tag{A.1}$$

where I is the beam illumination function and $\vec{R}$, $\vec{r}$ are position vectors defined in Fig. A.1. Because 10^6 - 10^8 particles lie within a typical illuminated volume (Fig. A.1), a velocity spectrum is produced. For pulsed Doppler radars, spectral moments [reflectivity, mean radial velocity (V_R) and variance of the Doppler spectrum (σ_v^2)] are typically estimated from time series consisting of usually 64 samples by a pulse-pair covariance technique (Miller and Rochwarger, 1972).

If I ($\vec{R}$, $\vec{r}$) exhibits significant amplitude at solid angles greater than two degrees from the primary beam center such that velocity information is extracted from the outer fringes (i.e, side lobes are significant), then the true radial velocity at $\vec{R}$ may not be well-represented by $V_R(\vec{R})$ in regions of high wind and reflectivity gradients, a problem considered by Sloss and Atlas (1968).

Fig. A.2 illustrates how artificial divergence in radial velocity (V_r) may be generated for 2-D motion when such gradients coexist. For this ideal case, uniform shear flow with w = 0 is superimposed on a 2-D reflectivity pattern similar to that observed. Resulting radar-measured winds within the given reflectivity exhibit the qualitative behavior shown in Fig. A.2. Artificial divergence ($\partial V_R/\partial r > 0$) and a

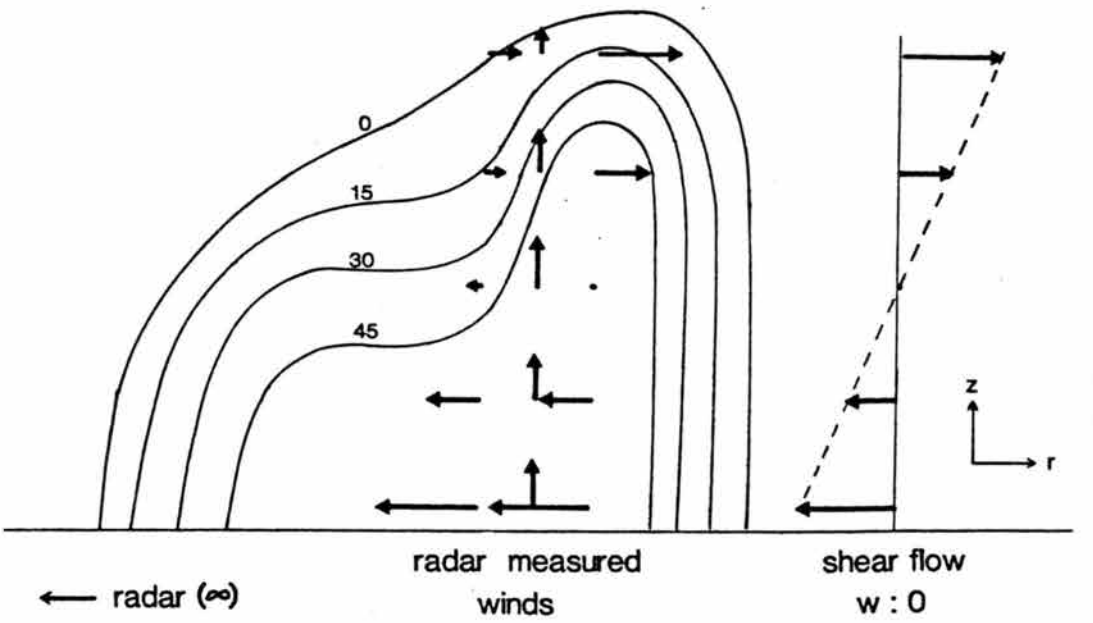

Fig. A.2. Schematic illustrating how artificial analyzed divergence and vertical motion (obtained by continuity) are produced when uniform shear flow with w = 0 is superimposed on the reflectivity pattern as shown. Contours are labeled in dBZ.

corresponding updraft are produced in the upper half where $\partial Z/\partial r > 0$ (Z is reflectivity factor) due to side lobe contamination from higher Z and different V_R at low levels. A requirement for generation of such artificial divergence is

$$\frac{\partial}{\partial z}\left(\frac{\partial Z}{\partial r}\right) \neq 0$$

in the presence of $\partial V_R/\partial z \neq 0$ over the solid angle of the primary beam and side lobes. In severe storms which commonly exhibit high reflectivity and large wind shear, this effect can conceivably lead to considerable error in measured radial velocity, particularly in upper cloud regions.

A.2 Data Editing and Synthesis

Raw Doppler radar data are normally edited to eliminate bad radial velocities and are unfolded to correct aliased velocities. In this study two different methods were employed to accomplish this editing. As shown in Table 3.1, SPACE Doppler data were edited in radar space and then interpolated to a Cartesian grid. This interpolation was done using a spherical filter having inverse distance linear weighting such that points at the volume center received a weight of unity while points at and beyond the maximum radius were weighted at zero. Radii ranged between 1.0 and 1.5 km for the two cases examined. Such a low-pass filtering operation reduces peak amplitudes of 1 - 1.5 km motion scales by ~0.5 (see Frank and Foote, 1982). The number of radar points contributing to each Cartesian grid point typically ranged between 10 and 100.

The CCOPE data were edited and interpolated using a more efficient method outlined by Miller and Mohr (1983). Raw unedited radar data are first interpolated to a Cartesian grid using a bilinear interpolation between 4 adjacent beams, two separated in azimuth and two separated in elevation as shown in Fig. A.3. Averaging of data points in the radial direction may also be done prior to interpolation to increase the number of points used. A quality field proportional to the standard deviation of points included in the interpolation can be used to delete noisy data in subsequent editing stages. Once the data are interpolated to Cartesian grid points, editing and synthesis of wind components and other manipulations were accomplished in batch mode using software documented in Mohr and Miller (1983). While this interpolation process also acts as a low-pass filtering operation, smaller scales will

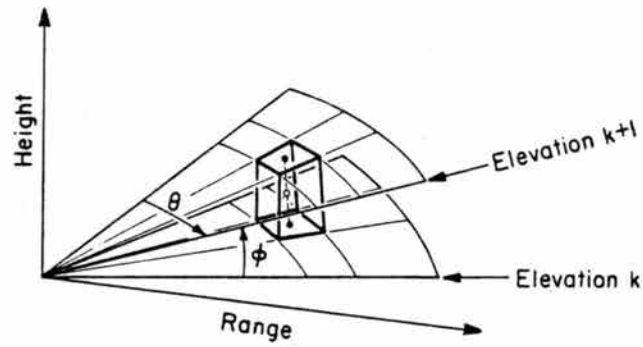

Fig. A.3. Illustration of sampling volume used for Cartesian rectification. The volume is defined by the eight adjacent radar space samples surrounding a Cartesian location in space. Solid dots indicate projection points of the Cartesian grid location (shown as an open dot) on consecutive elevation scan planes k and k + 1. From Mohr et al. (1981).

typically be passed with this process than with the spherical interpolation process described above.

Because data are usually acquired over a 2-5 minute time period, corrections due to advection of data points from ground-relative storm motion need to be applied. This problem has been analyzed in detail by Gal-Chen (1982). In this study simpler advection corrections based on observed movement speeds were applied only to Cartesian grid point data for all cases considered.

Once in final edited form, radial velocity data from two or more radars were synthesized to form horizontal velocity components. Such a process utilizes a least squares solution to the dual or triple Doppler radar equations (see Bohne and Srivastava, 1975). The dual Doppler solution is subject to geometrical errors from contamination by nonzero particle motion. The general magnitude and distribution of such errors are described in Knupp (1983).

Vertical motion is obtained by integrating the anelastic mass continuity equation, downward from echo top,

$$w = \rho^{-1} \left[(\rho w_{top}) + \int_{z}^{z_{top}} \rho \left(\frac{\partial u}{\partial x} + \frac{\partial v}{\partial y} \right) dz \right], \qquad (A.2)$$

where a boundary condition

$$w_{top} = \frac{DIV_{top} \, (\Delta z)}{2}$$

is assumed. This condition, equivalent to setting w = 0 one half grid point above, is considered a good approximation since cloud top is typically ~ 500 m above radar echo top [(see Knight et al., 1983)]. Horizontal divergence is calculated in finite difference from using a centered 3-point finite difference formulation on u,v velocity components, which were smoothed with a 9-point horizontal Hanning filter prior to calculating divergence. This additional low pass filtering operation further increases resolvable scales such that w velocity amplitudes of 2-3 km horizontal scale are reduced by ~ 0.5 in the analysis.

A.3 Errors in Derived Wind Fields

Errors in derived wind fields originate from several sources, listed in order of inferred importance: (1) radial velocity bias discussed in Section A.1; (2) improper advection correction procedures; (3) boundary condition errors; (4) evolution of velocity fields during the time taken to scan a volume; (5) errors in estimating radial velocity from the Doppler spectrum (i.e., turbulence); and (6) random errors due to a fluctuating Doppler spectrum. While determination of individual effects is impossible, collective errors may be inferred in the w field by examining patterns at the lowest grid level where errors have accumulated in the downward integration. Such an examination

indicates maximum grid point errors of up to 15 m/s in w. Regional patterns, however, exhibit more well-behaved w fields at low levels due to the fact that downward integration of Eq. (A.2) tends to dampen errors since density decreases with height according to

$$\rho(z) \simeq \rho_o \, e^{-z/10}.$$

Errors in the horizontal velocity components are usually considered to be ~1-2 m/s, while errors in w are $\pm$ 5 m/s. However, in regions of strong reflectivity and radial velocity gradients (Section A.1), errors in each may be over twice as large.

APPENDIX B. DOPPLER RADAR CHARACTERISTICS AND DATA QUALITY

Doppler radar data presented in previous sections were acquired from one of six radars listed in Table B.1. Three of the radars used during the 1977 South Park Area Cumulus Experiment (SPACE), CP-3, NOAA-C and NOAA-D, exhibited less sensitivity than in the 1981 Cooperative Precipitation Experiment (CCOPE). All radars have beamwidths (defined as the angular separation between half-power points) around one degree. Minimum reflectivities during the CCOPE program were such that boundary layer echoes (~ -10 dBZ_e) could be detected. All radars recorded reflectivity factor and mean radial velocity, generally determined in real time by a covariance (pulse-pair) technique from on-board processors. During the 1977 SPACE program the X-band NOAA radars recorded complete time series which allowed calculation of Doppler spectra by post processing.

In each experiment processing problems were detected after the fact. The CP-3 radar exhibited sticking-bit processing problems which were apparently most significant during the first half of the SPACE program. Effects of this malfunction surfaced as biases toward zero in radial velocity in regions of weak return power. The magnitude of such a bias for the SPACE data presented herein was not determined, but appeared to be small. During the CCOPE program the CHILL radar displayed a similar processor problem. For the 12 June case CHILL

radial velocity data quality was generally poor in echo regions having reflectivity factors less than ~ 20 dBZ_e.

Tables B.2-B.5 list scanning characteristics for each radar of each case study. For the 26 July and 4 August 1977 SPACE cases (Tables B.2 and B.3) data quality is considered good despite the fact that successive scans were spaced ~ 10 min in time and typically lasted 5 min. Close ranges between each radar and storm allowed good spatial resolution, and consequently multiple Doppler-derived flow fields were qualitatively good. The CCOPE data (12 June and 1 August - Tables B.4 and B.5) were generally acquired at greater frequency in shorter times, but longer radar-to-storm distances degraded spatial resolution. Consequently, generally poorer results (due to effects described in Appendix A) were generated wherever large reflectivity gradients were measured, particularly in the 12 June case.

Table B.1. Doppler radar parameters

Parameter	Radar CP-2	CP-3,4	NOAA-C,D	CHILL
Wavelength(cm)	10.7	5.5	3.2	10.9
Beamwidth(deg)	1.0	1.1	0.8	1.0
Peak Power(kw)	1000	200	12.5	600
Pulse duration(μs)	1.0	1.0	1.0	1.0
Antenna gain(dB)	44.0	42.5	44.0	43.3
Min. reflectivity at 10 km (dBZ_e)	-23	-19	-12	-18
No. of samples in estimate	64	64,128*	64,128*	32,64*
Max. unambiguous range (km)	156	120*	75*	154
Max. unambiguous velocity (m/s)	25.7	19.5*	16.1*	26.7

* These parameters varied.

Table B.2. Doppler radar scanning characteristics for 26 July 1977 (SPACE)

Volume time(MDT)	Radar	Begin time (MDT)	End time (MDT)	Total time (s)	Δ elev. (deg)	Δ azim. (deg)	Δ r (km)	Range to target core(km)
1738	3	1738:01	1743:02	301	5.0	0.8	0.16	10
	C	1738:00	1742:01	241	1.5	1.3	0.30	28
	D	1738:17	1741:02	165	1.8	2.0	0.45	24
1754	3	1754:32	1801:13	379	5.0	0.8	0.16	10
	C	1754:31	1758:16	225	1.5	1.3	0.30	30
	D	1754:32	1757:32	180	1.7	2.0	0.45	25
1804	3	1803:30	1810:13	377	5.0	0.8	0.16	10
	C	1803:26	1808:26	300	1.5	1.3	0.30	30
	D	1803:35	1807:55	260	1.5		0.45	25
1813	3	1813:00	1819:43	403	5.0	0.8	0.16	10
	C	1813:06	1818:46	340	1.5	1.1	0.30	30
	D	1813:00	1817:00	240	1.5	2.0	0.45	30
1821	3	1820:30	1827:21	411	5.0	0.8	0.16	10
	C	1820:46	1826:26	340	1.5	1.1	0.30	30
	D	1820:46	1825:16	280	1.5	2.0	0.45	30
1829	3	1829:01	1832:53	232	5.0	0.8	0.16	10
	C	1829:02	1834:53	351	1.0	2.15	0.30	32
	D	1828:50	1832:50	240	1.0	2.0		32
1846	3	1846:35	1851:10	275	5.0	0.8	0.16	15
	C	1846:14	1850:01	227	1.0	1.8	0.30	36
	D	1846:21	1850:32	251	1.0	1.8	0.45	36

Table B.2. (cont)

Volume time(MDT)	Radar	Begin time (MDT)	End time (MDT)	Total time (s)	Δ elev. (deg)	Δ azim. (deg)	Δ r (km)	Range to target core(km)
1852	3	1852:00	1856:38	278	5.0	0.8	0.16	16
	C	1852:02	1857:01	299	1.0	1.8	0.30	45
	D	1851:57	1855:57	240	1.0	18	0.45	45
1913	3	1912:30	1917:18	288	1.0	0.8	0.16	37
	C	1912:38	1917:02	264	1.5	2.1	0.225	19
	D	1912:32	1917:20	288	2.1	2.1	0.45	11
1920	3	1919:20	1923:54	274	1.0	0.8	0.16	40
	C	1919:26	1924:02	264	1.5	2.1	0.225	24
	D	1919:38	1923:14	276	2.1	1.9	0.45	15
1932	3	1932:37	1933:51	74	5.0	0.8	0.16	40
	C	1932:02	1935:02	180	2.0	2.1	0.225	24
1941	3	1941:00	1945:34	274	1.0	0.8	0.16	40
	C	1941:02	1944:38	216	1.5	2.1	0.225	25
1948	3	1948:00	1952:21	261	1.0	0.8	0.16	40
	C	1948:02	1952:14	252	1.5	2.1	0.225	25

Table B.3. (cont)

Volume time(MDT)	Radar	Begin time (MDT)	End time (MDT)	Total time (s)	Δ elev. (deg.)	Δ azim. (deg.)	Δ r (km)	Range to target core (km)
1433	3	1432:30	1435:36	186	1.0	0.8	.16	49
	C	1432:35	1437:35	300	1.0	1.4	.375	28
1443	3	1442:31	1445:22	171	1.0	0.8	.16	53
	C	1442:45	1446:45	240	1.0	1.5	.375	33
1450	3	1450:00	1452:52	172	1.0	0.8	.16	57
	C	1450:07	1454:22	255	2.0	1.6	.375	38
1504	3	1503:30	1505:53	143	1.0	0.8	.16	62
	C	1503:39	1507:09	210	1.0	1.5	.375	42

Table B.4. Doppler radar scanning characteristics for 12 June 1981 (CCOPE)

Volume time(MDT)	Radar	Begin time (MDT)	End time (MDT)	Total time (s)	Δ elev. (deg)	Δ azim. (deg)	Δ r (km)	Range to target core(km)
1637	2	1637:21	1638:43	82	1.0	0.5	0.20	55
	H	1636:39	1639:00	141	1.6	0.5	0.15	35
	3	1637:15	1639:21	126	0.5	0.6	0.23	85
	D	1637:09	1639:57	168	0.6	0.5	0.15	80
1642	2	1641:56	1643:35	99	0.5	0.9	0.20	57
	3	1641:36	1643:42	126	0.5	0.6	0.23	82
	D	1642:22	1644:34	132	0.6	0.6	0.15	79
1648	2	1648:15	1650:03	108	0.5	0.8	0.20	57
	H	1647:29	1650:05	154	2.0	0.6	0.15	29
1651	2	1650:07	1651:53	106	0.5	0.8	0.20	58
	H	1652:12	1654:42	150	2.0	0.6	0.15	28
	C	1652:26	1654:42	136	1.3	0.4	0.30	60
	3	1652:36	1653:41	65	1.0	0.6	0.23	76
1655	2	1655:04	1657:03	119	0.5	0.8	0.20	58
	H	1654:43	1657:58	195	2.0	0.6	0.15	26
	3	1654:54	1655:59	65	0.6	0.9	0.23	73
	4	1654:08	1656:07	119	1.0	0.5	0.23	89

Table B.4. (cont)

Volume time(MDT)	Radar	Begin time (MDT)	End time (MDT)	Total time (s)	Δ elev. (deg)	Δ azim. (deg)	Δ r (km)	Range to target core(km)
1704	2	1704:19	1706:10	111	0.8	0.5	0.20	58
	H	1704:30	1707:53	203	4.1	0.6	0.15	23
	3	1704:30	1706:38	68	0.6	0.5	0.23	70
	4	1704:30	1706.29	119	1.0	0.5	0.23	87
1711	2	1710:41	1712:25	104	0.7	0.5	0.20	59
	3	1708:56	1711:05	129	0.5	0.6	0.23	65
	4	1710:51	1712:58	127	1.0	0.5	0.23	83
1717	2	1716:45	1718:26	101	0.7	0.5	0.20	60
	C	1717:05	1719:28	133	0.9	1.0		50
1720	2	1720:13	1721:53	100	0.6	0.5	0.20	59
	H	1720:28	1724:07	219	4.0	0.4	0.15	15
	C	1719:33	1721:54	141	0.9	1.0	0.30	50
	3	1721:14	1723:21	127	0.5	0.6	0.23	60
1729	2	1729:22	1731:00	98	0.6	0.5	0.20	62
	H	1729:11	1732:41	210	4.0	0.6	0.15	14
	C	1729:38	1732:00	142	0.9	1.0	0.30	48
	3	1729:00	1731:06	126	0.6	0.5	0.23	57
	4	1729:00	1731:00	120	1.0	0.5	0.23	77

Table B.4. (cont)

Volume time(MDT)	Radar	Begin time (MDT)	End time (MDT)	Total time (s)	Δ elev. (deg)	Δ azim. (deg)	Δ r (km)	Range to target core(km)
1740	2	1740:33	1741:59	86	0.4	0.5	0.20	67
	H	1740:38	1743:41	183	4.0	0.6	0.15	13
	C	1740:00	1743:10	190	1.0	0.9	0.30	44
1748	2	1747:24	1748:48	84	0.4	0.5	0.20	69
	H	1748:00	1751:29	209	4.0	0.5	0.15	14
	4	1748:00	1750:00	120	1.0	0.5	0.23	69
	C	1748:00	1750:22	142	1.3	0.9	0.30	42
	D	1748:07	1749:07	60	0.8	0.6	0.15	65
1753	2	1753:19	1754:51	92	0.4	0.5	0.20	70
	C	1752:55	1755:16	141	1.2	0.9	0.30	41
	3	1752:12	1753:52	100	0.6	0.8	0.23	45

Table B.5. Doppler radar scanning characteristics for 1 August 1981 (CCOPE)

Volume time(MDT)	Radar	Begin time (MDT)	End time (MDT)	Total time (s)	Δ elev. (deg)	Δ azim. (deg)	Δ r (km)	Range to target core(km)
1635	2	1635:50	1637:38	108	0.6	0.4	0.15	80
	H	1635:44	1638:13	139	0.5	0.5	0.15	55
	3	1635:31	1637:53	142	3.7	0.9	0.23	25
	C	1635:54	1638:32	158	2.5	1.9	0.15	25
	D	1634:45	1637:05	140	1.0	1.1	0.15	40
1851	2	1851:33	1853:38	125	1.0	0.6	0.15	50-100
	H	1851:02	1853:57	175	1.0	0.5	0.15	40-90
	3	1851:31	1854:34	183	2.0	0.9	0.15	20-50

APPENDIX C. CLOUD MODEL EQUATIONS AND PARAMETERIZATIONS

Section 6 contains a summary of a series of experiments designed to examine the sensitivity of downdraft structure on cloud model microphysical parameterizations. To aid the reader in relating these parameterizations to model framework, the prognostic equations and relevant kinematic equations and parameterizations are listed and briefly described below in Section C.1. Section C.2 describes the diagnostic model heavily exercised in Sections 4, 5 and 6. This model borrows equations of melting and evaporation from the cloud model. All symbols are defined at the end of this section.

C.1 The CSU Cloud Model

The CSU cloud model consists of a full set of nonhydrostatic compressible dynamic equations, a thermodynamic equation, and a set of microphysical equations for water- and ice-phase cloud and precipitation. The 10 prognostic equations averaged over some resolvable grid scale for a Cartesian grid system are:

(1) the equations of motion (for prediction of u_i),

$$\frac{\partial}{\partial t}(\rho_o \bar{u}_i) = - \frac{\partial \overline{p'}}{\partial x_i} - \delta_{i3}\, g(\overline{\rho_a'} + r_T) + \rho_o\, ADV(\bar{u}_i) + \rho_o\, TURB(\overline{u_i}) + \varepsilon_{ijk}\, f_j\, \overline{u_k'} \quad ; \tag{C.1}$$

(2) the fully elastic continuity equation (for prediction of ρ_a'),

$$\frac{\partial \overline{\rho_a'}}{\partial t} = - \frac{\partial}{\partial x_j} (\rho_o \overline{u_j}); \tag{C.2}$$

(3) the microphysical equations (for prediction of mixing ratios of total water, rain, ice crystals, graupel and aggregates, respectively),

$$\frac{\partial \bar{r}_T}{\partial t} = ADV(\bar{r}_T) + TURB(\bar{r}_T) - PR_r - RP_i - RP_g - PR_a \,, \tag{C.3}$$

$$\begin{aligned}\frac{\partial \bar{r}_r}{\partial t} = {} & ADV(\bar{r}_r) + TURB(\bar{r}_r) + PR_r + VD_{vr} + CL_{cr} + CN_{cr} \\ & - CL_{ri} - CL_{rg} - CL_{ra} + ML_{gr} + ML_{ar} \\ & + SH_{gr} + SH_{ar},\end{aligned} \tag{C.4}$$

$$\begin{aligned}\frac{\partial \bar{r}_i}{\partial t} = {} & ADV(\bar{r}_i) + TURB(\bar{r}_i) + PR_i + VD_{vi} - ML_{iv} + SP_{vi} \\ & + NUA_{vi} + NUB_{vi} + NUC_{vi} + NUD_{vi} \\ & + CL_{ci} + CL_{ri} - CL_{ig} - CN_{ig} \\ & - CL_{ia} - CN_{ia},\end{aligned} \tag{C.5}$$

$$\begin{aligned}\frac{\partial \bar{r}_g}{\partial t} = {} & ADV(\bar{r}_g) + TURB(\bar{r}_g) + PR_g + VD_{vg} + CL_{cg} \\ & + CL_{rg} + CL_{ig} + CL_{ag} + CN_{ig} + CN_{ag} \\ & - ML_{gr} - SH_{gr}\end{aligned} \tag{C.6}$$

$$\frac{\partial \bar{r}_a}{\partial t} = ADV(\bar{r}_a) + TURB(\bar{r}_a) + PR_a + VD_{va} + CL_{ca}$$

$$+ CL_{ra} + CL_{ia} - CL_{ag} + CN_{ig} - CN_{ag}$$

$$- ML_{ar} - SH_{ar}; \qquad (C.7)$$

(4) and the thermodynamic energy equation,

$$\frac{\partial \theta_{il}}{\partial t} = ADV(\theta_{il}) + TURB(\theta_{il})$$

$$- \frac{\theta_{il}^2}{\theta} \frac{[L_{vl} PR_r + L_{iv}(PR_g + PR_i + PR_a)]}{\max(T,253)} \quad . \qquad (C.8)$$

All scalar and vector quantities may be decomposed as $A = A_o + A' + A''$, where basic state values have zero subscripts, deviations from basic state values (e.g., updrafts and downdrafts) are single primed, and turbulent fluctuations upon deviations from basic state values are double primed.

The advective and turbulence operators acting on a quantity A in (C.1) - (C.8) are defined in Tripoli and Cotton (1982) as

$$ADV(\overline{A}) = - \frac{1}{\rho_o} \frac{\partial}{\partial x_k} \left[(\rho_o \overline{u_j} \bar{A}) - A \frac{\partial}{\partial x_k} (\rho_o \overline{u_j}) \right] \qquad (C.9)$$

and

$$TURB(\bar{A}) = - \frac{\partial}{\partial x_k} [\overline{A'' u_j''}]. \qquad (C.10)$$

Turbulent fluxes for velocity and scalar variables are obtained from the first-order closure schemes

$$\overline{u_i'' \, u_j''} = - K_m \left[\frac{\partial \overline{u_i}}{\partial x_j} + \frac{\partial \overline{u_j}}{\partial x_i} \right], \tag{C.11}$$

$$\overline{\varphi'' u_j''} = - K_H \frac{\partial \bar{\varphi}}{\partial x_j}, \tag{C.12}$$

where the eddy exchange coefficients K_H and K_m are related by $K_H = 3 K_m$. In the cloud model K_m is expressed as (Cotton and Tripoli, 1978)

$$K_m = [(0.25)^2 \, 2^{-1/2}] \, \Delta^2 \, |D_{ij}^2| \, (1 - K_H K_m^{-1} R_i) \tag{C.13}$$

where Δ (the mixing length), D_{ij} (the deformation tensor), and R_i (the modified Richardson number) are all defined in Tripoli and cotton (1982).

Standard temperature variables are related to θ_{il} through the expressions (from Tripoli and Cotton, 1982)

$$\theta = \theta_{il}[1 + (L_{lv} r_l + L_{iv} r_{ice}/C_p \, \mathrm{MAX}(T,253)]$$

and

$$T = \theta \left(\frac{p}{p_{oo}}\right)^{R/c_p}.$$

Finally, pressure perturbations are diagnosed from the linearized equation of state

$$\frac{1}{\gamma} \frac{p'}{p_o} = \frac{\overline{\rho_a'}}{\rho_o} + \frac{\overline{\theta'}}{\theta_o} + 1.61 \, \bar{r}_v \tag{C.16}$$

Cooling rates within cloud model downdrafts are determined from parameterized equations for melting and sublimation of graupel and aggregates, and evaporation of rain. The rain evaporation equation is

$$VD_{rv} = \left[0.5 + 0.349 \left[\frac{(\rho_w g \rho_o R_m^3)^{1/2}}{\mu^{1/2}} \right] \right] G(T,p)(S-1)\ R_m^{-2}\ \rho_o^{-1}\ \overline{r_r} \qquad (C.17)$$

which is derived from diffusion theory, modified for drop motion (ventilation) and integrated over the drop spectrum.

Here, $S = r_v/r_{vs}$ is relative humidity and the thermodynamic function G(T,p) is defined as

$$G(T,p) = \frac{1}{\frac{\varepsilon L_{vl}^2}{KRT^2} + \frac{RT}{\varepsilon D_v e_s}} \quad . \qquad (C.18)$$

Sublimation from graupel and aggregate particles is given as:

$$VD_{vg} = (S_i - 1)\ G(T,p)\ K_{3g} \qquad (C.19)$$

$$VD_{va} = \frac{4.03 D_a^{-1.4}}{\beta_1}\ G(T,p)\ f_2(Re_a)(S_i - 1)\ \overline{r}_a, \qquad (C.20)$$

where

$$K_{3g} = [0.76 \rho_g^{-1} D_g^{-2}] \overline{r}_g^{-2/3} + [1.28 (\frac{g\rho}{\mu^2 C_D \rho_g^3})^{1/4}\ D_g^{-5/4}]\ \overline{r}_g \qquad (C.21)$$

and

$$\beta_1 = .015 \text{ g cm}^{-2.4}$$

Equations for melting of graupel and aggregates are, respectively,

$$ML_{gr} = \frac{K_{3g}}{L_{il}}\Big[[K(T-T_f) + D_v L_{iv}\rho_o(\overline{r_v}-r_{vs}(T_f))] \qquad \begin{matrix}(a) \\ \\ \\ \end{matrix} \qquad \begin{matrix}(b) \\ \\ \\ \end{matrix}$$

$$-\frac{c_w}{L_{il}}(T-T_f)(CL_{cg}+CL_{rg})\Big]h(T - T_f) \qquad (c) \qquad (C.22)$$

$$ML_{ar} = \frac{4.03f_2(Re_a)}{L_{il}\beta_1}\Big[[K(T-T_f)+D_v L_{iv}\rho_o(\overline{R}_v=r_{sl}(T_f))]D_a^{-1.4}\,\overline{r_a} \qquad \begin{matrix}(a) \\ \\ \\ \end{matrix} \qquad \begin{matrix}(b) \\ \\ \\ \end{matrix}$$

$$-\frac{c_w}{L_{il}}(T-T_f)(CL_{ca}+CL_{ra})\Big]\,h(T - T_f) \qquad (c) \qquad (C.23)$$

where $T_f = 273.16$ K and $h\,(T - T_f)$, the heaviside step function, is unity when the argument is greater than zero, and zero otherwise.

Individual terms labeled in Eqs. (C.22) and (C.23) represent the following physical processes; (a) conduction of heat to the ice particle by air, (b) latent heating by condensation of water vapor on the ice particle surface (this also acts to cool the particles if $T_w \leq 0$), and (c) transfer of heat from cloud and rainwater, which the ice particle is collecting.

Equations (C.17), (C.19) and (C.20) were derived assuming that raindrops and ice particles (graupel and aggregates) obey exponential size distributions of the form

$$\phi(r) = \frac{NR}{R_m} \exp\left(-\frac{r}{R_m}\right) \tag{C.24}$$

for raindrops and

$$\phi(d) = \frac{k}{D_m} \exp\left(-\frac{d}{D_m}\right) \tag{C.25}$$

for ice particles. Values of R_m (.027 cm), D_{mg} (0.1 cm), and D_{ma} (0.33 cm), characteristic sizes of rain, graupel and aggregates are typical values derived from observations (see Tripoli and Cotton, 1982). The sensitivity of downdraft structure to changes in R_m, D_m is examined in Section 6.

C.2 Diagnostic Model Description

In Sections 4, 5 and 6 a diagnostic model is used to estimate thermodynamic quantities along given downdraft trajectories computed from Doppler data, given velocity u_i and radar reflectivity factor Z_e along a particular trajectory. A description of this diagnostic model is given here.

Multiple Doppler analyses will commonly produce four products, the velocity components (u_i) and reflectivity factor (Z_e) as function of space (x_i) for discrete times. Because the vertical velocity component is usually derived from integration of the anelastic mass continuity equation, the velocities are in anelastic balance, with errors included. The kinematic values along a given downdraft trajectory can be used with

a simplified thermodynamic equation and other assumptions to estimate thermodynamic variables.

First, estimates of rainwater and graupel mixing ratios are obtained from a reflectivity-water content (Z-M) relation and assumed vertical profiles of relative rain-graupel mass fraction. The Z-M relation used here has the form

$$M = \left(\frac{Z_e}{10^4}\right)^{0.4} \qquad (g\ m^{-3}) \tag{C.26}$$

which is similar to formulae for rain derived empirically by Douglas (1964). In this case, the exponent was adusted so that water contents were not excessive for reflectivity factors exceeding 50 dBZ_e. Table C.1 lists values of M for selected Z_e. Eq. (C.26) must be used with caution, whenever large particles may be present, since large particles would produce high reflectivities ($\sim D^6$) but low water contents. Precipitation mixing ratio was then obtained from $(\bar{r}_g + \bar{r}_r) = M/\rho_o$.

Table C.1. Precipitation contents (M) for given Z_e as computed from $M = (Z_e/10^4)^{0.4}$

Reflectivity factor (dBZ_e)	Precipitation content ($g\ m^{-3}$)
0	0.03
10	0.06
20	0.16
30	0.40
40	1.00
50	2.51
60	6.31

A second major assumption regards the partition of total precipitation into rain and graupel mixing ratios. To this end, observations and cloud model output were used to construct general vertical profiles thought to be representative of distributions within downdrafts. Aircraft observations (e.g., Heymsfield and Musil, 1982) often indicate that downdrafts are composed primarily of ice-phase precipitation above the melting level in Great Plains storms.

Using this observation it is assumed that the graupel fraction, defined as $f_g = \overline{r_g}/(\overline{r_g} + \overline{r_r})$, varies linearly with height, being 1.0 one kilometer above the melting level (probably conservative) and generally falling off to some fraction two kilometers below the melting level. Specific formula used in each case are given in Table C.2

Table C.2. Graupel fraction (f_g) formula used in the case studies

Case	Formula		Comments
7/26/77 (SPACE)[1]	$f_g =$ Z/3	(Z < 3)	Sporadic hail at the surface
	1.0	(Z > 3)	
8/4/77 (SPACE)[1]	"		Probably very little hail at the surface
6/12/81 (CCOPE)[2]	$f_g =$ 0.40 (Z - 0.8)	(Z > 3.3)	Some hail possible; radar signature
	1.0	(Z < 3.3)	
8/1/81 (CCOPE)[3]	$f_g =$ 0.4 (Z - 1.3)	(Z > 3.8)	Numerous reports of large hail
	1.0	(Z < 3.8)	

Once $\overline{r_g}$ and $\overline{r_r}$ have been estimated, the thermodynamic energy equation can be applied. For this model it has the following form in which temperature changes are accomplished only by water phase transition (mixing and radiation are ignored):

$$\frac{d\bar{\theta}}{dt} = \frac{\theta_o}{c_p T_o}(L_{vl}(VD_{rv} + VD_{cv}) + L_{vi} \cdot VD_{gv} + L_{il} \cdot ML_{gr}), \tag{C.27}$$

where rain evaporation (VD_{rv}) is given by Eq. (C.17), graupel sublimation is given by Eq. (C.19), and graupel melting is given by a truncated form of Eq. (C.22) in which the accretion term (c) has been deleted. VD_{cv} is a rate of cloud condensation or evaporation which is obtained by calculating the adiabatic liquid water content, $\overline{r_c} = r_{vslcl} - r_{vs}(T)$. It is assumed that the cloud is composed entirely of liquid water which maintains saturation and which evaporates immediately if subsaturated conditions are encountered.

Water vapor mixing ratio varies according to the amount of rain and cloud evaporation/condensation and graupel sublimation/desposition along a trajectory:

$$\frac{d\bar{r}_v}{dt} = - VD_{vc} - VD_{vr} - VD_{vg}$$

The final two equations allow one to make inferences on downdraft thermodynamics. For example, total accumulated cooling produced by evaporation and melting can be computed along trajectories. Moreover, the two following buoyant acceleration components can be obtained:

$$g\,(\overline{r_g} + \overline{r_r} + \overline{r_c}) \quad , \qquad \text{(loading)}$$

$$g\,(\frac{\theta_v'}{\theta_{vo}}) \quad . \qquad \text{(thermal buoyancy)}$$

One may also draw inferences on the behavior of perturbation pressure along the trajectory by two methods. In the first, the

pressure gradient force can be inferred (assuming that pressure buoyancy and eddy-stress terms are small) by forming the residual

$$-\frac{1}{\rho_o}\frac{\partial p'}{\partial z} = \frac{dW}{dt} - g\left(\frac{\theta_v'}{\theta_{vo}} - gr_T - \frac{c_v}{c_p}\frac{p'}{p_o}\right) \qquad (C.28)$$

where values on the RHS are estimated from Doppler data and from kinematic model output and $\overline{r_T} = \overline{r_g} + \overline{r_r} + \overline{r_c}$.

Using an alternative procedure, the behavior of pressure along a streamline can be inferred (assuming steady state) using a Bernoulli (energy) equation of the form (Moncrieff and Miller, 1976)

$$\frac{1}{2}V^2 + \frac{p'}{\rho_o} + \int_{z_o}^{z} g\left(\frac{\theta_v'}{\theta_{vo}} - r_T\right) dz = \frac{1}{2}V_o^2 = \text{const along a streamline,}$$

where $V^2 = u^2 + v^2 + w^2$ is kinetic energy along the trajectory and $V_o^2 = u_o^2 + v_o^2 + w_o^2$ is the initial (kinetic) energy in the undisturbed environment. Here, $p'(z)$ can be solved as a residual when all other parameters are known or can be easily estimated. This application is truly accurate only for steady conditions when streamlines and trajectories coincide.

List of Symbols

Symbol	Definition
A	Any time dependent variable
AC	Accretion tendency of one water category by another (s^{-1})
ADV	Advective operator
CL	Collection of one water category by another (s^{-1})
CN	Conversion tendency between two water categories (s^{-1})
C_p	Heat capacity of dry air ($C_p = 1003 \times 10^3$ J K^{-1} kg^{-1})
C_w	Coefficient of heat for water
d	Ice particle diameter (cm)
D_{ij}	Deformation tensor
D_a	Characteristic diameter of aggregates distribution (0.33 cm)
D_g	Characteristic diameter of graupel distribution (0.1 cm)
D_v	Diffusivity of water vapor in air
f	Coriolis parameter
FR	Freezing tendency of liquid water (s^{-1})
g	Acceleration due to gravity (9.8 m s^{-1})
K	Thermal conductivity of air
K_H	Eddy exchange coefficient for heat (m^2 s^{-1})
K_m	Eddy exchange coefficient for momentum (m^2 s^{-1})
L_{il}	Latent heat of freezing (J kg^{-1})
L_{iv}	Latent heat of sublimation (J kg^{-1})
L_{lv}	Latent heat of vaporization (J kg^{-1})
m_d	Molecular weight of dry air (kg/mole)
m_w	Molecular weight of water (kg/mole)
M	Precipitation water density
ML	Melting tendency (s^{-1})

n	Number concentration of precipitation-sized particles
N_R	Raindrop concentration
NU	Tendency for nucleation of ice from vapor (s^{-1})
P	Total pressure (kPa)
PR_k	Precipitation tendency of water phase k (s^{-1})
P_{oo}	100 kPa
R	Gas constant for dry air (287 J K^{-1} kg^{-1})
R_m	Characteristic radius of raindrop distribution (.027 cm)
r	Raindrop radius
r_c	Mixing ratio of cloud water
r_g	Mixing ratio of graupel
r_i	Mixing ratio of ice crystals
r_l	Mixing ratio of ice water
r_r	Mixing ratio of rain water
r_T	Total mixing ratio of condensate
r_v	Mixing ratio of water vapor
r_{is}	Saturation mixing ratio with respect to ice
r_{vs}	Saturation mixing ratio with respect to water
r_{ice}	Mixing ratio of frozen water
R_i	Richardson number
RM_{ik}	Riming rate of one phase ay another (s^{-1})
S_i	Saturation with respect to ice ($S_i = r_v/r_s$)
S_v	Saturation with respect to water ($S_v = r_v/r_{vs}$)
SH	Shedding tendency
t	Time (s)
T	Temperature (K)
T_f	Temperature of the melting point of water (273.16 K)

T_v	Virtual temperature [$T_v = T(1+0.61\ r_v)$]
u_i	Velocity tensor in Cartesian coordinates (m s^{-1})
V	Magnitude of the three-dimensional wind vector
V_g	Mean terminal velocity of graupel (m s^{-1})
V_i	Mean terminal velocity of ice crystals (m s^{-1})
V_r	Mean terminal velocity of rainwater (m s^{-1})
VD	Vapor deposition tendency
X_i	Vapor deposition tendency
Z	Radar reflectivity factor
Z_e	Equivalent radar reflectivity factor
γ	C_p/C_v
ε	Molecular weight of water vapor
Γ	Moist adiabatic lapse rate for potential temperature
Δ	Mixing length
δ_{ig}	Kroneker delta function
ϕ	Any scalar time-dependent variable
ρ	Total density of air (kg m^{-3})
ρ_a	Density of dry air (kg m^{-3})
ρ_w	Density of liquid water
ρ_s	Density of graupel
θ_{il}	Ice liquid water potential temperature (K)
θ_v	Virtual potential temperature
μ	Dynamic viscosity